Edge Plasma Phenomena in the Alcator C-Mod Tokamak measured by High Resolution X-Ray Imaging Diagnostics

by

Thomas Sunn Pedersen

Submitted to the Department of Physics
in partial fulfillment of the requirements for the degree of

Doctor of Philosophy

at the

MASSACHUSETTS INSTITUTE OF TECHNOLOGY

June 2000

Author .....
Department of Physics
February 16, 2000

Certified by .....
Robert S. Granetz
Principal Research Scientist
Thesis Supervisor

Certified by .....
Miklos Porkolab
Professor of Physics
Thesis Supervisor

Accepted by .....
Thomas J. Greytak
Professor, Associate Department Head for Education

Edge Plasma Phenomena in the Alcator C-Mod Tokamak measured by High Resolution X-Ray Imaging Diagnostics

by

Thomas Sunn Pedersen

Submitted to the Department of Physics
on February 16, 2000, in partial fulfillment of the
requirements for the degree of
Doctor of Philosophy

Abstract

In this thesis high resolution soft x-ray measurements from the Alcator C-Mod plasma edge are presented for a variety of different plasma conditions. These measurements provide radial profiles of the soft x-ray emissivity with 1.5 mm resolution or better, and temporal resolution down to 12 μs. These profiles show a distinct and very narrow pedestal shape in H-mode, indicative of the H-mode transport barrier. The soft x-ray emissivity pedestal at the outboard edge is typically 10 mm inside the last closed flux surface, near the top of the electron density and temperature pedestals. Modelling shows that the inward shift of the x-ray pedestal implies an inward shift of the impurity density pedestal. This inward shift is explained by an inward impurity pinch located in the region of strong electron density gradient, as predicted by neoclassical impurity transport theory. Calculations using the impurity transport code MIST support the existence of a neoclassical-like inward pinch. Changes in the soft x-ray pedestal width can be interpreted as changes in the edge impurity diffusion coefficient. We find several scaling laws of the edge diffusion coefficient with various plasma parameters in EDA H-mode.

A second array views the top of the plasma. The x-ray emissivity measured with this array also shows a distinct and narrow pedestal in H-mode. However, it is located significantly closer to the separatrix and is often narrower. Both of these differences increase with the safety factor at the edge, q_{95}. Thus, there is a significant poloidal asymmetry in the impurity density in the H-mode edge region, which increases with q_{95}. Therefore, the impurity transport in the H-mode edge is highly two-dimensional. The strong poloidal asymmetries measured show some quantitative agreement with theories developed to explain poloidal impurity asymmetries. However, none of the theories are stricly applicable to the Alcator C-Mod edge, and they all significantly underestimate the actual asymmetries that we observe.

Thesis Supervisor: Robert S. Granetz
Title: Principal Research Scientist

Thesis Supervisor: Miklos Porkolab
Title: Professor of Physics

Acknowledgments

This thesis would not have been possible without the help, support and guidance that I have received since I arrived at MIT. First, I would like to thank my advisor, Dr. Robert Granetz, for the countless hours he spent with me, teaching me hands-on diagnostic techniques, helping me with everything from the fundamental physics to the secrets of postscript files, as well as constantly inspiring me with his energy, enthusiasm, and always good spirit. I would also like to thank him for introducing me to cold water diving off the coast of New England. I would like to thank the whole Alcator group, including fellow graduate students, for the constructive criticism and support that I have received. In particular I would like to thank Professor Ian Hutchinson, Dr. Earl Marmar, Dr. John Rice, Dr. Jim Terry, Dr. Steve Wolfe, and Professor Miklos Porkolab, whose ideas, suggestions, and insights I have used extensively in my thesis.

I would also like to acknowledge the financial support I have received from the Danish Research Academy and the MIT Alcator Group.

Last but not least I would like to thank my wife Ann and my son Kasper for their support and patience.

Contents

Chapter 1

Introduction

1.1 Controlled thermonuclear fusion as a future energy source

The global demand for energy is projected to continue to grow rapidly in the 21st century. At present, most of this energy demand is met by burning fossil fuels, but the reserves of fossil fuels are shrinking. Presently, it is believed that the reserves of oil and natural gas will be exhausted within 100 years[1]. It is also becoming increasingly clear that the carbon dioxide released into the atmosphere when fossil fuels are burned is likely to cause global warming as a result of the greeenhouse effect. It is therefore important to find sustainable, environmentally safe alternatives to fossil fuels for energy production. Nuclear fusion, which releases nuclear energy by fusing light nuclei into heavier ones, would be a highly sustainable source of energy. It would release no carbon dioxide or other polluting chemicals, produce small amounts of benign radioactive waste, and small amounts of harmless helium gas. In addition, a fusion power plant would be inherently much safer than a fission power plant, since the reactor will only contain small amounts of the fusion fuel at any given time, eliminating the risk of runaway processes such as those which have led to accidents

[1]This number depends on estimates of the reserves of oil and natural gas, predictions of the growth in the human population on Earth, and estimates of the future energy consumption per capita.

in fission power plants. The fusion process envisioned for the first commercial fusion power plants is the following:

$$ {}^{3}_{1}\mathrm{T} + {}^{2}_{1}\mathrm{D} \rightarrow {}^{4}_{2}\mathrm{He} + {}^{1}_{0}\mathrm{n} + 17.6\,\mathrm{MeV} \tag{1.1} $$

Deuterium is a naturally occurring isotope of hydrogen, and can be extracted from sea water in quantities sufficient to cover many millions of years of energy consumption. Tritium is radioactive and is not present in significant amounts on Earth. It can, however, be bred from lithium. There is enough lithium available on land that the D-T fusion process can meet our energy demands for thousands of years, and much larger reserves are available on the bottom of the oceans. 80 % of the 17.6 MeV fusion power released in each fusion process is carried by the neutron, and the rest is carried by the α particle.

The fusion process in Equation 1.1 has a very high activation energy. If it is to happen spontaneously at a non-negligible rate in a thermonuclear reactor, the D-T mix must have a very high temperature, on the order of 15 keV (165 million Kelvin). At these temperatures, the D-T mix is a fully ionized plasma. The basic idea behind magnetic confinement fusion is to confine the charged particles of the plasma in a magnetic field. The energetic α particle must be confined by the magnetic field so that it can transfer its energy to the bulk plasma. If the fusion power from the α particles thus delivered to the deuterium/tritium plasma exceeds the various energy loss mechanisms, such as radiation losses, and energy transport across the magnetic field lines, the fusion process can sustain itself without external heating sources, and *ignition* is achieved. The energetic neutrons created in the D-T fusion process escape the magnetic field and must be absorbed in a thick blanket material surrounding the fusion plasma resulting in some activation of the blanket material and plasma facing components. The energy deposited in the blanket can then be converted into electricity. The best magnetic confinement has been achieved in the tokamak configuration [1], which was developed in the former Soviet Union in the 1960's [2]. No magnetic confinement device has achieved sufficient energy confinement and fusion power to reach ignition, although

progress has been very significant [2]. Ignition is likely to be reached within the next 20 years, in a future large scale experiment such as the International Thermonuclear Experimental Reactor (ITER), which is one of several proposed experiments which would be able to reach ignition. For readers unfamiliar with the concepts introduced in this section, excellent reviews of the basic physics of plasmas, magnetic confinement, thermonuclear fusion, and the tokamak confinement concept can be found in [3], [4], [1], [5].

1.2 The Alcator C-Mod tokamak project

The Alcator C-Mod tokamak, the second largest tokamak project in the United States, is located at the M.I.T. Plasma Science and Fusion Center in Cambridge, MA. It is regularly operated at currents up to 1.5 MA and toroidal magnetic fields of 7.9 T, electron densities of up to 10^{21} m^{-3}, and central electron temperatures near 5 keV. It has a major radius of 68 cm, and a minor radius of 22 cm. It is usually operated in a shaped, elongated, lower x-point configuration. The high magnetic field, high density operational range is unique for shaped tokamaks, and thus provides important measurements of plasma parameters in the regime relevant for the compact, high field tokamak approach to a fusion reactor [7].

1.3 Tokamak transport phenomena

1.3.1 Anomalous transport

The cross-field transport of particles, momentum, and energy in tokamak experiments, although superior to other magnetic confinement concepts, is usually orders of magnitude larger than the predictions of neoclassical theory. This "anomalous" transport is due to the existence of turbulent fluctuations. There is a large number of plasma instabilities which could potentially be causing the turbulent fluctuations.

[2]For instance, the JET tokamak achieved 16 MW of fusion power with about 25 MW of heating power in a D-T plasma in 1996

1.3.2 L-mode and H-mode

In the low confinement mode (L-mode), the transport is highly anomalous across the whole plasma profile, which results in low global confinement of particles and energy. If the plasma heating is increased above a certain threshold, a spontaneous transition occurs to a state where the confinement is improved significantly in a narrow region near the last closed flux surface. Because of the confinement improvement, this new state is called the high confinement mode (H-mode). The H-mode was discovered on the ASDEX tokamak in 1982 [8]. The phenomenon is not fully understood, but is believed to be caused by a suppression of the turbulence in the edge region, thus reducing the turbulent transport. In the region of reduced transport, often referred to as the *transport barrier*, a large radial electric field exists. It is generally believed that the turbulence is suppressed because of the sheared $E \times B$ flow caused by the radially varying electric field [6]. The reduction in transport leads to very sharp gradients in various plasma parameters such as electron and ion temperature and density in the edge region. As a result, the radial profiles of these quantities become pedestal-like, and the transport barrier region is therefore also known as the *pedestal* region.

1.3.3 H-mode confinement and ELMs

It has been found experimentally that the core electron and ion temperatures are very sensitive to the edge values [9], [10]. Such observations are also predicted from *stiff* transport models, such as the ion temperature gradient (ITG) model [11]. In agreement with these findings, experiments show that the increased confinement at the edge in H-mode not only raises the edge temperatures and densities, but also improves the core confinement. This results in an increase in the global energy confinement, as measured by the energy confinement time, by a factor of 2-3. It also results in increased particle and impurity confinement times which can be as much as 50 times larger than the L-mode values. The increased energy confinement compared to L-mode makes the H-mode a very attractive confinement mode for a future fusion reactor. The even stronger increase in impurity confinement represents a problem

though, because it means that the impurities accumulate, and may eventually lead to a radiative collapse of the H-mode. It is imperative to limit the impurity density in order to reach ignition, because the impurities dilute the fuel and increase the radiative losses significantly. Impurities are always present in trace amounts in experiments because of the plasma interactions with material walls and other invessel components. In a burning fusion reactor, helium will also be continually produced in the central plasma region. One mechanism for degrading the impurity and particle confinement is to trigger repeated edge localized modes (ELMs) [12]. ELMs are short bursts of instabilities in the pedestal region, which transiently increase the edge transport and carry particles and heat into the scrape-off layer. Thus, an ELMy H-mode can be steady-state, combining good energy confinement with a particle and impurity confinement which is still much higher than L-mode, but low enough to achieve an acceptable steady state density and impurity density. Although the global energy confinement is not strongly degraded, the transient power loss during an ELM is high, and this is a significant power load on the plasma facing components, in particular the divertor structure. If one scales up the transient heat loads during ELMs to a reactor size tokamak, these heat loads become unacceptable. A continuous mechanism for degrading the H-mode particle and impurity confinement, without significantly degrading the energy confinement, is therefore highly desirable. Such a confinement mode has been found in Alcator C-Mod. This H-mode is called the Enhanced D_α (EDA) H-mode after one of its signatures, an increased level of D_α radiation compared to normal H-mode values [13]. In EDA H-mode, the particle and impurity particle confinement times are much reduced compared to ELMfree H-modes, while the energy confinement is only slightly lower than that of ELMfree H-modes. This makes the EDA H-mode a very attractive confinement mode for a future reactor, but at this point it can only be produced reliably in Alcator C-Mod, although it may have been observed on other tokamaks [14], [15]. It is necessary to understand the underlying physics of this mode in order to obtain this mode in other experiments (such as a future fusion reactor based on the tokamak concept). Therefore, one of the present goals of the Alcator C-Mod experiment is to increase our understanding

of the EDA H-mode.

1.4 The importance of high-resolution edge x-ray measurements

As mentioned in the previous section, it is very important for the overall goal of the magnetic confinement fusion program to understand improved confinement modes, in particular those which can be run in steady-state in a future reactor, such as the EDA H-mode. In order to understand the physics of the H-mode barrier, it is necessary to have detailed measurements of plasma quantities such as temperatures and densities of the plasma components (ions, electrons, and the various impurity ions). This will help us understand the underlying physics of the transport barrier, so that an accurate theoretical basis can be developed. We must understand the basic physics in order to predict the character of the H-mode transport barrier in a future fusion reactor. It is a very challenging task to obtain adequate radial resolution of the H-mode transport barrier in the Alcator C-Mod tokamak, because the transport barrier region is very narrow, often less than 10 mm. This means that radial resolution on the order of a few millimeters is required. High temporal resolution is also desirable in order to study fast phenomena such as ELMs, L to H-mode transitions, H to L-mode back transitions, etc. The first diagnostic on Alcator C-Mod to provide coverage of the whole transport barrier region with close to 1 millimeter resolution was the edge soft x-ray array, with a 12 μs time resolution and a 1.5 mm radial resolution, installed and operated in the 1997-1998 run campaign. As we will show in this thesis, measurements from this diagnostic provide detailed information about the radial transport of impurities in the H-mode transport barrier, thus improving our understanding of impurity confinement in H-mode, in particular in the EDA H-mode. Since impurity accumulation is a problem in H-mode discharges, this is important for the overall goal of the tokamak fusion program. The two-array soft x-ray diagnostic which was designed and installed for the 1999 run campaign, provides information about the impurity transport in the

poloidal direction, in addition to the radial direction. It also provides a way to measure the poloidal propagation of edge instabilities, so that one can gain insight into the underlying physics of these instabilities. This thesis describes the soft x-ray diagnostics, the analysis of the measurements made with the diagnostics, and the physics results which can be extracted.

1.5 Overview of the thesis

The first soft x-ray diagnostic was installed prior to the 1997-1998 run campaign. Chapter 2 describes the diagnostic, and the calibration procedures used. In Chapter 3 we outline the various software analysis routines which have been developed, e.g. to process the raw data into radial profiles of soft x-ray emissivity. Chapter 4 describes many of the measurements of edge plasma phenomena obtained with this diagnostic. The radiative processes responsible for the soft x-ray emission from the edge plasma are analyzed in Chapter 5. This analysis is complicated, and requires spectroscopic information about the intrinsic impurities, as well as some knowledge of the electron density and temperature, and some knowledge of the impurity transport near the plasma edge. We establish that one can infer the density profile of medium Z impurities (fluorine and neon) from the measurements of the soft x-ray emissivity, if the electron density and temperature profiles are known in the edge region with high accuracy. Recent additions of other high resolution edge diagnostics, in particular a visible continuum diagnostic from which the electron density profile can be derived with millimeter radial resolution, have made it possible to perform such a detailed analysis, deriving impurity density profiles from the soft x-ray profiles. These profiles can in turn provide information about the radial impurity transport in the H-mode edge, a topic which is investigated in Chapter 6 and Chapter 7. We find that many of our observations of soft x-ray emissivity profiles yield important information about the transport in EDA and ELMfree H-modes. An algorithm to automatically determine if a given plasma discharge is in H-mode or L-mode is presented in Chapter 8. Prior to the 1999 run campaign, the soft x-ray diagnostic was upgraded to two si-

multaneous views of the plasma edge, one at the top of the plasma, and one at the outboard edge just above the midplane. The details of the new two-array diagnostic are described in Chapter 9. The results obtained from the two new arrays are described in Chapter 10. These measurements show that there are poloidal asymmetries in the soft x-ray emissivity, implying that poloidal, as well as radial, impurity transport is important in the H-mode transport barrier region. Possible theoretical explanations for the observed phenomena are discussed in Chapter 11. Finally, the main conclusions are summarized in Chapter 12.

Chapter 2

Description and calibration of the first edge x-ray array

The first x-ray edge array, which was installed in Alcator C-Mod in March 1997 and operated until April 1998, consisted of an array of 38 PIN photodiodes viewing the edge plasma through a slit aperture, 0.5 mm in the poloidal direction and 36 mm in the toroidal direction. Figure 2-1 shows the layout of the diagnostic. Each photodiode is rectangular and extends 0.94 mm in the poloidal direction and 4 mm in the toroidal direction. The photodiodes are operated in the photovoltaic mode and produce a current which is proportional to the incident photon power, such that

$$P_{incident} = c \times I_{detector} \tag{2.1}$$

where $c \approx 3.6$ W/A. The simple relationship in Equation 2.1 is valid for photon energies in the range 10 eV-20 keV. Outside this range, the photo diodes are less sensitive. A 10 μm beryllium foil located behind the aperture cuts out all photons with $h\nu$ below 0.6 keV but transmits almost all photons with $h\nu$ above 2 keV (see Figure 2-3). The beryllium filter ensures that photons with energies less than 10 eV are not transmitted. The low plasma temperature at the edge (typically in the range 50-800 eV) ensures that there is negligible radiation in the hard x-ray region above 20 keV photon energy, so therefore Equation 2.1 is true for the edge plasma radiation which is transmitted by the beryllium filter.

The aperture is located 175 mm from the center of the detector array, and the viewing chords of adjacent detectors are separated by roughly 1 mm in the radial direction in the confined plasma region. The system was designed so that the center photodiode would be viewing along a chord tangent to the last closed flux surface (LCFS), since other diagnostic measurements indicated that the H-mode pedestal region is at or near the LCFS.

2.0.1 Data acquisition

The currents in the detectors are amplified before digitization and storage. The amplification circuit is designed such that each detector sees zero impedance, otherwise the simple relationship in Equation 2.1 does not apply. The amplified signals are then digitized and stored on disk, and can subsequently be read from the XTOMO data tree, which is part of the Alcator C-Mod data storage structure.

The sampling rate can be set up to 83.3 kHz (12 μs sampling time) but frequencies above 5 kHz are not amplified as much as lower frequencies because of the frequency response of the amplification circuit[1]. The RC time constant is 30 μs, that is, an instantaneous jump in incident photon power would be seen as a gradual exponential rise in signal level with a time constant of 30 μs. It is possible to decrease the time constant of the amplification circuit but this would reduce the signal to noise ratio. Detector currents are measured before each plasma discharge so that the baseline (dark current) of each detector can be estimated and subtracted. Finally, the measured currents can be converted into detected photon power by Equation 2.1.

2.1 Calibration of the first edge x-ray array

2.1.1 Absolute calibration

The absolute position of the detector viewing chords was determined at the bottom of the machine with an uncertainty of less than 1 mm with respect to the inner divertor

[1] 5 kHz is the 3dB point for the amplification circuit

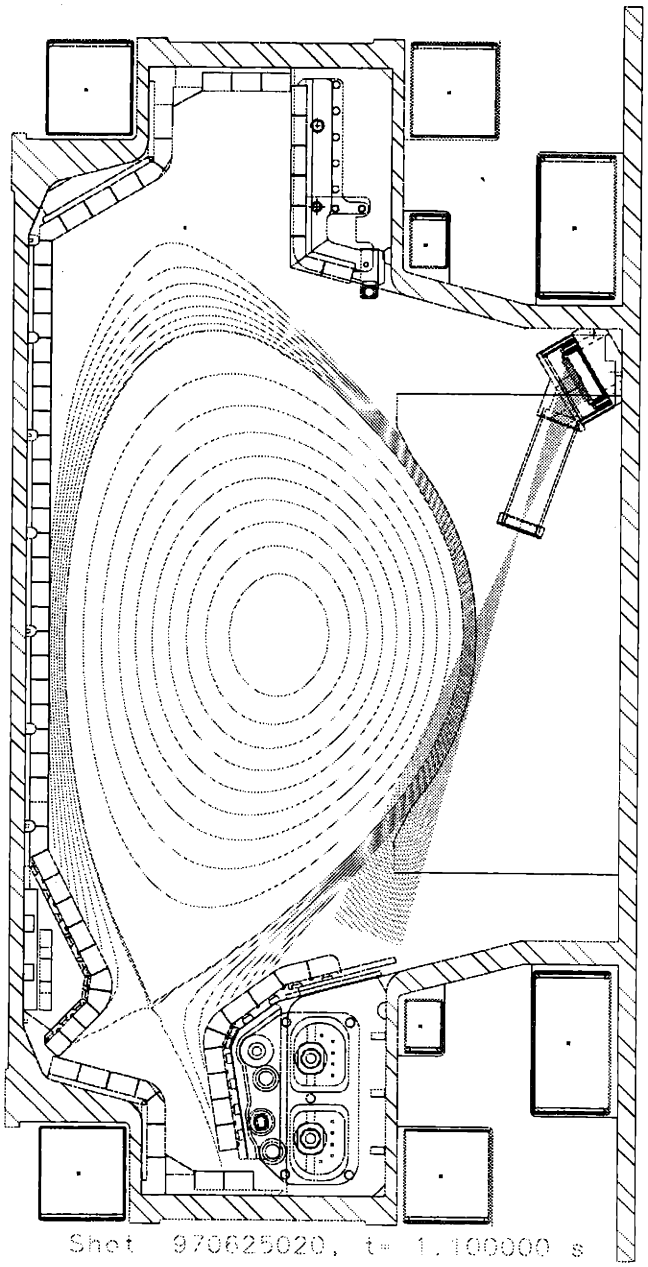

Figure 2-1: CAD drawing of the edge x-ray array in Alcator C-Mod. The yellow lines show the views of the 38 detectors. Flux surfaces for a typical plasma are also shown in blue.

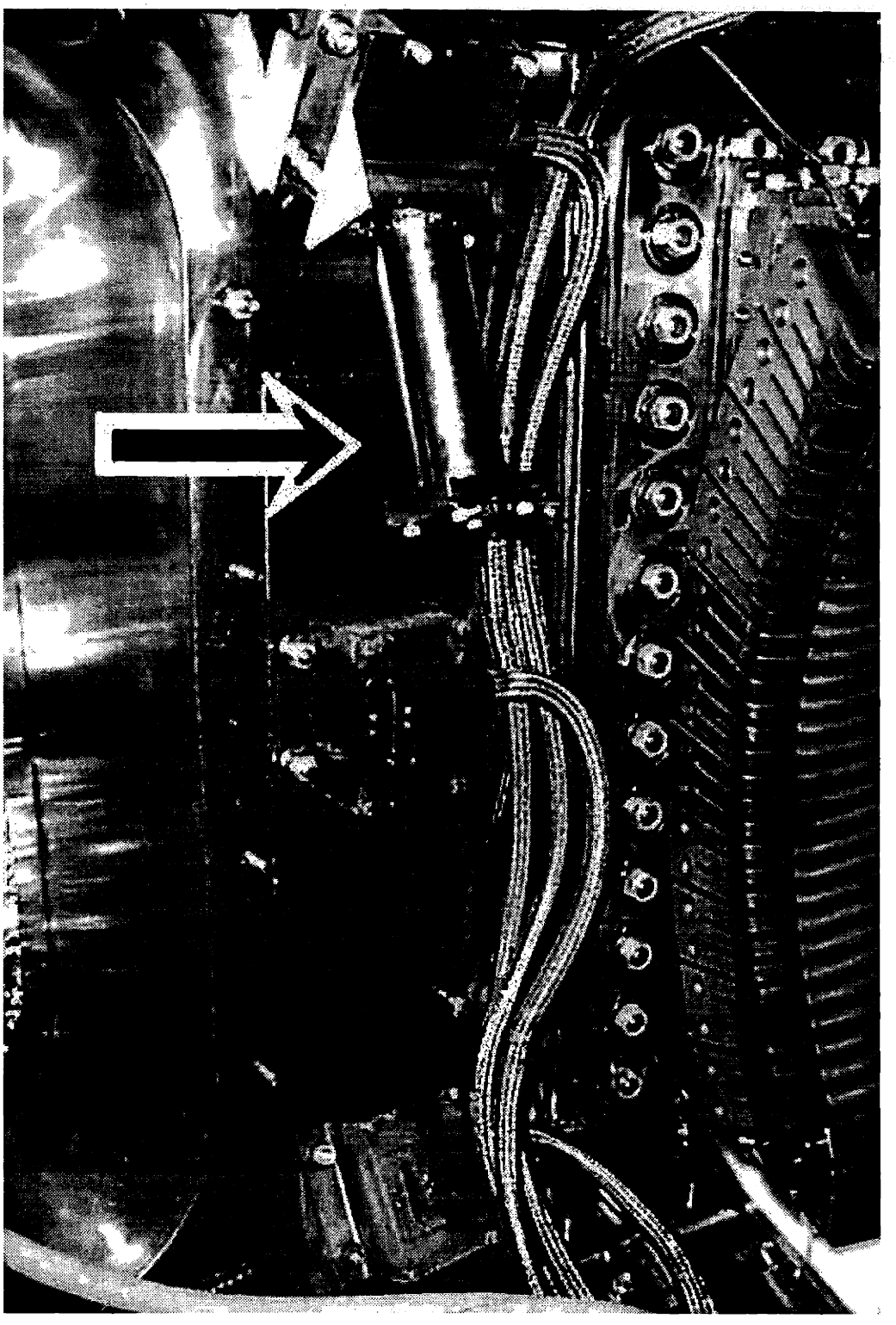

Figure 2-2: A photo of the edge x-ray imaging system, indicated by an arrow, as installed in the Alcator C-Mod vacuum vessel.

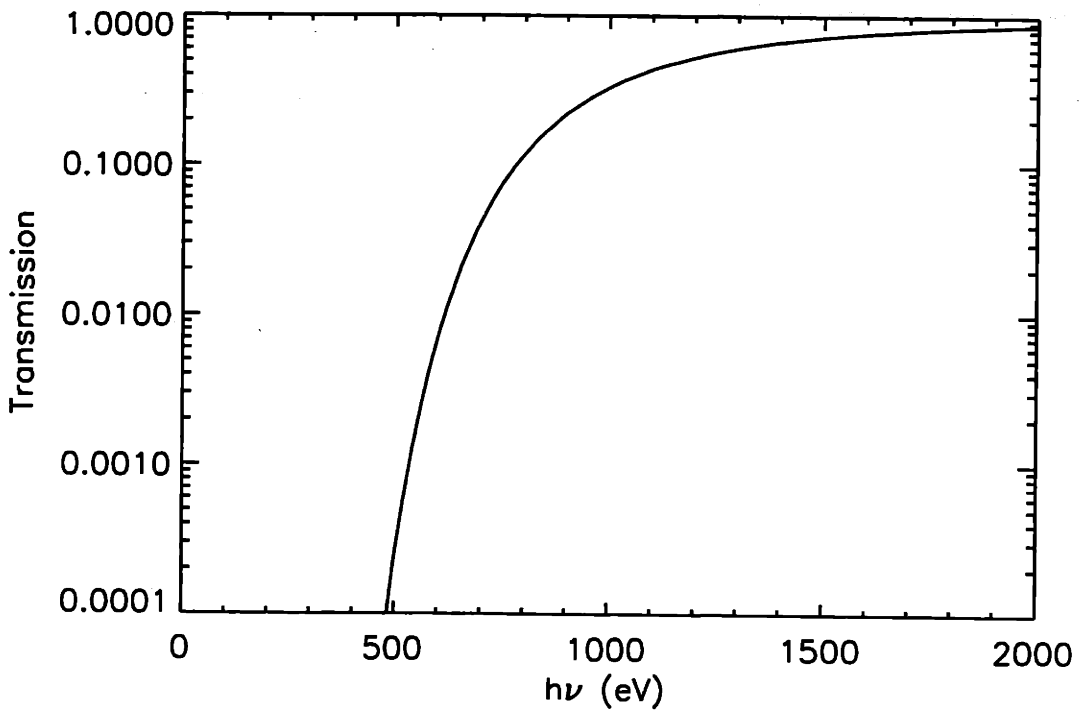

Figure 2-3: Plot of the transmission coefficient for the 10 μm beryllium filter. The filter cuts out essentially all photons with hν below 500 eV and transmits most photons above 2 keV.

tiles, whose positions are known to within 1 mm. These measurements were made prior to the 1997 experimental campaign with a small halogen bulb (1 mm filament) with the beryllium filter removed. The filter can be removed and reinstalled without changing the viewing optics. A divertor profile gauge, which accurately fits into the shape of the divertor, was fitted with a ruler, such that the position of the halogen bulb fixture could be determined with respect to the ruler. The position of the innermost and outermost viewing chords were determined in this way and found to be shifted by 3 mm outwards compared to the design CAD drawing. This represents an error on the collimator angle below the specification of 0.25°. The CAD drawing was then changed to fit the calibration. The absolute position was re-measured at the end of the run campaign (in spring 1998) and was found to be within 0.7 mm of the original calibration, that is, within the measurement accuracy. The outward shift of 3 mm meant that the three outermost detectors were completely in the shadow of the limiter. This provided us with an extra consistency check for the spatial positions of the chords, since it is evident in the raw data that the outermost 2-3 chords are in

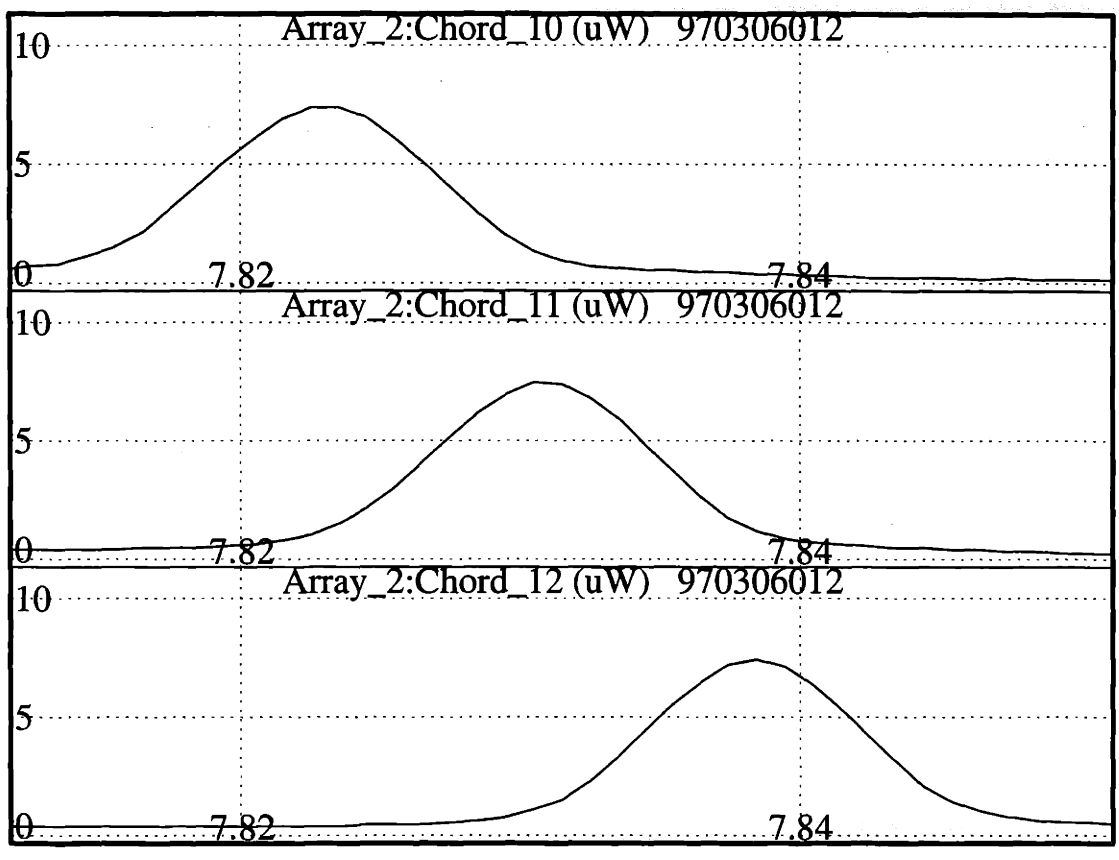

Figure 2-4: Time traces of three adjacent detectors as the halogen bulb is swept across the view of the detector array. The signals on detectors 10 and 12 are down to roughly 10% of the maximum signal when the light bulb is centered on detector 11. Since the bulb was swept at approximately constant speed, the time axis can be interpreted as a radial coordinate as well.

the shadow of the limiter. These data are described in Section 4.2.

2.1.2 Measurement of detector view overlap

By moving the halogen bulb around in the view of the array, it was confirmed that the overlap between detector views is minimal. When the bulb was in the center of one viewing chord, such that the incident photon power was maximized on a particular detector, the two adjacent detectors received a photon power which was 10% of the signal of the centered detector. These results are shown in Figure 2-4.

This measurement also confirmed that all detectors were connected correctly and that they were functioning properly.

Chapter 3

Data analysis

3.1 Inversion

The power incident on each detector is essentially the integral of the plasma emissivity along a viewing chord, convolved with the beryllium filter function. For convenience, we will refer to the spectral convolution of the plasma emissivity with the beryllium filter function simply as the "x-ray emissivity". Following this definition of x-ray emissivity, the diagnostic measures the chord-integrated x-ray emissivity. In order to deduce the local x-ray emissivity from this one-dimensional set of measurements of chord-integrated emissivities, it is necessary to assume that the emissivity is a function of one single scalar coordinate. We have chosen to assume that the emissivity is constant on a flux surface, which has previously been found to be a good, but not exact, approximation in Alcator C-Mod [16]. The chord integrations only extend over a small region in the poloidal coordinate so even if there are large global asymmetries in the soft x-ray emissivity, the asymmetries may be small in the view of the detectors. In fact, large top-outboard asymmetries have been observed with the two-array diagnostic. These results and the implications for the accuracy of the inversions are discussed in Chapter 10. The general conclusion is that the observed asymmetry may cause errors in the inversions on the order of 5-15%, which is generally not significant. During fast transients such as Edge Localized Modes (ELMs) there may be larger asymmetries, which may lead to more substantial inversion errors.

When the emissivity is assumed constant on a flux surface, the raw signals can be inverted to yield profiles of the emissivity as a function of the flux coordinate, mapped to the midplane radial coordinate for convenience. The relationship between the emissivity profile and the signal on a detector is linear, since the plasma absorptivity is very small in the x-ray range of photon energies. The relationship between the emissivity (e) and the signal on a particular detector can be discretized by dividing the plasma into a number of flux shells, which all have the same thickness at the midplane. If we denote the emissivity of the i'th flux shell by e_i and the signal on the j'th detector by s_j, the relationship between the two is:

$$s_j = \sum_i c_{ij} e_i \tag{3.1}$$

The coefficients c_{ij} are calculated for a given plasma equilibrium, as given by EFIT [17], by the following finite element method. The volume viewed by the detectors is broken into a large number (about 30000) of small volume elements (pixels), with dimensions 0.4 mm radially by 0.8 mm poloidally by 1 mm toroidally, and the contributions from all pixels within a given flux surface are added. Each of these contributions is determined by calculating the solid angle, as seen from the pixel, of the fraction of the j'th detector which is visible through the aperture, taking the angle of incidence into account. The calculation of all the solid angles from about 30000 pixels onto 38 detectors is rather CPU intensive but only needs to be done once and can then be stored. For a given detector and flux shell, one just has to determine which pixels contribute from this shell and sum up their contributions. Since the flux surfaces change shape dynamically during a plasma discharge, this assignment of pixels to flux shells changes dynamically too. We follow these changes dynamically on a 20 msec timescale, which is the standard EFIT timebase. Equation 3.1 implies that the total system of equations for all detectors can be written in matrix form as:

$$\mathbf{s} = \mathbf{C} \times \mathbf{e} \tag{3.2}$$

The emissivity vector $\mathbf{e}$ can now be calculated by computing the pseudo-inverse of $\mathbf{C}$ by Singular Value Decomposition (SVD). In order to get a solution which is well

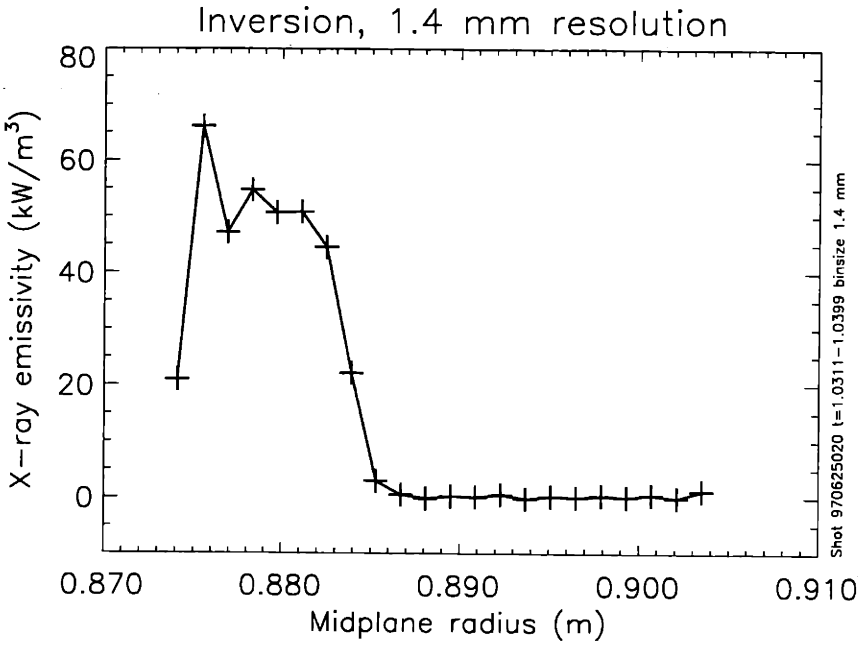

Figure 3-1: An example of how the matrix inversion starts yielding bad results when the flux shell thickness is decreased below 1.7 mm. In this case the bin size is 1.4 mm, and a large fluctuation can be seen on the innnermost emissivity bins. The raw signals and the plasma shape are taken from a discharge in the ELM-free H-mode.

defined and not too sensitive to noise, one must make sure the system is sufficiently overdetermined, ie. that the number of flux shells is somewhat smaller than the number of detectors. One must also establish an SVD cutoff, such that noisy equations are excluded from the problem. The SVD cutoff is set to 10^{-2} normalized to the largest eigenvalue, consistent with the fact that typical values of the signal to noise ratio are 100. The flux shell thickness at the midplane was originally chosen to be 1.7 mm, the lowest value which consistently gave good inversions. Decreasing the thickness further resulted in increased noise sensitivity and spurious results, characterized by large oscillations in the innermost emissivities, as seen in Figure 3-1, where the shell thickness (also referred to as the bin size), was set to 1.4 mm. Such oscillations are also seen on artificial data, where the emissivity profile is known not to have the oscillatory behavior. Artificial data are calculated by assuming a certain emissivity profile and then multiplying it by the coefficient matrix to get the equivalent raw signals, then random noise is added to the raw signals. These noisy raw data are

then inverted to an emissivity profile, and can be compared to the original emissivity profile. From such artificial data, it is known that the phenomenon is an artifact of the inversion. Initially, this phenomenon limited the spatial resolution to 1.7 mm, which is significantly greater than the chord spacing of approximately 1 mm. The chord spacing mapped back to the midplane gives the lowest possible value for the bin size, since a bin size smaller than that will yield more unknowns than equations, so that the system is underdetermined.

3.1.1 Improved inversion algorithm

An improved inversion algorithm has been developed which eliminates the phenomenon described above, and allows the spatial resolution to be improved significantly. The first step in developing this improvement was to analyze what caused the extreme error sensitivity for the emissivity of the innermost flux shell. The matrix elements of $\mathbf{C}$ in Equation 3.2 for a plasma of a typical H-mode shape, and a flux shell thickness of 1.4 mm, were examined. This represents a case where the inversions are not reliable. The matrix elements relevant to solving for the emissivity of the innermost bins are shown in Figure 3-2. It is seen that the innermost detector only views a very small volume of the innermost flux shell. It views a much larger volume in the next flux shell, since the center of the view is tangent to the second flux shell. The next detector does not see the innermost flux shell at all, and sees just a small fraction of the second flux shell. Thus, the signal on the innermost channel is relatively insensitive to the value of the innermost emissivity, yet it is the only measurement that has any component of the innermost emissivity. At the same time, the second emissivity bin is determined mostly by the signal on the innermost detector. Thus, these two emissivity values are *both* determined by the signal on the innermost detector (number 38). Very little extra information about these two emissivities can be gathered from the next detector signal (detector 37) since it is dominated by radiation from the third flux shell. In the full SVD pseudo-inversion, this manifests itself in the way that one of the singular values of $\mathbf{C}$ becomes very small, which means that the pseudo-inverse becomes ill-defined, and the inversions become very noise sensitive.

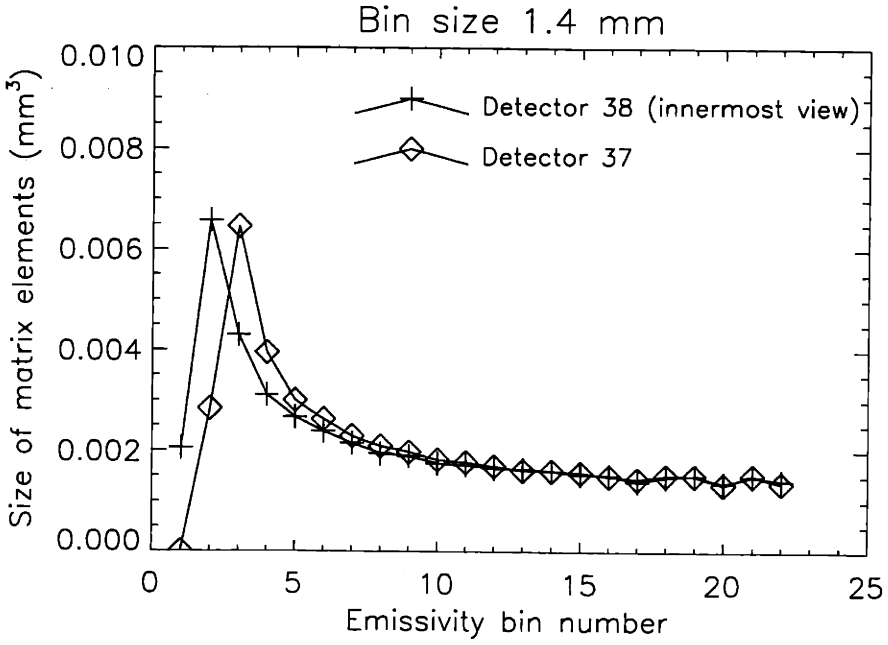

Figure 3-2: Matrix elements for a typical plasma, with a flux shell thickness (bin size) of 1.4 mm.

A successful solution to this problem has been developed. One adds the two innermost flux shells together, thus essentially assuming that their emissivities are equal. This turns out to be a rather good assumption in general, and is clearly a much better approximation than assuming, for instance, that the emissivity is zero for the innermost flux shell[1]. It is very easy to implement, one simply adds the first two columns of the matrix together to form one. All other columns in the matrix are left unchanged. Once that is done, the matrix elements are as shown in Figure 3-3. The inversion of the matrix is now performed again, and a new emissivity profile calculated. It is seen in Figure 3-4 that the new emissivity profile is well-behaved around the innermost bins, even though it has a spatial resolution of 1.4 mm (with the exception of the innermost emissivity, which has a resolution of 2.8 mm). In fact, with this new improved algorithm, it is possible to get as low as 1.2 mm, and even in some cases to 1.0 mm binsize, although at this resolution, the inversions become

[1]If one were to simply omit the equation corresponding to the emissivity on the innermost flux shell, that would be equivalent to assuming that the emissivity in that flux shell is zero

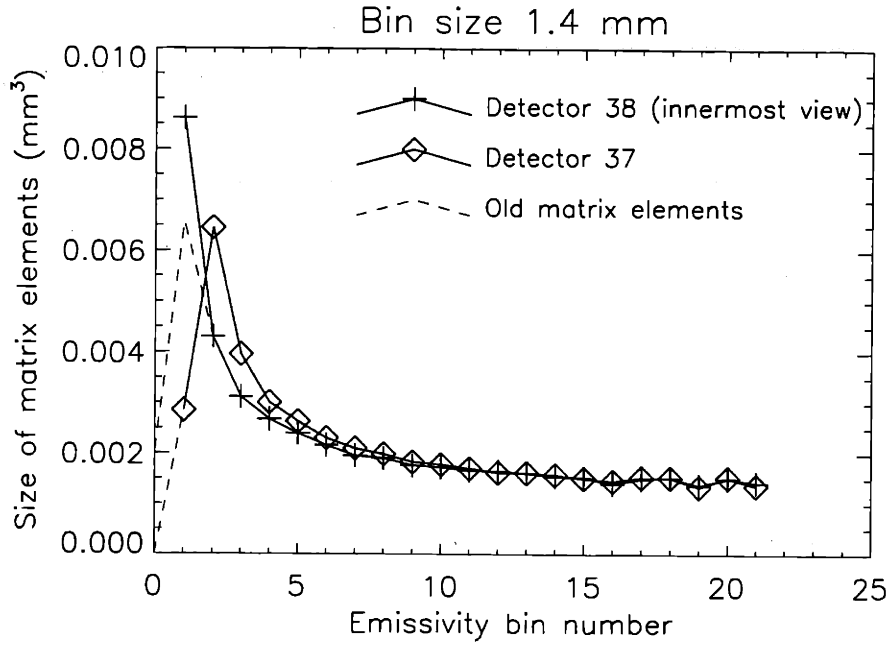

Figure 3-3: Matrix elements for the two innermost detectors once the two innermost bins have been lumped together into one.

rather sensitive to noise so such a high resolution is only useful for measurements with very high signal/noise ratios.

3.2 H-mode pedestal analysis

As shown in Chapter 4, and exemplified in Figure 3-4, the x-ray emissivity profiles show a pronounced pedestal shape in the high confinement mode (H-mode), indicative of an edge transport barrier. In order to quantitatively describe the pedestal shape, the emissivity profiles are fitted to a tanh-like function [18]:

$$f(r) = A \times \frac{1}{2}\left(\tanh\left(\frac{r_0 - r}{\delta}\right) + 1\right) + B \times (r_0 - \delta - r) \times \Theta(r_0 - \delta - r) \qquad (3.3)$$

where Θ is the Heaviside step function. Here, A is the emissivity at the top of the pedestal, B is the linear slope inside the pedestal, r_0 is the position of the largest gradient (the center position of the pedestal), and $\Delta = 2\delta$ is a measure of the pedestal width. A nonlinear fitting routine automatically fits A, B, δ $(= \Delta/2)$, and r_0 for each profile. In well confined H-modes this provides a very good description of the

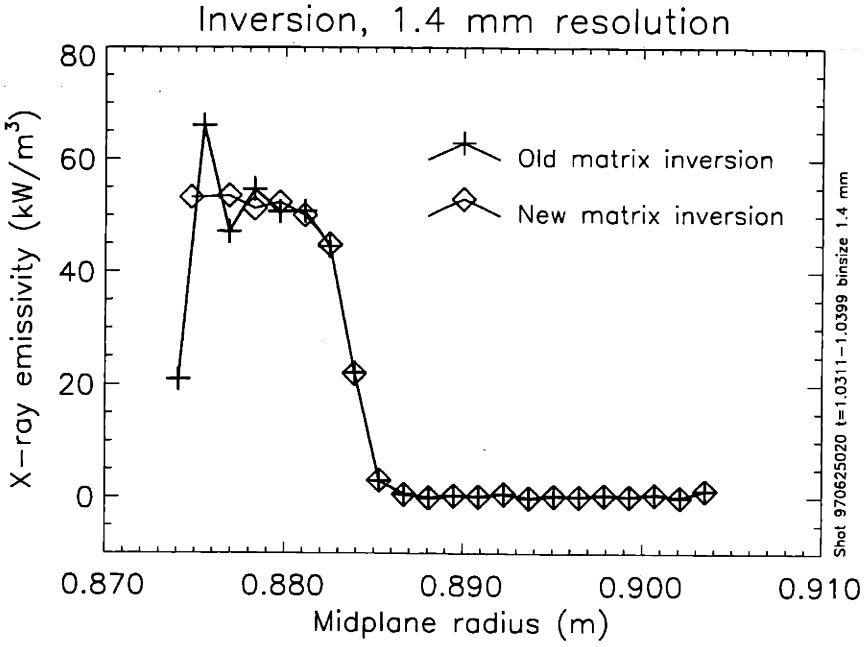

Figure 3-4: A comparison between inverted emissivity data obtained from the same raw signals, but using the two different matrices. The emissivity calculated by inverting the new matrix no longer has the oscillatory character at the innermost flux shell seen when using the old matrix.

emissivity profile, whereas the fit is poor for L-mode emissivity profiles, which usually do not have a pedestal-like shape, and have low signal/noise ratios. Because of this, the automatic pedestal routine often yields spurious results for L-mode data. Note that since the soft x-ray emissivity is close to zero outside the pedestal, it is not necessary to include an offset in the fitting function in Equation 3.3.

3.2.1 Effects of the radial resolution on the pedestal width

In certain discharges, the best fit to the data is a pedestal which has a width smaller than the spatial resolution. This can be a problem for some ELM-free H-mode discharges, in particular when the spatial resolution was limited to 1.7 mm. When the improved inversion algorithm described in Section 3.1.1 was developed, allowing the spatial resolution to be improved significantly, this problem was addressed. Real data from an ELM-free H-mode, averaged over 8.8 ms to reduce noise, is used in the following as an illustrative example. In Figure 3-5 the inverted emissivity profile is

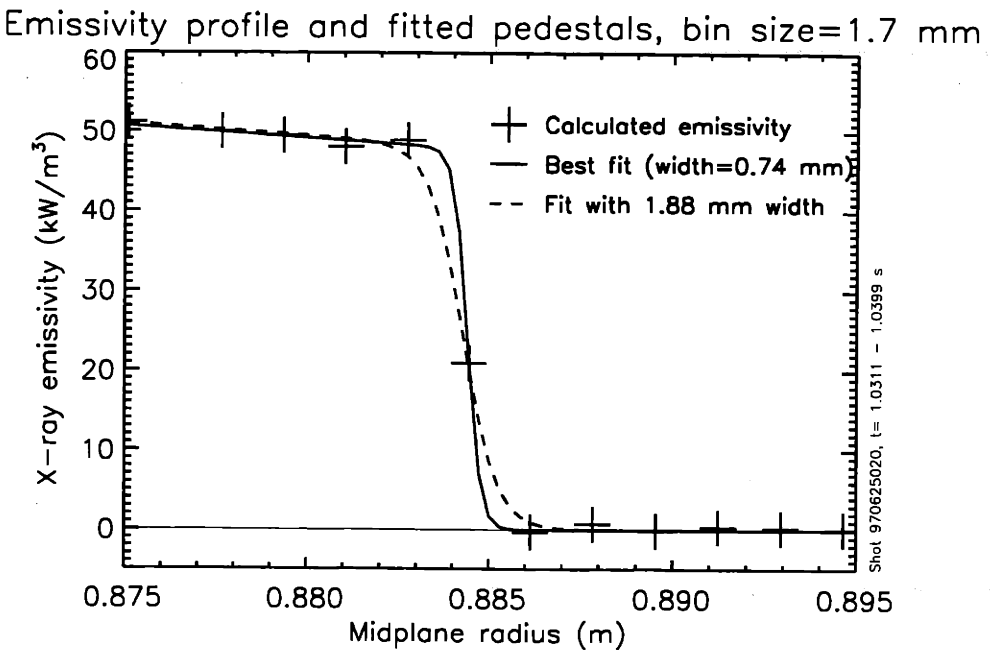

Figure 3-5: Emissivity profile for an ELM-free H-mode, calculated with a spatial resolution of 1.7 mm. The tanh-like pedestal function which best fits the data has a width of only 0.74 mm, far below the spatial resolution. For comparison, a pedestal fitting function with 1.88 mm width does not fit the data as well, although it is a reasonable fit.

shown for a bin size of 1.7 mm. It is seen that the pedestal is so narrow, that there is essentially only one point in the steep gradient region. The best pedestal fit is also shown, fitting the data very well, but with a pedestal width Δ of 0.74 mm, far below the spatial resolution. A 1.88 mm pedestal is also shown for comparison, and although it does not fit these data as well, it is actually more accurate, as shown in Figure 3-6, where the emissivity is now calculated with a bin size of 1.25 mm.

In this case, there are two points in the steep gradient region, and the 1.88 mm wide pedestal is the best fit to the data, whereas the 0.74 mm pedestal clearly does not fit the data well. Pushing the resolution further to 1.0 mm (Figure 3-7), which for this particular plasma equilibrium is very close to the theoretically best possible resolution, reveals a somewhat noisier profile, but still with a well-defined pedestal shape, which is now best fitted with a pedestal function with a width of 1.96 mm. Summing up this result, we plot the estimated width of the pedestal as a function of the spatial resolution in Figure 3-8. It is seen that the width converges quickly to a

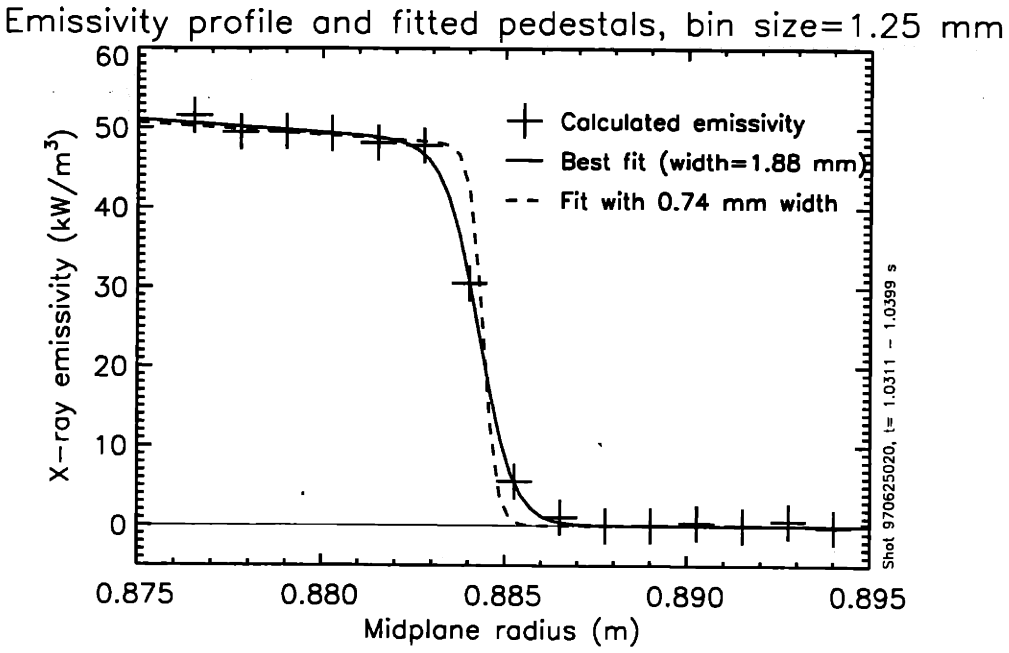

Figure 3-6: The same raw data as in Figure 3-5, now inverted with a spatial resolution of 1.25 mm. The best fit now has a width of 1.88 mm, whereas the 0.74 mm wide pedestal does not fit the data well.

value of about 1.9 mm as soon as the spatial resolution is improved to below 1.5 mm. It is therefore important to keep in mind that fitted pedestal widths which are below the spatial resolution are unreliable.

3.3 Noise reduction

Most of the noise on the raw signals of edge x-ray diodes is random Poisson-like electronic noise[2] which can be reduced by time-averaging the data, thus lowering the temporal resolution. Systematic noise is also found in the data, and this is sometimes a problem. Two sources of systematic noise have been identified in the soft x-ray signals. One is related to voltage pickup in the amplification electronics, the other is a high frequency oscillation related to the fast power supplies controlling the EFC magnet. In Figures 3-9 and 3-10 we show an example of the extent to which it

[2]Photon shot noise is negligible compared to the electronic noise

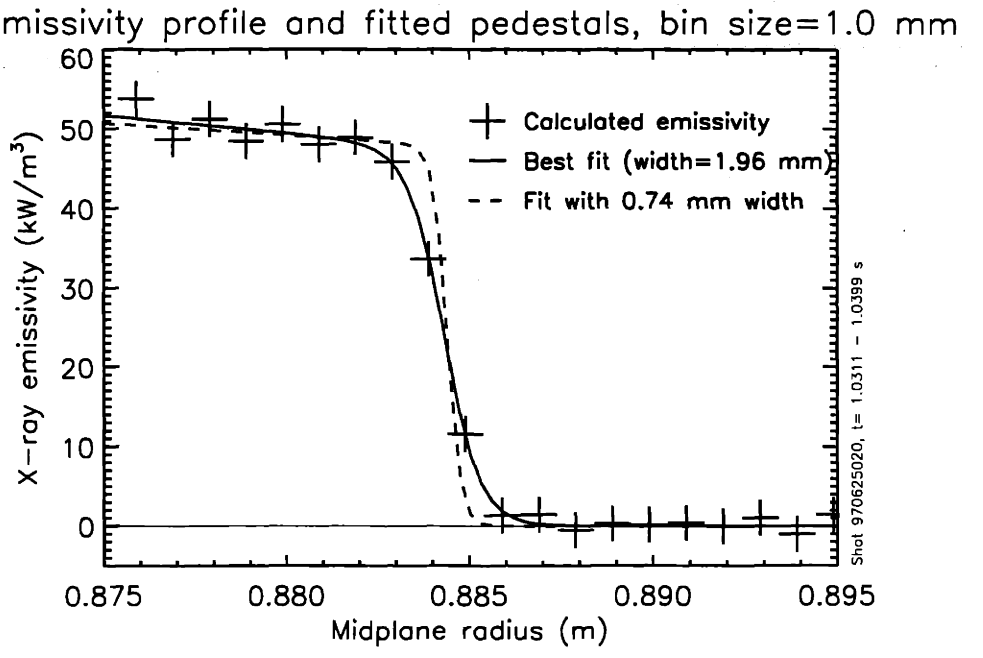

Figure 3-7: The same data, now inverted with a bin size of 1.0 mm, begins to show increased noise but still has a pedestal-like shape and fits a tanh-pedestal function with a width of 1.96 mm.

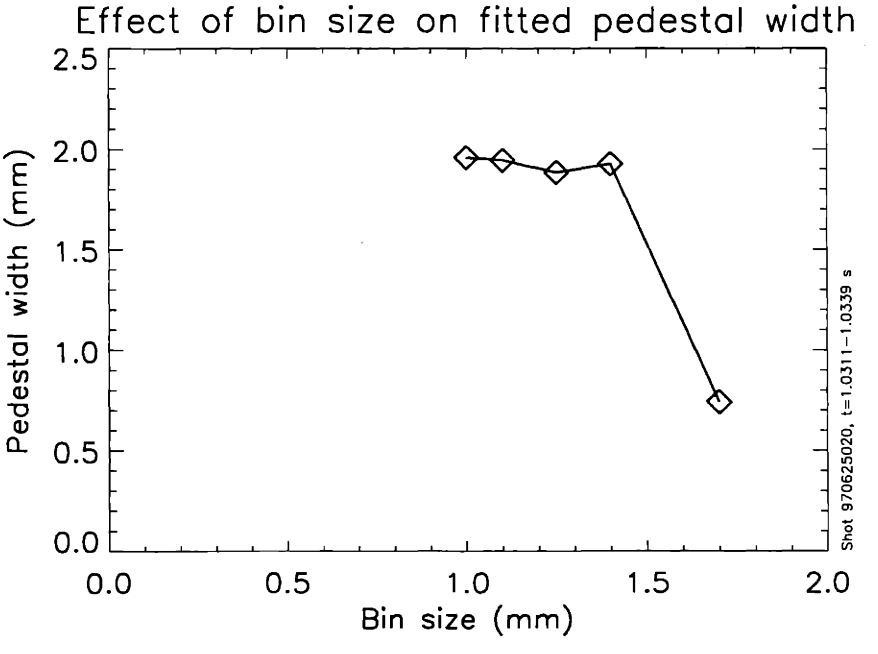

Figure 3-8: The estimated width of the x-ray emissivity pedestal is plotted here versus the radial resolution (bin size). It is seen that the width converges quickly to a value around 1.9 mm, once the bin size is decreased to 1.4 mm or less.

has been possible to decrease the circuit board voltage pickup. This noise source is relatively benign and is usually only a problem in L-mode where the signal levels are very low. In Figure 3-11 we show an example of the pedestal position as a function of time before and after the power supply noise oscillation is reduced. In the case of the EFC magnet noise, it is necessary to reduce the noise in all fast sampled data[3] even in good quality H-modes, since the pedestal parameters are affected by this noise source. The details of the identification of the noise sources and the algorithms employed to reduce the systematic noise are in Appendix A.

[3]Data sampled at 50 kHz or 83 kHz

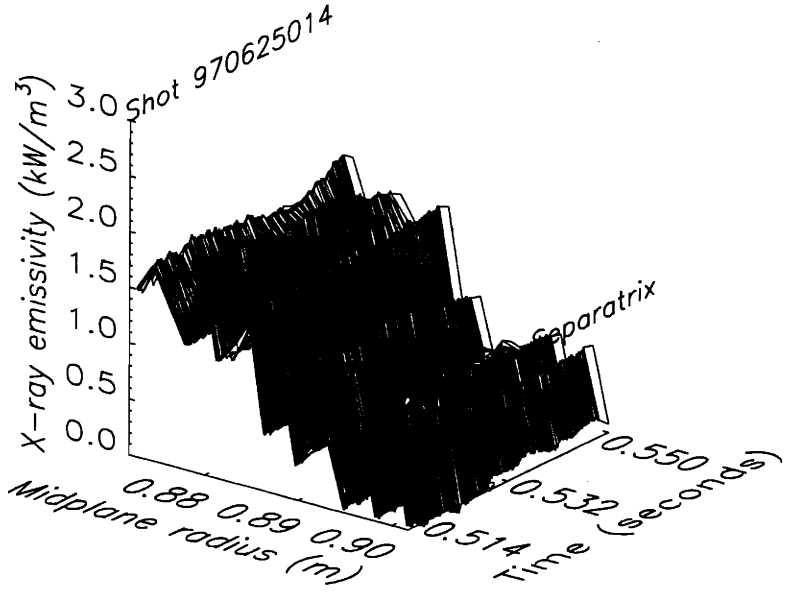

Figure 3-9: A surface plot of the radial emissivity profile during an L-mode shows the pickup noise very clearly. The real plasma signal is difficult to make out, even though the data has been smoothed over 13.6 ms.

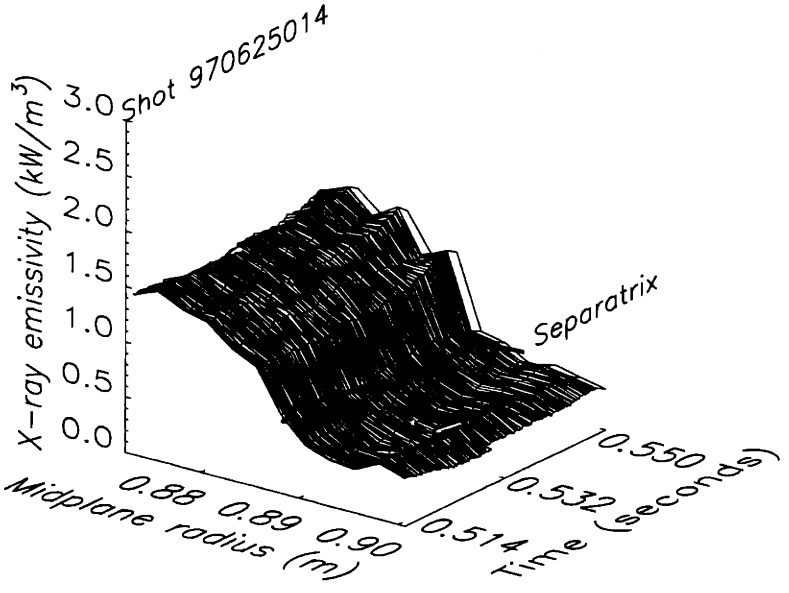

Figure 3-10: A surface plot of the radial emissivity profile with the pickup noise removed and the radial resolution degraded from 1.7 mm to 2.5 mm. Now the pickup noise has been reduced to very low levels. Signals have been smoothed in time over 13.6 ms.

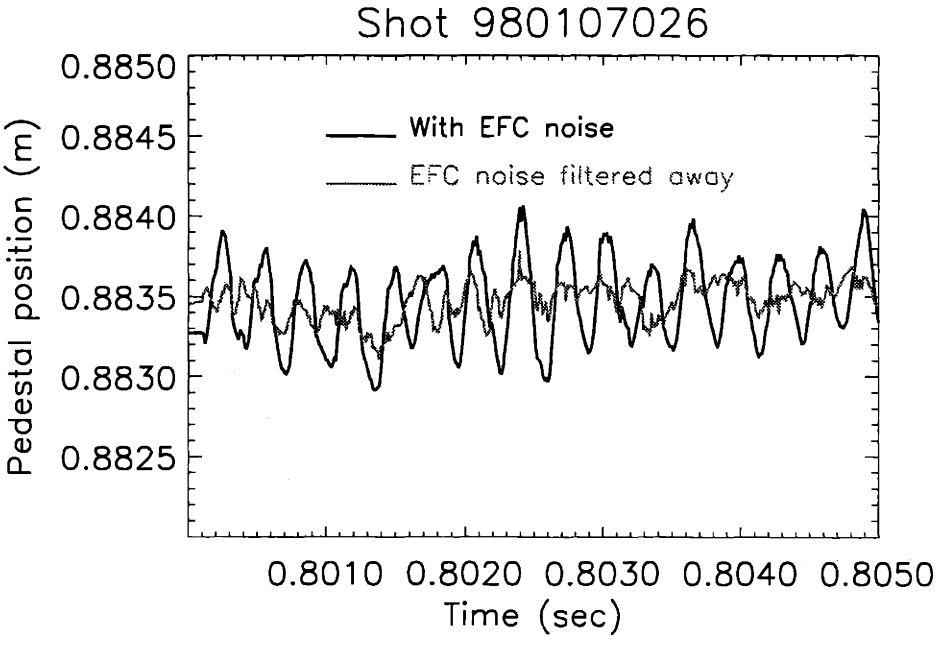

Figure 3-11: Effects of the EFC noise on the fitted pedestal position in H-mode. In this case a 1 mm oscillation is visible before filtering. Filtering reduces the noise amplitude by more than a factor of two.

Chapter 4

Measurements made with the first edge x-ray diagnostic

4.1 Typical example of soft x-ray data

4.1.1 Chord integrated brightness profiles

In Figure 4-1 we show a typical example of raw data, ie. chord integrated brightness profiles, in a discharge which undergoes a transition from the low confinement mode (L-mode) to the high confinement mode (H-mode) and back to L-mode. Time traces of various plasma parameters are shown in Figure 4-2. The signal levels are very low during L-mode but rise rapidly on the detectors with the innermost views once the plasma goes into H-mode. Typically, the signal level rises by a factor of 10 on detector 38, which is the detector with the innermost view, ie. the one that receives the most plasma x-ray radiation. The signals on the outermost detectors do not change very much, but generally tend to decrease when the plasma goes into H-mode. This is consistent with probe measurements which show that the region outside the separatrix actually experiences a decrease in electron density when the plasma goes into H-mode, presumably because the plasma gets pinched inward during the H-mode. Thus, from the raw soft x-ray data alone, it is almost always clear if the plasma is in H-mode or L-mode. No pedestal is seen in the raw data. We would not

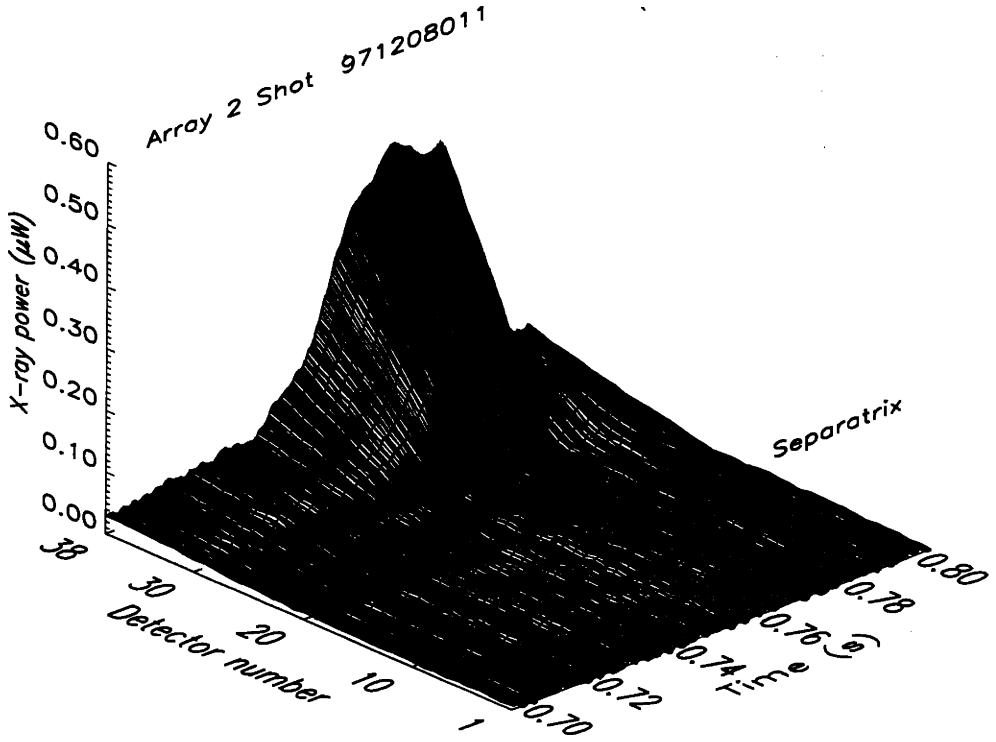

Figure 4-1: An example of the time history of the brightnesses of the 38 detectors. During L-mode, the signal levels are very low, but they increase by an order of magnitude for the innermost detectors when the plasma enters H-mode. The line showing the separatrix indicates which detector is tangent to the last closed flux surface.

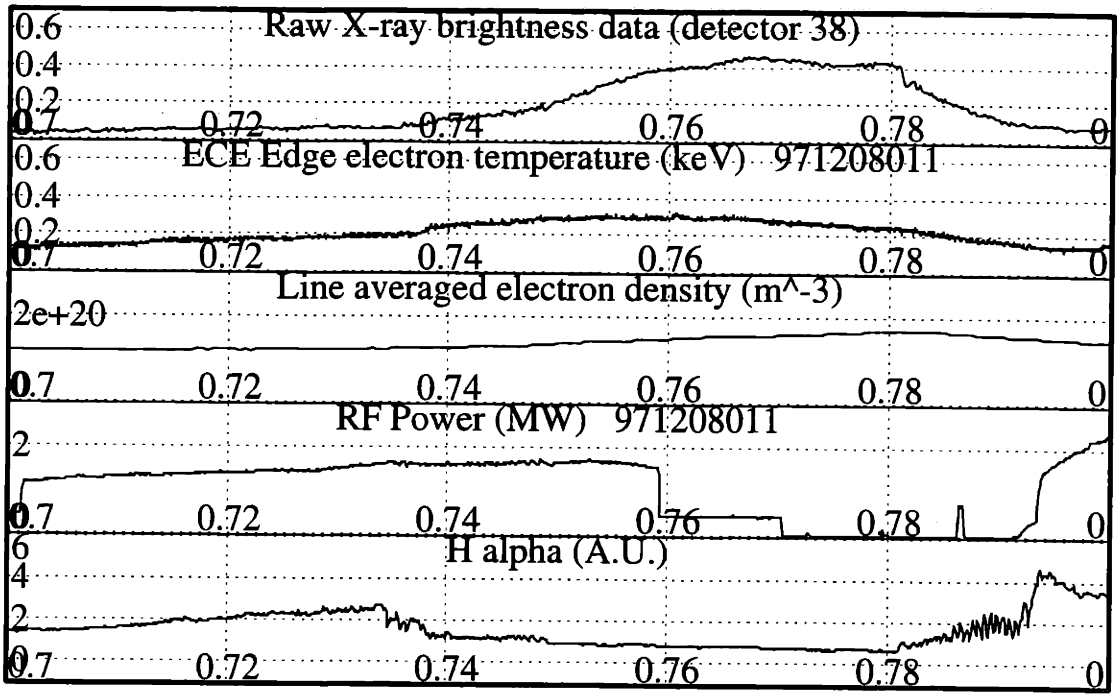

Figure 4-2: The time history of various plasma parameters shows a transition into H-mode around t=0.74 sec and a back transition to L-mode around t=0.78 sec because the ICRF heating was turned off.

expect a pedestal in the raw data since the raw data are chord integrals of the local x-ray emissivity.

4.1.2 Emissivity profiles

By using the matrix inversion described in Section 3.1 it is possible to invert the raw data, which are chord integrals of the soft x-ray emissivity, to get radial profiles of the local soft x-ray emissivity. Thus, one can obtain the emissivity as a function of the flux coordinate at the edge of the plasma. For convenience, we express the flux coordinate as the major radial coordinate of the particular flux surface at the plasma midplane. The time evolution of the emissivity as a function of major radial coordinate at the plasma midplane is shown in Figure 4-3. The emissivity profile is calculated from the raw data in Figure 4-1 and also shows a distinct difference between L-mode and H-mode. In H-mode, a steep narrow region develops, and the emissivity inside this pedestal increases by more than an order of magnitude from

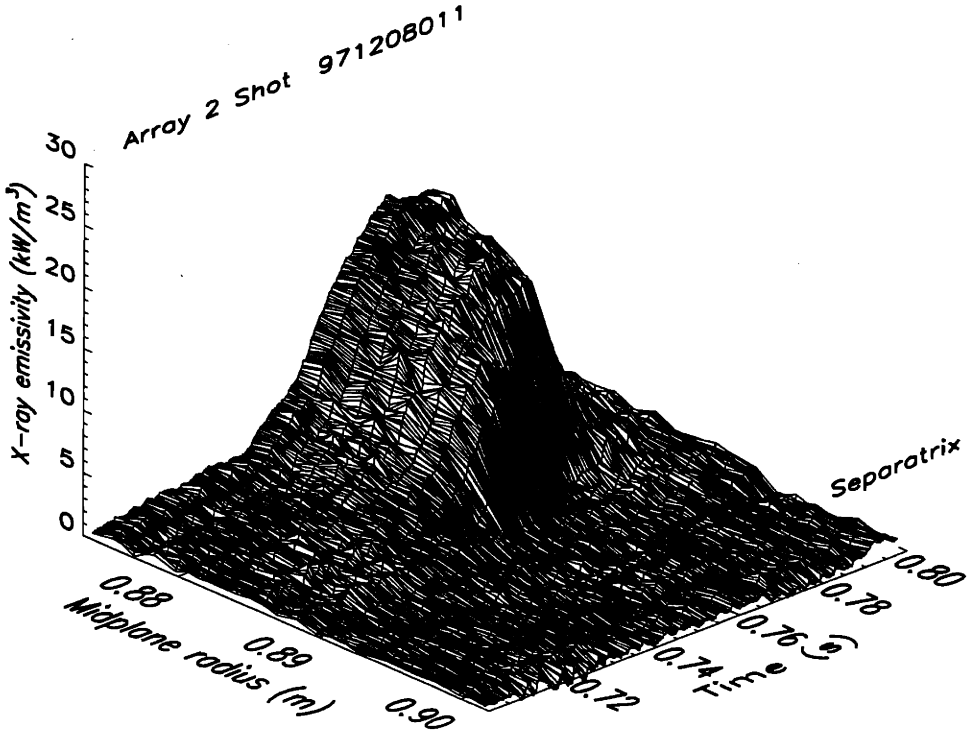

Figure 4-3: This figure shows the time evolution of the soft x-ray emissivity as a function of the major radius at the midplane for the same plasma shown in Figures 4-1 and 4-2. During H-mode, the emissivity has a pronounced pedestal shape. The width of the pedestal is only a few mm and it is located about 10 mm inside the EFIT separatrix.

its L-mode level, as first published in [20]. A pronounced, and usually very narrow, pedestal in the soft x-ray emissivity is always seen during H-mode. The pedestal is located about 10 mm inside the separatrix. This inward shift is discussed in more detail in Chapter 7. Occasionally L-mode profiles have a hint of a pedestal but usually not. L-mode emissivity profiles are discussed in more detail in Section 4.5.

4.2 Evidence for the shadow of the limiter

In some cases the shadow of the limiter is evident in the raw data. The signal levels decrease as one goes from the innermost detector (38) to the outermost detector, as expected, but there is a distinct break in slope at the outermost 2-3 chords where the signal levels decreases much faster. Since the signal levels are very low in that

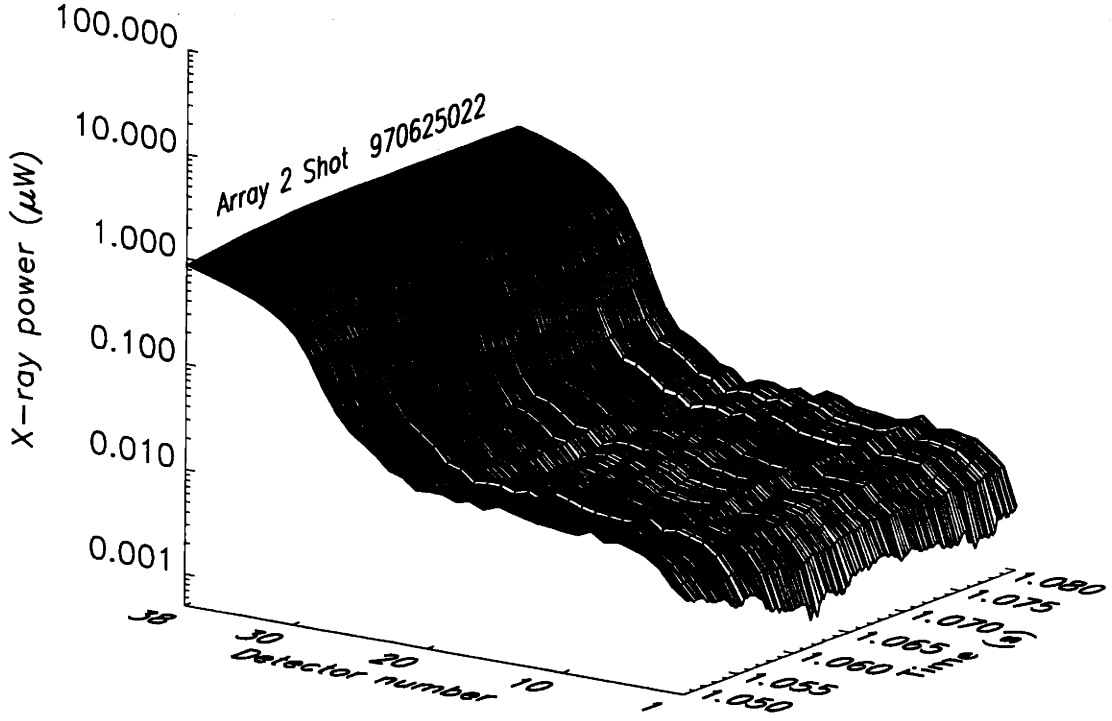

Figure 4-4: This figure shows raw data from an ELM-free H-mode plotted on a logarithmic scale. The data has been smoothed over 20 msec and pickup noise has been removed so that the sharp drop in x-ray brightness at the three outermost channels can be seen. Note that there are about 3 orders of magnitude difference between the innermost chord and the outermost chords.

region of the plasma in the first place, this effect is not always visible, and it always requires temporal smoothing and pickup noise removal (see Section A.0.1) for it to be evident. Nevertheless, it is seen in a variety of discharges, mostly during H-modes, but sometimes also in L-mode. We show here two H-mode examples, an ELM-free H-mode from June 1997 in Figure 4-4, and an EDA H-mode from January 1998 in Figure 4-5. In the first example, the three outermost detectors are in the shadow of the limiter, as seen by the sharp drop in brightness, and in the second example it appears that only two detectors are in the shadow of the limiter. From our measurements of the absolute positions of the detector views, and our knowledge of the limiter shape and position, we expect 3-4 detectors to be in the shadow of the limiter. Thus, our findings are consistent within one chord spacing, ie. about 1 mm. This could easily be explained by uncertainties in the limiter shape and position, or

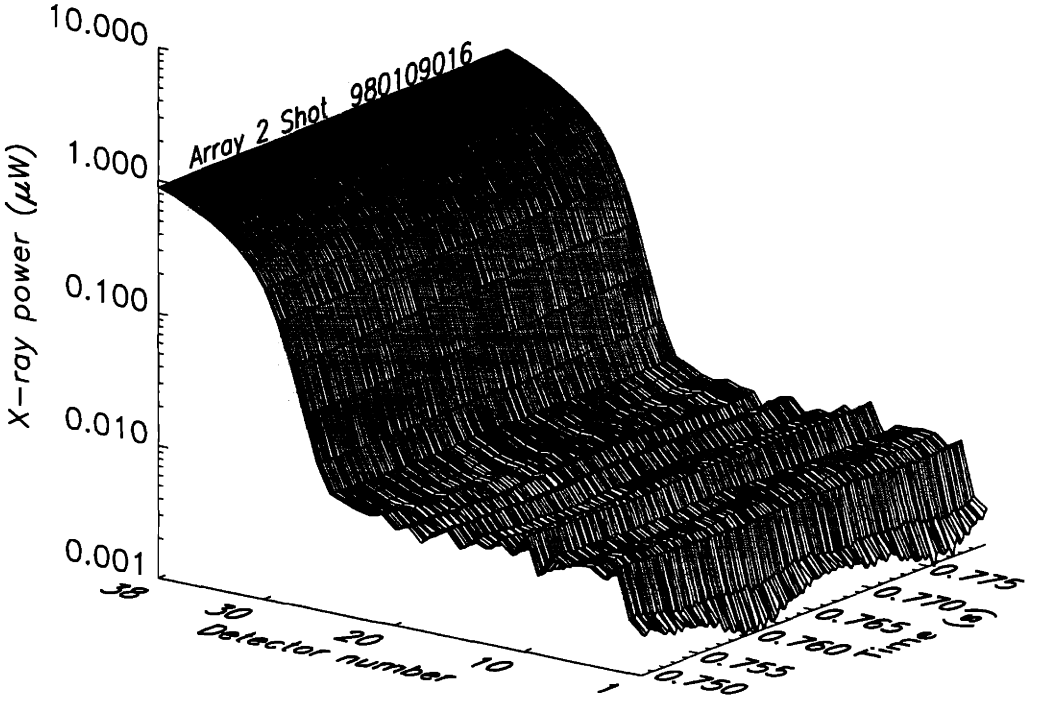

Figure 4-5: This figure shows raw data from a quasi-steady state EDA H-mode plotted on a logarithmic scale, also smoothed over 20 msec and with the pickup noise removed. In this case only two chords are in the shadow of the limiter.

by the 1 mm uncertainty in the measurement of the chord view locations. For the plasmas that exhibit clear evidence of the limiter shadow, the number of chords in the shadow does not change during the course of the shot, and also does not change from shot to shot, which indicates that the plasma shape does not matter. Some parts of a flux surface may be intersecting the limiter, but this does not affect the emission on that field line much. The signals are only significantly lower on the detector viewing entirely in the shadow of the limiter.

4.3 Pedestal width differences in various H-mode regimes

In ELMfree H-mode, the soft x-ray emissivity pedestal width at the outboard edge is typically very narrow, on the order of 2 mm. In many cases the radial resolution of 1.5 mm is barely adequate to resolve the pedestal shape in ELMfree H-modes. When there are large, isolated ELMs, as shown in Section 4.6, the pedestal is transiently destroyed, but reforms at or near its previous value. Sometimes, when the plasma is in H-mode, but near the threshold to L-mode, small ELMs appear with repetition rates on the order of 1 kHz. This type of confinement is called type III ELMy H-mode, and it is usually characterized by a rather low confinement, usually closer to L-mode confinement than to ELMfree H-mode confinement. When this occurs, the soft x-ray pedestal becomes very wide, typically 5-8 mm, and may even disappear in some cases, although the emissivity levels, much reduced compared to ELMfree values, typically remain above L-mode values. In EDA H-mode, we also observe a widening of the pedestal compared to ELMfree H-mode, but typically only to 3-5 mm, depending on the plasma current and triangularity, as described in Section 4.4. There is always a distinct pedestal in EDA H-mode, and the emissivity levels typically reach a steady state at levels much higher than L-mode values, and often comparable to ELMfree H-mode values. Examples of representative data can be found in Section 10.4 as well as in previously published articles [21].

4.4 Pedestal scaling laws

It is important to determine experimentally which plasma parameters affect the H-mode transport barrier. We characterize the x-ray pedestal in terms of the tanh-like fit described in Section 3.2, which yields the height, width and position of the x-ray emissivity pedestal, as well as a fourth parameter which describes the slope inside the pedestal. We will primarily be focusing on the pedestal width and height, and defer analysis of the pedestal position to Chapter 10. The construction of a database containing pedestal data, as well as a host of other available plasma parameters has greatly facilitated the analysis presented in this section. However, the clearest trends were obtained by varying the parameter in question during *a single plasma discharge* rather than using the database, which inevitably will contain more data, but also many discharges under different conditions. This tends to increase the scatter in the data even if the database points are carefully selected to decrease scatter by choosing discharges with very similar characteristics. The database approach is still very important, as it makes it possible to investigate many more possible cross-correlations than have been investigated through dedicated experiments. Once a correlation has been identified in the database, it may be possible to confirm this and investigate it in detail in a dedicated experiment.

4.4.1 Pedestal width scalings

The pedestal width is an important characteristic scale length of the transport barrier. In the following, we will describe soft x-ray emissivity pedestal width scalings with several plasma parameters. Pedestal width scalings yield information about the physics of the transport barrier. Only a few of the H-mode theories actually have predictions for the pedestal widths, and only for the bulk plasma parameters. A review of pedestal scalings on various tokamaks compared to theoretical predictions can be found in [22]. For the case of the soft x-ray pedestal, the physics of the pedestal width is made clear in Chapter 7.

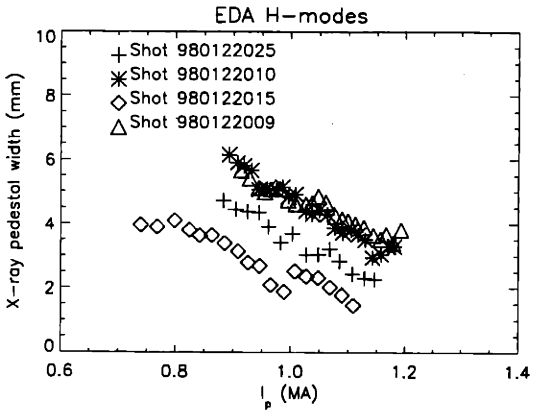

Figure 4-6: Four discharges where the plasma current was ramped during a quasi steady-state EDA H-mode. On shots 9 and 10 the current was ramped up, whereas it was ramped down on shots 15 and 25. In all four cases the pedestal width is a strongly decreasing function of the plasma current.

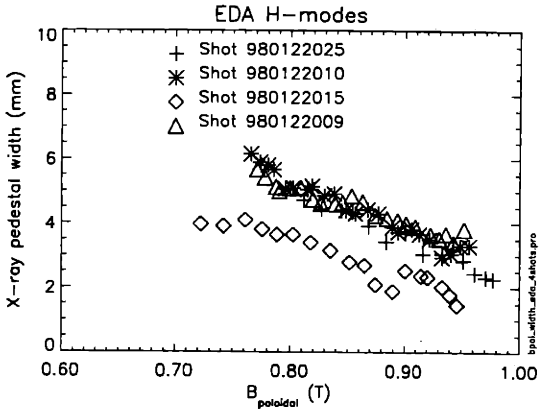

Figure 4-7: The pedestal width for the same four discharges as in Figure 4-6, plotted versus the poloidal magnetic field at the edge. A clear tendency for the pedestal width to decrease with increasing B_θ is seen for all four discharges.

Dependence on plasma current

The x-ray emissivity pedestal width is very sensitive to the plasma current during EDA H-modes. This was demonstrated during a dedicated series of experiments investigating the effects of varying the safety factor q, the plasma current I_p (directly proportional to the poloidal magnetic field strength at the plasma edge), and toroidal magnetic field strength, B_t on the H-mode characteristics. Two discharges (shot 9 and 10) were run where the plasma current was ramped up during a quasi-steady state EDA H-mode, while B_t, plasma shape, heating power and other externally controllable parameters were held fixed. Two other discharges (shots 15 and 25) were run where the plasma current was ramped down under very similar conditions. The results of these four discharges are shown in Figure 4-6. In all four cases we see that the pedestal width decreases with increasing plasma current. In fact, the pedestal width increases faster than linearly with $1/I_p$ in all four cases. The strong correlation found between the x-ray emissivity pedestal width and the plasma current indicates a strong scaling with the poloidal magnetic field at the plasma edge, since the poloidal magnetic field is directly proportional to I_p/a where a, the minor radius of the plasma, does not change much from shot to shot. In a cylindrical plasma the

relation is simply $B_\theta(r = a) = \mu_0 I_p/(2\pi a)$ but the relation is more complicated in shaped toroidal plasmas such as those in Alcator C-Mod. The value of the poloidal magnetic field can be calculated from the magnetic equilibrium code EFIT[17], so we can also plot the pedestal widths in Figure 4-6 as a function of edge poloidal magnetic field at the midplane, as shown in Figure 4-7. The plot confirms the tendency for the pedestal width to strongly decrease as a function of B_θ, and in addition, the shot to shot variation is somewhat smaller than in Figure 4-6. Shot 15 still has a smaller width than the other three, and shot 25 has a slightly smaller width than shots 9 and 10. For the same I_p, shots 9 and 10 have similar, rather broad pedestals, whereas the pedestal width in shot 15 is systematically about 2 mm smaller, and shot 25 is in between. This shows that there is at least one more parameter affecting the pedestal width besides the plasma current (or B_θ). Care was taken to choose the discharges so that all (controllable) plasma parameters were the same between these discharges. However, as mentioned previously, the plasma current was ramped up [1] (positive dI_p/dt) during shots 9 and 10, but ramped down (negative dI_p/dt) during shots 15 and 25. On shot 9, the ramp rate was 0.65 MA/s, on shot 10 also 0.65 MA/s, shot 15 had a ramp rate of -1.06 MA/s, and shot 25 had a ramp rate of -1.00 MA/s, all averaged over the time spanned in Figure 4-6. This leads us to speculate that the ramp rate is also an important parameter for the width of the x-ray emissivity pedestal. By using the database, we have investigated this further. The results of a database query are shown in Figure 4-8. The number of data points is somewhat low since the discharges are generally designed to reach EDA H-modes during the flattop (when the current is kept approximately constant), but there is a rather systematic tendency for the width to be larger for higher dI_p/dt. The data plotted are taken from 38 different discharges. A dedicated series of discharges designed to address this question was scheduled and run but due to lack of consistent RF heating power it was not possible to obtain good quality steady-state EDA H-modes so we were unable to

[1] We are taking the plasma current to be a positive quantity for convenience. In fact, by the sign convention used on Alcator C-Mod, these discharges were run with a negative current, as are most discharges.

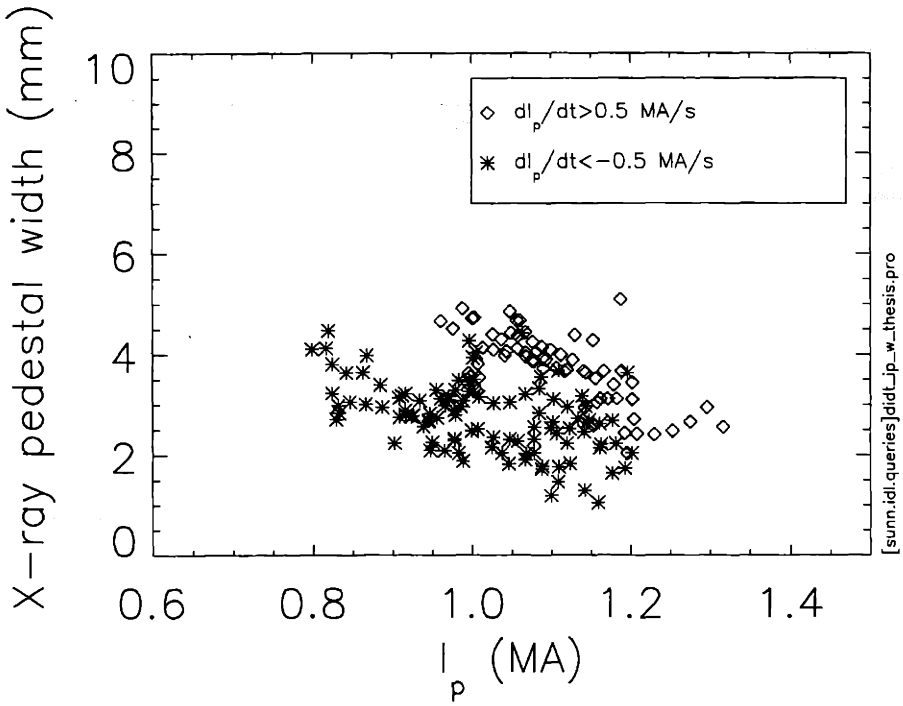

Figure 4-8: This figure shows the pedestal width during EDA H-modes as a function of I_p, divided into two types - those ramping up (diamonds), and those ramping down (*). For the same current, the rampup discharges have larger x-ray pedestal widths. This represents data from 38 different discharges.

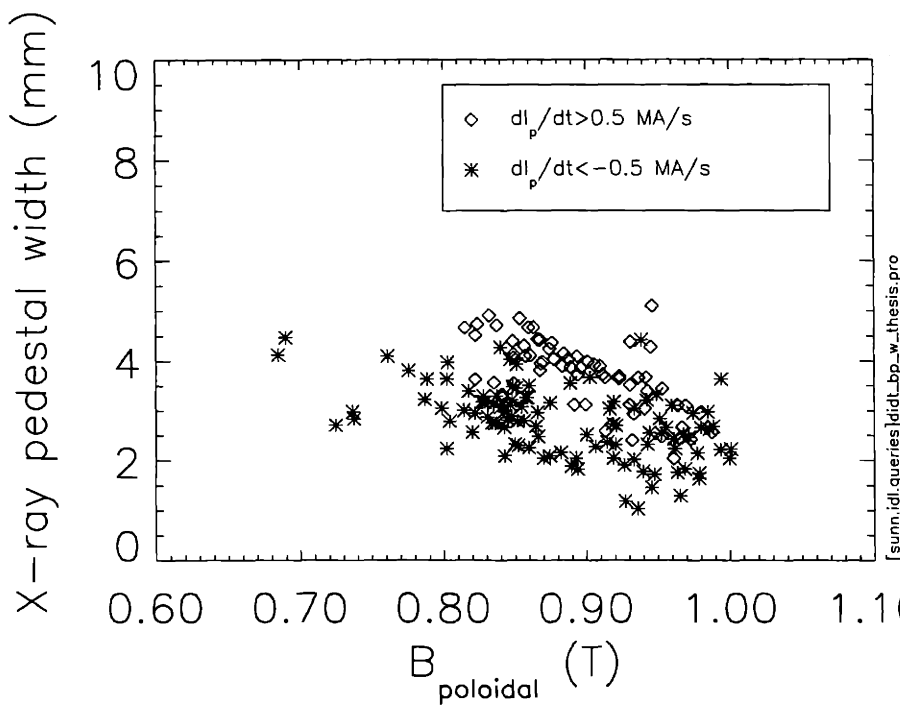

Figure 4-9: The pedestal width plotted as a function of B_θ rather than I_p, for shots either ramping up (diamonds) or ramping down (*). The same tendency is seen as in Figure 4-8.

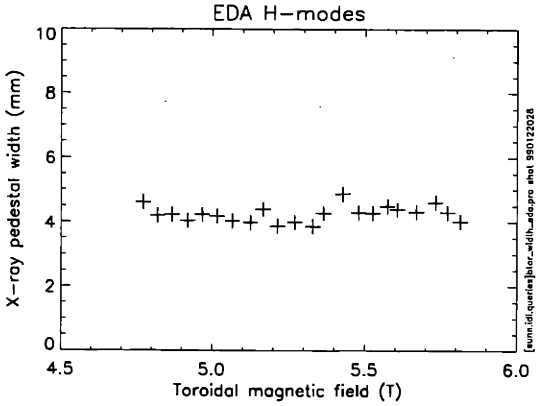

Figure 4-10: During shot 980122028, the toroidal B-field, B_t, was ramped keeping the input heating power, plasma shape, I_p etc. constant during a steady state EDA H-mode. The x-ray emissivity pedestal width remained practically constant during the ramp, ruling out any strong dependence on B_t.

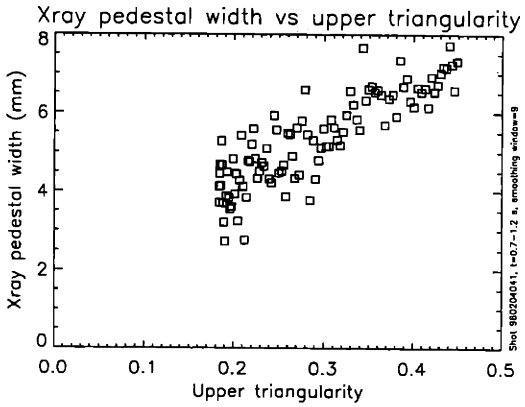

Figure 4-11: The x-ray emissivity pedestal width varies approximately linearly with the upper triangularity, δ_u. Other quantities such as I_p, B_t, and the RF power were kept constant during the ramp.

resolve this issue.

Dependence on toroidal magnetic field

The toroidal magnetic field, B_t, was also ramped in one of the discharges, allowing us to investigate whether the pedestal width depends on the toroidal magnetic field strength. The toroidal magnetic field is much stronger than the poloidal magnetic field so it is roughly equal to the total magnetic field. The RF heating in these discharges is absorbed where the minority ion (hydrogen) cyclotron frequency matches that of the RF wave (which is fixed to 80 MHz), so when the toroidal magnetic field is ramped, the absorption layer moves too. This means that it is not possible to perform large ramps of B_t without moving the absorption layer too far off axis. Therefore the B_t ramp presented in Figure 4-10 is rather limited. Nonetheless we observe no change in the pedestal width at all during the ramp, which means that we can rule out any strong scaling of the pedestal width with B_t. However, due to the relatively limited range of B_t values in the ramp, we cannot rule out that there could be a weak scaling with B_t.

Dependence on plasma shape

The plasma cross section in shaped tokamaks (such as Alcator C-Mod) is not circular. The shape is more "D" shaped, with elongation larger than 1, and finite triangularity. One can define an upper (lower) triangularity measuring to what degree the field lines at the top (bottom) are pulled towards the inboard side to form the upper (lower) part of a "D" shape rather than an elliptical shape. The triangularity is calculated by EFIT, and the upper triangularity is defined as $\delta^{upper} = (R_0 - R_{upper})/a$, where R_0 is the plasma major radius, a is the plasma minor radius, and R_{upper} is the major radius of the uppermost point of the last closed flux surface. The lower triangularity is defined similarly. During an EDA H-mode, the upper triangularity was scanned systematically, and we found an approximately linear relationship between the upper triangularity and the pedestal width, as seen in Figure 4-11.

4.4.2 Pedestal height scalings

During the EDA H-mode current ramp experiments it was noticed that the pedestal height increased with increasing plasma current. In Figure 4-12, we show the results of the four current ramp experiments also mentioned in Section 4.4.1. In all four cases, there is a clear tendency for the pedestal height to increase with plasma current. We take this to indicate that the edge confinement of the impurities (fluorine) gets better with increasing current. This is similar to the measurements in L-mode on Alcator C-Mod which show that the global particle confinement improves with plasma current [23]. However, care should be taken since we do not know if the source rate is also changing. During these shots, the source of fluorine is presumably constant, and since modelling shows that we are sensitive to highly ionized fluorine transported from the core plasma, we should not be particularly sensitive to any change in the ionization rate at the edge. The whole database has also been used to investigate if this trend holds across all EDA discharges. The results are shown in Figure 4-13. There does not seem to be a systematic trend. This is probably because the fluorine source varies significantly from discharge to discharge, and might depend on a number of other

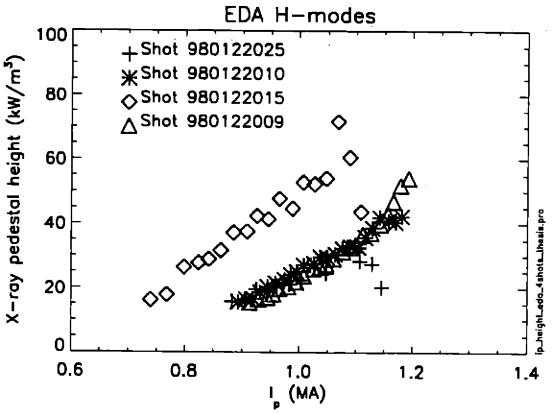

Figure 4-12: The pedestal height increases as the plasma current is increased during four EDA discharges.

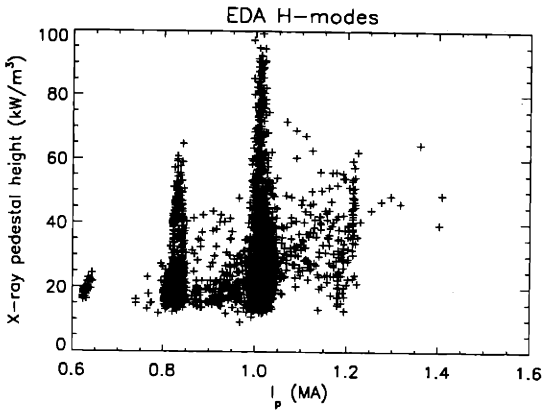

Figure 4-13: When looking at all discharges in the database, no trend is apparent in the pedestal height for different values of the plasma current. This implies that the shot to shot variation in x-ray pedestal height is much larger than the variation purely due to the plasma current.

variables, which are kept constant in the series of discharges in Figure 4-12 but vary significantly from shot to shot in the database.

4.5 L-mode emissivity profiles

In L-mode, the soft x-ray emissivity near the plasma edge is typically only 0.5-3 kW/m^2. This means that the signal/noise ratio is low, so one has to average over many time samples to eliminate the random noise and use the methods described in Appendix A to reduce the systematic noise sources. Even when this is done, most of the time L-mode emissivity profiles are very noisy. However, when the noise reduction algorithms work particularly well, or when neon puffing increases the signal levels sufficiently, it is possible to get good emissivity profiles in L-mode. Typically some RF heating helps increase the L-mode emissivity. In Figure 4-14 we show a typical L-mode profile. In this case, a small pedestal can be seen near the separatrix. In general, L-mode emissivity profiles show a break in slope near the separatrix, but often no pedestal.

One way of getting better signal levels in L-mode is to inject neon gas. Such an injection can increase emissivity levels by more than a factor of two, both in L-mode

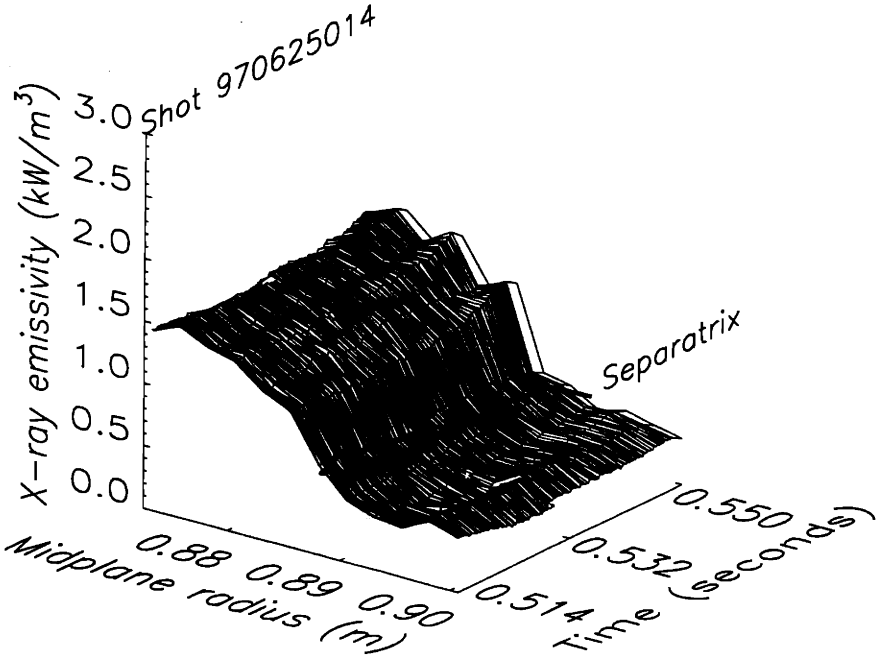

Figure 4-14: This is a rather typical L-mode profile, showing a very small pedestal within a few mm of the separatrix, and emissivity levels around 1-2 kW/m^2. In many L-mode cases, there is no clear pedestal.

and in H-mode. An example of a neon injected L-mode is shown in Figure 4-15. Even though the signal levels are rather high, there are still traces of the pickup noise described in Appendix A, giving the profile a rather "bumpy" shape. It appears that the soft x-ray emissivity has a significantly steeper gradient inside the separatrix than outside.

4.6 Edge Localized Modes

Edge Localized Modes (ELMs) [12] are short bursts of instabilities located in the H-mode edge transport barrier. They briefly increase the transport of particles and heat, so often a burst of plasma is released from the edge with each ELM. ELMs are divided into various categories, the most important being the type I and type III ELMs. Type I ELMs are observed at high heating power and become more frequent if the heating power is increased, implying that they are triggered when an edge gradient exceeds a certain value. One of the leading theories is that type I ELMs are ballooning-like

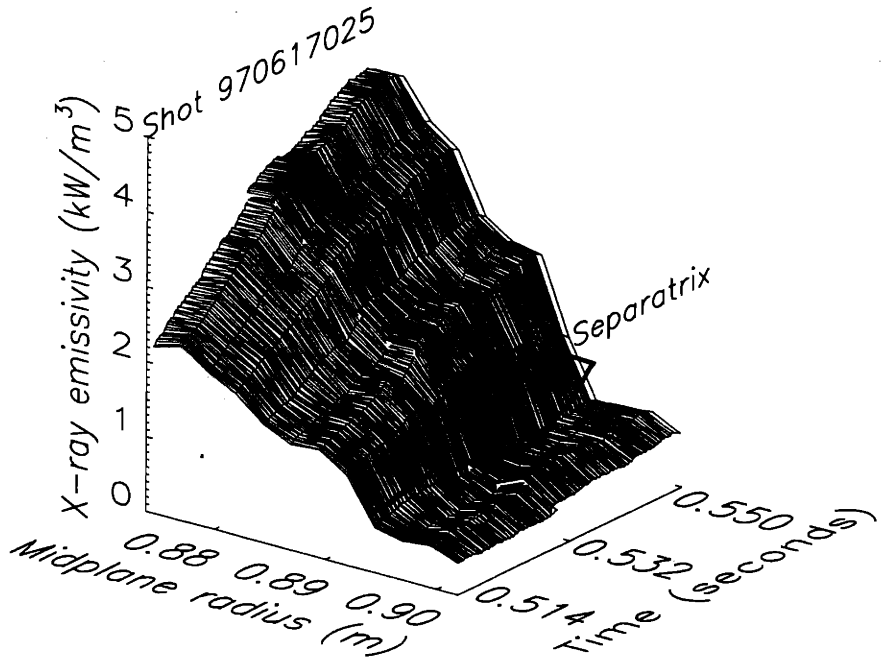

Figure 4-15: This shows an L-mode emissivity profile reaching 5kW/m^2 due to a neon gas injection. In this case, several bumps appear in the emissivity profile. They may simply be artifacts of the pickup noise described in Appendix A.

instabilities driven by the edge plasma pressure gradient. Type I ELMs are not seen on Alcator C-Mod. Type III ELMs are observed when the plasma is in H-mode but is near the H-L threshold. Type III ELMs are not as large as type I ELMs, and often have very high repetition rates, around 1 kHz. They become less frequent and eventually disappear if the heating power is increased. Type III ELMs are observed on Alcator C-Mod under certain conditions, for instance when the heating power is low, or the radiation losses are large.

4.6.1 The importance of ELMs

Although an ELM transiently decreases the confinement, one does not necessarily want to avoid ELMs in a fusion device. One of the problems with ELM-free H-modes is that the impurity particle confinement is so high that impurities accumulate until the radiation reaches levels where the H-mode can no longer be sustained, and an H-L transition occurs. ELMs can provide a mechanism for releasing some of the impurities,

so that a steady state can be achieved. A single ELM usually does not cause the loss of a large fraction of the plasma energy, so one can maintain the good energy confinement which makes the H-mode so attractive. However, a type I ELM carries enough energy in a short time as to be a significant transient power load on the divertor structure. In present devices, this is not critical, but these transient power loads are likely to be unacceptably high for a future reactor size tokamak [24], [12]. This is one of the reasons why the EDA H-mode is such an attractive confinement mode for a future reactor, as it degrades the impurity and particle confinement in a continuous way. It is also important to study ELMs to better learn what the fundamental physics is. Since the soft x-ray diagnostic provides excellent spatial resolution in the edge region, as well as good temporal resolution, it can provide measurements of ELMs which are well resolved both in time and space, so it may help us understand the nature of ELMs. In the following we will describe measurements of the soft x-ray emissivity at the outboard edge of the plasma. In Chapter 10 we will present simultaneous measurements at the top and outboard edge.

4.6.2 Measurements of the soft x-ray emissivity during ELMs

The combination of high radial resolution and good temporal resolution makes the soft x-ray diagnostic well suited for detailed measurements of ELMs [25]. In Figure 4-16 the time evolution of the raw data for a series of discrete ELMs is shown. In each case, the emission is very low near and outside the separatrix between the ELMs, but there is significant emission well past the separatrix during the ELMs. In fact, the emission extends into the shadow of the limiter, where the field lines directly intersect the limiter structure. It is clear from the figure that ELMs indeed are very transient events. With the 12 μs sampling time, and the 30 μs response time of the electronics, we can follow the time evolution of each ELM. In Figure 4-17 we show an example where the time evolution can be followed. The ELM changes the brightness profile significantly in a very short time (around 100 μs) and that the brightness profile returns to roughly the same shape (but lower amplitude) after the ELM very quickly as well. The time evolution is well resolved. We can also show the time evolution of the

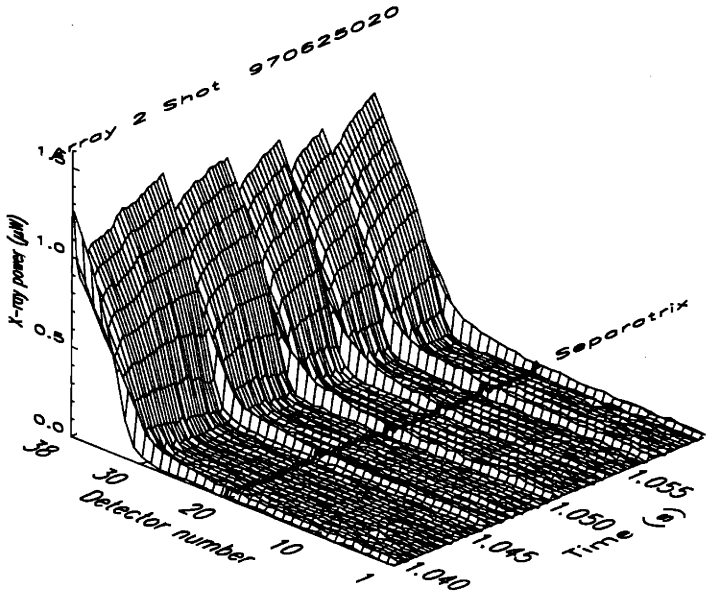

Figure 4-16: A series of ELMs shows up clearly on the soft x-ray detectors. During each ELM, a burst of emission is seen, extending well beyond the separatrix into the scrape-off layer.

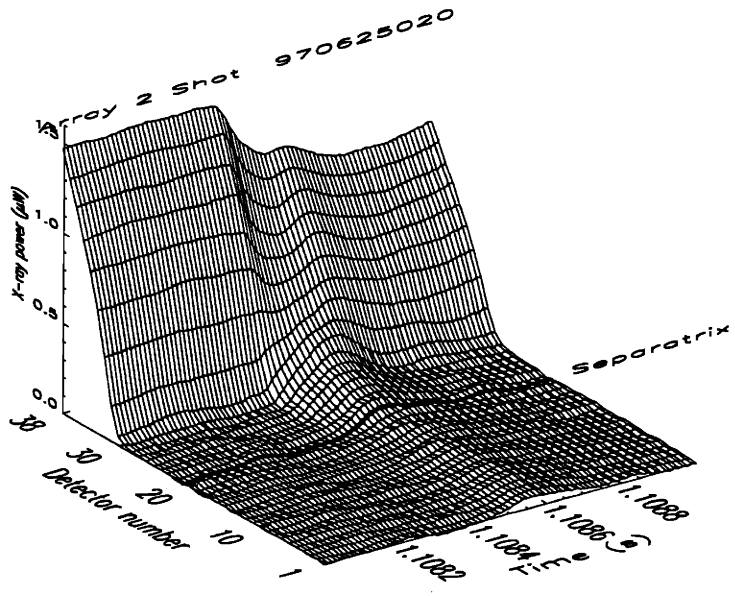

Figure 4-17: The time evolution of a particular ELM is well resolved. The x-ray burst associated with this ELM also extends well beyond the separatrix and even into the shadow of the limiter.

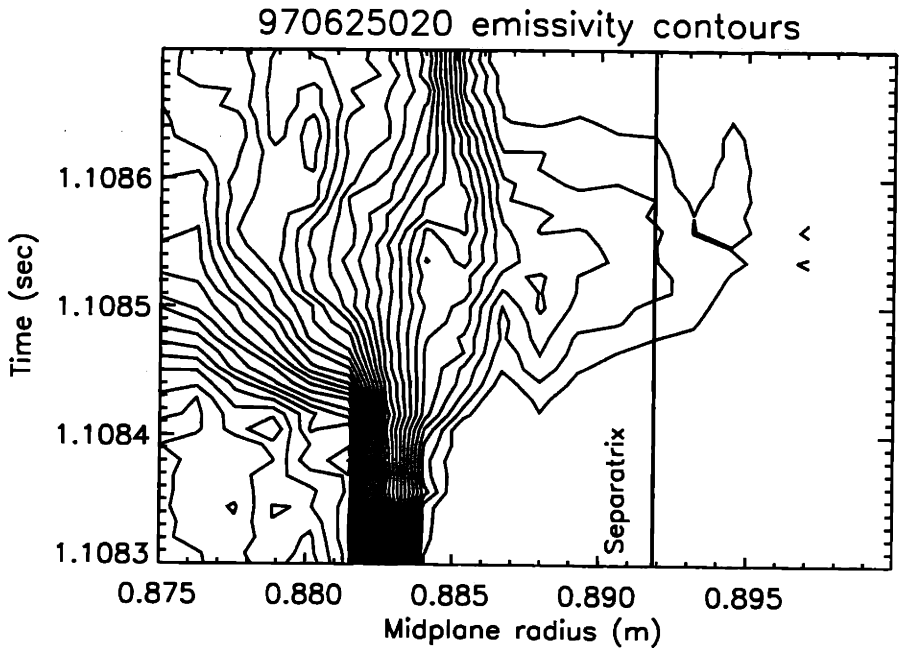

Figure 4-18: The time evolution of the soft x-ray emissivity shows the outward propagation of the x-ray burst, as the x-ray pedestal is briefly flattened. The pedestal reforms shortly thereafter, slightly outside its original location. No smoothing was applied to the data.

emissivity profile, which reveals more details about the propagation of the soft x-ray burst. It should be noted that the inversion assumes that the emissivity is constant on a flux surface, and that the outermost surface with finite emissivity must be viewed in order to give good inversions. When there is finite emission all the way into the shadow of the limiter, the inversion becomes inaccurate, in particular near the edge of the view, since neither of the two conditions are fulfilled. The emissivity is unlikely to be constant on a flux surface during the transient bursts of radial transport, since there is finite emission on open field lines, even those which intersect the limiters nearby. Even so, the inversion should yield accurate information about the time evolution in the pedestal region, and it should also yield accurate information about the propagation front of x-ray emitting plasma during the burst, until the front reaches the edge of the view of the detectors. A contour plot of the soft x-ray emissivity shows that the first sign of the ELM is seen in the steep region of the x-ray pedestal, and its effect propagates inward and outward as the pedestal is flattened. The burst propagates outward at a rate of approximately 300 m/s. The radial transport must be able to compete with the parallel transport, otherwise there could not be soft x-ray emitting

plasma on field lines directly intersecting the limiter, since the limiter is a sink of heat and plasma density. If one assumes a fluorine ion temperature of 100 eV, the thermal velocity along a field line of the fluorine is approximately 20 km/s, so it can move approximately 1 m along a field line in 50 μs. In the scrape-off layer just outside the separatrix, the nearest material surface is several meters away along a field line. In the shadow of the limiter, the field lines intersect the limiters within roughly 1 m, so the characteristic parallel transport time is near 50 μs. Since the x-ray emitting burst of plasma can travel about 15 mm radially in that time, it makes sense that a relatively hot x-ray emitting plasma can exist transiently on these open field lines. It illustrates that the radial transport can actually dominate the parallel transport during ELMs. This indicates that the transient loss of radial confinement during large ELMs is very significant. It appears that the transport barrier completely disappears during the ELMs, but reforms quickly, within about 200 μs.

We note that the outward convection of 300 m/s is the same order of magnitude as the neoclassical inward impurity convection which competes with the outward diffusion in the steady state impurity density pedestal region, as discussed in detail in Chapter 7.

Chapter 5

Origin of the edge soft x-ray emission

The soft x-ray edge diagnostics provide measurements of the soft x-ray emissivity of the plasma edge with very high radial resolution and good temporal resolution, and are very reliable diagnostics, providing continuous measurements for more than 99 % of the plasma discharges since 1997. We are interested in relating the x-ray emissivity to more fundamental plasma parameters such as electron temperature (T_e) or electron density (n_e) or impurity density (n_I), and this is not straightforward. By establishing the physical processes responsible for the soft x-ray emissivity near the edge of the plasma, it will be possible to find out its dependence on T_e, n_e, and n_I, so that it will be possible to extract information about these quantities. In this chapter we will show that the x-ray emissivity is dominated by radiation from medium-Z impurities, and that we can extract the radial density profiles of these impurities by comparing measured profiles of x-ray emissivity, electron density and electron temperature.

5.1 Origin of the soft x-ray emission in Alcator C-Mod

The plasma emissivity is due to bremsstrahlung, recombination, and line radiation, and has to be summed over all plasma species and all charge states. The 10 μm beryllium foil acts as a highpass filter, only allowing soft and hard x-rays to penetrate. This means that it is not necessary to consider radiation processes which produce radiation below approximately 500 eV photon energy, and this greatly reduces the radiation processes that need to be considered. Near the plasma edge, the electron temperature ranges from a few eV to 700 eV, with typical edge pedestal values of 50-500 eV. This also restricts the processes that need be considered. By looking at the x-ray emission before and after injection of particular impurities one can establish experimentally whether or not that particular impurity could be a major contributor to the observed soft x-ray emissivity. This way, it has been determined that B (Z=5), C (Z=6), N (Z=7), Si (Z=14), Ar (Z=18), and Mo (Z=42) do not contribute significantly to the soft x-ray emission. Similarly, it has been confirmed that the x-ray emission rises significantly after injections of fluorine or neon. Neon is usually not present in the machine, but when injected, it has been observed to increase the x-ray emissivity as much as a factor of 5 in some cases. From spectroscopic data [26], it is known that fluorine is one of the most abundant intrinsic impurities in standard plasmas, whereas neon is only present in the plasma when it has been actively injected. Oxygen is known to be an intrinsic impurity but the levels are kept very low by regularly coating the plasma facing components with boron (boronization). Therefore, oxygen is unlikely to be a major contributor to the soft x-ray emissivity, but could be significant in an unboronized machine. In the following, we will present both simulated data and experimental data for oxygen, fluorine, and neon in order to establish how efficiently they radiate through the beryllium filters, and which species dominate the soft x-ray emission near the plasma edge.

5.1.1 Fluorine

Experimental evidence

Spectroscopic measurements show that fluorine is one of the most abundant intrinsic impurities in Alcator C-Mod plasmas [26]. In the 1999 run campaign, CaF_2 was injected into a number of different discharges, and in all H-mode cases, there was a clear rise in the soft x-ray emissivity a few msec after the injections. Simulations show that Ca is unlikely to be a strong source of x-ray radiation near the plasma edge which confirms our suspicion that it is the fluorine which is causing the rise in the soft x-rays.

Transport and radiation analysis

A detailed analysis of transport of, and radiation from, fluorine has been performed using the MIST code described in Chapter 7. From MIST, the radial steady-state density profiles of all charge states are obtained, and these are used in detailed calculations of the emission from radiative recombination, line radiation, and (bulk plasma) bremsstrahlung, based on theoretical modelling [27], [31]. The spectral emissivity profiles are convolved with the beryllium transmission function (see Figure 2-3) to yield the soft x-ray emissivity which can be directly compared to that measured in the experiments. In Figure 5-1 we plot the radial profile of the x-ray emissivity for a simulation where we assumed a central fluorine density of 0.14 % of the central electron density. We choose 0.14 % because this makes the simulated x-ray emissivity agree (remarkably well) with the actual measured x-ray emissivity for the plasma discharge which was being modelled in the MIST simulation. It is seen that the dominant source of x-ray emissivity is line radiation, and there is a significant contribution from recombination of fully ionized fluorine. The bulk plasma bremsstrahlung is not a major factor although it is not completely negligible in the warmer parts of the edge plasma. In Figure 5-2 we plot the strongest lines that make up the total line radiation. The line radiation is dominated by the Lyman α line (the 2p-1s transition of hydrogen-like fluorine). The second largest contributor is the Lyman β line (3p-1s

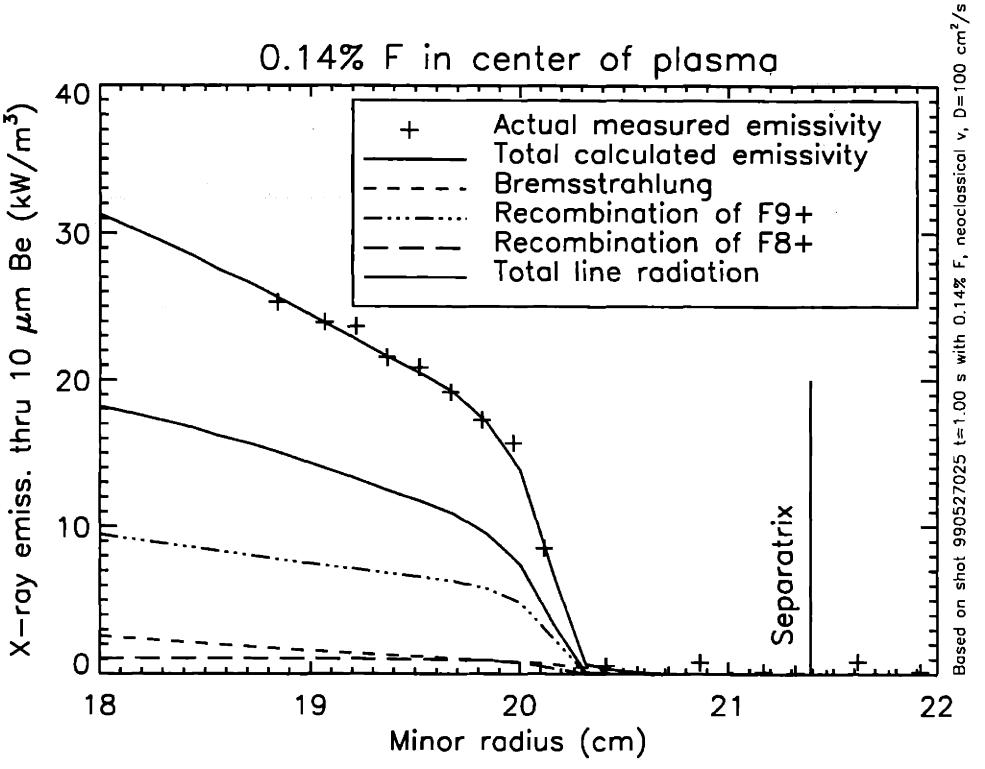

Figure 5-1: The radial x-ray emissivity profile from a MIST simulation with a central F fraction of 0.14 %. For comparison, the actual measured profile for the discharge in question is plotted as well. The dominant sources of soft x-ray radiation are line radiation and recombination of fully ionized fluorine.

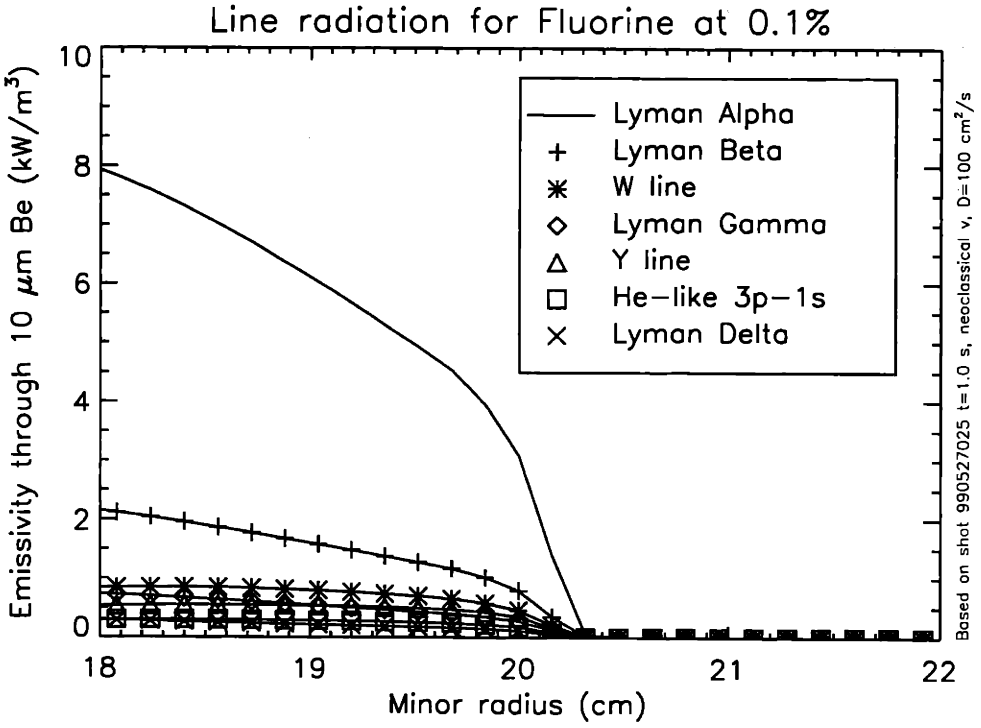

Figure 5-2: The radiation profiles of the strongest lines show that the line radiation mostly comes from hydrogen-like fluorine. The lines are listed in order of descending strengh. The Lyman α line dominates all other lines. Note that this calculation is done for a fluorine fraction of 0.1%, unlike that in Figure 5-1 which was done at 0.14% fluorine.

of H-like F), which is at a higher photon energy so it has a higher transmission coefficient through the Be filter, which partly compensates its lower intensity. All other lines are rather unimportant, including the 3p-1s, the W ($1s2p\ ^1p \rightarrow 1s^2\ ^1S_0$), and the Y ($1s2p\ ^3p_1 \rightarrow 1s^2\ ^1S_0$) lines of helium-like F, so the line radiation is completely dominated by lines from hydrogen-like fluorine. The fluorine is almost completely in the fully ionized (F^{+9}) state at $T_e = 700$ eV but near the x-ray pedestal, about one third is in the hydrogen-like state, which is enough to create strong line radiation. In our previous publication [21], the line radiation was ignored, although it we did mention that the Lyman α line might be important. This detailed calculation clearly demonstrates that the line radiation is in fact very significant, and cannot be left out of the analysis. The line radiation is proportional to $n_e \times n_F^{+8} \times f_1(T_e)$ whereas the radiation from recombination of fully ionized fluorine is proportional to $n_e \times n_F^{+9} \times f_2(T_e)$ where f_1 and f_2 are functions which describe the temperature dependence. The total x-ray emissivity can be written as

$$e = n_e \times n_F \times f(T_e) \tag{5.1}$$

where n_F now denotes the total fluorine density, which is distributed among the various charge states depending on the temperature profile and the transport properties of the plasma [1]. In Figure 5-3 we show the distribution among various charge states of fluorine for the same simulation as in Figure 5-1. It is seen that the fluorine does remain mostly in the fully ionized state but a significant fraction is in the hydrogen-like state. There is even some helium-like fluorine, although it is less than 10%. In Figure 5-4 we plot the x-ray emissivity at constant n_e and constant n_F as a function of T_e in order to determine $f(T_e)$ in Equation 5.1. It is seen that the temperature dependence is rather weak above 400 eV, but does show a 50% variation from 150 eV to 400 eV. From the Figure we derive the following practical formula, assuming that radiation from other impurity species is negligible[2]:

$$e[kW/m^3] = 2.5 \times n_{e,20} \times n_{F,17} \times f(T_e) \tag{5.2}$$

[1] If one ignores the effects of transport, the usual collisional excitation - radiative decay model will lead to coronal equilibrium

[2] We shall address this assumption later in this Chapter

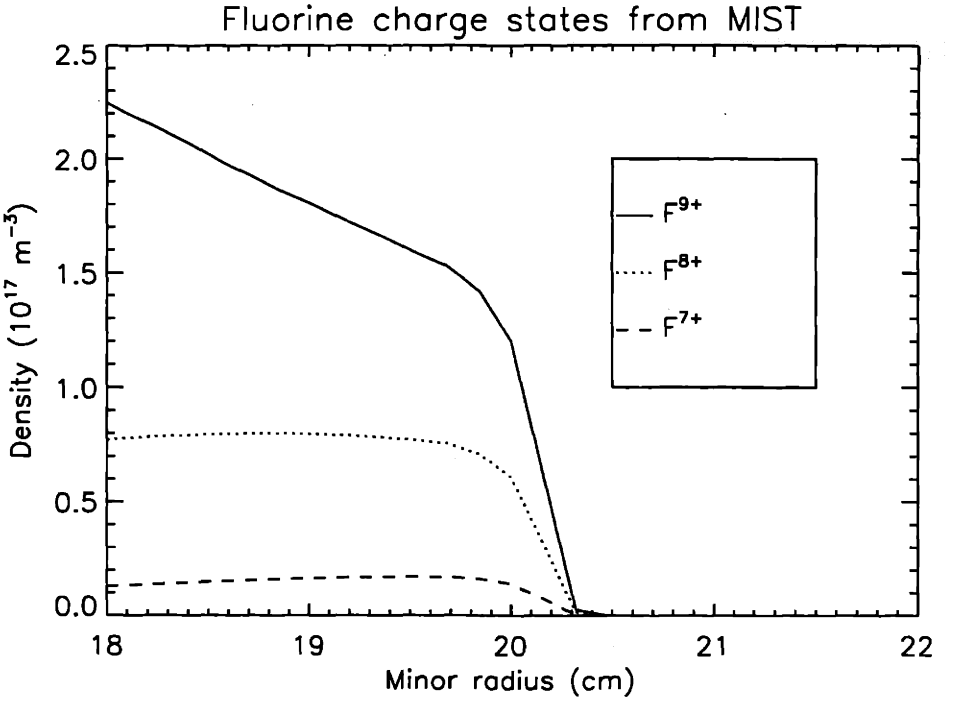

Figure 5-3: Profiles of the various charge states of fluorine for a particular simulation. Most of the fluorine is fully ionized but about 1/3 is in the hydrogen-like state. Less than 1/10 of the fluorine is in the helium-like state.

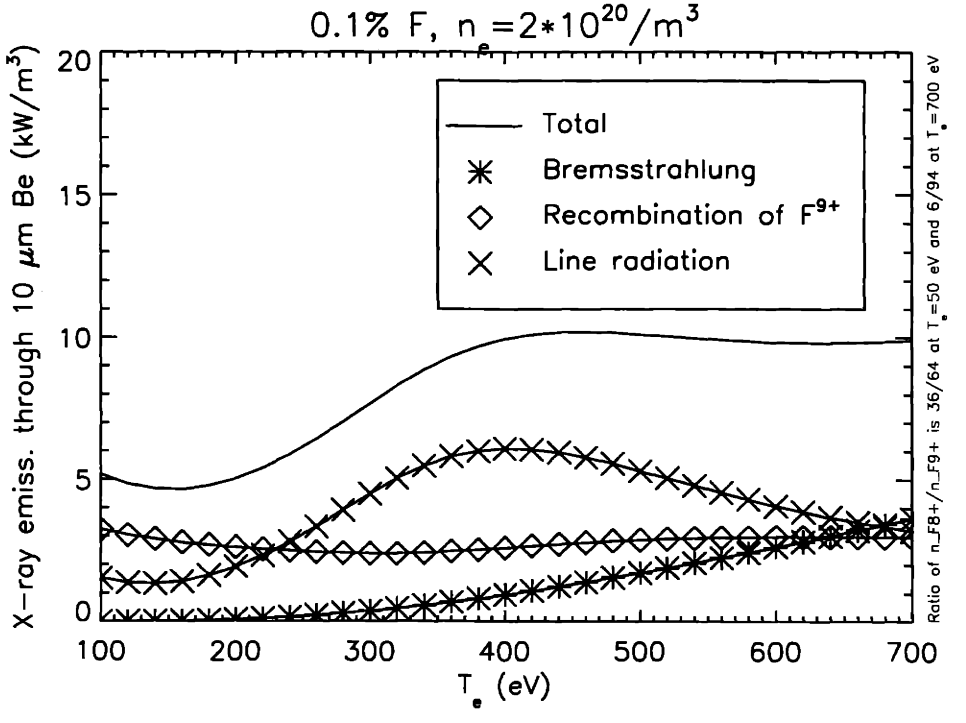

Figure 5-4: The temperature dependence of the x-ray emissivity is very weak above 400 eV but shows a 50% variation below 400 eV.

where e is the soft x-ray emissivity in kW/m^3, $n_{e,20}$ is the electron density measured in units of 10^{20} m^{-3}, $n_{F,17}$ is the total fluorine density measured in units of 10^{17} m^{-3}, and $f(T_e) \approx 1$ for $T_e > 400$ eV and varies between 0.5 and 1 below 400 eV.

5.1.2 Neon

Experimental evidence

Neon is not an intrinsic impurity, but can be injected into the plasma in a controlled way. The x-ray emission increases significantly when this is done. In Figure 5-5 we show the time evolution of some key parameters for a plasma which is in a quasi-steady state EDA H-mode. At t=0.85 sec, a 35 msec neon injection is initiated. The neon injection is small enough that it only perturbs the plasma slightly, as evidenced by a very slight decrease in the edge electron temperature due to the associated radiation loss. The electron density and the H_α emission are virtually unchanged by the injection. The x-ray emission starts rising around t=0.88 sec and continues to rise until the raw signal level on detector 38 is roughly twice the pre-injection level at t=1.1 sec. The rise in soft x-ray level is delayed because it takes time for the neon to diffuse into the core plasma, lose its electrons and then diffuse out again to the edge and recombine. Although the overall emissivity levels increase dramatically, the pedestal shape remains the same, that is the pedestal width and major radial position remains unchanged by the injection, as seen in the lower time traces in Figure 5-5. Figure 5-6 shows the time evolution of the emissivity profile and it confirms the dramatic rise in soft x-ray emissivity, and it shows that the pedestal remains in the same major radial position. Since the separatrix position does not change either, the pedestal location also remains constant with respect to the separatrix. The pedestal height increases by more than a factor of two, and the peak emissivity levels inside the pedestal increase by about a factor of 4 after the injection. Therefore, it may be concluded that at t=1.1 sec, the x-ray emissivity is dominated by emission from neon, rather than the intrinsic impurities (presumably fluorine). Since the pedestal position and width has not changed at all, it follows that the transport processes for neon in

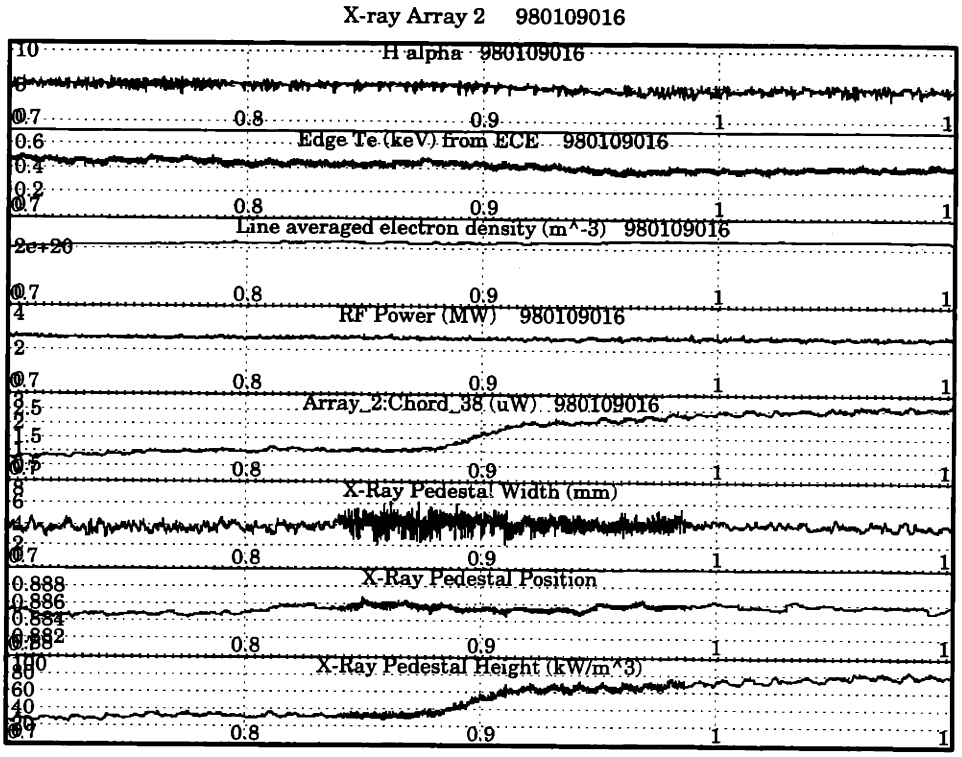

Figure 5-5: A quasi-steady state EDA H-mode is perturbed slightly by a neon injection initiated at t=0.85 sec. The main plasma parameters are virtually unaffected by the injection, but the x-ray brightness more than doubles after the injection. However, the pedestal width and position remain constant, only the pedestal height is affected. The increased noise level seen on the data from 0.85 sec to 0.99 sec is caused by the higher sampling frequency (the soft x-rays are sampled at 83 kHz from 0.85 sec to 0.99 sec and at 5kHz the rest of the time).

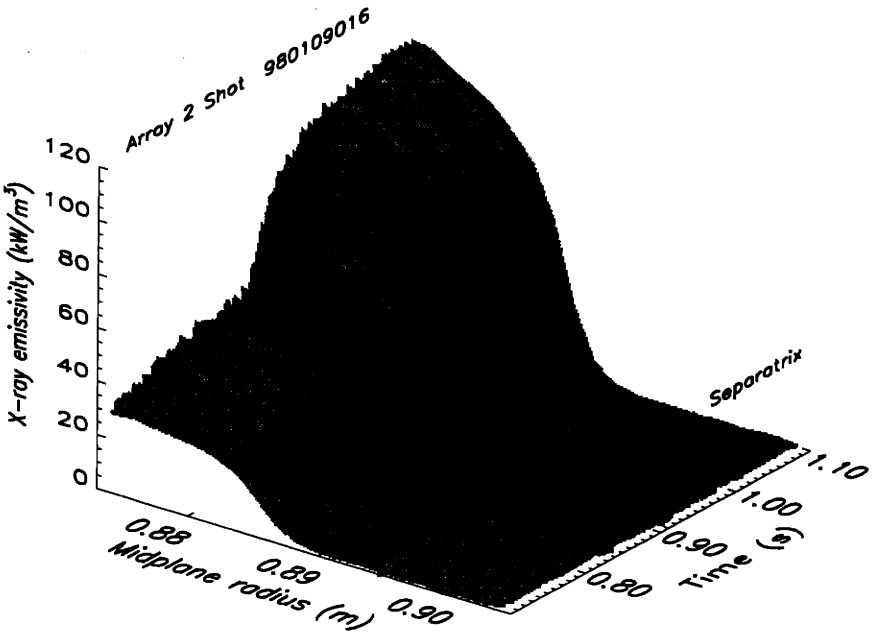

Figure 5-6: The soft x-ray emissivity profile is in a quasi-steady state before the neon injection which starts at t=0.85 sec. With a short delay, the emissivity starts rising and eventually reaches a level more than 4 times higher than the pre-injection level. The shape and position of the pedestal is not changed, however, indicating that the radiation and transport processes of neon in the edge plasma are very similar to those for the intrinsic impurities (presumably fluorine).

the edge plasma must be very similar to the transport of the intrinsic impurities.

Transport and radiation analysis

Simulations of neon transport and radiation have been performed using the same procedure which was outlined for fluorine. A neon impurity fraction of 0.1 % in the core plasma was assumed in these calculations. The same background plasma and transport coefficients were used so that a direct comparison could be made between x-ray emissivity profiles originating from neon and fluorine. The simulated radial profile of soft x-ray emissivity is shown in Figure 5-7. The soft x-ray emissivity is about a factor of 2 larger for 0.1 % of neon than it is for 0.14 % of fluorine. The soft x-ray diagnostic is about 3.5 times more sensitive to an injection of neon than to an injection of the same number of fluorine atoms. This is consistent with the experimental observation that neon injections show up much more clearly than

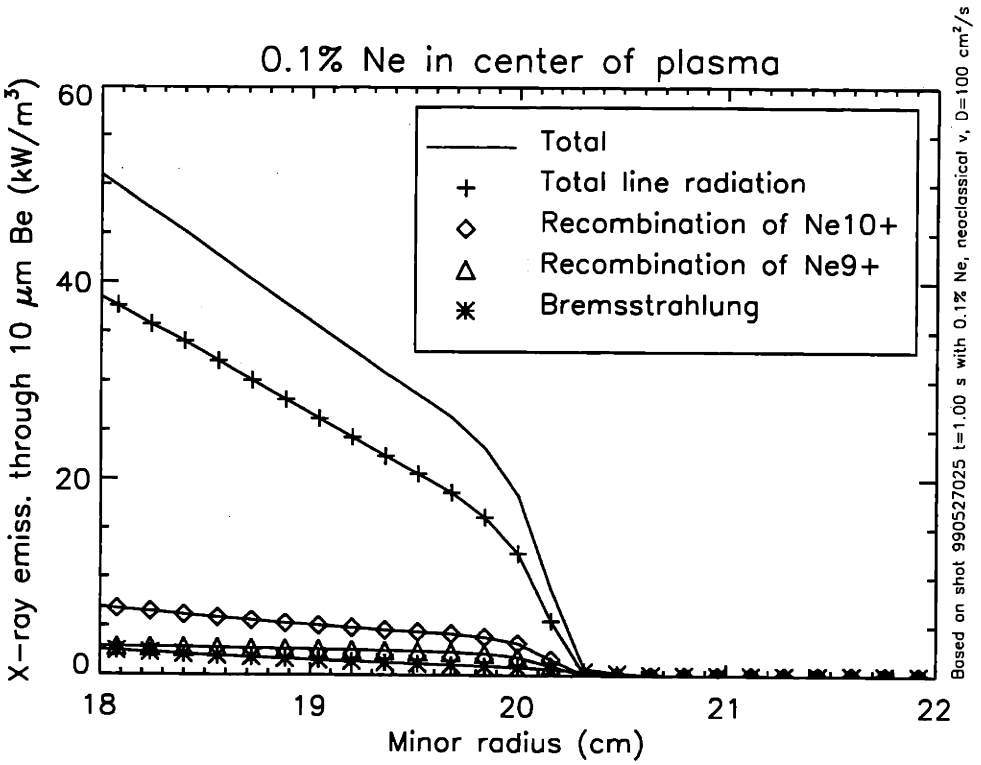

Figure 5-7: The soft x-ray emissivity from 0.1 % of neon exceeds that from 0.14 % of fluorine by more than a factor of 2. Most of the radiation comes from line radiation. Only a small part comes from radiative recombination.

freon or CaF_2 injections. It should be noted that the position and width of the x-ray emissivity profile is virtually the same as that obtained for fluorine. This is consistent with fluorine being the major intrinsic source of soft x-ray emission at the plasma edge, since we also observe no change in pedestal position or width in experiments when neon is injected, as described in the previous section. The various contributions to the overall x-ray emissivity are also shown. The line radiation dominates strongly. In Figure 5-8 we show the strongest lines from neon at the edge of the plasma. As was the case for fluorine, the Lyman α line is the dominant line. Most of the neon is in the hydrogen-like state at the edge, which explains why the Lyman series dominates the recombination of fully ionized neon to such a large degree.

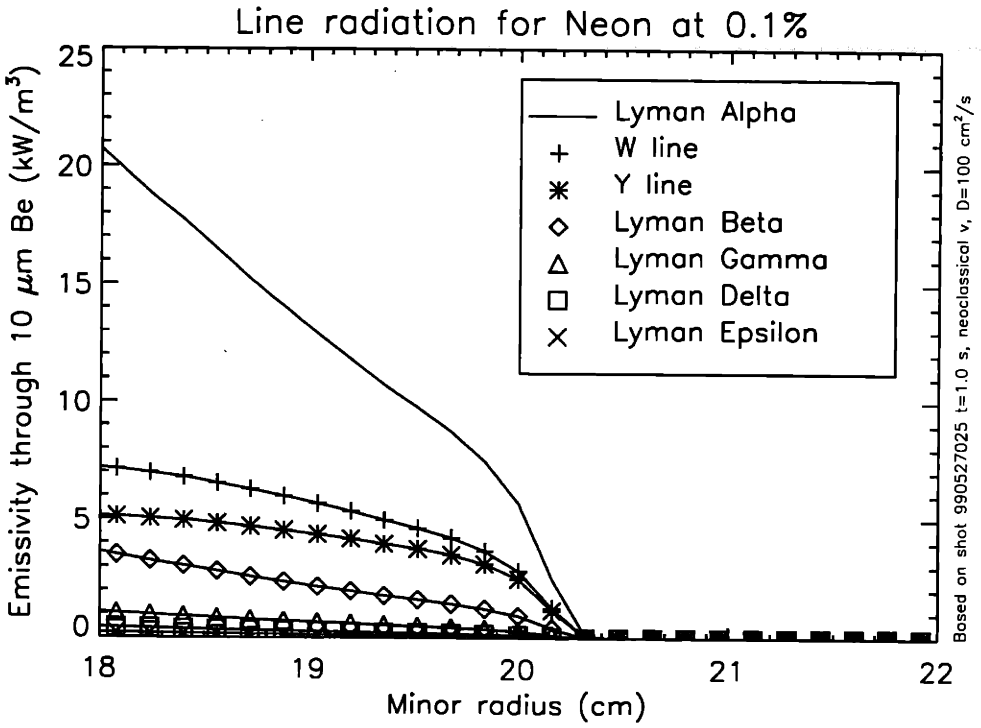

Figure 5-8: The line radiation from neon is dominated by the Lyman α line, once filtered through the beryllium foil. The rest of the Lyman series also contributes to some extent.

5.1.3 Oxygen

Experimental evidence

Like fluorine, oxygen is an intrinsic impurity in Alcator C-Mod plasmas. The oxygen level is monitored by spectroscopy, and the machine is regularly boronized, which reduces the amount of oxygen to very low levels. There have been no controlled oxygen injections in Alcator C-Mod during the operation of the soft x-ray diagnostics so there is no direct evidence that the diagnostics are sensitive to oxygen, nor that they are insensitive to oxygen. The transport and radiation of oxygen can still be modelled, in the same way as was done for fluorine and neon. This analysis is presented in the following.

Transport and radiation analysis

We assume that there is 0.1 % oxygen in the core of the plasma, as was done for neon. In Figure 5-9 we show the radial profile of x-ray emissivity originating from

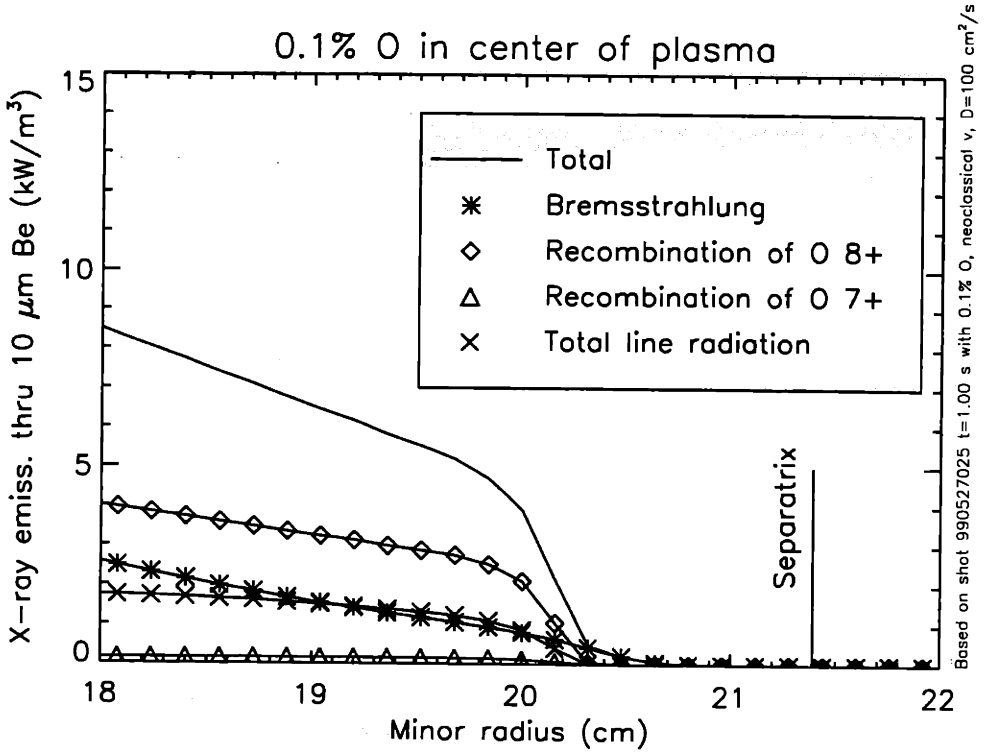

Figure 5-9: The x-ray emissivity arising from bulk plasma bremsstrahlung and various radiation processes from 0.1 % of oxygen shows the familiar sharp pedestal located well inside the last closed flux surface, as was the case for fluorine and neon. However, oxygen does not radiate as efficiently through the beryllium filter as neon or fluorine. For oxygen, the dominant source of soft x-ray radiation is recombination of the fully ionized state.

bulk plasma bremsstrahlung and various radiation processes from oxygen. The soft x-ray emissivity from 0.1 % of oxygen is significantly lower than for similar fractions of fluorine or neon. The profile still has the same shape as that arising from fluorine or neon radiation but its magnitude is much lower. The dominant source of radiation for oxygen is recombination of the fully ionized state, whereas line radiation is less important, though not negligible. The Lyman α radiation is the strongest line for oxygen as well. The reason for the line radiation being much weaker for oxygen than for fluorine and especially neon is that the fully ionized fraction is very high, so the hydrogen-like fraction is very small in the pedestal region for oxygen, and the line photon energy is also somewhat smaller than for fluorine or neon, so the transmission coefficient through the beryllium filter is smaller. It follows that one would require signficantly more oxygen than fluorine in the plasma in order to make their soft x-ray contributions equal.

5.2 Discussion

From experiments and computer simulations we find that neon is very efficient at radiating soft x-rays at the plasma edge. However, neon is not present in the plasma unless actively injected, so it cannot explain the bulk of our H-mode observations which were made without neon injections. We must therefore turn our attention towards intrinsic impurities. Experiments and rough theoretical estimates show that impurities with Z<8 are not important contributors to the soft x-ray emission. Computer simulations show that oxygen can radiate through the beryllium filter but not very efficiently. It would require rather high levels of oxygen to explain the emissivity levels we see, and this is in contradiction with spectroscopic information showing that oxygen levels become very low after boronization. Fluorine is known to be an intrinsic impurity which is quite abundant. The source of fluorine is believed to be teflon insulation exposed to plasma. It radiates quite efficiently through the beryllium filter, and our modelling shows that for a representative H-mode x-ray emissivity profile, the emissivity levels are consistent with 0.14 % of fluorine, which is a level in agreement with rough estimates from spectroscopy. Modelling and injections of other impurity species (controlled as well as uncontrolled) support the finding that fluorine dominates the edge soft x-ray emission for normal plasma discharges. It should be mentioned that some iron injections have shown significant, transient increases in soft x-ray emission, presumably because of an inner-shell excitation process. Iron is usually present in the plasma in extremely low quantities.

5.3 Temperature and density profile effects

In the previous section it was established that the soft x-ray emission near the plasma edge is usually dominated by fluorine. We may ask if the very sharp pedestal shape observed in experiments reflects rapid changes in T_e, n_e, or n_F, or perhaps a combination of those. The soft x-ray emissivity can vary from more than 30 kW/m^3 at the top of the pedestal to less than 1 kW/m^3 at the bottom of the x-ray pedestal in

only 2-3 mm in ELM-free H-mode. Since $f(T_e)$ in Equation 5.2 only varies at most a factor of two across the range from 100 eV to 700 eV (typical of the temperatures in the outermost 20 mm of the plasma), then there is at most a factor of 2 change in x-ray emissivity due to T_e, and this would only be the case if one would invoke a change from 150 eV to 400 eV over 2 mm, which is a somewhat stronger temperature gradient than what has been measured from ECE in even the hottest H-modes. However, a factor of two cannot be neglected completely. In Figure 5-10 we compare the edge profiles of n_e, T_e, and xray emissivity for a particular ohmic ELMfree H-mode (990527025). It is seen that the soft x-ray emissivity profile is sharper than the T_e and n_e profiles, and that the soft x-ray emissivity pedestal is located near the top of the n_e and T_e profiles[3]. Thus, neither n_e nor T_e varies significantly in the region where the soft x-ray emissivity varies the most. We are therefore led to conclude that pedestal in soft x-ray emissivity is caused by a similar pedestal in the fluorine density profile, and that the T_e and n_e profiles only affect the shape of the soft x-ray emissivity to a small degree. We make this observation more quantitative in the following. In Figure 5-11 we plot the fluorine density profile inferred from measured profiles of n_e, T_e, and e (the soft x-ray emissivity). In the same Figure we also plot what would be inferred if we completely ignored the T_e dependence, and what would be inferred if we completely ignored the n_e dependence. It is seen that neither T_e nor n_e are particularly important for the n_F profile. In other words, the very rapid variation in soft x-ray emissivity is almost entirely due to the very rapid variation in the density of the highly ionized states of fluorine. The T_e variation can at most explain a factor of two x-ray emissivity increase but the soft x-ray emissivity is just as sensitive to the electron density as it is to the impurity density, so it is not immediately obvious why the n_e profile does not affect the soft x-ray profile to a large extent. The electron density effect is less important because the soft x-ray emissivity pedestal is located just inside the electron density pedestal, ie. in a region where n_e does not change rapidly. It is crucial for this argument that we know the shape and location of the

[3]In Chapter 7 we will explain why the soft x-ray emissivity pedestal is located near the top of the n_e pedestal

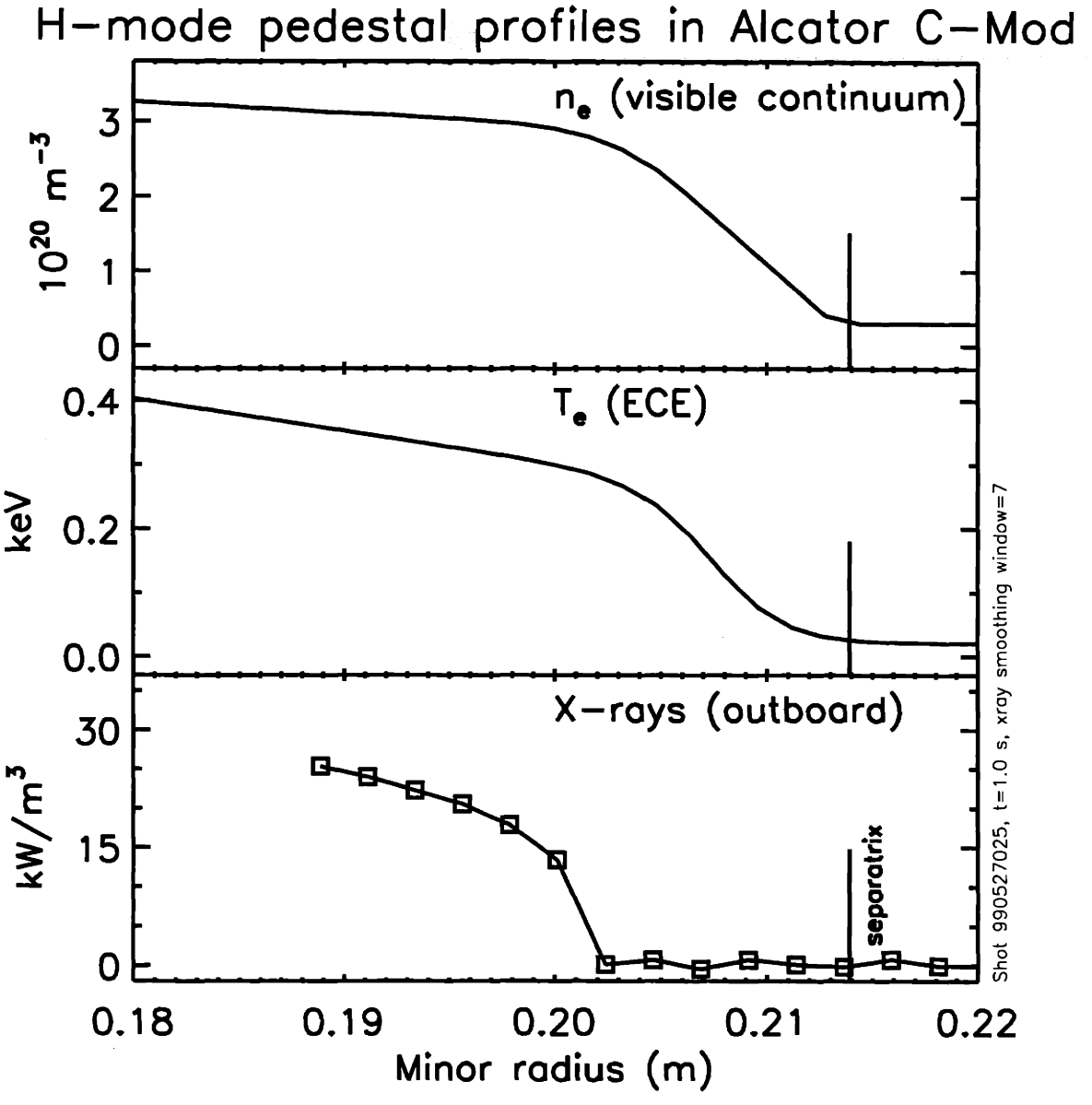

Figure 5-10: The profiles of outboard edge soft x-ray emissivity, electron density, and electron temperature all show pedestal-like shapes near the separatrix in H-mode. However, the soft x-ray emissivity is typically narrower than the n_e and T_e pedestals, and it is always located well inside the n_e and T_e pedestals.

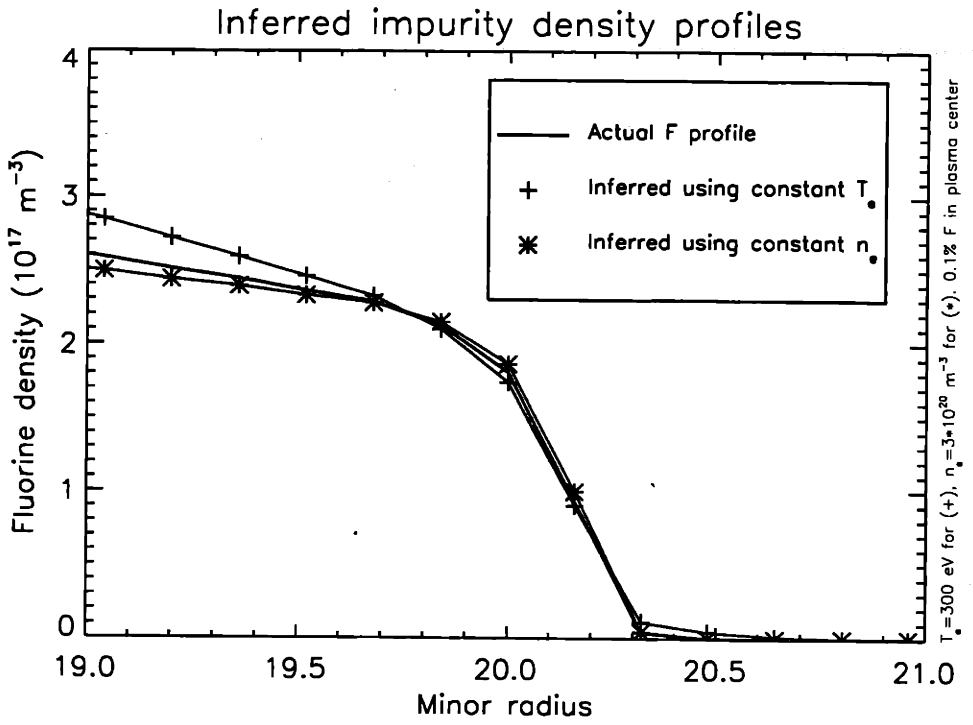

Figure 5-11: When one infers the fluorine density profile from the soft x-ray profile, it does not make a large difference to the result if one includes the effects of a radially changing T_e or n_e.

n_e pedestal with high accuracy, so this result could not have been obtained without high resolution measurements of the n_e pedestal. Detailed measurements of the T_e pedestal are not as important since even a large variation in T_e from 100 eV to 700 eV only results in a factor of two change in soft x-ray emissivity. Thus, to a good approximation, one can think of the soft x-ray emissivity profile as having the same shape as the impurity (fluorine) density profile. This point is illustrated in Figure 5-12 where we compare directly the x-ray emissivity profile with the fluorine density profile. The two profiles are located within 0.1 mm of each other and the x-ray pedestal width is 3.3 mm, whereas the fluorine density pedestal is 2.8 mm wide, a difference of 15 %. The slopes inside the pedestals do not agree particularly well because the slope inside the x-ray pedestal also includes the effects of the finite slopes of n_e and T_e.

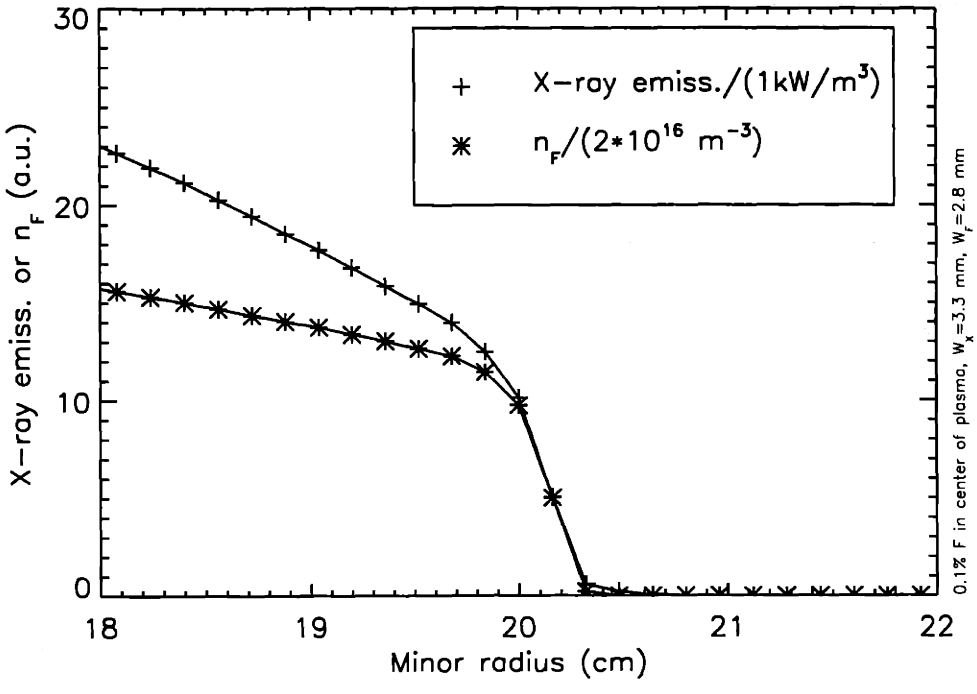

Figure 5-12: A direct comparison between the soft x-ray emissivity and the fluorine density profiles shows that the x-ray pedestal width and position is nearly identical to the width and position of the fluorine density pedestal.

Chapter 6

One-dimensional theory of impurity transport

6.1 Theory of impurity transport

The transport of impurities in a tokamak is a complex phenomenon. The local density of a particular charge state Z of an impurity species I depends on the diffusion coefficient, the convective velocity, and the relevant sources and sinks [32]:

$$\frac{\partial n_I^Z}{\partial t} + \nabla \cdot (-D_I^Z \nabla n_I^Z + \mathbf{v}_I^Z n_I^Z) = R_I^{Z+1} n_I^{Z+1} + I_I^{Z-1} n_I^{Z-1} - (R_I^Z + I_I^Z) n_I^Z + S \quad (6.1)$$

The sources are due to recombination of the charge state $Z+1$ (the same impurity with one less electron), $R_I^{Z+1} n_I^{Z+1}$, and ionization of the $Z-1$ state, denoted by $I_I^{Z-1} n_I^{Z-1}$. The sinks are due to either recombination ($R_I^Z n_I^Z$) or ionization ($I_I^Z n_I^Z$) of the charge state of interest. Any other sources or sinks, such as beam fuelling, can be introduced into the equation via the S term. However, we assume that such terms are negligible, which is a good approximation in Alcator C-Mod, which does not have beam fuelling. If the state of interest is the fully ionized state, then there is only one source term (ionization of the hydrogenlike species) and one sink term (recombination of the fully ionized state). Regardless of which charge state is of interest, one has to solve, self-consistently, for all of the possible charge states of the impurity since they are coupled through these recombination and ionization terms.

In addition, all of the recombination and ionization terms depend on the electron density and temperature, which therefore must be either specified or also calculated self-consistently. Neoclassical impurity transport theory, described in Section 6.1.1, also shows that the diffusion coefficients and convection velocities of impurities depend on the density and temperature of the background plasma.

6.1.1 Neoclassical impurity transport

In a tokamak, the collisional transport is enhanced over the classical level because particles experience excursions from the magnetic flux surfaces much larger than their gyroradii. These excursions are the results of cross-field particle drifts driven by field inhomogeneities, often referred to as ∇B drifts. The resulting *neoclassical* transport can be more than an order of magnitude larger than the classical transport, and considerable effort has been put into developing the theory of neoclassical transport [28], [29], [30]. Even so, the neoclassical diffusion is usually much lower than what is observed in experiments. This enhancement over neoclassical transport is usually referred to as *anomalous* transport, and is believed to be caused by small-scale turbulence. However, when the turbulent transport is suppressed, as it is believed to be in the H-mode transport barrier region near the plasma edge, the transport can be close to neoclassical values. Since the soft x-ray edge diagnostics were specifically designed to study the transport barrier region, it is of interest to compare the results of neoclassical impurity transport theory to our measurements. If one assumes a circular cross section and no variation along field lines, the transport problem becomes one-dimensional (in the radial direction), and the impurity flux becomes [30]:

$$\Gamma_I = \frac{\nu_{iI} q^2 \rho_i^2}{T_i Z_I} \left[(c_1 + \frac{c_2^2}{c_3})(\frac{\partial p_i}{\partial r} - \frac{n_i}{n_I Z_I} \frac{\partial p_I}{\partial r}) - \frac{5c_2}{2c_3} n_i \frac{\partial T_i}{\partial r} \right] \tag{6.2}$$

where $\nu_{iI} = 1/\tau_{iI}$ is the ion-impurity collision frequency, q is the plasma safety factor, $\rho_i = \sqrt{2m_i T_i}/(eB)$ is the ion gyroradius, T_i is the ion temperature (the impurity temperature, T_I, is assumed equal to T_i). We measure temperatures in units of energy. Z_I is the charge state of the impurity, p_i is the ion pressure, p_I is the impurity pressure, n_i is the ion density, n_I is the impurity density. The constants c_1, c_2, and

c_3 are functions of the parameter α, which is assumed to be small:

$$\alpha = Z_I^2 n_I / n_i \ll 1 \tag{6.3}$$

where Z_I is the net charge of the impurity, n_I is the density of the impurity charge state, and n_i is the main ion density. Equation 6.3 ensures that $\nu_{II} \ll \nu_{Ii}$ and that $\nu_{iI} \ll \nu_i$ where ν_{II} is the impurity-impurity collision frequency, ν_{Ii} is the impurity-main ion collision frequency, ν_{iI} is the main ion-impurity collision frequency, ν_i is the ion-ion collision frequency. Thus, if and only if $\alpha \ll 1$ then the impurity density is so much lower than the background density, that for the impurity dynamics, one may ignore impurity-impurity collisions compared to collisions between impurities and the main ions. One can also infer that the ion-impurity collisions are unimportant for the main ion dynamics, since the ion-ion collision frequency is much larger than the ion-impurity collision frequency. Because of the Z_I^2 dependence, this actually places a rather severe constraint on the impurity fraction. Alcator C-Mod generally operates with very low impurity fractions, so Equation 6.3 is usually satisfied for all intrinsic impurities, but this is not the case in most other tokamaks, which often have high levels of intrinsic impurities. In the limit where $\alpha \to 0$, we simply have $c_1 + c_2^2/c_3 = 1$ and $5c_2/2c_3 = 1$, so Equation 6.2 becomes

$$\Gamma_I = \frac{\nu_{iI} q^2 \rho_i^2}{T_i Z_I} \left[\frac{\partial p_i}{\partial r} - \frac{n_i}{n_I Z_I} \frac{\partial p_I}{\partial r} - n_i \frac{\partial T_i}{\partial r} \right] \tag{6.4}$$

By using the relations $p_i = n_i T_i$ and $p_I = n_I T_i$, and collecting terms proportional to $\partial n_I / \partial r$ and n_I, we obtain:

$$\Gamma_I = \nu_{iI} \frac{n_i}{n_I Z_I^2} q^2 \rho_i^2 \left[n_I \left(Z_I \frac{1}{n_i} \frac{\partial n_i}{\partial r} - \frac{1}{T_i} \frac{\partial T_i}{\partial r} \right) - \frac{\partial n_I}{\partial r} \right] \tag{6.5}$$

We note that $\nu_i = \nu_{iI} n_i / (n_I Z_I^2)$, where ν_i is the ion-ion collision frequency, which can conveniently be calculated from [33]:

$$\nu_i = 4.80 \times 10^{-8} n_i Z^4 \sqrt{m_p / m_i} \ln \Lambda \, T_i^{-3/2} \tag{6.6}$$

where n_i is in cm^{-3}, m_p is the proton mass, m_i is the ion mass, T_i is in eV, and $\ln\Lambda$ is the Coulomb logarithm, and the resulting collision frequency is in s^{-1}. In the case

of a deuterium plasma, we have $m_p/m_i = 1/2$, and Z=1. Since

$$\Gamma_I = -D\frac{\partial n_I}{\partial r} + vn_I \tag{6.7}$$

Equation 6.5 yields the following expressions for D and V:

$$D_{neoc} = \nu_i q^2 \rho_i^2 \tag{6.8}$$

$$v_{neoc} = \nu_i q^2 \rho_i^2 (Z_I \frac{\partial}{\partial r} \ln n_i - \frac{\partial}{\partial r} \ln T_i) = D_{neoc}(Z_I \frac{\partial}{\partial r} \ln n_i - \frac{\partial}{\partial r} \ln T_i) \tag{6.9}$$

One may note that D_{neoc} is independent of the charge state whereas v_{neoc} is not. Since the radial density and temperature derivatives are usually negative, we see that the presence of a background density gradient produces an inward pinch, whereas the background ion temperature gradient will produce an outward pinch. For high-Z impurities, one may expect the density term to dominate since it is proportional to Z_I, resulting in a net inward pinch across the profile. For low values of Z_I there may be situations where v_{neoc} is directed outward in at least some part of the plasma.

6.1.2 Collisional regimes in the Alcator C-Mod transport barrier region

In neoclassical theory, the transport is divided into three regimes of different collisionality, each leading to its own scaling law for the diffusion. In this section, we will show that in the Alcator C-Mod transport barrier, the main (deuterium) ions are collision-dominated, and medium-Z impurities are highly collisional, being strongly coupled to the main ions through collisions. The ion collisionality, ν_i^*, is defined as [28]:

$$\nu_i^* = qR_0\nu_i/v_{th} = qR_0/l_f \tag{6.10}$$

Here, q is the plasma safety factor, R_0 is the major radius, ν_i is the ion collision frequency, v_{th} is the thermal ion speed, and $l_f = v_{th}/\nu_i$ is the mean free path for 90 degree scattering of the momentum. Thus, ν_i^* can be interpreted as a measure of the number of collisions that an ion experiences when travelling a significant fraction of a full poloidal turn along a field line. Three regimes are defined, the banana

(collisionless) regime for $\nu_i^* < \epsilon^{3/2}$, the plateau regime for $\epsilon^{3/2} < \nu_i^* < 1$, and the Pfirsch-Schlüter (collisional) regime, for $\nu_i^* > 1$. ϵ, the inverse aspect ratio is defined as the ratio of the minor radius to the major radius, $\epsilon = a/R_0$. In the collisionless regime, trapped particles perform full banana orbits before being untrapped by collisions, hence the name "banana regime". In the collisional regime, particles only perform a small fraction of a full poloidal orbit between collisions, so there are no banana orbits. Particles perform random walk processes, leading to diffusion enhanced above the classical level, because of the ∇B drifts. The plateau regime represents the situation between these two extremes.

For Alcator C-Mod, $\epsilon = 0.22/0.68 = 0.32 \Leftrightarrow \epsilon^{3/2} = 0.18$, and qR_0 is in the range of 1.7-4.0 m near the plasma edge, depending on the edge value of q. A typical temperature in the H-mode transport barrier region is 100 eV, and a typical density is 10^{20} m^{-3}. A typical density of fully ionized fluorine is 10^{17} m^{-3}, based on our measurements and the modelling described in Chapter 5. Given these values, the deuterium-deuterium collision frequency is $\nu_i \approx 4.5 \times 10^4$ s^{-1} (21 μs collision time). The deuterium-fluorine collision frequency, as calculated from [34], is $\nu_{iI} \approx 660$ s^{-1} (1.5 ms collision time). This yields a deuterium mean free path of approximately 1.5 m. Thus, taking $qR_0 = 2$ m as a representative edge value, $\nu_i^* \approx 1.3$, ie. ions are in the Pfirsch-Schlüter regime, although not by a large margin[1]. We confirm that the deuterium-fluorine collision frequency is much smaller than the deuterium-deuterium collision frequency, as assumed in Section 6.1.1. For fully ionized fluorine, the fluorine-fluorine collision frequency is $\nu_{II} \approx 7.6 \times 10^4$ s^{-1}, and the fluorine-deuterium collision frequency is $\nu_{Ii} \approx 5.0 \times 10^5$ s^{-1} $\Leftrightarrow \tau_{Ii} \approx 2.0\mu$s. Thus, the for the fully ionized fluorine, the collisions with deuterium ions dominate over the collisions with its own species, as assumed in the neoclassical theory described in Section 6.1.1. For a fluorine ion, the parallel mean free path between collisions with deuterium ions is approximately 4.6 cm. Thus, the fluorine ions are strongly coupled to the deuterium ions through collisions, and they are clearly in the Pfirsch-Schlüter regime ($\nu_I^* \approx 43$). These

[1]For some H-mode plasmas, the deuterium ions in the edge transport barrier region are in the plateau regime.

conclusions hold for the high charge states of other medium Z impurities such as oxygen and neon.

6.2 Previous impurity transport studies in tokamaks

The results from neoclassical theory summarized in Section 6.1.1 provide explicit formulas for D and v, but in tokamak experiments, the transport of impurities as well as that of the bulk plasma particles and heat, is usually not well described by neoclassical theory. The outward transport of particles and heat is usually much faster, presumably driven by microturbulence. This phenomenon is known as *anomalous* transport, and the energy confinement degradation associated with anomalous heat conduction is one of the most important problems in fusion plasma physics. One way to measure D and v experimentally is to inject trace amounts of impurities and following the densities of specific charge states as they penetrate into the plasma and eventually decay away, and then compare these observations to computer simulations which solve the set of coupled equations for all charge states. Once can then adjust the D and v profiles in the simulation to get the best match to the experimental data. Measurements of steady state conditions also provide information about the transport, but to a much smaller degree. In either case, one has to make simplifying assumptions about the radial variation of both D and v — for instance that the plasma can be divided into a small number of radial zones, where the D and v are constant, so that the problem does not become underdetermined. Typically the measurements are compared to numerical simulations which solve the coupled set of equations of the type shown in Equation 6.1 given initial guesses for D and v. Below are summarized results from several tokamak experiments.

6.2.1 Results from Alcator C-Mod

Radial profiles of D and v have previously been determined in Alcator C-Mod for a variety of plasma conditions [35]. These previous findings are briefly summarized in this section. In L-mode the transport appears purely diffusive, so $v \approx 0$ across the plasma. D is highly anomalous, at about 0.5 m^2/s across the profile, except close to the edge of the plasma where it decreases rapidly to roughly 0.05 m^2/s near the last closed flux surface, located near $r = 21$ cm. Thus, L-mode impurity transport does not resemble neoclassical transport. In ELM-free H-mode, $D = 0.2$ m^2/s and $v \approx 0$ in the region $0 < r < 18$ cm. Toward the edge of the plasma, D drops significantly to a value near 0.005 m^2/s in the region near the last closed flux surface. In the same region, a large inward convection velocity is present, which reaches a value on the order of -30 m/s close to the separatrix. The convection velocity qualitatively resembles the neoclassical convection velocity, the inward pinch increasing dramatically at the plasma edge where the density gradient scale length is smallest. The measured diffusion coefficient does not in general resemble the neoclassical value, being much larger in the core region of the plasma. Near the edge the difference between the measured D and the neoclassical D is not as large, although the measured D is smaller than the neoclassical value. In some cases, quantitative agreement between the measured values of D and v and the neoclassical values in the edge region has been observed [36]. During ELMy H-modes, the transport in the core region is similar to ELM-free H-modes, but the edge transport is different. Near the separatrix D is close to its neoclassical value, about 0.05 m^2/s, and v reaches a value of about -7 m/s, somewhat below the neoclassical values. The spatial resolution of these measurements is on the order of 2-3 cm, which is adequate in the core of the plasma but not near the plasma edge where the characteristic radial scale lengths, eg. density and temperature gradient scale lengths, are typically less than 1 cm.

6.2.2 Results from other diverted tokamak experiments

Results from JET

Results from JET [37] are in general similar to those found in Alcator C-Mod. The diffusion is found to be much larger than neoclassical in L-mode, except in the core region. However, these results are obtained between sawtooth crashes whereas the results for Alcator C-Mod are averaged over many sawtooth crashes, which may explain this difference, since the sawteeth tend to increase the transport in the core region. In H-mode, a narrow region near the edge has a much lower value of D and a strong inward convection velocity v, similar to what is observed in Alcator C-Mod. During the LPC H-mode [14], which is very similar to the EDA H-mode observed on Alcator C-Mod, D in the edge region is near L-mode values (ie. much larger than in normal H-modes).

Results from DIII-D

The transport of intrinsic impurities in DIII-D H-mode plasmas has been studied in some detail [38]. It is found that a spatially constant (anomalous) diffusion coefficient $D \approx 1$ m^2/s together with a convective velocity of $v = 3D\frac{\partial}{\partial r}\ln n_i$ reproduce the impurity transport behavior for Co and Ni. This not only resembles the neoclassical convection term qualitatively, there is also quantitative agreement, when it is taken into account that D is much larger than D_{neoc}. Thus, it is concluded that the diffusion coefficient is much larger than the neoclassical prediction but the convective term is consistent with the neoclassical profile in DIII-D.

Results from ASDEX

In the ASDEX tokamak, it is concluded that during H-mode, the transport is well modelled by an anomalous diffusion coefficient D, and a neoclassical convective term [39]. In particular, it is found that there is a strong inward convection of impurities near the plasma edge, where the plasma density gradient is strongest.

6.2.3 Summary

Experimental values of D and v have been derived from a number of tokamak experiments. In L-mode, D is anomalous, and v is small. In H-mode, D is anomalous in the core region, but is reduced near the transport barrier at the plasma edge to values close to the neoclassical diffusion, with the exception of DIII-D, where a spatially constant anomalous diffusion coefficient is consistent with the measurements. In all four tokamaks there is a strong inward convective velocity near the edge, qualitatively in agreement with v_{neoc}. In most cases, there is also quantitative agreement between the experimentally derived velocity profiles and the neoclassical predictions.

Chapter 7

Computer modelling of one-dimensional transport

7.1 Simulations of edge impurity transport and comparison to experiments

As described in Section 5.1, the soft x-ray emissivity e is proportional to $(n_F^{+9} + n_F^{+8}) \times n_e$ with a relatively weak temperature dependence in the vast majority of H-mode discharges. With a highly spatially resolved measurement of the electron density and temperature profiles at the plasma edge, we are able to determine the fluorine density profile with very high resolution near the edge. These measurements provide information about the impurity transport properties of the plasma edge. The transport of fluorine is complex, since one has to take into account not only the diffusive and convective transport, but also recombination and ionization terms which couple all the possible charge states of fluorine together. The convective and diffusive fluxes can be calculated if D and v are specified, and the recombination and ionization rates can be determined if the electron density n_e and temperature T_e are known. This calculation is done numerically using the impurity transport code MIST [32]. This is a one-dimensional code, and thus ignores poloidal and toroidal variations of all quantities. In fact, poloidal variations are significant, but a one-dimensional

analysis may still provide useful insight. We defer a discussion of poloidal variations to Chapter 10. Since T_e and n_e are measured routinely in Alcator C-Mod by several different diagnostics, and D and v have been measured for several impurities (see Section 6.2.1) we have in principle all necessary variables to calculate the expected density profiles of the highly charged fluorine species to within a constant factor[1]. We can therefore check if the experimental values previously derived are consistent with our measurements. However, the values of D and v derived from impurity injection experiments by Rice et al. [35], are obtained at a spatial resolution of a few cm, so they only provide a rough guideline for the detailed edge values. The soft x-ray measurements provide additional information about D and v on a much finer spatial scale in the edge region of the plasma.

7.1.1 Simulation details

The MIST code calculates the radial density profile of all charge states of a user-specified impurity. It can be run in time-dependent as well as time-independent mode. In the time-independent mode, MIST simply calculates the equilibrium distribution of all the charge states. Note that this does NOT imply coronal equilibrium, unless one sets $D = 0$ and $v = 0$. In these simulations, we concentrate on steady state H-mode conditions, so the time-independent mode is used. The user specifies radial profiles of D, v, n_e, and T_e, and MIST calculates the steady state density profiles of all the charge states of fluorine. These profiles, together with the background T_e and n_e profiles, are then used to calculate the soft x-ray emissivity arising from line radiation, recombination radiation, and bremsstrahlung, as described in Chapter 5.

7.1.2 Localizing the inward pinch

As noted in Section 6.2, there is a strong inward pinch velocity near the H-mode transport barrier, usually consistent with the inward pinch predicted from neoclassical theory. However, the spatial resolution of the previous impurity transport studies is

[1] In MIST, one specifies the core fluorine density.

several cm, and the typical scale lengths in the H-mode edge are less than 1 cm. With the highly resolved profiles of x-ray emissivity, electron density, and electron temperature now available, it is possible to make a comparison on a much finer spatial scale using MIST. We take the electron temperature and density profiles at the plasma midplane for an H-mode plasma where detailed pedestal profiles are available, and keep those fixed for all the simulations. The profiles we use for T_e and n_e are smoothed fits to the electron density derived from the visible bremsstrahlung diagnostic, and the ECE electron temperature profiles from a discharge where high resolution edge measurements were available (see Figures 7-2 and 7-1). The discharge in question, 990527025, was an ohmic H-mode which was essentially ELMfree, although a slight enhancement of H_α was observed. Because there was no auxiliary heating, the T_e pedestal was not as high as seen on many RF heated H-mode discharges. The high resolution edge electron temperature profile is obtained by sweeping the B-field, thus moving the location of the electron cyclotron frequency. The instrument function, which is about 8 mm wide, has been deconvolved to increase the spatial resolution. The high resolution density profile is inferred from the emissivity pedestal of the visible bremsstrahlung array. The diffusion coefficient D is chosen to be 2000 cm^2/s over most of the core region, consistent with previous findings [35], and we vary its size in the edge region from 100 to 1000 cm^2/s to cover both ELMfree H-modes (50-100 cm^2/s) and type III ELMy/EDA-like diffusivity values, which are somewhat higher (up to 500 cm^2/s). The shapes are illustrated in Figure 7-3. For the convection velocity, we take a simple triangularly shaped inward pinch, 1 cm wide, which peaks at 100 m/s, also consistent with previous findings. It is the exact location of this pinch that we are interested in in this section. We define the location of the pinch as the innermost point of the triangular shape, as seen on Figure 7-4. We vary this location from 0 to 20 mm inside the separatrix in steps of 1 mm, and for each location ,and each choice of D at the edge, MIST is used to calculate the density profiles of the various charge states of fluorine, so that the x-ray emissivity profile can be calculated. We fit a tanh-like function, as defined in Equation 3.3, to the emissivity profile to get the width and location of the x-ray emissivity pedestal. These simulated values can

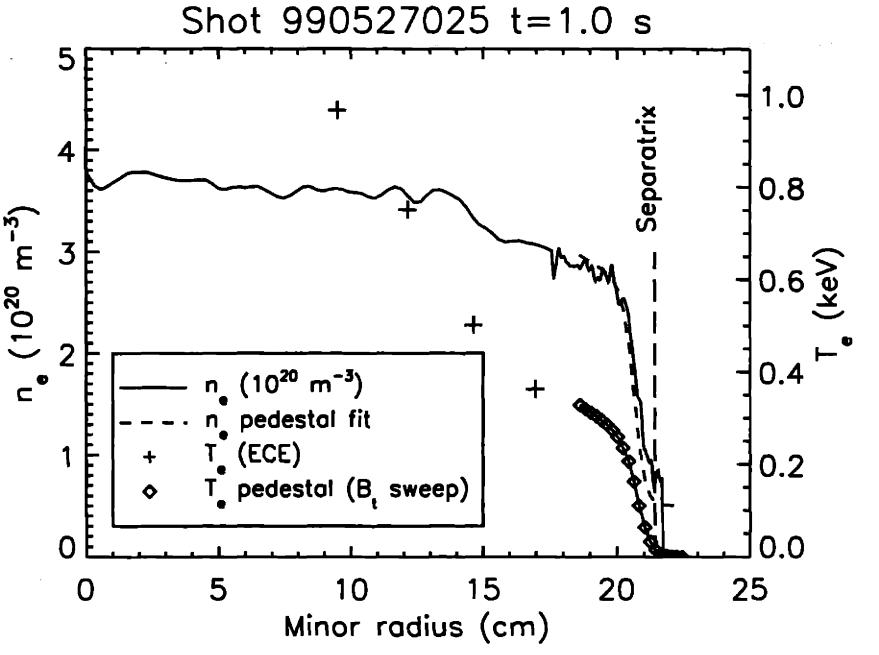

Figure 7-1: Measured density and temperature profiles for the H-mode discharge being used in the simulations investigating the location of the inward pinch.

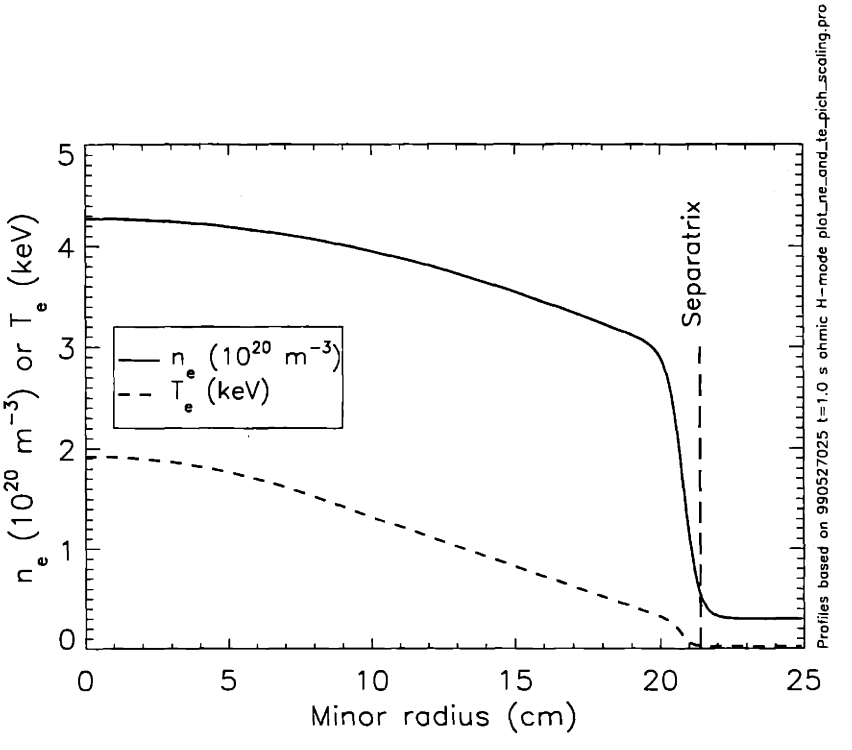

Figure 7-2: Synthetic density and temperature profiles based on the measured profiles in Figure 7-1. These profiles are used in the simulations investigating the location of the inward pinch.

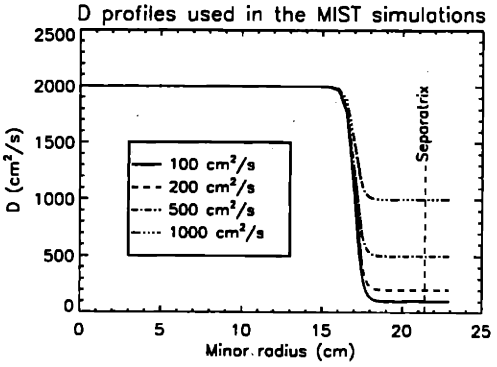

Figure 7-3: The D shapes used in the simulations where the location of v is varied. The lowest value of 100 cm^2/s represents ELMfree H-modes, the two intermediate values represent EDA-like or type III ELMy H-modes. The value of 1000 cm^2/s in the edge region is higher than what has been reported for H-modes in previous studies.

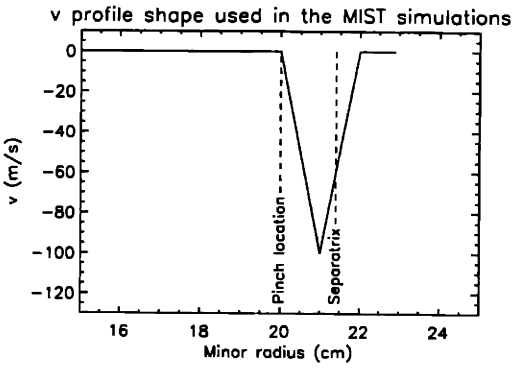

Figure 7-4: The convective velocity profile used in the MIST simulations. As shown on the figure, we define the position of the profile as the innermost point of the triangular shape. In the case shown above, the pinch is located at 20.0 cm, 14 mm inside the separatrix.

then be directly compared to actual x-ray emissivity pedestal values.

Effects on the x-ray pedestal location

The results for the x-ray pedestal location as a function of the pinch location are shown in Figure 7-5. It is found that the location of the pinch region coincides with $r_{top} = r_0 - 0.4\Delta$ where r_0 and Δ are the pedestal (center) position and widths as defined in Section 3.2. The factor of 0.4 has been chosen to minimize the spread of r_{top} results from different values of D, and it turns out that this choice makes r_{top} coincide with the location of the pinch. r_{top} is located near the top of the pedestal (regardless of the width). The top of the x-ray pedestal coincides with the location of the pinch only when the pinch is located at least 11 mm inside the separatrix. If located further out, the fluorine will diffuse out into the region where the temperature is low and the atomic physics dominates. At low temperatures the recombination sink of the highly ionized fluorine starts dominating over the effects of D and v, and the location of the x-ray pedestal becomes rather independent of the location of the pinch.

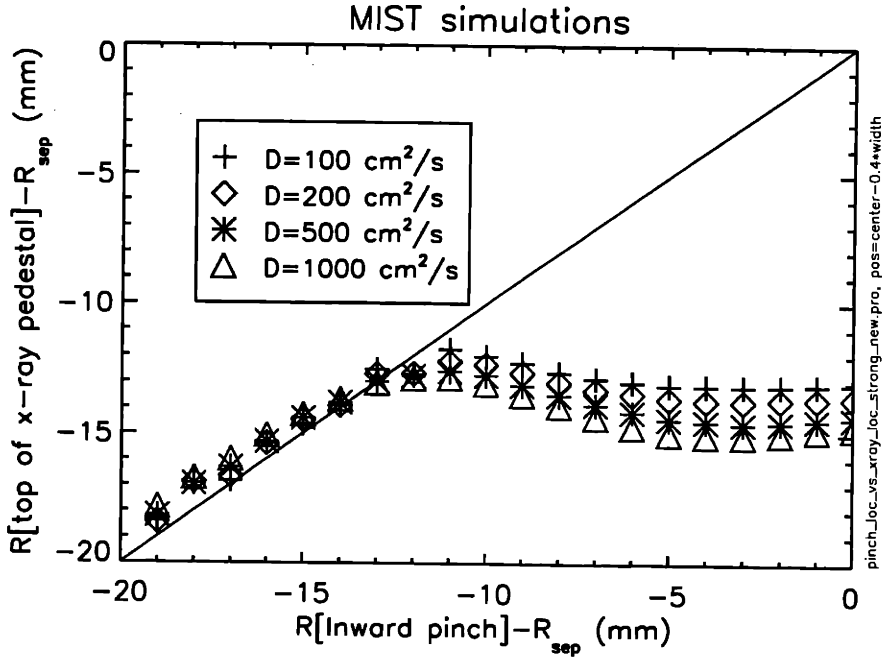

Figure 7-5: The location of the pinch region coincides with the top of the x-ray emissivity pedestal, which we define here as $r_{top} = r_{center} - 0.4\Delta$ where r_{center} is the radial location of the center of the x-ray pedestal, and Δ is the full width of the pedestal. This holds for all the chosen values of D, as long as the pinch is localized at least 11 mm inside the separatrix. If the pinch is localized further out, the atomic physics starts playing a role, and the two no longer coincide.

Effects on the x-ray pedestal width

The effects of the pinch position on the pedestal width are summarized in Figure 7-6. The pedestal width seems independent of the location of the inward pinch region, as long as the pinch is located at least 11 mm inside the separatrix. The width does depend on D. It is systematically larger for higher values of D. For D=100 cm^2/s, the pedestal width is around 1.5-2.0 mm, near the computational grid size (1.5 mm) for the MIST simulations. The widths get larger as D is increased toward (and beyond) values consistent with type III ELMy H-modes and EDA H-modes. The agreement with experimentally obtained pedestal widths will be discussed in the section below. When the pinch region is moved further out toward the separatrix, the pedestal widths no longer depend primarily on D, and approach large values near 10 mm. As with the pedestal position, this can be explained by the recombination becoming relatively more important than D and v, as the fluorine is allowed to diffuse out into the colder edge region. This interpretation can be tested, since the MIST

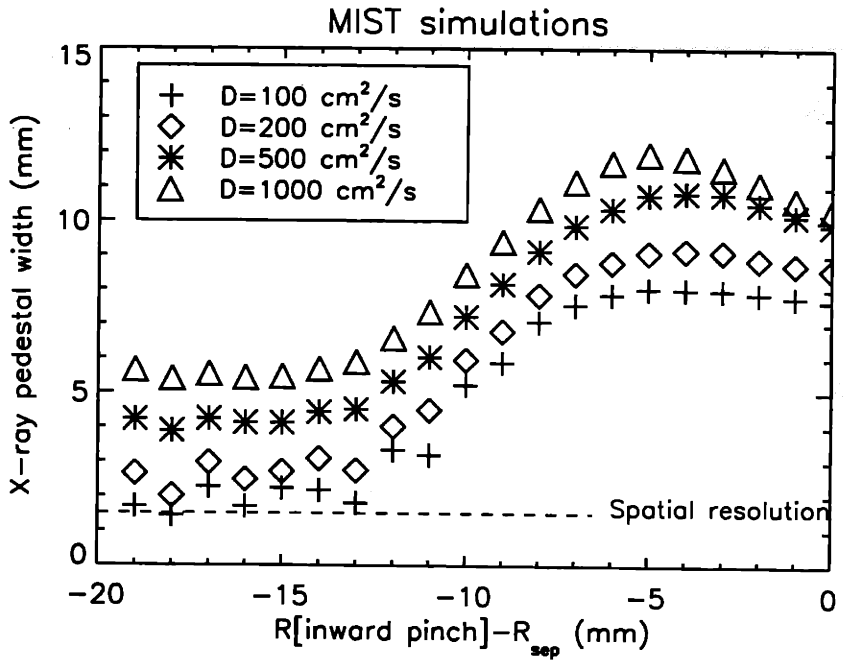

Figure 7-6: When the pinch is more than 11 mm inside the separatrix, its position does not affect the x-ray pedestal width. As the pinch is moved further out, recombination becomes increasingly more important. Increasing D clearly increases the pedestal width.

simulations yield the density profiles of all charge states of fluorine. Thus, we can calculate the fraction of highly ionized fluorine:

$$f_{hi} = \frac{n_F^{+8} + n_F^{+9}}{n_{F,\text{total}}} \tag{7.1}$$

where $n_{F,\text{total}}$ is the total local fluorine density. If f_{hi} does not change significantly from the top of the pedestal to the bottom of the pedestal, then the recombination term is not a significant factor in determining the pedestal width, height, and position, although it remains an important term in the transport equations. If, on the other hand, f_{hi} decreases significantly from the top of the pedestal to the bottom, then a significant part of the decrease in x-ray emissivity across the pedestal is caused by the recombination sink. We define the relative change in f_{hi} as:

$$r_{hi} = f_{hi}(r = r_0 - \Delta) - f_{hi}(r = r_0 + \Delta) \tag{7.2}$$

We plot r_{hi} for the four different values of D in Figure 7-7. It is confirmed that the recombination term is not significant if the inward pinch is at least 11 mm inside the separatrix but can be very significant if the inward pinch location is closer than 11 mm to the separatrix.

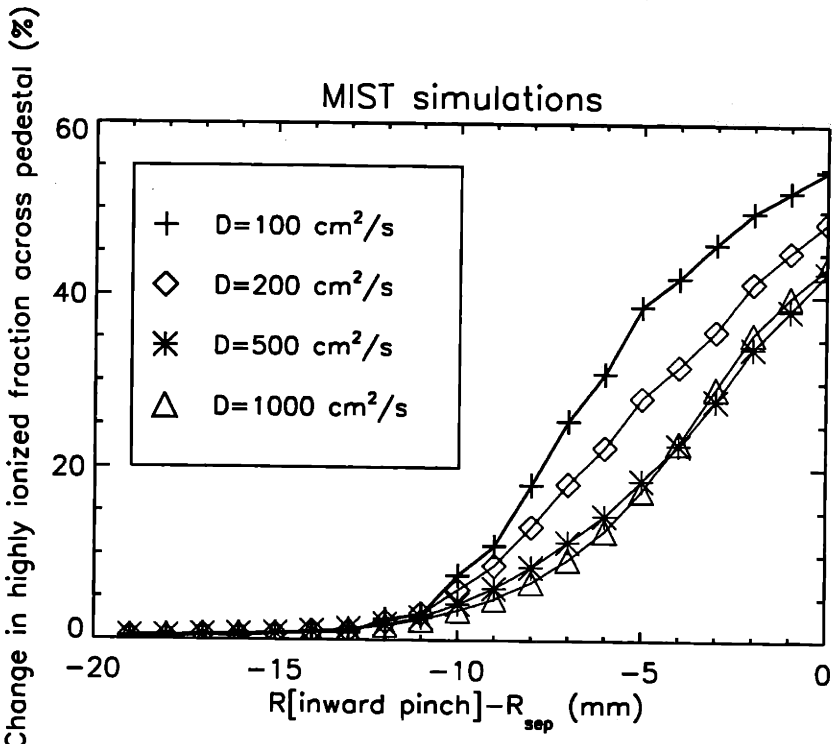

Figure 7-7: The fraction of highly ionized fluorine does not change significantly across the pedestal if the inward pinch is located at least 11 mm inside the separatrix, regardless of the size of the diffusion coefficient. If the inward pinch is closer to the separatrix, there is a significant change in the highly ionized fraction, indicating that the recombination sink becomes important. The y-axis is defined in Equation 7.2.

Comparison to real data

In the previous section simulations showed that the top of the x-ray pedestal should coincide with where the inward pinch is located. It seems intuitively obvious that there can be no significant inward pinch in the region where the impurity density profile is relatively flat inside the pedestal so it was expected that the MIST simulations would show this. The simulations lead us to other conclusions as well. First, this simple relation is only true if the top of the x-ray emissivity pedestal is at least 11 mm inside the separatrix (for the particular T_e and n_e profiles here). Second, there can be no strong pinch velocity for $r < r_{\text{top}} = r_0 - 0.4\Delta$ but the inward pinch velocity has to be large for $r \geq r_{\text{top}}$. Thus, from the real x-ray emissivity profile for this plasma, we can locate where the region of strong inward pinch begins by computing $r_{\text{top}} = r_0 - 0.4\Delta$, if $r_{\text{top}} - r_{\text{sep}} < -11$ mm. The x-ray emissivity profile at the plasma midplane for an H-mode during the discharge being analyzed is shown here in Figure 7-8. The value of $r_{\text{top}} - r_{\text{sep}}$ for this particular discharge has been determined from the pedestal fitting

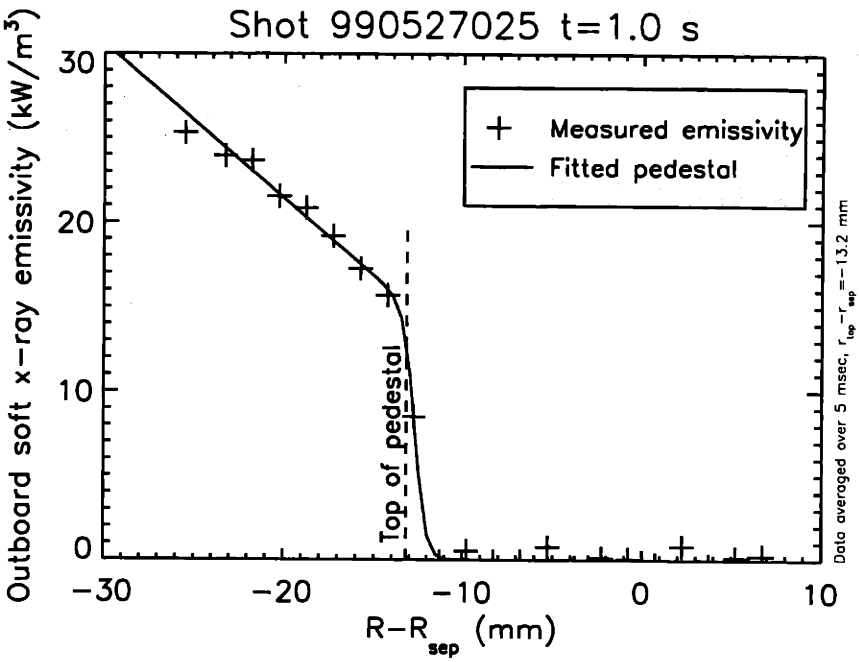

Figure 7-8: The x-ray emissivity at the outboard midplane. The top of the emissivity pedestal is located 13.2 mm inside the separatrix.

routine to be -13.2 mm at t=1.0 s. Thus, we can confirm that for this discharge, the atomic physics plays a smaller role than D and v, and that the inward pinch is located at -13.2 mm (with an uncertainty of about 2 mm). We can now check to see if this location is in agreement with neoclassical theory, which predicts that the inward pinch should be located where the density gradient is large. By taking $n_e = n_i$ and $T_e = T_i$, we can calculate the neoclassical convection velocity, and compare it to the triangular pinch velocity we used here. As seen in Figure 7-9, the location of the triangular pinch is within 3 mm of the location of the neoclassical pinch. The triangular pinch used here has a much smaller peak value than the neoclassical pinch though. The x-ray pedestal width at t=1.0 s is nominally 1.24 mm, but the spatial resolution is 1.5 mm, so we cannot trust this value completely — it indicates that the width is less than 2 mm, and that there is not sufficient spatial resolution to get the precise value. The best fit with the MIST calculations is obtained for D near 100 cm^2/s, consistent with the fact that the plasma was in an H-mode at t=1.0 sec which was ELMfree. It should also be noted that the MIST results showing that the pedestal width should be about 5 mm for values of D consistent with type

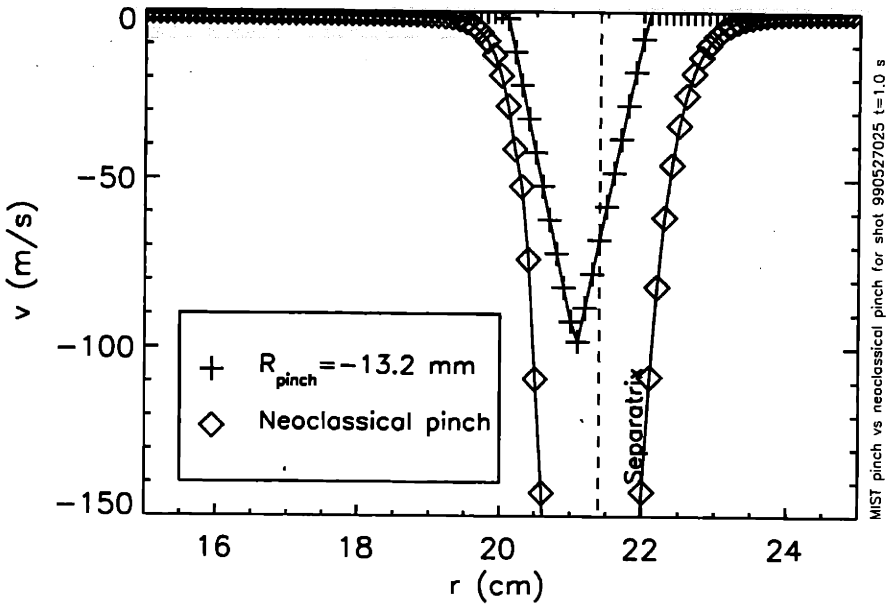

Figure 7-9: The location of the neoclassical pinch agrees well with that of the pinch used in the MIST simulations. The peak value of the pinch used in MIST is much smaller than the peak value of the neoclassical pinch, however.

III ELMs, are similar to the values obtained in type III ELMy H-modes and low current EDA H-modes. However, this comparison only makes sense if the top of the x-ray pedestal generally is far enough inside the separatrix so as to make the recombination effects on the pedestal shape small. Using the x-ray database, we plot a histogram of $r_{\rm top} - r_{\rm sep}$ for all shots in the 1999 run campaign in Figure 7-10, and this confirms that $r_{\rm top} - r_{\rm sep} < -11$ mm ($r_{\rm sep} - r_{\rm top} > 11$ mm) for the vast majority of outboard midplane pedestals. A histogram of pedestal widths, shown in Figure 7-11 also shows that the pedestal width rarely exceeds 8 mm, which is also evidence that the recombination term is not important for the outboard midplane x-ray pedestal, since the simulations show that pedestal widths on the order of 10 mm should be observed if the recombination term is important. However, the 11 mm criterion separating where the atomic physics becomes important is not necessarily applicable to all discharges, it depends on the specific n_e and T_e pedestals. In particular, the T_e pedestal height in the discharge used in the simulations shown here, although not atypical, is somewhat lower than what is observed in RF heated discharges. Thus, we expect that for RF electron temperature pedestals, the recombination effect should

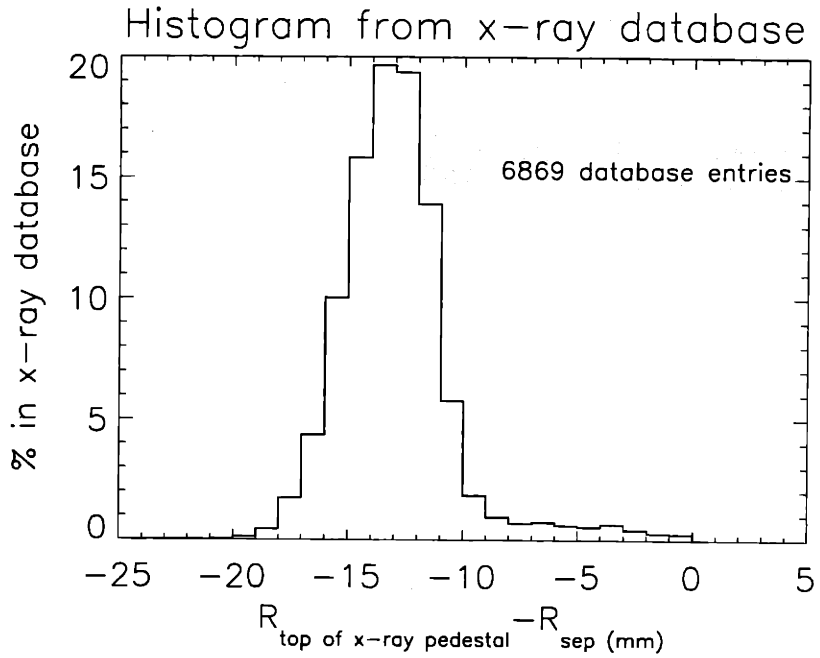

Figure 7-10: The x-ray database can be used to investigate if the top of the x-ray emissivity is generally more than 10 mm inside the separatrix. This histogram shows that it is generally 11-16 mm inside the separatrix, so we expect the atomic physics to play a small role in determining the x-ray emissivity pedestal character.

be even less important. With this caveat in mind, we find that the x-ray emissivity profile at the outboard midplane is dominated by D and v for the vast majority of plasma discharges, since the top of the x-ray pedestal is generally far enough inside the plasma to make the recombination sink unimportant for the shape and position of the pedestal, and since the x-ray pedestal widths generally are much smaller than those we would expect if recombination was the dominating effect.

The pinch velocity used in these simulations is about a factor of 3 less than the neoclassical pinch velocity. In order to address if this has any effect on the results, we have also done these calculations with a triangularly shaped velocity pinch which peaks at -300 m/s, close to the neoclassical peak value. As seen on Figure 7-12, we find also for this strong pinch that the pinch location coincides with the top of the pedestal, as long as it at least 11 mm inside the separatrix. We also find that the x-ray pedestal width depends on D, although the widths are somewhat smaller than for the weaker pinch, as seen on Figure 7-13. It is reasonable that a steeper pinch profile leads to narrower pedestals, so it is not a surprising result. The widths derived

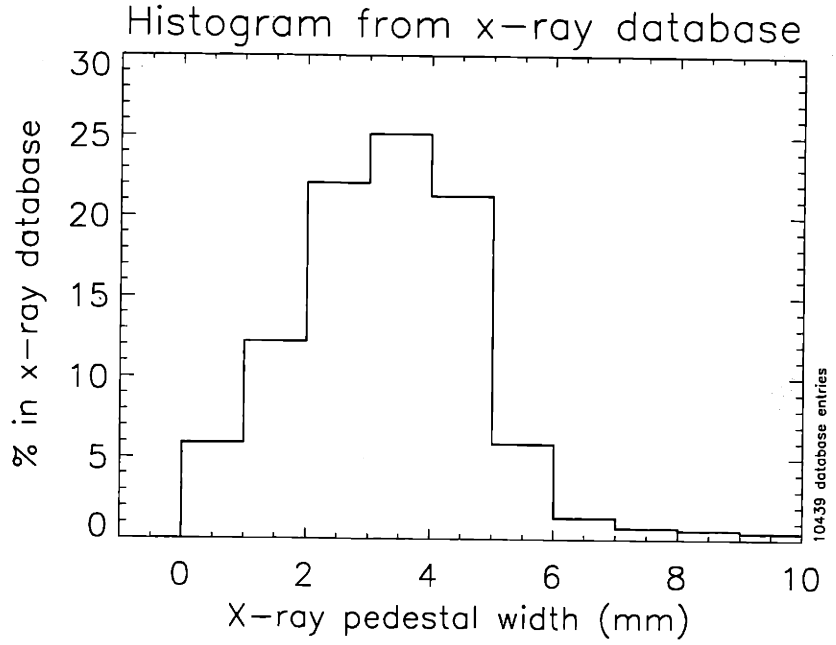

Figure 7-11: A histogram of the x-ray pedestal widths at the outboard midplane for discharges in 1999. Almost all pedestals are less than 6 mm wide. Note that the spatial resolution is 1.5 mm, so it cannot be concluded from this graph that there is a significant fraction of x-ray pedestals with widths less than 1 mm.

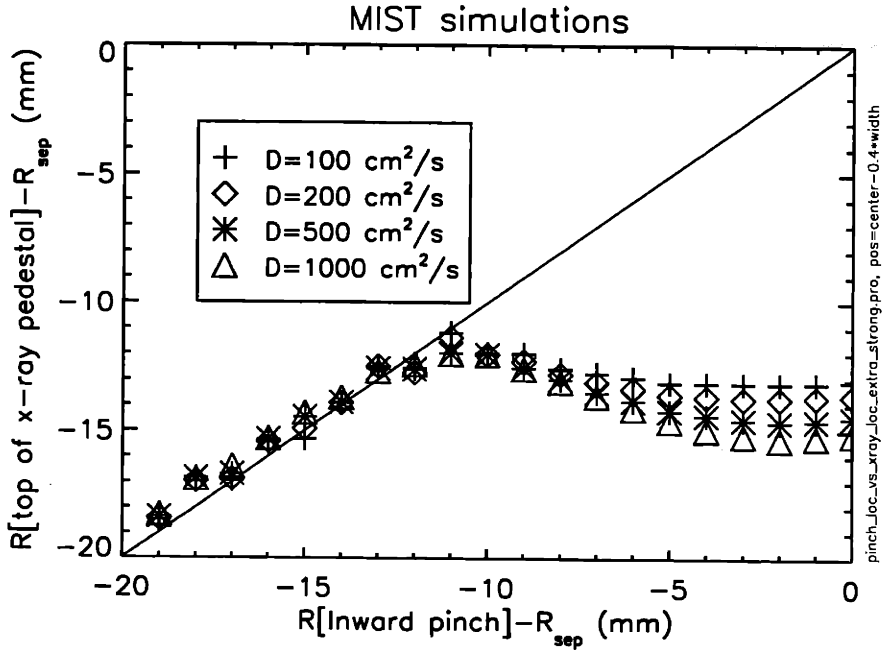

Figure 7-12: With a 3 times stronger pinch, we still find that the location of the pinch coincides with the top of the x-ray pedestal.

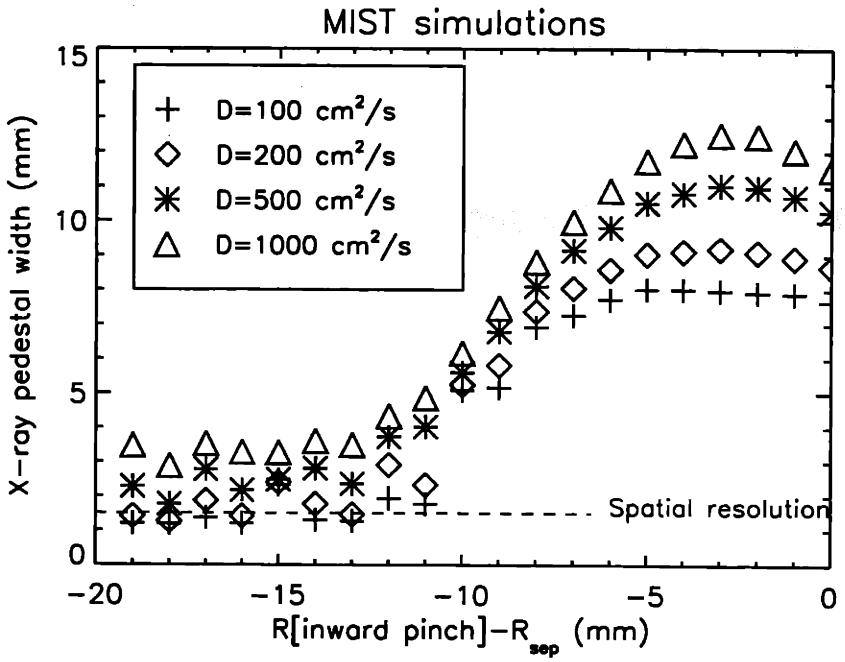

Figure 7-13: The pedestal width is independent of the position of the strong inward pinch, as long as the pinch is at least 11 mm inside the separatrix. However, the widths are significantly smaller than those obtained with the weaker pinch.

from these simulations are slightly smaller than those observed in real experiments, although probably not significantly smaller. It should be noted that previous impurity transport studies using injections have found that the inward pinch is not as strong in type III ELMy plasmas as in ELMfree plasmas. In the preceding analysis we have implicitly assumed that we could simulate the difference between type III ELMy edge confinement and ELMfree edge confinement simply by varying D, but keeping v the same. It is important to keep in mind that it is very hard to separate effects of D and v in steady state, unless some assumptions are made about either one.

7.1.3 Effects of a neoclassical pinch

The previous section shows that the location of the inward impurity pinch at the plasma midplane is in good agreement with where the neoclassical pinch is located. As discussed in Section 6.2, it has been found on tokamaks around the world that the observed inward convection velocity v is consistent with neoclassical values, whereas typically D is not. The findings in the previous section support the theory that the

actual impurity pinch in Alcator C-Mod is indeed close to the neoclassical prediction. In order to test this, additional transport simulations have been performed using the neoclassical v profile rather than the simplified triangular shapes used in the previous section. We calculate v_{neoc} from Equation 6.9 with $n_i = n_e$, and $T_i = T_e$. $n_i = n_e$ is a good approximation in pure ($Z_{\text{eff}} \approx 1$) plasmas, such as Alcator C-Mod, and the assumption of $T_i \approx T_e$ is believed to be a good approximation at the plasma edge in Alcator C-Mod because of the high edge density and rather low temperatures which result in a high ion-electron collision frequency, so there is fast temperature equilibration between ions and electrons. D and v are assumed the same for all charge states in the current version of MIST, which is not consistent with the assumption of $v = v_{neoc}$, because v_{neoc} depends on the charge state. However, since we are only concerned with the highly ionized states of fluorine, it seems reasonable to assume that it does not matter much if the density profiles of the lowest charge states are not exactly right. For the detailed shapes of the density and temperature pedestals we use the tanh-like shapes described in Section 3.2. The density profile inferred from the visible bremsstrahlung emissivity has been derived using the detailed temperature profile at the plasma edge derived from the ECE sweep. The steady state x-ray emissivity profiles are then calculated from MIST, for two different choices of edge D, and we plot those simulated profiles together with the actual measured x-ray emissivity in Figure 7-14. The transition from large core D to the lower edge value of D was chosen to be near the top of the electron density pedestal for the simulations with neoclassical profiles. This gave the best fits with the experimental soft x-ray profiles, and is the most natural choice since the region of large electron density gradients should coincide with the region of reduced particle diffusivity. Since the absolute fluorine density is not determined by the simulations, we choose to normalize the simulated profiles to the measured value at $R - R_{\text{sep}} = -20$ mm. We find that for both values of D chosen here, the simulated profiles are located a few mm radially inside the measured profile. The $D = 100$ cm^2/s profile yields the narrowest pedestal, in good agreement with the measured profile, and the $D = 500$ cm^2/s profile yields a broader profile which is located closer to the measured profile.

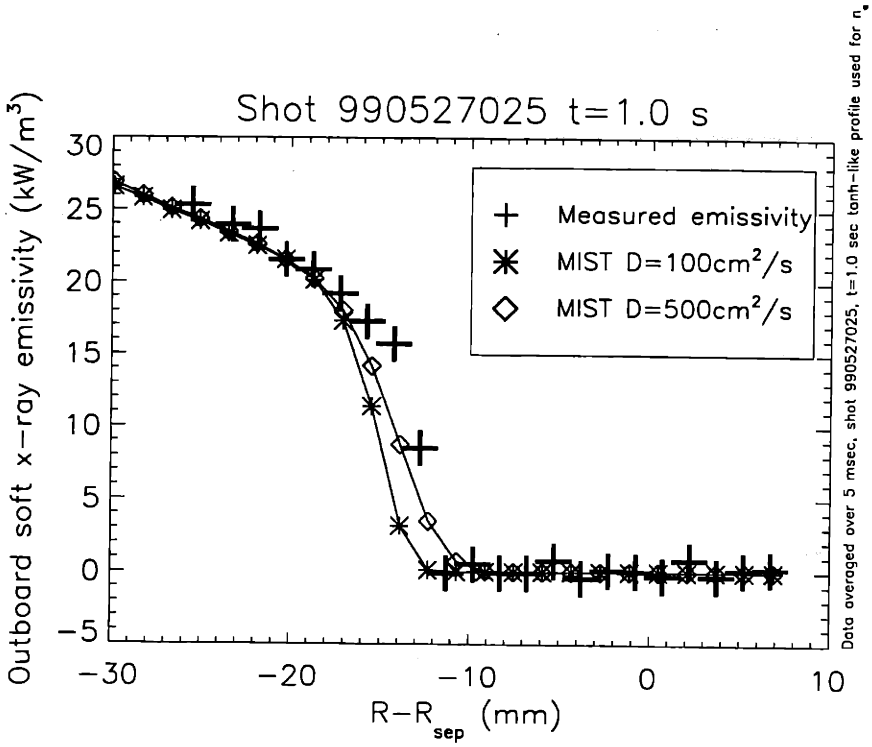

Figure 7-14: A comparison between the actual measured x-ray emissivity profile and profiles calculated from MIST with the assumption of a neoclassical v, derived from tanh-like fits to the n and T profiles. The simulated profiles are normalized to the emissivity at $R = R_{sep} = -20$ mm. The simulated profiles are qualitatively similar to the real profile but they are located a few mm radially inward of the actual emissivity profile.

In either case, a very good, but not perfect agreement is found. The simulated profiles are located a few mm inside the actual profiles. This implies that the actual inward pinch does not extend as far inward as the neoclassical pinch used in the simulation. The neoclassical pinch depends mostly on the density gradient, so a slightly different density profile might produce a neoclassical pinch which reproduces the x-ray emissivity profile perfectly. By iteration, we arrived at a density profile whose equivalent neoclassical pinch reproduces the measured x-ray emissivity profile perfectly, as shown in Figure 7-15. This does not prove anything unless the density profile used to get the neoclassical pinch is consistent with the measured profile. In Figure 7-16 we compare the density profile used to get the perfect x-ray emissivity agreement with the actual measured profile. It is seen that the two profiles easily agree within the uncertainties of the real measurement. We may therefore conclude that a neoclassical impurity pinch is completely consistent with our measurements.

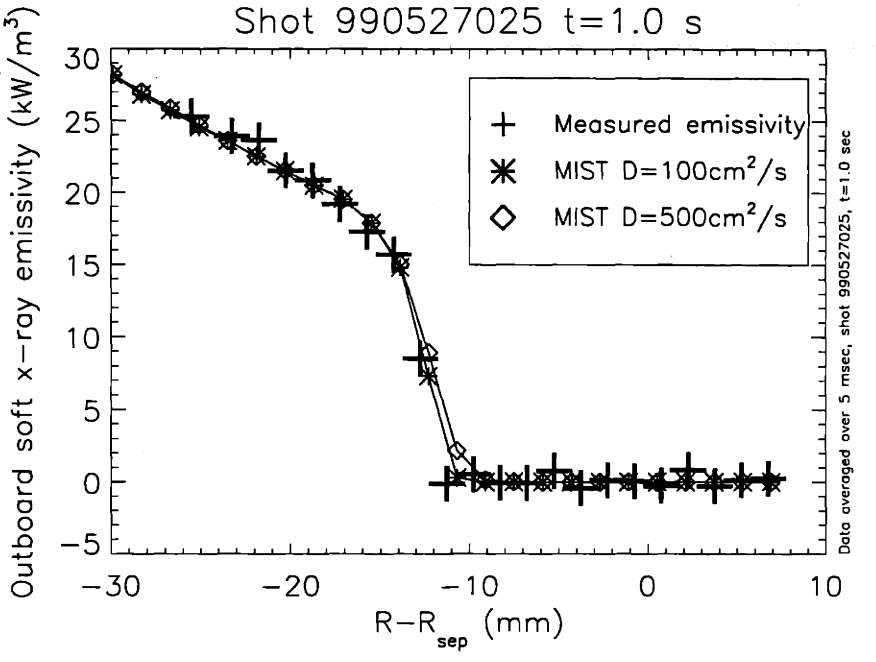

Figure 7-15: By using a slightly different density profile than the tanh-like pedestal profile, we arrive at a neoclassical pinch profile which reproduces the measured x-ray emissivity profile to within the measurement errors. The best agreement is obtained with D=100 cm^2/s, but even for D=500 cm^2/s there is very good agreement.

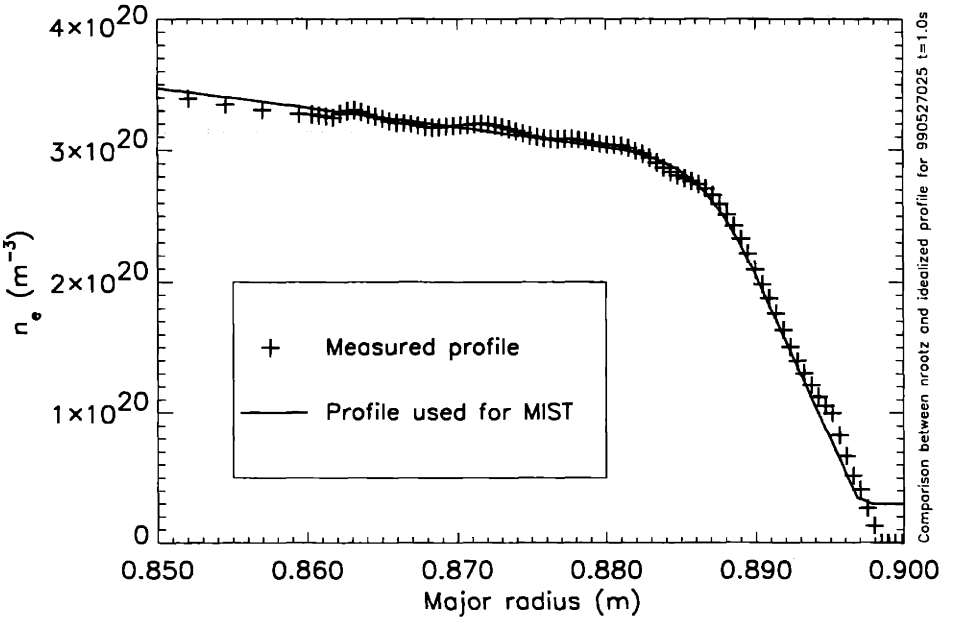

Figure 7-16: This figure shows a comparison between the actual density profile and the density profile used in the MIST calculation which yields an x-ray profile matching the measured x-ray profile perfectly. The two profiles agree very well.

7.1.4 Correlations between the x-ray and electron density pedestal locations

In Section 7.1.3 we showed, for a particular H-mode plasma, that the region of inward pinch is also the region of large electron density gradient. The soft x-ray pedestal database can be used to demonstrate that this is generally the case. Highly resolved electron temperature measurements at the midplane are available on a relatively small amount of discharges. Therefore, the electron density pedestal data are not routinely available, only the continuum emissivity pedestal data. The continuum emissivity pedestal is believed to be a good approximation to the electron density pedestal. The soft x-ray database contains many discharges where both the soft x-ray pedestal data and the visible continuum pedestal data are available, so we can investigate if our single shot observations are generally true for H-mode plasmas. In Figure 7-17 we plot the location of the foot of the soft x-ray pedestal versus the location of the foot of the visible continuum pedestal. Here, we define the foot as $R_{foot} = R_0 + \Delta/2$, where R_0 is the location of the center of the pedestal, and Δ is the full width of the pedestal. The figure shows that the foot of the soft x-ray pedestal is located about 9 mm inside the foot of the visible continuum pedestal, confirming that the soft x-ray pedestal is located well inside the visible continuum pedestal (and therefore, well inside the electron density pedestal) in general. 112 different plasma discharges are shown in this figure. This shift is evidence for the inward impurity pinch. Our simulations show that $R_{pinch} \approx R_{\mathrm{xtop}} = R_{\mathrm{x0}} - 0.4\Delta_X$, ie. that the innermost location of the inward pinch is located near the top of the soft x-ray emissivity pedestal. If we assume that the inward pinch is caused by the plasma density gradient, as predicted by neoclassical theory, then we should expect R_{xtop} to be very close to the location where the plasma density gradient changes from being rather small (in the core region) to being very large (in the pedestal region). This occurs at the top of the electron density pedestal so we can approximate that location as $R_{\mathrm{vctop}} = R_{\mathrm{vc0}} - \Delta_{\mathrm{vc}}$, where R_{vc0} is the center of the visible continuum emissivity pedestal, and Δ_{vc} is the full width of the visible continuum emissivity pedestal. In Figure 7-18 we plot R_{xtop} versus R_{vctop}, and find

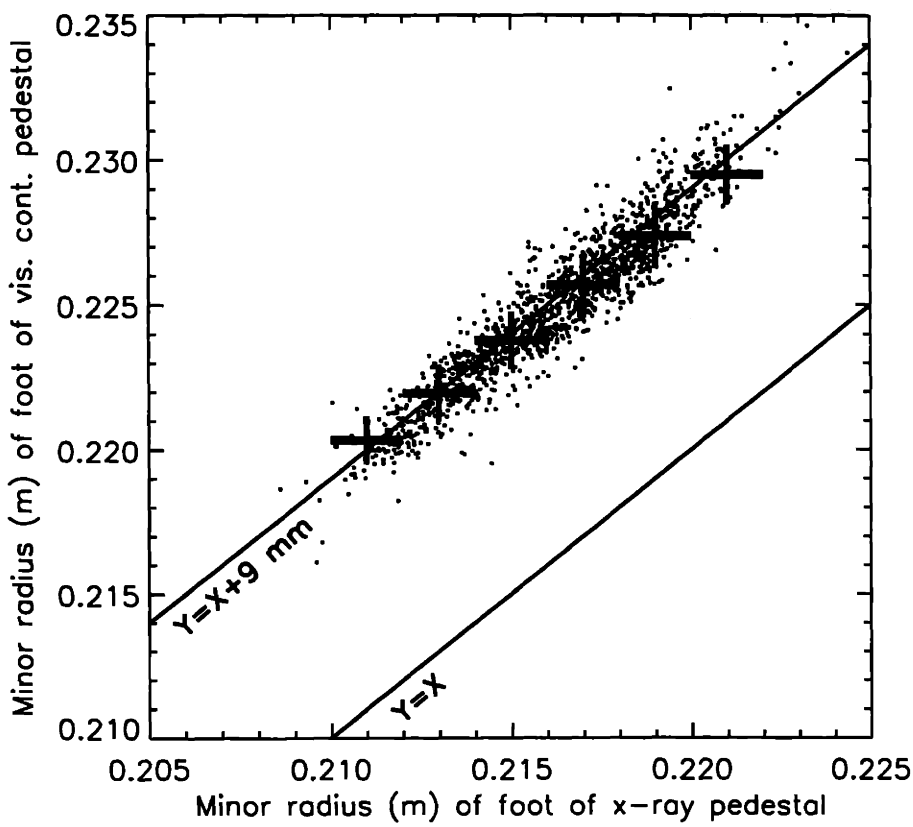

Figure 7-17: The foot of the soft x-ray pedestal is located about 9 mm inside the foot of the visible continuum pedestal for a wide range of locations. Binned averages and the standard deviations of the bins are also shown.

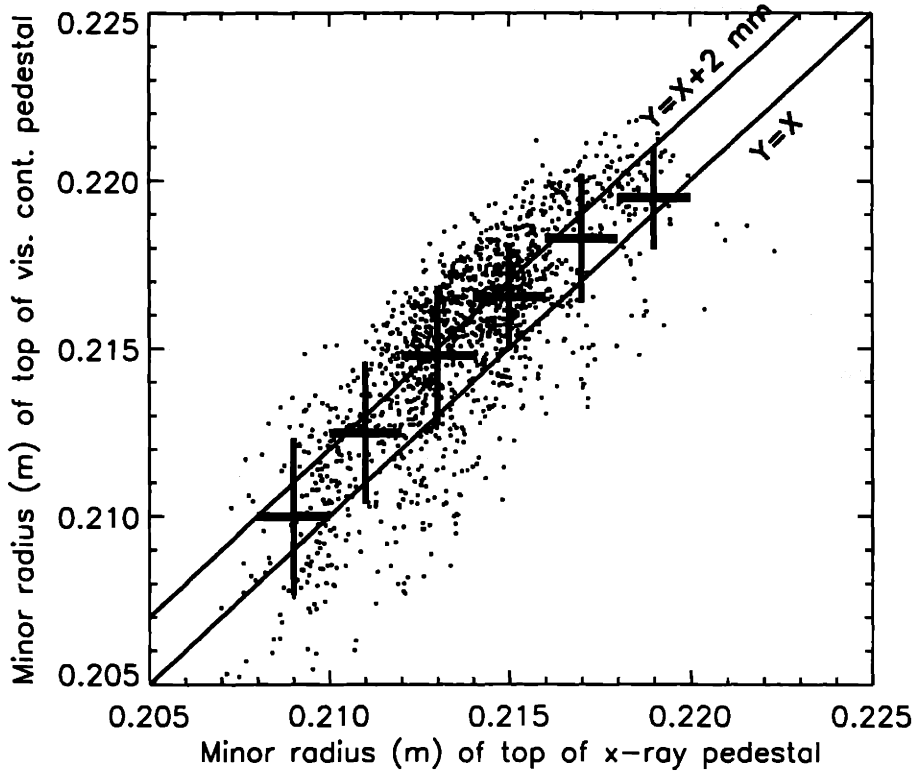

Figure 7-18: The top of the soft x-ray pedestal is located within 2 mm of the top of the visible continuum pedestal for a wide range of locations. Binned averages and the standard deviations of the bins are also shown.

that the two locations are very well correlated with a systematic shift of less than 2 mm. This confirms that the inward pinch region is in the region of large plasma density gradient, not just for the one discharge that has been studied in detail, but for a wide variety of discharges (112 total).

7.2 Summary of the MIST simulation results

The MIST simulations presented in this Chapter show that the x-ray emissivity pedestal top is located where the pinch velocity changes from a weak, spatially constant pinch to a strongly increasing inward pinch. Real x-ray pedestal tops are located within a few mm of where the neoclassical inward pinch (derived from measured profiles of n_e and T_e) makes the same transition, that is, near the top of the density pedestal, implying that the pinch is associated with the density gradient, and that it may be neoclassical in the edge region. Density and temperature edge profiles consistent with measured edge profiles actually reproduce the measured x-ray profile exactly when v is assumed to be neoclassical across the whole plasma profile. We therefore conclude that our measurements agree completely with a neoclassical v. The value of D mostly influences the width of the pedestal, Δ, and has little effect on the position of the top of the pedestal for the v profiles studied here. By varying D in the range 100-1000 cm^2/s we find x-ray pedestal widths varying from $\Delta \approx 1$ mm to $\Delta \approx 6$ mm, in agreement with measured values of Δ. However, outside the x-ray pedestal region, ie. in the plasma region within roughly 10 mm of the separatrix, the only information about the v profile that can be extracted from the x-ray emissivity measurements is that it is rather strong, since the x-ray emissivity is very low there. Injection experiments can better quantify the inward convection velocity there by measuring the time it takes to transport the impurities from the separatrix region to the region 10 mm inside it. In the region 10-30 mm inside the separatrix the x-ray emissivity measurements place strong constraints on the inward pinch, showing a rather abrupt change in the v profile at the top of the x-ray emissivity pedestal.

7.2.1 Magnetic surface mapping and diagnostic position issues

The MIST simulations of fluorine transport with a neoclassical pinch velocity show a remarkable agreement with the soft x-ray measurements. In particular, the radial location of the neoclassical pinch is within 2-3 mm of the location which yields fluorine profiles that agree perfectly with the experimental data. It should be noted here that the analysis presented in the previous section is *not* sensitive to EFIT mapping errors, as all the diagnostics used in the analysis are located at or very close to the plasma midplane. The uncertainty in the position of the separatrix appears to be important, since the q profile approaches infinity at the separatrix, and the neoclassical pinch depends on q. The results we have found are not sensitive to this because the impurity density pedestal is found near the top of the electron density pedestal, which is well inside the separatrix. The absolute location of the soft x-ray view is known with about 1 mm accuracy, and a recent calibration of the location of the visible continuum diagnostic view showed that the inferred electron density profiles are actually located 2.6 mm radially outward of what has been presented here. This shift does not change our conclusions, since it is in the direction which makes the discrepancy between the measured and calculated x-ray emissivity in Figure 7-14 virtually disappear. Correspondingly, the agreement shown in Figure 7-15 is not quite as good as it would appear. Since the soft x-ray pedestal is not particularly sensitive to temperature effects, the position uncertainty in the ECE diagnostic position, which is on the order of 5 mm, is unlikely to be important, in particular since the indications are that if it is inaccurate, it should be shifted outward, thus making the recombination terms even less important for the soft x-ray emissivity pedestal shape and position.

7.3 Physics of the x-ray pedestal scaling laws

The MIST simulations show that one can interpret changes in the soft x-ray emissivity pedestal width as changes in the edge diffusion coefficient D. Narrow pedestals with widths on the order of 2 mm or less correspond to D values in the range of 50-100 cm^2/s, whereas wide pedestals on the order of 5 mm or more correspond to D values near 500 cm^2/s. Therefore, the increase in x-ray pedestal width seen when the plasma goes from ELM-free H-mode to EDA H-mode indicates that the edge diffusion coefficient has increased. This is completely consistent with previous measurements of the impurity transport differences between ELMfree H-modes and EDA H-modes as reviewed in Section 6.2.1. During type III ELMy periods even wider pedestals are observed (5-8mm widths) implying that the edge confinement is degraded further, to levels which are almost L-mode like. This is also consistent with the previous studies. The pedestal width scaling laws which were described in Section 4.4 can now be interpreted directly in terms of the edge diffusion coefficient. We find that the edge diffusion coefficient increases with decreasing plasma current (decreasing edge poloidal field, or increasing q_{95}) in EDA H-mode. This is similar to previously published data showing that the impurity confinement time increases with plasma current in L-mode [23]. This also explains why the x-ray pedestal height increases with the plasma current in EDA H-mode, because the edge confinement improves (D at the edge decreases) as the current is increased. The observation that the pedestal width in EDA H-mode also depends on the current ramping direction implies that dI_p/dt affects the edge D and the impurity confinement too. Based on our observations, we expect the impurity confinement time to be lower when the plasma current is ramping up than when the current is ramping down. This has not been observed previously. Since presumably the enhanced transport in EDA H-mode is due to some instability, it suggests that the instability drive is sensitive to the current ramp rate direction, as well as the absolute value of the current (or perhaps q_{95}). It has been observed that high q_{95} favors EDA H-modes over ELMfree H-modes, and that EDA H-modes are rarely observed for q_{95} less than 3.5 [13], but it has not been established if ramping

up the current favors EDA, or if ramping down the current favors ELMfree H-modes. Our measurements suggest that this might be the case. This finding also suggests that the edge current profile (and therefore, the edge profile of the safety factor q), is important for the EDA instability drive, since the edge current density is strongly affected by the direction of the current ramp. Our measurements also indicate that the edge diffusion coefficient increases with increasing plasma triangularity. It has been observed that moderate to high values of triangularity favor EDA, and low values of triangularity appear to prevent EDA H-modes in favor of ELMfree H-modes [13].

Chapter 8

Automatic determination of confinement mode

When the transition from L-mode to H-mode occurs, the soft x-ray emissivity profile increases from a rather flat profile to one with a clear and narrow pedestal. In L-mode, there is sometimes a hint of a pedestal too, but the x-ray emissivity we observe in the edge region peaks at 1-3 kW/m^3 in typical L-mode plasmas, whereas it peaks at 15-60 kW/m^3 in typical H-mode plasmas. In addition, the emissivity levels may actually drop near the separatrix after the transition from L-mode to H-mode, presumably because of the strong inward pinch. Therefore, the signature of H-mode is very clear in the soft x-ray emissivity, and in the raw incident power profiles as well. In Figure 8-1 we show a comparison of the raw signal profiles in L- and H-mode in a particular discharge. Given that the signature of H-mode is so clear in the soft x-ray data, it suggests that it may be possible to develop a computer algorithm which automatically determines if the plasma is in L-mode or H-mode, using the soft x-ray data as input. It is desirable to use the raw data as inputs rather than the inverted emissivity profiles, because the inversions are not always available in the data trees.

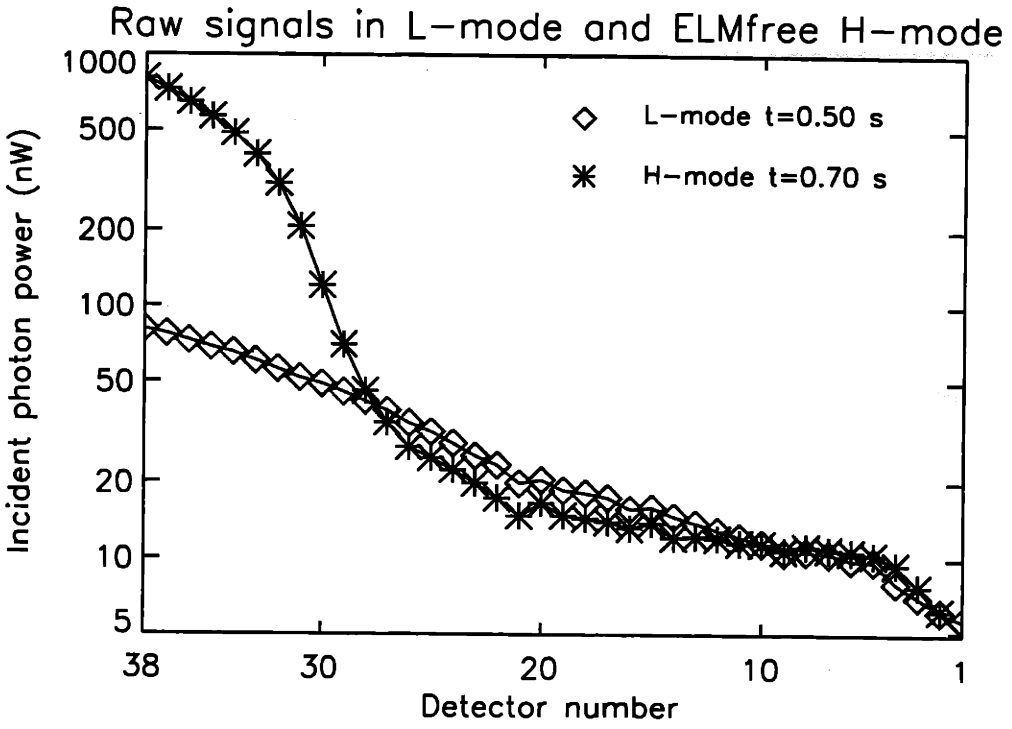

Figure 8-1: A comparison between the raw signal profiles in L-mode and H-mode shows that the raw signals increase by an order of magnitude in H-mode on the innermost detector but drop or remain unchanged further out. Note that the signal levels are plotted on a logarithmic scale. Also note that the shadow of the limiter is seen on the outermost 4 detectors.

8.1 Distinguishing parameters

It is important to identify the parameters which most clearly show the difference between L-mode and H-mode. One such parameter is the incident photon power on the innermost detector. Typically the signal level in the innermost detector is an order of magnitude higher in H-mode than in L-mode. However, when impurities such as neon or fluorine are injected into the plasma, the signal levels can rise substantially, even in L-mode. Therefore, the signal level itself is not enough to determine unequivocally if the plasma is in H-mode or L-mode. Such injections tend to increase the signal levels on all detectors by about the same factor, so the brightness profile shape remains the same. Therefore, the initial approach to separating L-mode and H-mode plasmas included two parameters, the signal on the innermost detector, S_{38}[1], and the ratio of the signal level on the innermost detector to one near the separatrix, S_{38}/S_{08}. The

[1]For the new arrays, the innermost detector is detector 1, so S_1 is used

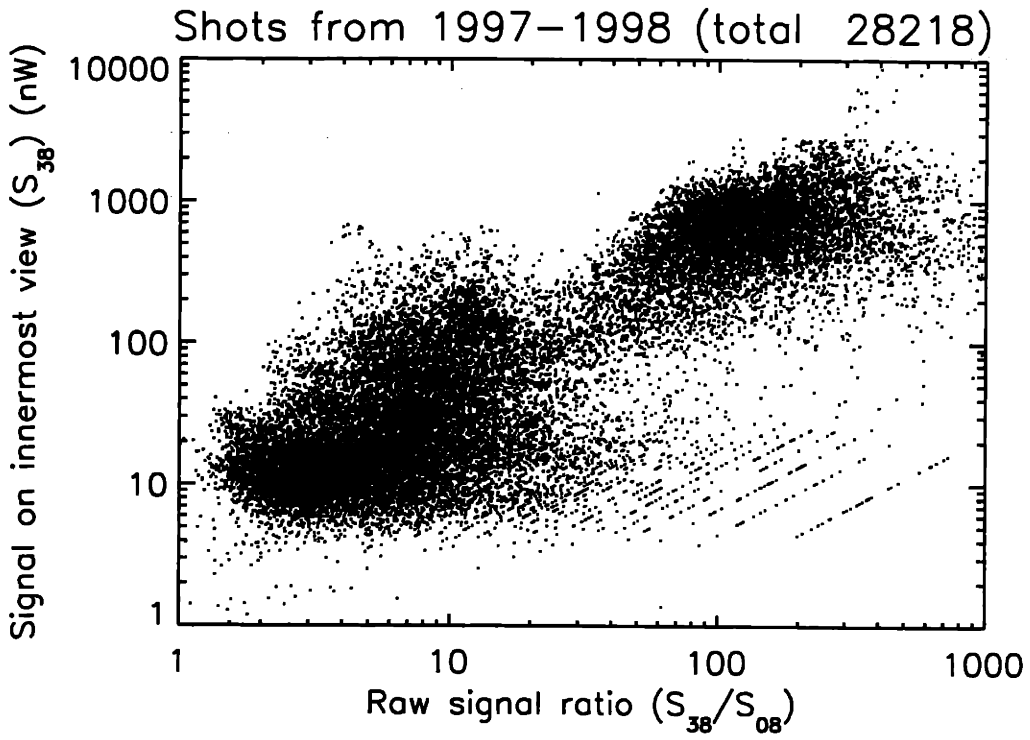

Figure 8-2: When plotting all discharges in the edge x-ray database against the innermost signal and its ratio to one of the outer channels, we find that most of the discharges end up in two clusters. We associate the lower left cluster with L-mode conditions and the upper right cluster with H-mode conditions.

edge x-ray database was used to plot all plasmas from the 1997-1998 run campaign against these two parameters to see if they fell in two distinct regions, corresponding to H-mode and L-mode. This scatter plot is shown in Figure 8-2. We find that indeed most of the discharges can be separated into two clusters, which we associate with L-mode and H-mode. Thus encouraged, a simple computer algorithm was implemented which determined for a given plasma discharge if it fell in one cluster or the other, and this was compared to independent information about the discharge in order to determine if the plasma was really in H-mode. We found that although the algorithm worked most of the time, there were plasma discharge conditions where it would fail consistently. One failure mode was when the plasma was positioned almost outside the views of the detectors, so that only the outermost part of it was viewed by the innermost detector, the signal levels on that detector would often be below normal L-mode values, even though the plasma was in H-mode. Although the x-ray emissivity pedestal was still very evident in the inverted data, the signal on the innermost

detector (which is proportional to the chord integral of the soft x-ray emissivity in its field of view), would be low, because only a small fraction of x-ray emitting plasma was viewed. Another failure mode was when an injection occurred. In some injection cases, the brightness would increase significantly for a short amount of time, and sometimes the brightness profile would change its shape to a profile which had low signals on the outermost channels, and high signals on the innermost channels, but without a pedestal in the corresponding x-ray emissivity profile. Other independent diagnostics would show that the plasma was clearly in L-mode, although S_{38} and S_{38}/S_{08} levels were similar to H-mode levels. Thus, a more sophisticated approach had to be developed, which took into account that the H-mode pedestal could be located further inside the x-ray diagnostic view, or perhaps even beyond it. The EFIT equilibrium was used to determine if the pedestal was in the view of the detector system at all, and if not, no attempt was made to distinguish between H-mode and L-mode, rather the algorithm would indicate that no data was available at that time. It also uses a more careful approach to distinguish the profiles right after impurity injections from H-mode profiles. The algorithm returns an integer value between -1 and 2 on a 1 ms time scale with the following meaning:

- -1 "No data". This means that either there were no x-ray data available for the particular discharge and time, or that the EFIT equilibrium indicates that the x-ray pedestal would be outside the field of view of the outboard array.
- 0 "L-mode". The algorithm has determined that the plasma must be in the low confinement mode (L-mode).
- 1 "?". Although the x-ray data were available, it was not possible to establish if the plasma at that time was in H-mode or L-mode.
- 2 "H-mode". The algorithm has determined that the plasma is in H-mode.

The algorithm usually only returns the value 1 ("?") right after impurity injections, around the transition times, or sometimes during type III ELMs, as discussed in Section 8.3. This is usually a very small fraction of the discharge time, although it

can be significant under certain conditions (see Figure 8-6). Out of 30770 plasma time slices in the edge x-ray database where the algorithm had been used to determine the confinement mode, only 2.2 % of these were classified as "?". 37.1 % were classified as H-mode, and the remaining 60.7 % were classified as L-modes.

8.2 Inclusion of H_α measurements

The soft x-ray emissivity pedestal builds up gradually over tens of milliseconds after the L-H transition, but disappears within less than one millisecond at the H-L transition. This means that the H-L transition can be determined from the soft x-ray data with about 1 ms accuracy, whereas there is a delay of 2-10 ms from the L-H transition until the soft x-ray emissivity (and raw signals) show that the plasma is in H-mode. In order to improve on the accuracy of the algorithm near the L-H transition, the time history of the H_α emission was included in the analysis. The H_α emission usually drops sharply immediately following the L-H transition, so it can be used to determine the time of the transition more accurately than what can be derived from the soft x-ray data alone. The H_α signal fluctuates a lot both in L-mode and in H-mode, so it would be difficult to base the H-mode discrimination algorithm on the H_α signal alone. The algorithm determines the L-H transition first from the soft x-ray data, and then it looks at the H_α signal in the preceding 15 ms, to see if there is any clear transition signature (defined as a drop of at least a factor of 2 in H_α signal level). If so, the plasma is assumed to be in L-mode before the H_α drop, and in H-mode after that. The H-L transition time is well diagnosed by the soft x-rays (see Section 10.5).

8.3 Examples of mode detection

The H-mode detection algorithm has been tested on a large number of discharges, for a variety of different plasma conditions. The algorithm is very accurate on shots that either stay in L-mode all the time or ones that have long, good confinement H-modes.

Examples of such discharges are shown in Figures 8-3 and 8-4. In Figure 8-3 an RF heated steady-state H-mode is correctly diagnosed, and in Figure 8-4 two ohmic H-modes, one ELMfree, and one EDA H-mode, are detected correctly. It performs well, but not perfectly on discharges where the plasma is switching between L-mode and H-mode many times, in particular when there are type III ELMs at high repetition rates. Type III ELMs occur near the H-mode power threshold and disappear or become less frequent as the power through the edge plasma is increased well above the threshold value. Often the algorithm returns the value 1 for these H-modes, indicating that it could not clearly distinguish them from L-mode. In fact, the type III ELMy H-mode confinement can be near L-mode confinement, and often there are no clear pedestals in the x-ray emissivity or the visible bremsstrahlung profile. The degraded confinement is sometimes evident in the line integrated electron density, which may drop if the confinement mode changes from ELMfree H-mode to type III ELMy H-mode. In Figure 8-5 we show an example of a plasma with multiple transitions between L-mode, ELMfree H-mode, and type III H-mode, and the algorithm still diagnoses the confinement mode with very high accuracy. In Figure 8-6 we show an example where the algorithm does not perform as well, returning the value 1("?") rather often. Given that other diagnostics show that type III ELMy H-modes have low confinement and no pedestals, it is not surprising that the algorithm cannot distinguish the confinement mode in this case, since it does not show many of the features usually associated with H-mode confinement.

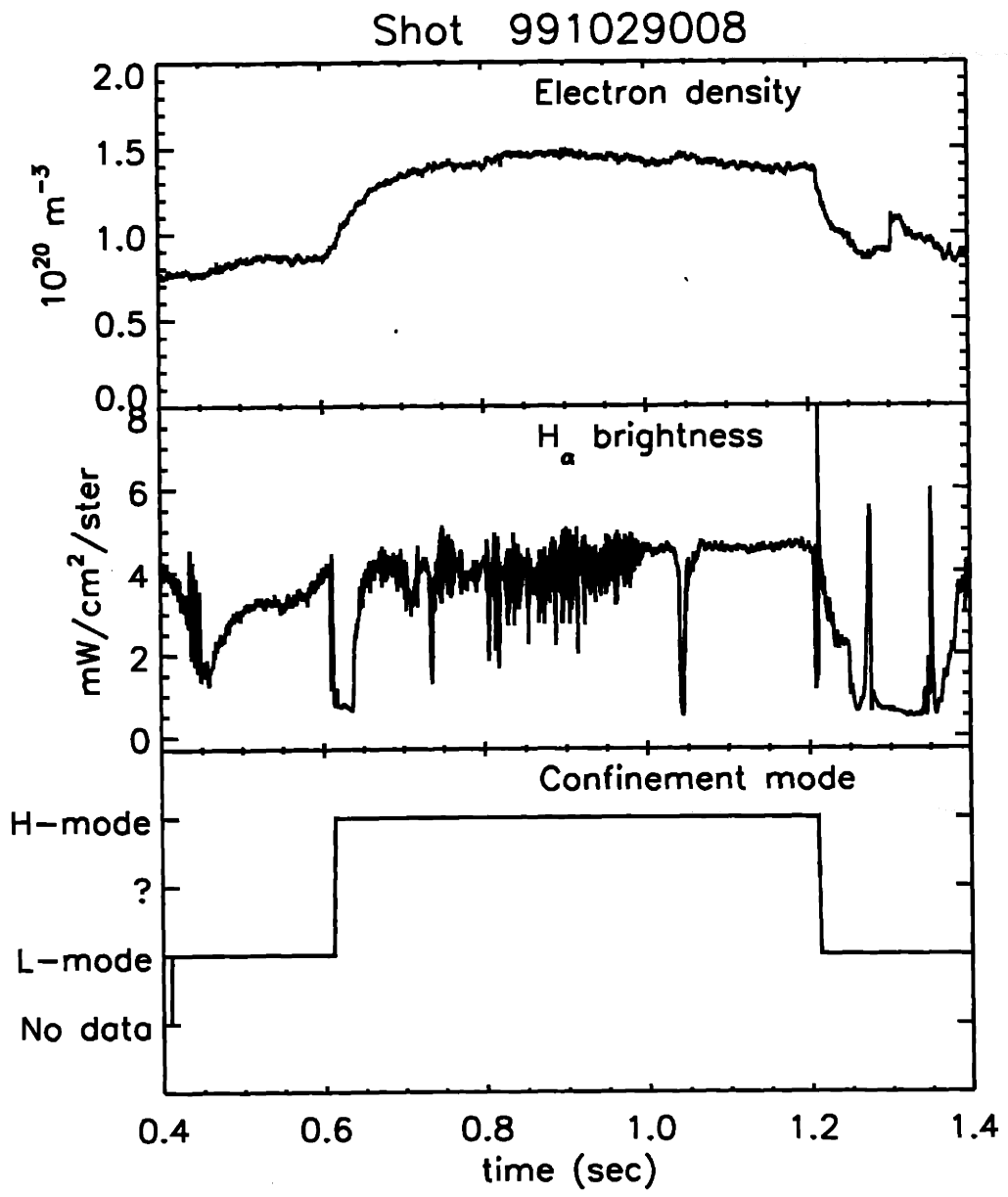

Figure 8-3: This shows an example of a steady state EDA H-mode with RF heating. On the lowest time trace, the output of the detection algorithm is shown. For comparison, we show the H_α emission near the plasma midplane, and the line integrated electron density. The algorithm correctly determines the mode throughout the entire discharge. Note that because of the highly enhanced H_α radiation, it is not obvious from the H_α radiation that the plasma is in H-mode. The density trace shows this somewhat more clearly.

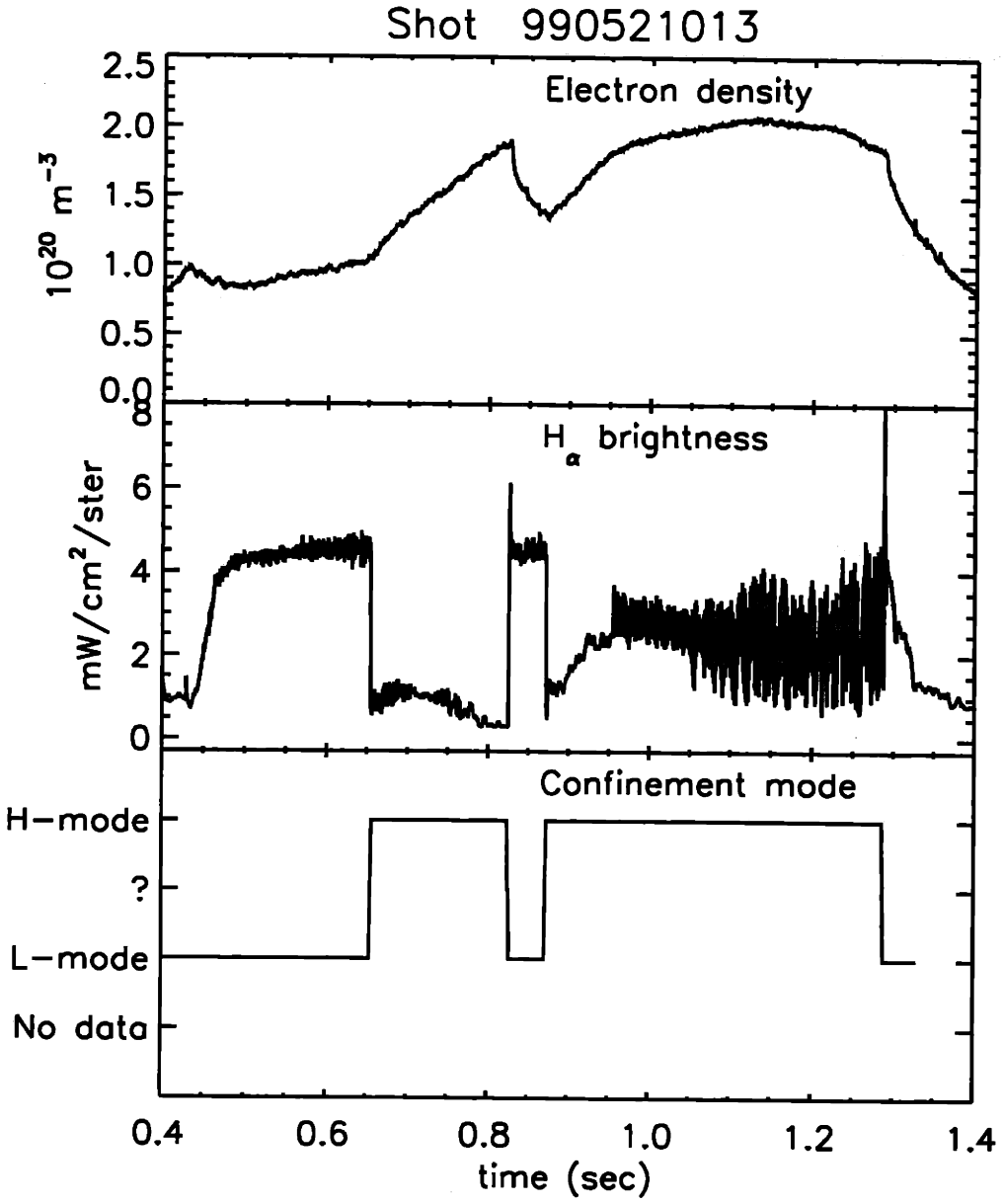

Figure 8-4: This shows a discharge without RF heating. Two ohmic H-modes are produced, the first one is ELMfree, and the second one is an EDA H-mode. In this case the algorithm also detects the mode correctly throughout the discharge. Both the density and H_α time histories show the transition times rather clearly in this case.

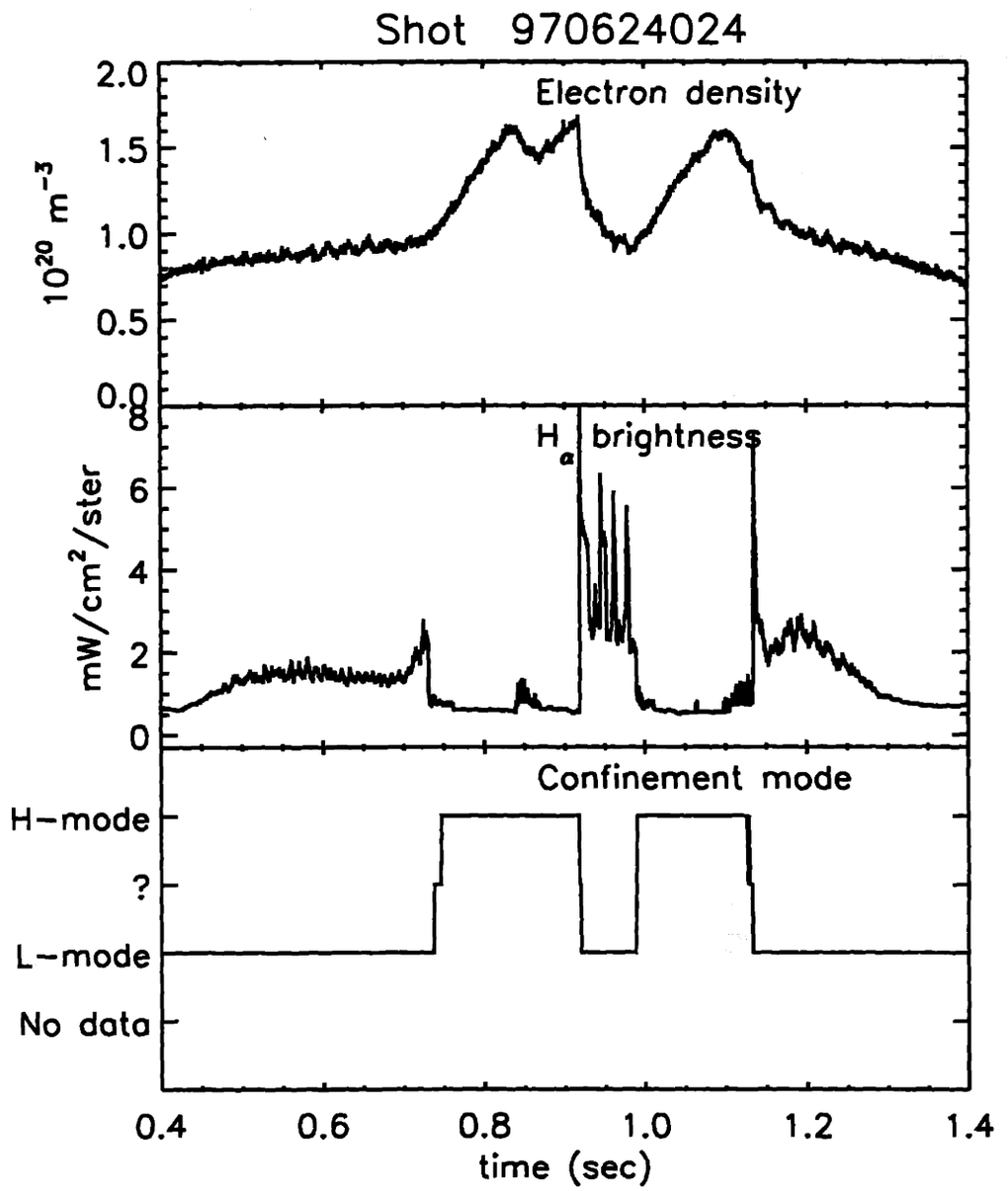

Figure 8-5: A plasma discharge with two H-mode periods. Both of the periods alternate from ELMfree to type III ELMy H-mode. During the type III ELMy periods, the plasma density actually decreases, since the edge particle transport is much enhanced over the ELMfree levels. Even so, the algorithm correctly determines the confinement mode throughout the discharge

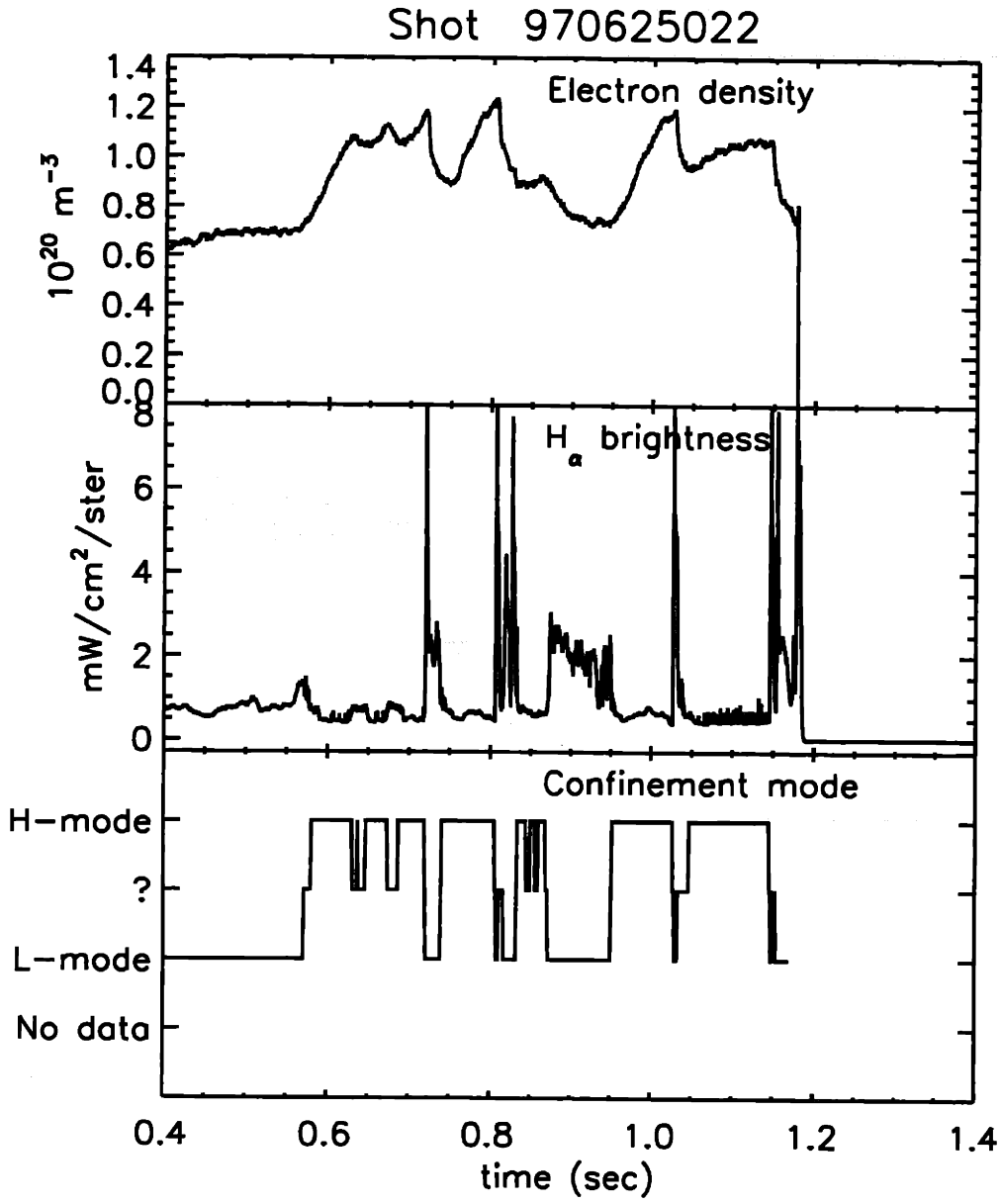

Figure 8-6: In this case the plasma is switching rapidly between ELMfree H-mode, type III ELMy H-mode, and L-mode. The algorithm correctly determines the mode most of the time but it is unable to determine the mode ("?" in the figure) during some of the type III ELMy periods, and around transitions. The density trace reflects the significant confinement changes between the three types of confinement.

Chapter 9

Design and description of the two-array diagnostic

The new edge x-ray system has two independent, poloidally separate, views of the plasma edge. The x-ray array 2, which was used in the 1997-1998 run campaign to measure the soft x-ray emissivity of the lower outboard midplane plasma edge as shown in Figure 2-1, was fitted with a different aperture so that it now views the edge plasma at the top of the machine. Array 4, which used to be part of the core x-ray tomography arrays, was fitted with an aperture which is essentially the mirror image of the old one for array 2, so it views the outboard midplane in a configuration which is almost exactly the mirror image of the old array. The two-array configuration is shown in Figure 9-3. Close-up pictures of the new x-ray diagnostics are shown in Figures 9-1 and 9-2.

9.0.1 Design considerations

The new two-array design provides simultaneous measurements of the soft x-ray emissivity at two poloidally separate locations (the top and the upper part of the outboard midplane). This allows us to address the following questions:

- To what extent does the x-ray emissivity vary on a flux surface? It is assumed in the matrix inversion that the emissivity is constant on a flux surface in the

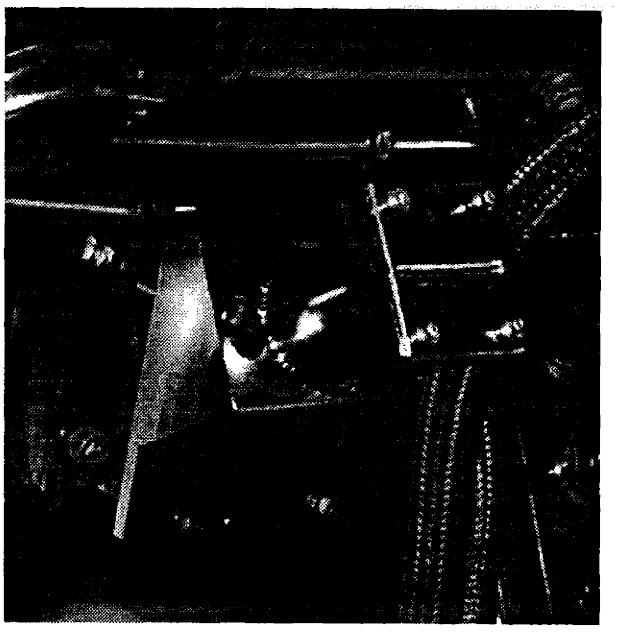

Figure 9-1: A picture of the new aperture box for array 2 installed in the Alcator C-Mod vacuum vessel. The array views the edge plasma at the top of the machine.

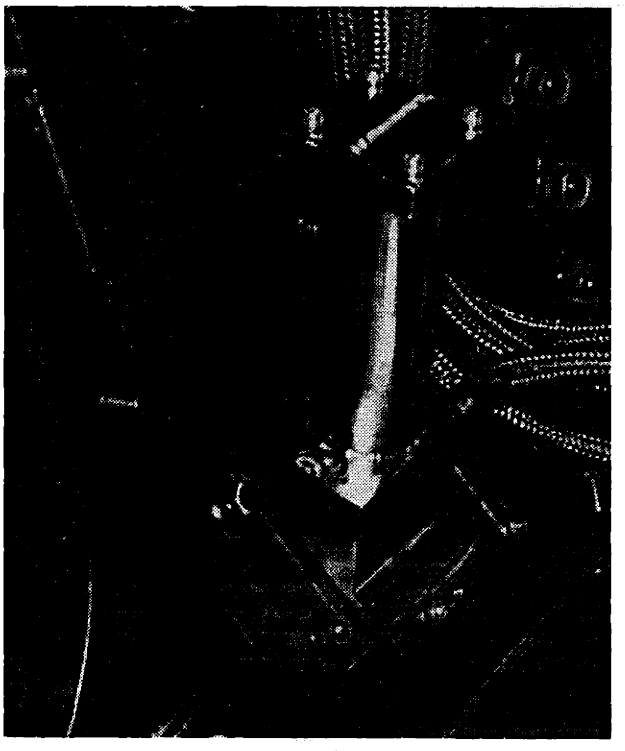

Figure 9-2: The outboard midplane diagnostic (array 4) installed in the Alcator C-Mod vacuum vessel.

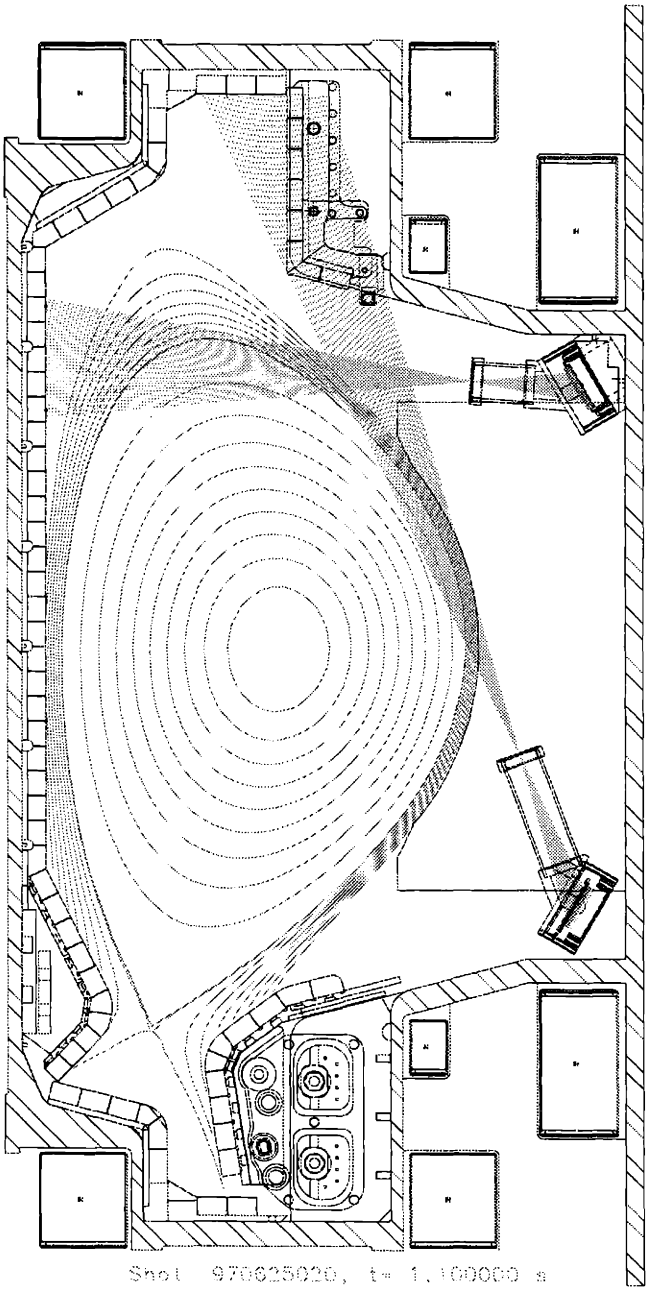

Figure 9-3: CAD drawing of the new two-array edge x-ray diagnostic in Alcator C-Mod. The yellow lines show the views of the 38 detectors for each array. Flux surfaces for a typical plasma are also shown in blue.

region viewed by the diagnostic, but previous measurements [16] have shown that this is a good, but not exact, assumption.

- If fast edge pedestal instabilities such as H-L transitions or ELMs originate in the bad curvature region at the outboard midplane and then propagate poloidally, we would be able to detect a timing difference if it is larger than 12 μsec, corresponding to a poloidal propagation velocity on the order of 20 km/sec or less. This also corresponds to a parallel propagation velocity of roughly 100 km/sec or less, depending on the safety factor q near the edge.

- Are the large ELM-like x-ray bursts much stronger at the outboard midplane than at the top of the machine, ie. are they of a ballooning-like nature? It is generally believed that type I ELMs[1] are of a ballooning-like nature.

In addition, it was observed with the first version of the soft x-ray edge array, that in ELM-free H-modes, the pedestal was so narrow that the width in some cases was on the order of the spatial resolution. At the top of the machine, the flux surfaces are further apart than at the midplane by roughly a factor of 2.5 (the flux expansion). Thus, by viewing at the top of the machine, it is possible to increase the resolution in terms of the flux function, without decreasing the chord spacing in real space. Or, one can increase the chord spacing, open up the view, and get the same resolution in terms of the flux function but get higher signal levels. Given that the signal to noise ratio was high in good H-modes (see Chapter 4) it was not a priority to increase the signal level, although it would benefit the study of L-modes, where the soft x-ray emissivity is very low. However, given that the array has 38 detectors, an increase in flux function resolution (or, resolution mapped to the midplane), inevitably means that one views a smaller region of the plasma. Thus, the major design considerations for the top view were:

- A significant increase in radial (flux function) resolution, so that even pedestals with widths on the order of 1.5-2 mm mapped to the midplane could be resolved.

[1] At the time this thesis was written, there had been no type I ELMs observed in Alcator C-Mod

- A broad enough view so that both the x-ray pedestal region would be viewed as well as the separatrix region. It is important to view parts of the SOL (scrape-off layer) for the ELM studies. It was assumed that the pedestal would be on the same EFIT flux surface as the pedestal was observed to be at the lower outboard midplane, ie. about 10 mm inside the separatrix. As shown in Chapter 10 this turned out not to be the case.

A detailed numerical study of the performance of various designs was performed by following a procedure outlined in Appendix B. With this procedure, estimates could be made of the expected signal levels, spatial resolution, and the coverage of the edge plasma. The orientation of the view was chosen such that the center of the view would be where the pedestal was expected to be, so about half of the channels would be looking through the x-ray pedestal in H-mode whereas the other half would be outside the x-ray pedestal, so they would be expected to have very low signal levels. The outer half of the channels would still be useful for studying x-ray bursts during ELMs and H-L transitions. Since the x-ray pedestal was determined to be about 10 mm inside the nominal EFIT separatrix, this would mean that almost all detectors would be viewing plasma inside the separatrix. It was considered important to establish if x-ray bursts extend beyond the separatrix, so the view was chosen to be broad enough that the 3-5 outermost detectors would be viewing along lines outside the separatrix for a typical equilibrium. (For some equilibria, the separatrix would be outside the field of view). The view was chosen narrow enough that the expected spatial resolution would be 1.1 mm, as opposed to 1.7 mm for the old array. Figure 9-4 shows the results of an error sensitivity analysis performed by the procedure above. It should be noted though, that this error analysis was performed before the improved algorithm described in Section 3.1.1 was developed, and that with the improved algorithm, the spatial resolution of both old and new data is much better (in the best cases 0.8 mm at the top of the plasma and 1.1 mm at the outboard edge). However, this improvement was not made until after the new arrays were designed and manufactured. By using this procedure it was found that an increase in the toroidal extent of the aperture from 36 mm to eg. 45 mm would increase the signal levels without compromising

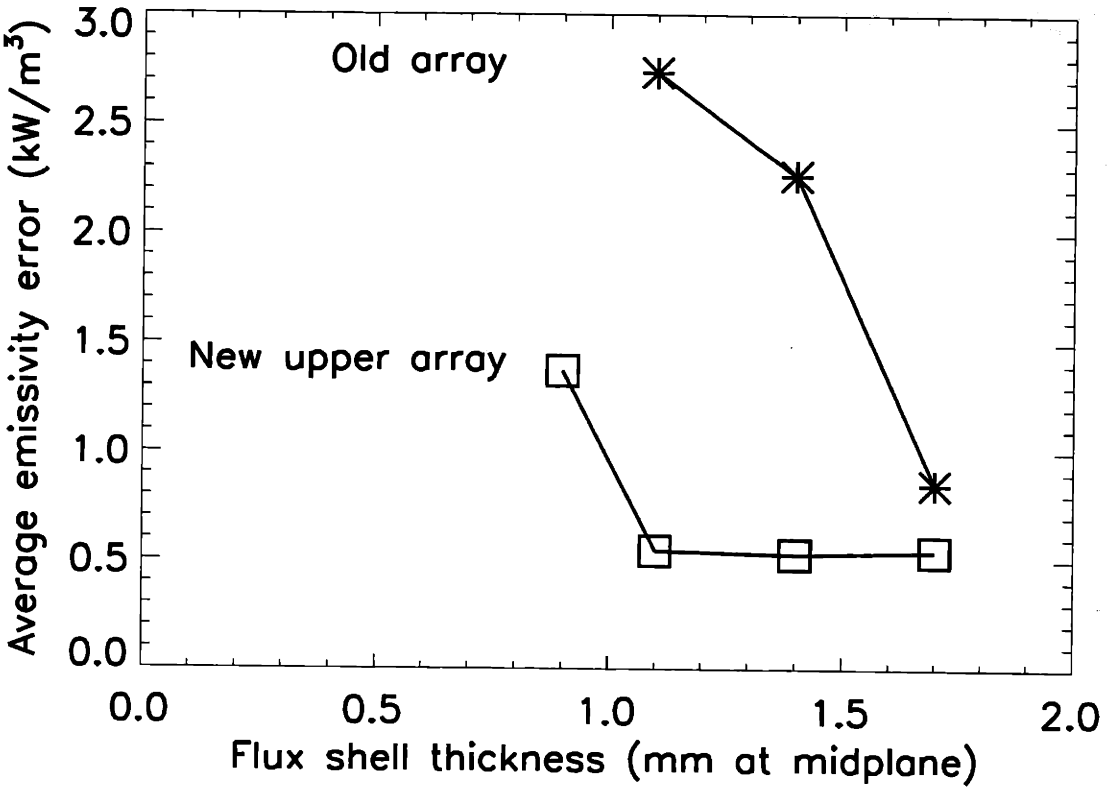

Figure 9-4: This figure shows a comparison of error sensitivities between the old and new design for array 2.as a function of the spatial resolution mapped to the midplane. The inversion algorithm used here is not the new and improved algorithm described in Section 3.1.1. Therefore, it appears that the spatial resolution for the old design is limited to 1.7 mm and to 1.1 mm for the new design.

the spatial resolution. However, the actual geometry of the x-ray boxes is such, that this would not be easy to implement, so it was decided to use 0.5 mm by 35 mm apertures, identical to those used for the first edge x-ray diagnostic, since the signal to noise levels were expected to be large. Even with the same aperture, the signal levels were expected to be about 3 times higher for the new design.

9.0.2 Data acquisition

The new two-array edge x-ray diagnostics use the same data acquisition system as the old array. The data acquisition system is described in Section 2.0.1.

9.1 Absolute calibration of the new two-array edge x-ray diagnostic

The new two-array x-ray edge diagnostic was installed in October 1998, and the views of both detector arrays were measured shortly thereafter.

9.1.1 Determination of the absolute position of the top view

Array 2, which was now viewing the top part of the plasma, was calibrated by using a halogen bulb with a small filament (the same one used for the calibration of the old viewing optics). For the calibration, the beryllium filter was removed, since the light from the halogen bulb would not penetrate. Removal or insertion of the beryllium foil can be done without changing the view of the diagnostic. The absolute positions of the upper array viewing chords were obtained by aligning a ruler with respect to the inner wall tile screws (not the inner wall tiles which are twisted several mm). The ruler was then used to determine the position of the halogen bulb fixture at the position which peaked the voltage of two particular detectors (3 and 36). The halogen light bulb was operated at 1.2 A, which provided plenty of signal. The locations of the detector views were found to deviate from those expected from the CAD drawings by being 1.5 mm higher at the inner wall. This difference is well inside the specifications

for the accuracy of the aperture. Since the viewing chord positions are known at the inner wall with less than 1 mm uncertainty, their positions in the region of plasma are known with roughly 0.5 mm uncertainty.

9.1.2 Determination of the absolute position of the outboard midplane view

The position of the view of array 4, which is looking up at the outboard edge plasma near the midplane from the bottom of the machine, was also determined by the use of the halogen bulb. For this array, a more complicated alignment had to be made. Metal pieces were clamped onto the upper array and a metal ruler was positioned to make an accurate (+/- 1 mm) position measurement of the viewing chords with respect to the upper array cover. The views were found to be 6 mm closer to the center of the machine than anticipated from the CAD drawings. This discrepancy corresponds to the angle of the x-ray cover, snout and aperture being off by 0.7^o. This is a small discrepancy but is significantly larger than the specifications which required this angle to be accurate within 0.25^o. The position of x-ray array 2 is known with about 1 mm accuracy. In order to confirm the results of the calibration, a second calibration was performed at the tiles at the top of the machine. The halogen bulb was fixed with respect to the tile cracks with about 1.5 mm accuracy at the top of the machine, and the signal peaked on the same detector as expected from the first calibration. This procedure was repeated at a different location (also at the top of the vessel), and again the signal peaked on the detector expected from the first calibration. It was therefore concluded that the first calibration was accurate to within 1.5 mm at the top of the machine. This corresponds to 1 mm uncertainty or less in the positions of the viewing chords in the plasma region.

9.2 Relative calibration of the areas of the apertures

The apertures used for the x-ray edge arrays are 0.5 mm by 36 mm. Each aperture consists of two knife edges squeezed together to form the aperture. Due to manufacturing uncertainties, the narrow dimension of the apertures could deviate as much as 10-15% from the specified 0.5 mm. It was therefore a concern that the actual areas of the two apertures might differ by up to 15%, which would then introduce a systematic difference in the inferred emissivities on the same order between the two locations if this was not properly accounted for. It was therefore very important to calibrate the aperture sizes of the two arrays. The light source used for this calibration was a high precision "Lab Sphere", a source of highly uniform brightness with a filament with an accurately controlled current. The lab sphere was operated at a fixed current of 2.780 A. For array 2, the voltages across selected photodiodes were measured when the lab sphere was placed directly in front of the aperture, filling the entire view of the detector array. Then the aperture on array 2 was replaced by the other aperture (the one for array 4), and the procedure was repeated. As an extra check, the same procedure was performed on array 4. In both cases the differences in the voltages recorded were so small between the measurements with the two different apertures, that we can conclude that the aperture areas are the same within a few percent. (Certainly less than 5%). For example, the voltage across one detector was 205.6 mV when array 2's aperture was used and 207.0 mV when array 4's aperture was used, so the difference in voltage was less than 1 %. Ideally, this relative calibration of the aperture areas should have been done by measuring the zero impedance currents in the detectors, which are known to be proportional to the incident photon power. This would require them to be connected to the amplification electronics described in Section 2.0.1. However, the calibration had to be done at a time when the detectors could not be connected to the proper amplification electronics, so we had to rely on measuring the voltage across the detector, which is a photodiode. The voltage is a growing function of the incident photon power, but cannot in general be assumed to

be a linear function. From our experience with the halogen light bulb, there is an approximately linear relation between the voltage and the incident photon power.

Chapter 10

Measurements made with the two-array edge x-ray diagnostic

10.1 Description of typical data

In Figure 10-1 we show a comparison between the x-ray emissivity profiles at the top of the plasma and at the outboard edge for an EDA H-mode. In order to compare the two profiles directly, we map the emissivity profiles to the plasma midplane using the EFIT magnetic surfaces. Although the two profiles both show a clear pedestal, there are significant differences between the pedestal at the top and the pedestal at the outboard edge with respect to the width, height, and position of the pedestal. Only the slope inside the pedestal is roughly the same in the two locations. Looking at Figure 10-1 the most striking difference is perhaps the difference in pedestal location. At the top of the plasma, the x-ray pedestal is just inside the separatrix (2 mm inside) whereas it is well inside the separatrix at the midplane (13.7 mm inside). The two pedestal widths are substantially different also. The pedestal is 5.0 mm wide at the midplane but only 1.8 mm at the top of the plasma. The heights differ too, being about 20 kW/m^3 at the outboard edge and 14 kW/m^3 at the top of the plasma. The slopes inside the pedestals are roughly in agreement (0.91 MW/m^4 at the outboard edge and 1.0 MW/m^4 at the top). We have chosen an RF heated EDA H-mode at

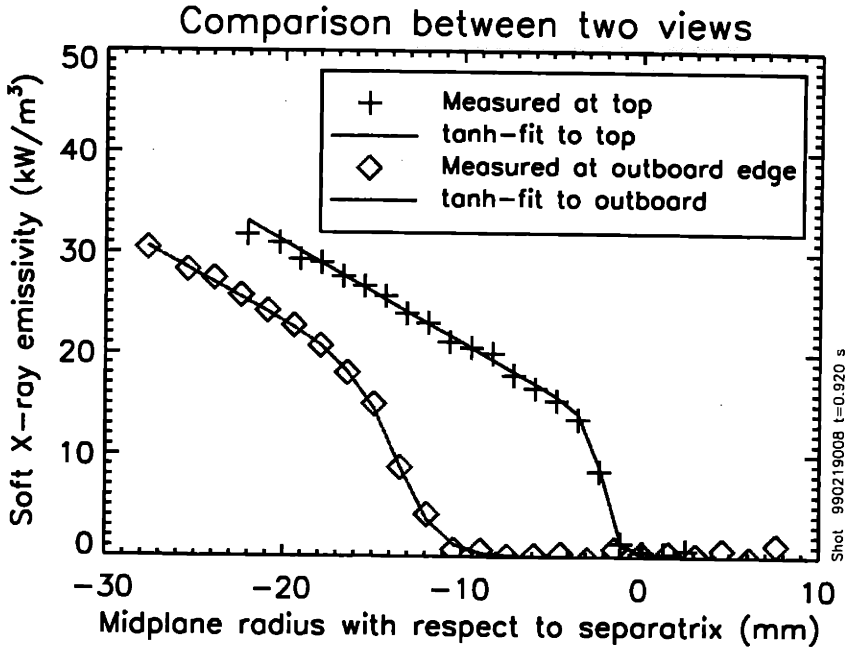

Figure 10-1: One may compare the x-ray emissivity profiles at the top and outboard edge by mapping both to the midplane using the EFIT equilibrium. In this figure we show profiles for an EDA H-mode. There is a clear pedestal both at the top and the outboard edge, but the two pedestals are not located on the same flux surface, and they also do not agree with respect to the width or the height of the pedestal. The slopes inside the pedestals seem to agree rather well.

high q_{95} [1], because these conditions lead to the largest differences between the two emissivity pedestals. More generally, the two pedestals can have the same width, but they are always located on different EFIT flux surfaces, with the pedestal at the top of the plasma being very close to the separatrix, and the pedestal at the outboard midplane being well inside the separatrix. All of the results that we found for the pedestal position, width etc. for the old outboard array, which was viewing the outboard edge below the midplane, are reproduced with the new outboard array, which views the outboard edge above the midplane. However, the pedestal at the top has very different properties. Most of this Chapter and Chapter 11 are devoted to analyzing and understanding the asymmetries between the outboard edge and the top of the plasma, but first, we must see what the implications of the asymmetry are for the accuracy of the inversion.

[1] q_{95} is the safety factor at the 95% flux surface, as given by EFIT

10.2 Inversion accuracy revisited

The inversion algorithm described in Section 3 assumes that the emissivity is constant on an EFIT flux surface. However, our results clearly show that this is not the case at the plasma edge in H-mode. This leads us to question the accuracy of the inversion since the observed difference in emissivity between the outboard midplane and the top of the plasma is very large just inside the separatrix. One has to keep in mind though, that each detector array views only a small poloidal cross section of the plasma, so even if the soft x-ray emissivity varies strongly poloidally, the variation in the view of a particular detector might still be small.

In order to perform the inversion we must know the shape of the emissivity contours, but this shape can only be accurately measured if we perform actual two-dimensional tomography at the plasma edge. With the present detector views, this is not possible. However, we can still *estimate* the magnitude of the error that is introduced via the erroneous assumption that the EFIT flux contours also are the contours of constant emissivity. We do this in the following manner:

- We assume a certain two-dimensional emissivity function whose contours do not follow the magnetic field lines but deviate from these. The deviation is chosen so that it fits the experimental data, that is, we simulate a narrow pedestal shape for the emissivity near the separatrix but place the pedestal right at the separatrix at the top of the plasma and about 10 mm inside it at the outboard plasma midplane. We shall refer to this emissivity as the "assumed emissivity".

- We then calculate the brightness seen by each detector simply by integrating the emissivity function along the line of sight of the detector.

- The brightness profiles obtained for the two arrays can thus be obtained, and should look similar to actual raw data.

- The brightness profiles are then inverted using the standard algorithm, that is, under the assumption that the emissivity *is* constant on a magnetic flux surface.

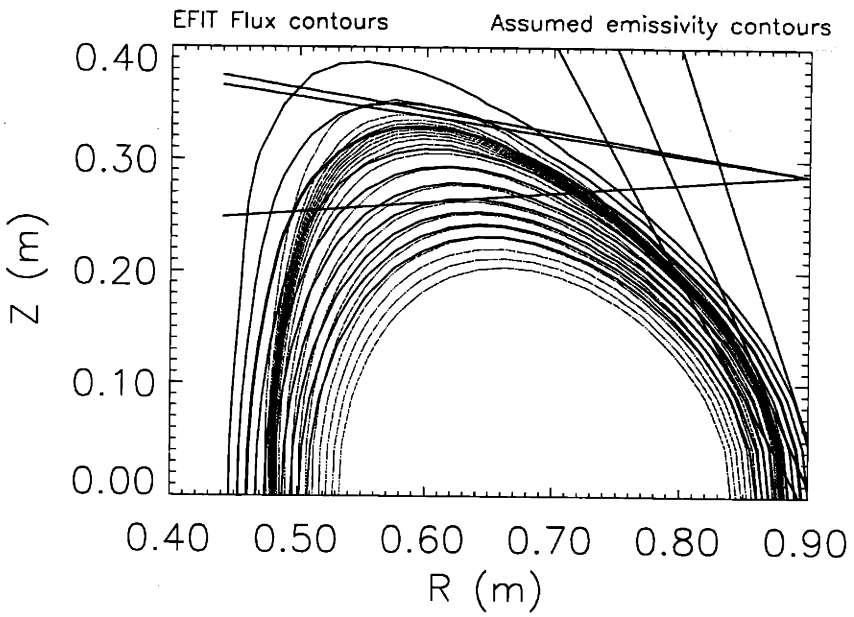

Figure 10-2: In red are shown contours of constant emissivity for a particular choice of two-dimensional emissivity function. The black contours are contours of constant ψ from EFIT, that is, they show the shape of the flux surfaces. The thick contour indicates where the separatrix is for this particular equilibrium. For each detector array, the lines of sight of three detectors are plotted as well. The innermost and outermost view of each detector are shown, and in between we plot the view of the detector where, in a typical H-mode, the brightness starts rising, indicating that this detector view is tangential to the bottom of the emissivity pedestal.

- The resulting emissivity profiles for the two arrays will not agree with each other once mapped to the midplane. However, we can compare the profile obtained from the outboard midplane array (array 4) with the assumed two-dimensional emissivity function in its field of view. Similarly, we can compare the assumed two-dimensional emissivity function at the top of the plasma with the emissivity deduced from the top array (array 2).

- This will give us a measure of how well the arrays measure the *local* emissivity. The error will be somewhat dependent on the particular choice of the two-dimensional emissivity function, so several different shapes have been used.

10.2.1 Two examples of simulated data

Figure 10-2 shows a particular choice of a two-dimensional emissivity function. The emissivity contours deviate significantly from the EFIT flux contours, in partic-

ular at the top of the plasma. The emissivity has been chosen to have a pedestal-like shape at the edge of the plasma, and we have attempted to place the pedestal near the separatrix at the top of the plasma, but about 10 mm inside it at the plasma midplane, in agreement with typical measurements. The next step is then to integrate the emissivity along the line of sight of each detector. This can be done rather easily by reusing the software program that performs the inversion. The program first calculates the matrix for the forward problem (which is to calculate the chord integrated brightness profiles given the emissivity function) and then it inverts the matrix equation using singular value decomposition (SVD), so that the emissivity can be calculated given the brightness profile. (See section 3 for details). Here, we only need to solve the forward problem, using the surfaces of constant emissivity seen on Figure 10-2 rather than the EFIT flux contours. Once the matrix is computed, the brightness profile can be computed for each array. We now use the inversion program again, this time assuming that the emissivity is constant on the EFIT contours, and invert the brightness profile for each array into an emissivity profile mapped to the midplane. These emissivity profiles are shown in Figure 10-3. It is seen that the pedestal derived from the outboard midplane array is located about 10 mm further inside the plasma than that derived from the top array, similar to what is observed in real experiments. This gives us confidence that the two-dimensional emissivity in Figure 10-2 deviates from being constant on flux surfaces by about the same amount as that seen in experiments. In the real data the pedestal is usually wider at the midplane, whereas it is slightly wider at the top in the simulated data used here.

Since the emissivity evidently is not constant on a field line, the assumed emissivity at the midplane will be different from both emissivity profiles mapped to the midplane. We need to know whether the emissivity profile derived from the array viewing the outboard midplane accurately matches the assumed emissivity profile in its field of view. We can choose to compare anywhere in the field of view of the array, but the best match is expected to be roughly in the center of the view. Such a comparison can be seen on Figure 10-4. Similarly, on Figure 10-5 we compare the assumed emissivity at the top of the plasma to that derived by the array viewing the top of the

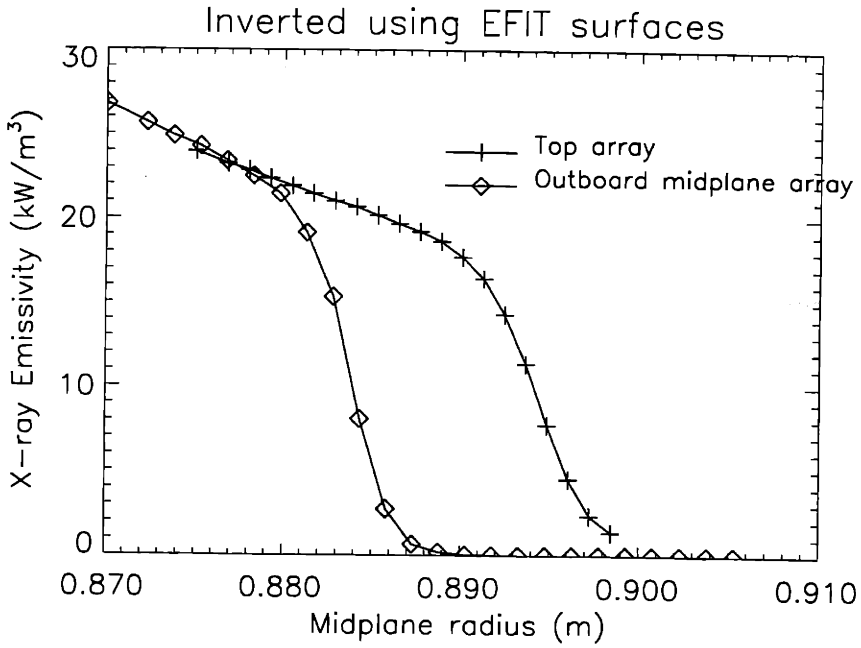

Figure 10-3: The emissivity profiles from the two edge x-ray arrays shown here are obtained by assuming (erroneously) that the emissivity is constant on a flux surface. They are similar to real data in that the pedestal derived from the outboard midplane array is located about 10 mm inside that derived from the top array, when both are mapped to the plasma midplane.

plasma. In both cases, the width and position of the local pedestal are accurately reproduced - the width is accurate to 2% at the outboard midplane and 9% at the top of the plasma, and the pedestal positions are within 1 mm of the pedestal position of the assumed emissivity. The emissivity derived from the outboard midplane array is larger than the assumed emissivity at the outboard midplane by about 5%, whereas the emissivity derived from the top array is smaller than the actual emissivity by about 10%. The outboard midplane array produces more accurate results because the assumed emissivity contours follow the flux contours rather well at the outboard midplane but deviate more strongly from them at the top. The fact that the top array underestimates the emissivity, and the outboard midplane array overestimates it, can also be understood qualitatively. Each detector at the top sees a brightness which is essentially an integral of the emissivity along the line of sight of the detector. At the top of the plasma, the emissivity contours have a smaller radius of curvature than the flux contours, so when we assume that the emissivity is constant on a flux surface, we are overestimating the radius of curvature, and thus the path length of the

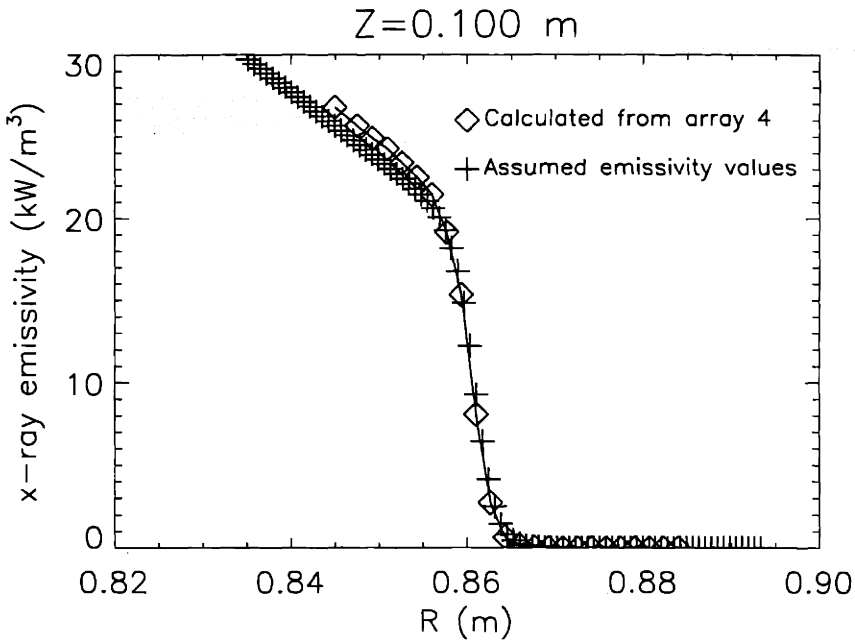

Figure 10-4: This shows a comparison between the assumed two-dimensional emissivity and the emissivity derived from the outboard midplane array, assuming that the emissivity is constant on a flux surface. The emissivity is plotted as a function of R (major radius) for a fixed value of the Z (height above the vessel midplane) coordinate. The assumption of constancy on a flux surface introduces an overestimation of the actual emissivity of 4%. The width is underestimated by 2%.

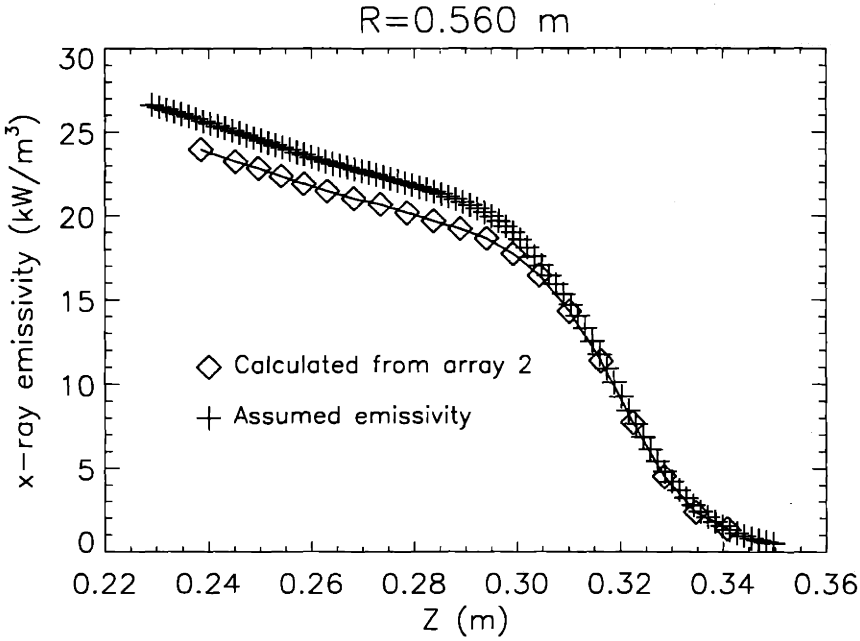

Figure 10-5: The assumed emissivity, and that derived from the top array (array 2) under the assumption that the emissivity is constant on a flux surface, plotted as a function of Z (the height above the plasma midplane) at fixed R (major radius). It is seen that the emissivity is systematically underestimated by about 10%, and the width is underestimated by 9% - barely visible to the naked eye.

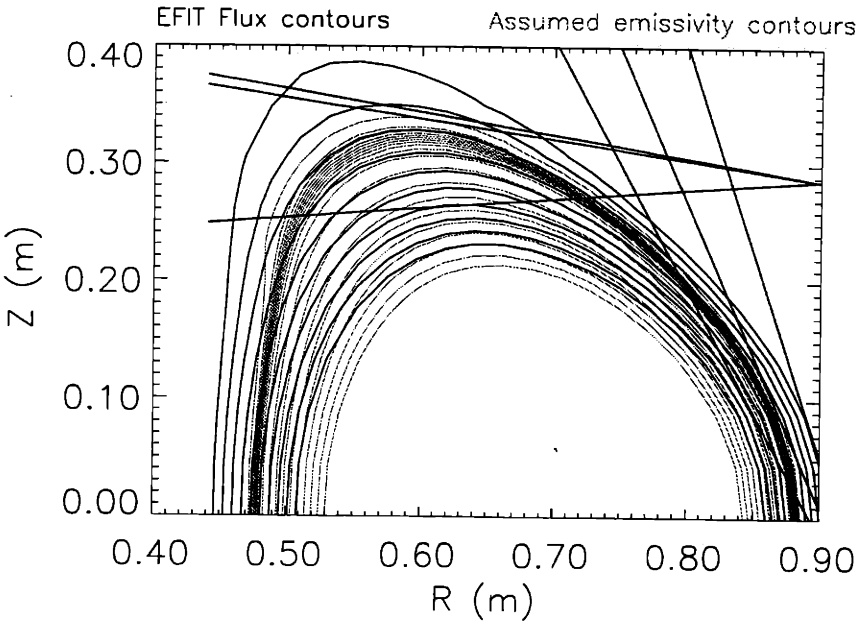

Figure 10-6: This shows another example of a two-dimensional emissivity function which does not follow the flux surfaces. In this case, the emissivity contours follow the flux contours quite well at the top of the plasma but deviate relatively strongly around Z=0.18 m.

integral. This will lead to an underestimate of the emissivity. In Figure 10-6 we show another choice of emissivity function - using the same EFIT magnetic equilibrium as in Figure 10-6. The emissivity contours in Figure 10-6 closely follow the field lines at the top of the plasma but deviate more strongly in the view of the outboard midplane array. We again follow the procedure outlined above, and obtain emissivity profiles for each array under the assumption that the emissivity is constant on a flux surface. Again, once mapped to the plasma midplane, the pedestal derived from the top array is about 10 mm further out than that derived from the outboard midplane array, as seen in Figure 10-8, consistent with real data.

Comparisons in real space for each detector array are shown in Figures 10-8 and 10-9. In this case, the height of the pedestal is reproduced accurately for the top array, although the width is overestimated by 11%. For the outboard midplane, the height is overestimated by 12%, and the width is underestimated by 3%. The fact that the height is accurately reproduced by the top array but somewhat overestimated at the outboard midplane is consistent both with the observation that the emissivity contours follow the flux contours well at the top of the plasma, as well as with

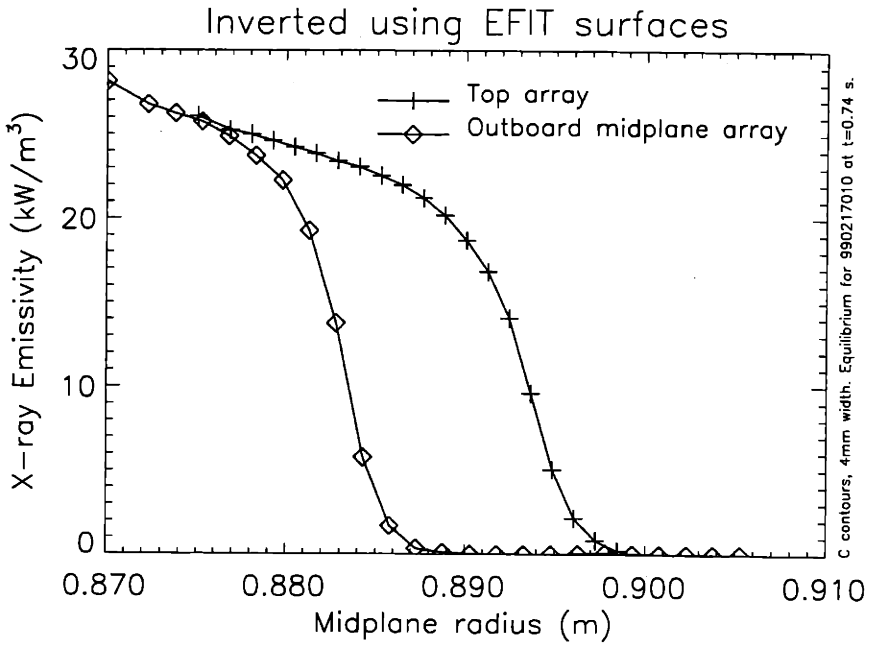

Figure 10-7: For each array, the emissivity profile is calculated assuming that the emissivity is constant on a flux surface, and then mapped to the plasma midplane. Here, we find that the pedestal derived from the top array is about 10 mm further out than that derived from the outboard midplane array, consistent with real data.

the argument that the emissivity generally will be overestimated at the outboard midplane.

10.2.2 Conclusions

In the previous section, we showed two examples of data simulating the effects of emissivity gradients along field lines. Of course the results obtained depend on the shape of the two-dimensional emissivity, and we only have limited information about this shape. The two choices of emissivity presented here are in a sense two extremes — the one in Figure 10-2 follows the field lines quite well in the view of the outboard midplane array, but not in the view of the top array, whereas the one in Figure 10-6 follows the field lines quite well in the view of the top array but does not follow the field lines well in the view of the outboard midplane array. Thus, we expect that the actual emissivity lies somewhere in between these two extremes.

We find that the emissivity profiles derived from both arrays are in very good agreement with the assumed emissivity profiles evaluated in the views of the detectors.

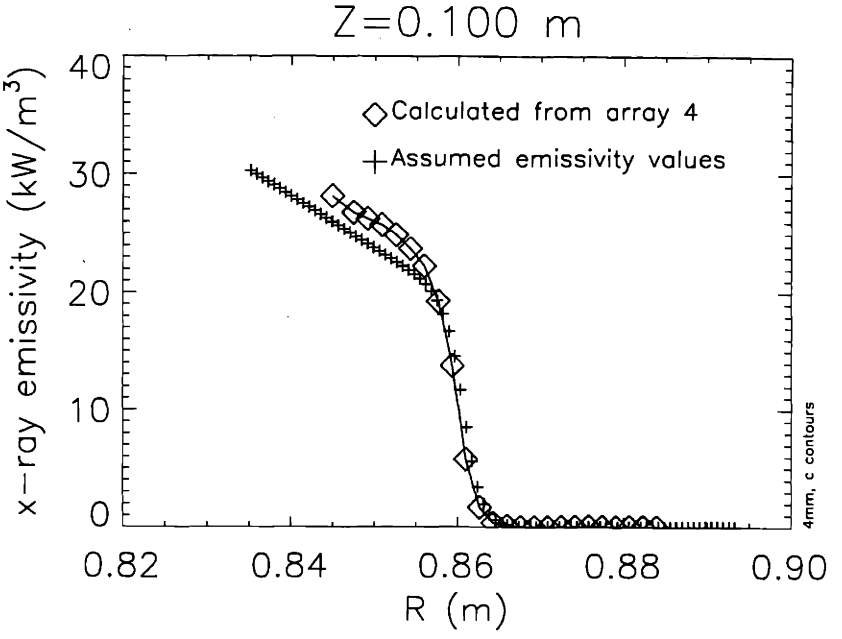

Figure 10-8: The emissivity profile derived from the outboard midplane array matches the assumed emissivity profile well at Z=0.1 m. The height of the pedestal is overestimated by 12%, whereas the pedestal width is 3% lower than the width of the assumed emissivity function.

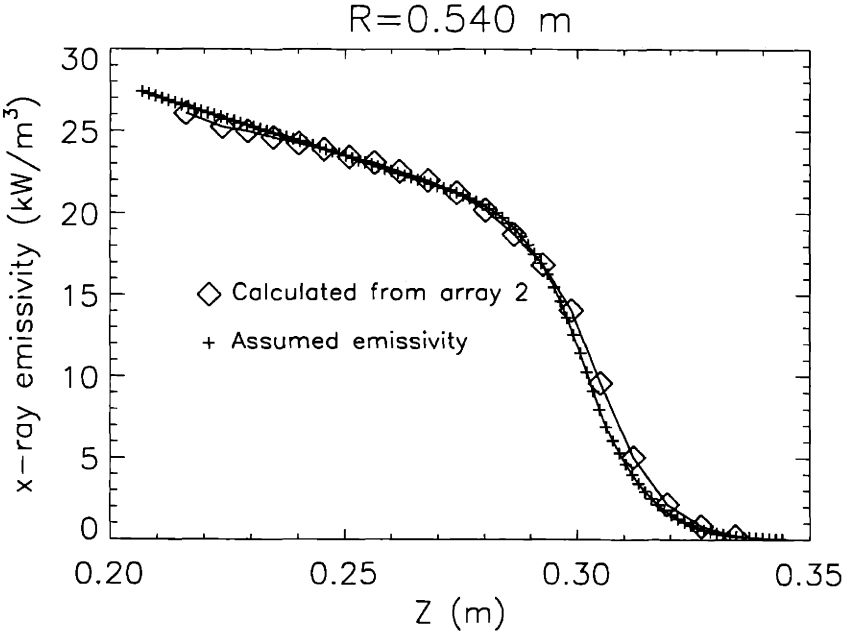

Figure 10-9: The emissivity profile derived from the top array (array 2) matches closely the assumed emissivity profile evaluated at R=0.54 m. The pedestal width is overestimated by 11%, whereas the height and slope deviate by less than 5%.

There is a systematic but small (less than 15%) overestimation of the emissivity at the outboard midplane and a similar underestimation at the top of the plasma. The widths are accurate to within 15% as well. This should be compared to the fact that the widths typically are measured with about 20% accuracy, depending on the signal to noise ratio, so this is not a large effect. The position of the pedestal can be derived within 1 mm. It should be kept in mind that these results apply to a position in real space roughly in the center view of each detector. Here, we found that the best fits were obtained near R=0.56 m for the top array and near Z=0.1 m for the outboard midplane array, but we cannot know exactly where the data fits the real emissivity profile best, in the case of the real measurements. A few other simulations were run, most of which had a smaller pedestal width (2-2.5 mm at the plasma midplane). They also support the findings summarized above.

10.3 Systematic pedestal asymmetries

Even though we have clearly found that the x-ray emissivity is far from constant on EFIT flux surfaces near the plasma edge, the analysis in Section 10.2 shows that we should still expect the inversions to yield results which have less than 15% systematic errors. Therefore, we can still perform detailed comparisons between the pedestals at the top of the plasma and the outboard edge. In particular, we can investigate if the pedestal asymmetries show any systematic trends with plasma parameters. We use the edge x-ray database to extract information about the pedestal parameters for a large number of plasma discharges.

10.3.1 Position asymmetries

One of the clearest trends identified in the database is shown in Figure 10-10. The figure shows a clear tendency for the difference in pedestal positions to increase with q_{95}. The difference in position is on average 6 mm at low q_{95} and increases to about 11.5 mm at high q_{95}. Because of the large number of points (more than 7000), there is some scatter in the points. In order to show the trend more clearly, averages over

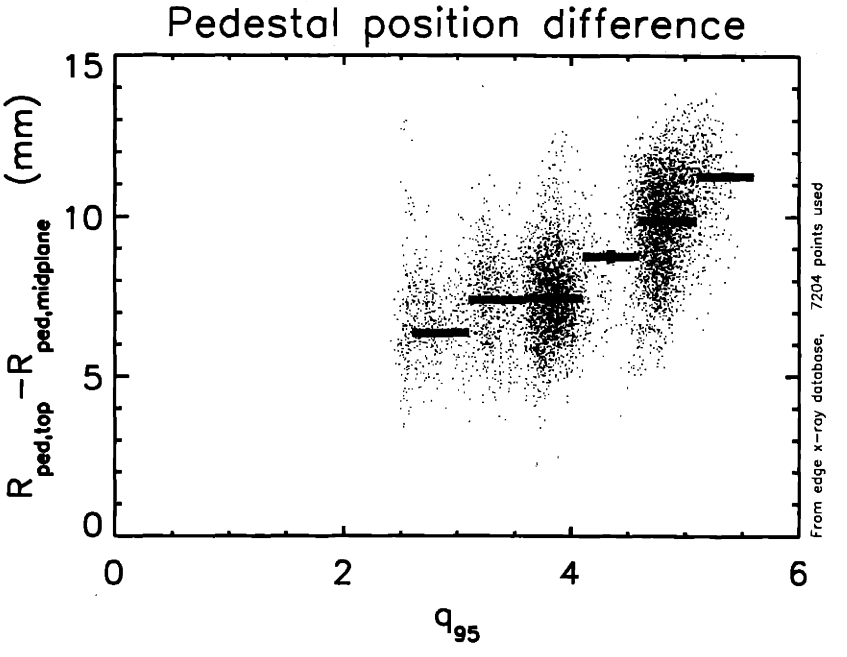

Figure 10-10: The difference between the soft x-ray pedestal position at the top of the plasma and at the outboard edge increases with q_{95}. In this plot we have used x-ray pedestal data from a large number of H-mode discharges, including both ELMfree and EDA H-modes. More than 7000 individual points are shown. In order to show the trend more clearly, we plot the binned averages as well as the individual points. The standard error of the mean for each bin is indicated by a vertical bar. The difference in location varies from 6 mm at low q_{95} to 11.5 mm at high q_{95}.

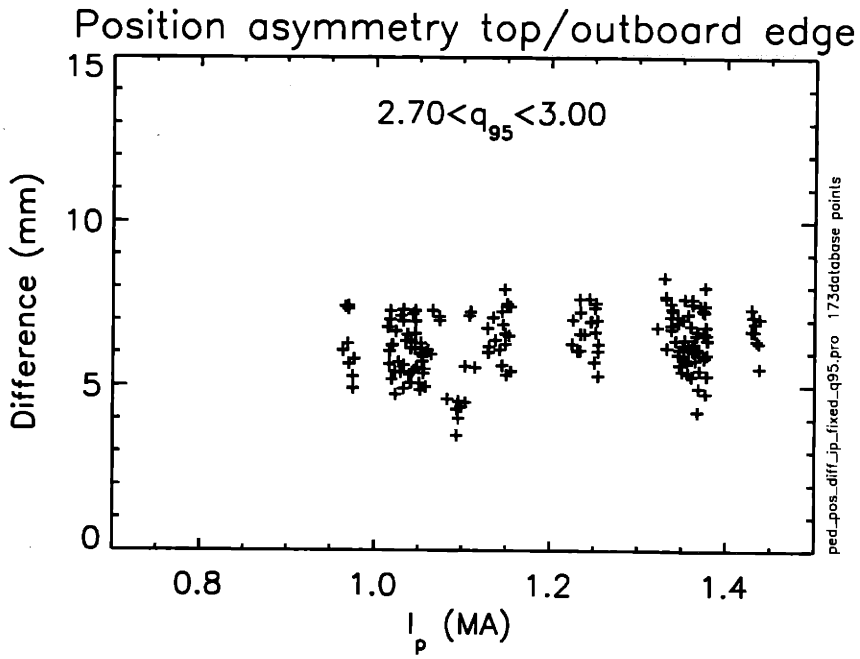

Figure 10-11: The difference in pedestal location shows no scaling with the plasma current for discharges with similar values of q_{95}.

different bins of q_{95} are shown in red. The large number of points ensures that the standard error of the mean of each bin is very small. We have used both EDA H-modes and ELMfree H-modes in this plot. Since q_{95} and I_p are approximately inversely proportional if the magnetic field is kept constant, one might suspect that there is also a correlation between the pedestal position difference and I_p, so the question arises if the relevant scaling parameter is q_{95} or I_p. The two parameters can be separated rather well in the database because of a number of ohmic H-modes at substantially lower toroidal fields which were produced in the 1999 run campaign. In Figure 10-11 we show the position difference as a function of I_p for a narrow range of q_{95} values. It is seen that there is no apparent scaling with I_p. Thus, the relevant scaling parameter is really q_{95}, not I_p. In Figure 10-12 we show $1/I_p$ versus q_{95} for H-mode discharges in the database. Most of the discharges fall on the curve which shows approximately a linear relationship between I_p and q_{95}. This is the curve corresponding to $B_T \approx 5.1$ T. The points above and to the left of this curve represent ohmic H-modes which had lower B_T values, allowing us to break the covariance between $1/I_p$ and q_{95}. These are the data points used in Figure 10-11 to rule out a significant dependence on I_p.

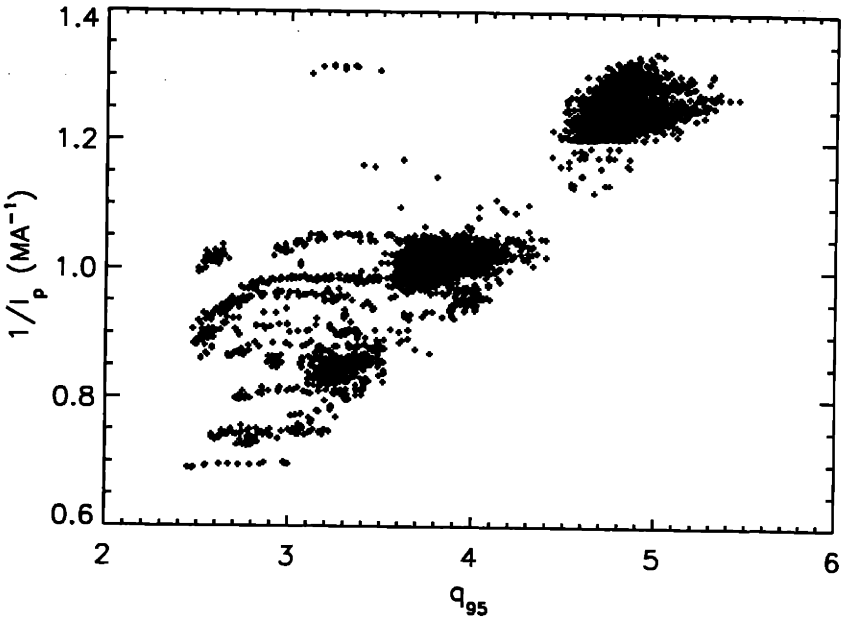

Figure 10-12: This figure shows the degree to which I_p and q_{95} are correlated for H-modes in the x-ray pedestal database. Most of the points line up on an approximately straight line (corresponding to a constant $B_T \approx 5.1$ T). The rest of the points represent ohmic H-modes at lower magnetic fields (and relatively low q_{95}), allowing us to break the covariance between $1/I_p$ and q_{95}.

10.3.2 Width asymmetries

In Section 4.4 we found a clear scaling of the pedestal width with plasma current, or edge poloidal field, in EDA H-modes. These measurements were made at the outboard edge just below the midplane, and we reproduce these results clearly with the new array which views the outboard edge just above the midplane. At the outboard edge we also reproduce the result that the pedestal width in EDA H-modes is wider than in ELMfree H-modes. However, the pedestal width at the top of the plasma does not seem to change between EDA H-mode and ELMfree H-mode, and it has no clear scaling with plasma current either. The pedestal width at the top is generally very close to 2 mm for a variety of different H-mode conditions. It does increase significantly during type III ELMy periods, however. In Figure 10-13 we show the pedestal widths in the two poloidal locations as a function of q_{95} in EDA H-modes, and it is clear that the widths scale differently. The width clearly increases with q_{95} at the outboard edge but no such tendency can be seen at the top of the plasma.

Figure 10-13: The pedestal width at the outboard edge clearly increases from about 2 mm at low q_{95} to about 5 mm at high q_{95}. The pedestal width at the top shows a weak tendency to decrease with q_{95}. There is no significant width asymmetry at low q_{95}, but there is more than a factor of 2 difference at high q_{95}.

At the top of the plasma, there is a weak tendency in the opposite direction, that is a weak tendency for the width to decrease with increasing q_{95}. The difference in width between the two locations is negligible at low q_{95}, but is more than a factor of 2 at high q_{95}. It should be noted that we have only included EDA H-modes in this plot, because there is not much of a width scaling in ELMfree H-mode in either location. Since there were very few EDA H-modes at magnetic fields much different from $B_t \approx 5.2$ T, we are not able to distinguish if the width asymmetry is determined by the value of q_{95} or I_p. However, we note that for the position asymmetry, it was demonstrated clearly that the relevant parameter is q_{95}, not I_p.

10.4 Pedestal character for different types of H-modes

It was observed with the first edge x-ray diagnostic that the soft x-ray emissivity pedestal at the outboard edge was generally significantly wider in EDA H-modes

than in ELMfree H-modes, especially at low current. Even wider pedestals were seen in type III ELMy H-modes. The new outboard edge diagnostic gives results which agree with these findings. Interestingly, the pedestal at the top of the plasma does not get wider in EDA H-mode. Typically, there is no clear change in the pedestal width at the top of the plasma even in cases where there is a clear increase in the pedestal width at the outboard edge of more than a factor of two. In some, relatively rare, cases, the pedestal width at the top even gets narrower when the plasma confinement mode changes from ELMfree H-mode to EDA H-mode, the opposite of what happens at the outboard midplane. For type III ELMy H-modes, the situation is different. When the plasma confinement mode changes into a type III ELMy H-mode, there is a large increase in the pedestal width at the top of the plasma, very similar to what is observed at the outboard edge. These points are illustrated in Figures 10-14 to 10-17. The measurements presented are all from one discharge, which had multiple transitions between ELMfree, ELMy and EDA H-modes.

10.4.1 Implications

One possible explanation for the x-ray pedestal width observations in EDA H-mode is that the fluctuations responsible for the enhanced diffusion of impurities through the transport barrier in EDA are localized to the outboard midplane region, ie. they are of a ballooning-like nature. This could be modelled by a poloidally varying edge diffusion coefficient, which would peak at the outboard midplane. This would be consistent with our observations, given the correlation between the edge diffusion coefficient D and the x-ray pedestal width found in Chapter 7. However, one should keep in mind that the parallel transport makes the physics complicated, and that there may be poloidal variations in the inward impurity pinch too. Since the soft x-ray pedestal width is large in both locations in type III ELMy H-mode, it could be modelled by a large diffusion coefficient which is poloidally uniform.

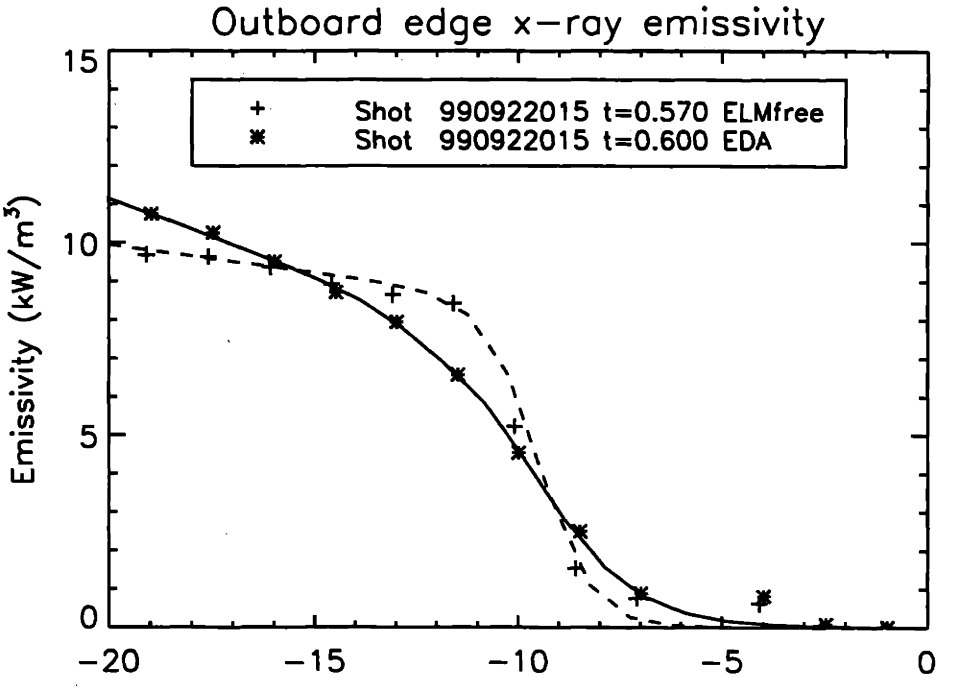

Figure 10-14: At the outboard edge, the soft x-ray pedestal width increases from 2.6 mm to 4.9 mm when the confinement mode changes from ELMfree H-mode to EDA H-mode

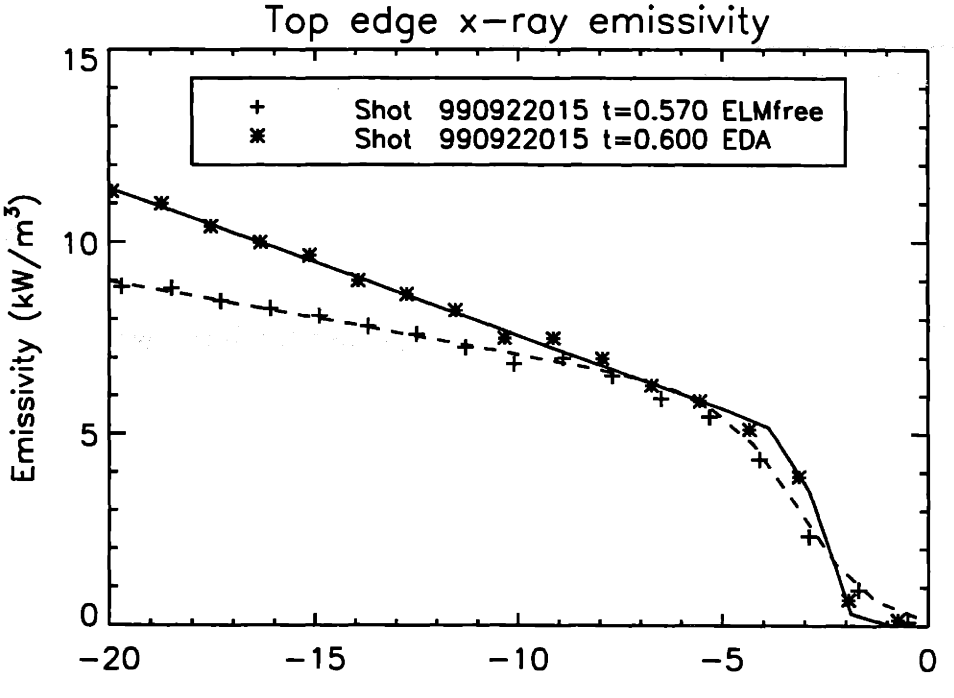

Figure 10-15: At the top of the plasma, the soft x-ray pedestal width decreases from 3.5 to 1.1 mm when the confinement mode changes from ELMfree H-mode to EDA H-mode. Such a large drop is unusual. Often there is no change.

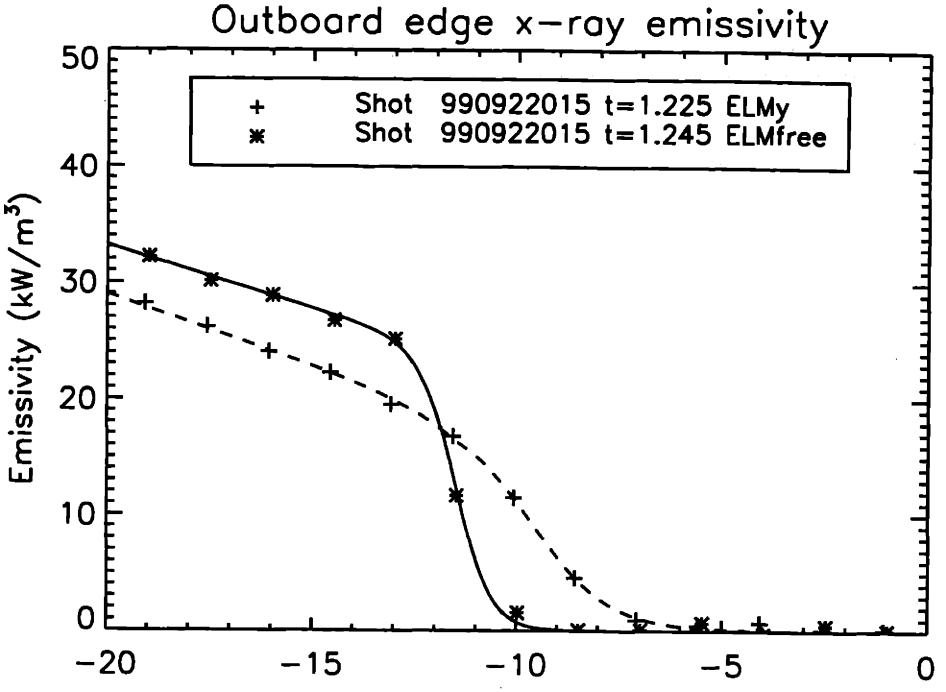

Figure 10-16: The soft x-ray pedestal at the outboard edge is significantly wider during a type III ELMy H-mode phase than during ELMfree H-mode. Here, the pedestal width is 3.8 mm during the ELMy phase and 1.7 mm during the ELMfree phase.

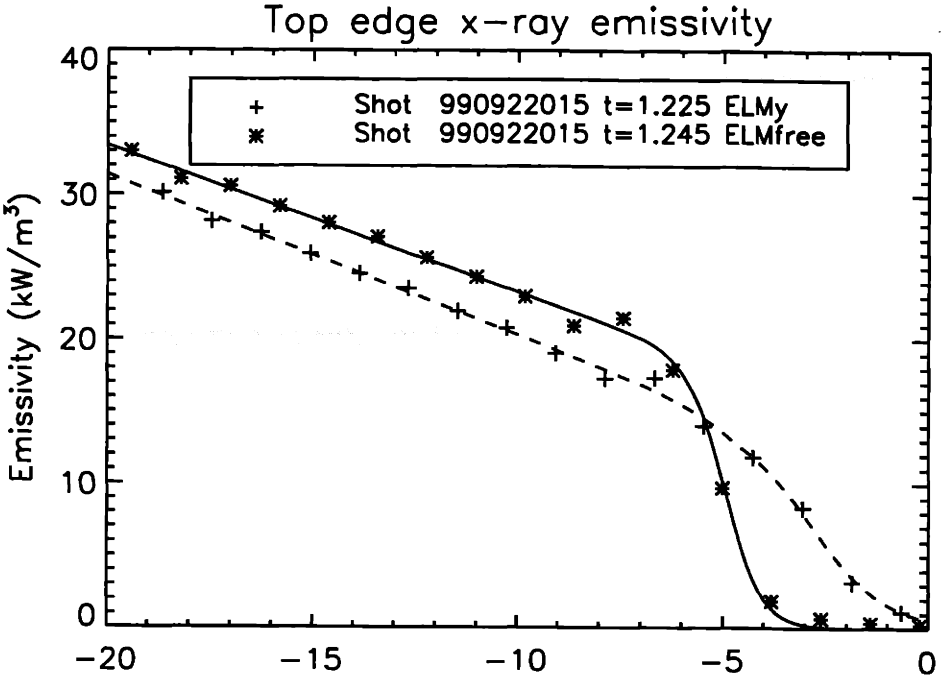

Figure 10-17: The soft x-ray pedestal at the top is significantly wider during type III ELMy H-mode than during ELMfree H-mode, just like at the outboard edge. Here, the pedestal width is 3.6 mm during the ELMy phase and 1.8 mm during the ELMfree phase.

10.5 H to L transitions and ELMs

One of the motivations for having two simultaneous measurements of the soft x-ray emissivity was to study if fast edge events such as ELMs and H to L transitions would show any poloidal asymmetries or a timing difference between the top and the outboard edge, indicating that the H to L transition or ELM at first was poloidally localized. In principle, timing differences down to 12 μs can be detected, even though the electronic amplification circuit has a 30 μs RC time constant, if the perturbation in question is rather large.

10.5.1 ELMs

Unfortunately, the giant ELMs observed in the 1997-1998 run campaign were not observed in the 1999 run campaign. It is unclear why this is the case. Smaller ELMs have been measured, and there does not seem to be a timing difference between these ELMs at the top and the outboard edge. However, since these ELMs did not cause large perturbations of the soft x-ray profiles, there could be a timing difference of less than 36 μs obscured by the random noise in the data. It is possible to rule out any timing differences larger than that.

10.5.2 H to L transitions

It was possible to obtain high quality observations of H to L transitions, and since the x-ray pedestal is destroyed during this transition, it was possible to find examples with very high signal to noise ratios, and timing differences down to 12 μs could be investigated. In Figure 10-18 we compare contour plots at the top and outboard edge of the emissivity *change* at the time of the H-L transition. In these contour plots, we plot the emissivity change relative to the emissivity at $t = t_0$, which is chosen about 80 μs before the H-L transition. It is seen that the emissivity profiles are quasi-steady state until the H-L transition. At the transition, the steep gradient region of the pedestal collapses first, and then the emissivity change propagates away from the steep gradient region both inward and outward. This is true at both pedestals,

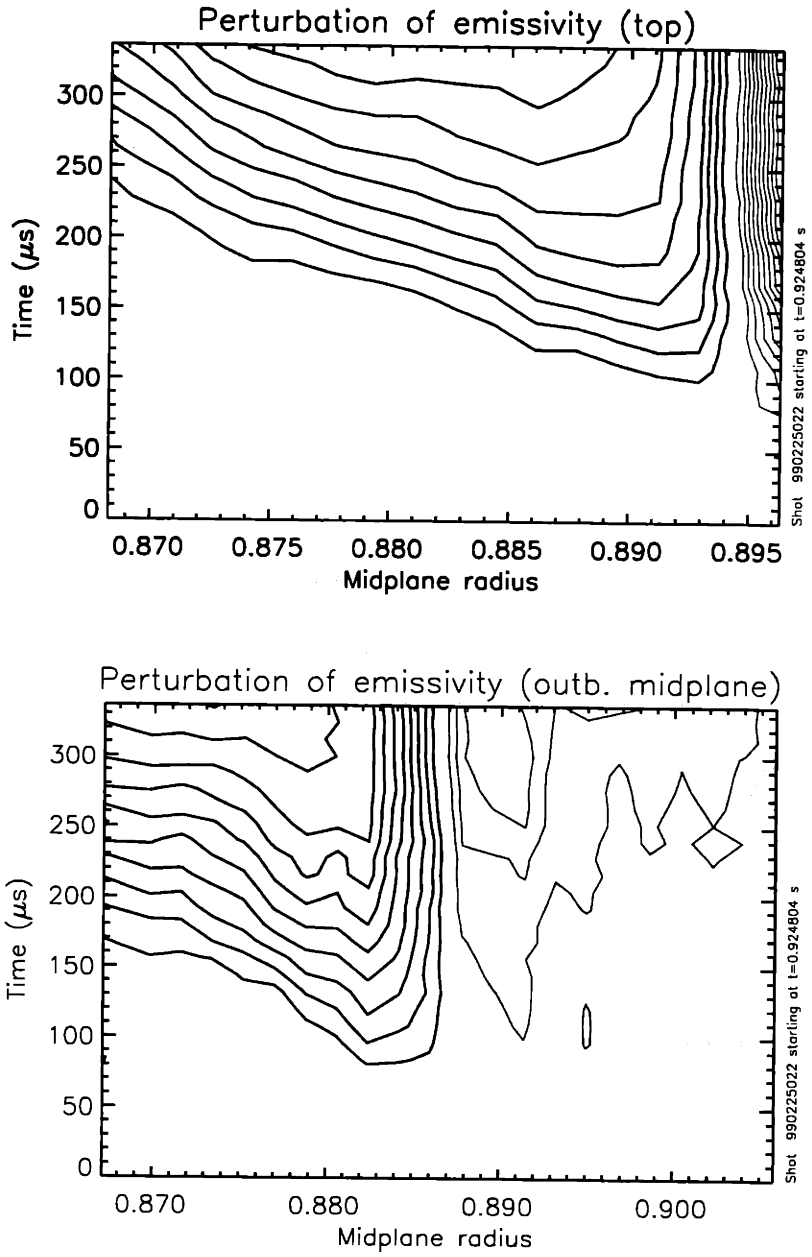

Figure 10-18: We plot contours of the change in emissivity compared to the emissivity shortly before the H-L transition at the top and the outboard edge. In both views the emissivity profile starts changing in the pedestal region, after which the change propagates inward and outward. On this plot it is not clear if there is a timing difference between the top and the outboard edge.

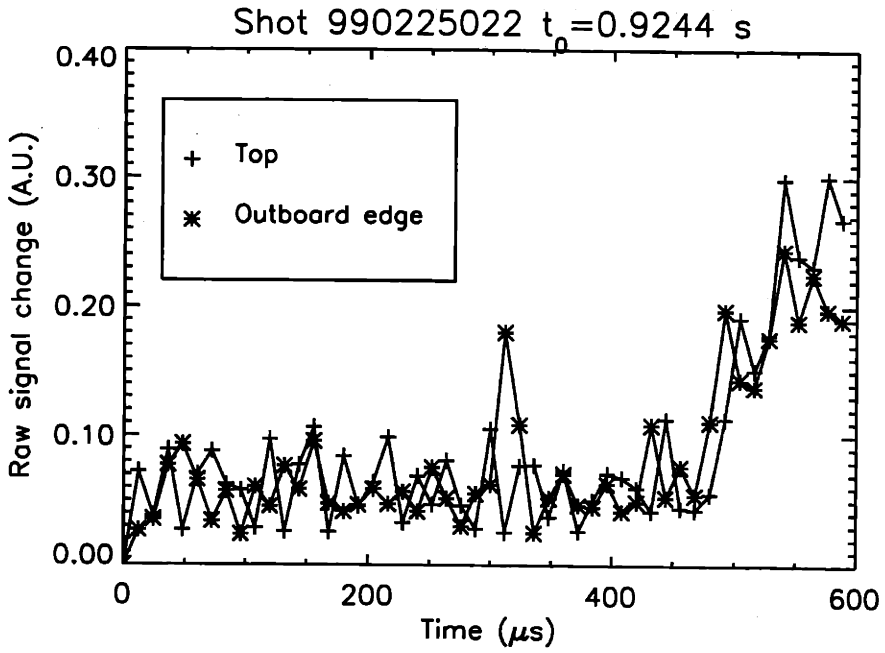

Figure 10-19: The time evolution of the raw signal changes for the two edge x-ray arrays shows the H-L transition rather clearly. The two arrays detect the transition within one time sample (12 μs) of each other, with the outboard array first.

and any timing difference between the transport barrier collapse is small, less than 40 μs. In order to get even better time resolution of the pedestal collapse, we use a more sophisticated method than simply comparing contour plots. We can measure the difference in the raw data from time sample to time sample in the following way:

$$\delta s^{\text{top}}(t) = \Sigma_{i=1}^{38} |s_i^{\text{top}}(t) - s_i^{\text{top}}(t - \delta t)| \tag{10.1}$$

where $s_i^{\text{top}}(t)$ denotes the signal on the i'th detector of array 2 (viewing the top of the plasma) at time t, and $\delta t = 12\,\mu$s is the sampling time. We define $\delta s^{\text{outboard}}(t)$ analogously. A slight detector to detector smoothing is applied at each point in time to reduce random noise, but no temporal smoothing can be applied as the time resolution is very important. The raw signals are used in this case rather than the inverted data because the raw signals are much less noisy. In Figure 10-19 we show the time evolution of s^{top} and s^{outboard} near the time of the H-L transition. We find that the timing of the pedestal collapse can be found within 1 time sample on both arrays. It seems that there is a delay of one time sample between the time where the pedestal starts collapsing at the outboard edge and when it starts collapsing at the

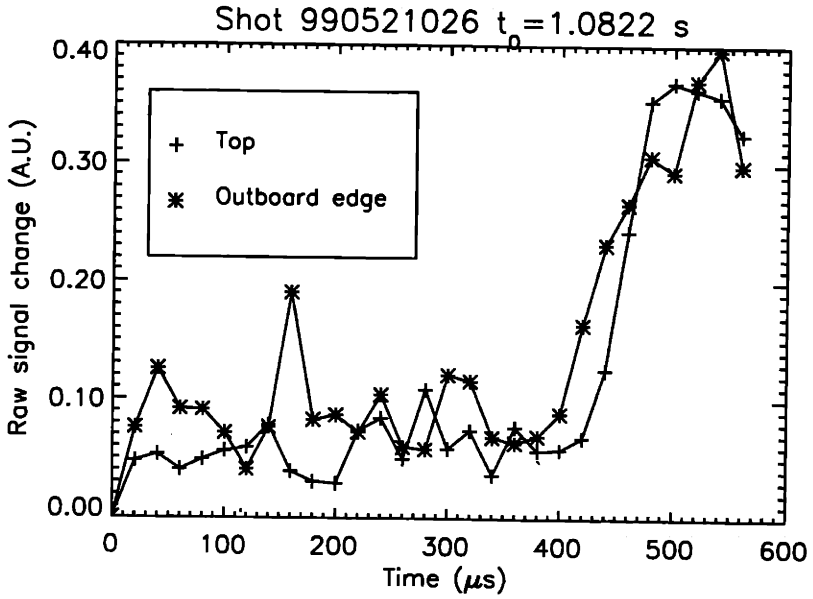

Figure 10-20: This shows an example where the x-ray pedestal collapse onset occurs first at the outboard edge, then at the top of the plasma. The sampling time is 20 μs.

top. This is just on the border of what can be resolved with the signal/noise of the data. In particular, there is a rather large spike on the outboard array before the transition, and this is probably due to noise rather than a real perturbation in the soft x-ray brightness. Therefore, we found H-L transitions with x-ray measurements at high time resolution and better signal/noise than the one found here. We found several examples where the timing difference, although still on the order of 1 or 2 time samples, appears to be real. We did not find a transition occurring first at the top of the plasma, only examples where the transition occurs first at the outboard edge, or where no timing difference was evident. We show two examples of such real H-L transition delays in Figures 10-20 and 10-21. In the example shown in Figure 10-21, the signal levels are high enough that the timing difference can be clearly seen in the time evolution of the inverted emissivity profiles. The difference becomes clearer if some modest spatial smoothing is applied, to reduce random spikes in the emissivity profiles. This smoothing does broaden the pedestal somewhat, but since we are concerned more with the timing difference than the exact width of the pedestal, this is not a problem. In Figure 10-22 we show the emissivity profiles at 4 consecutive time samples, two immediately before and two immediately after the

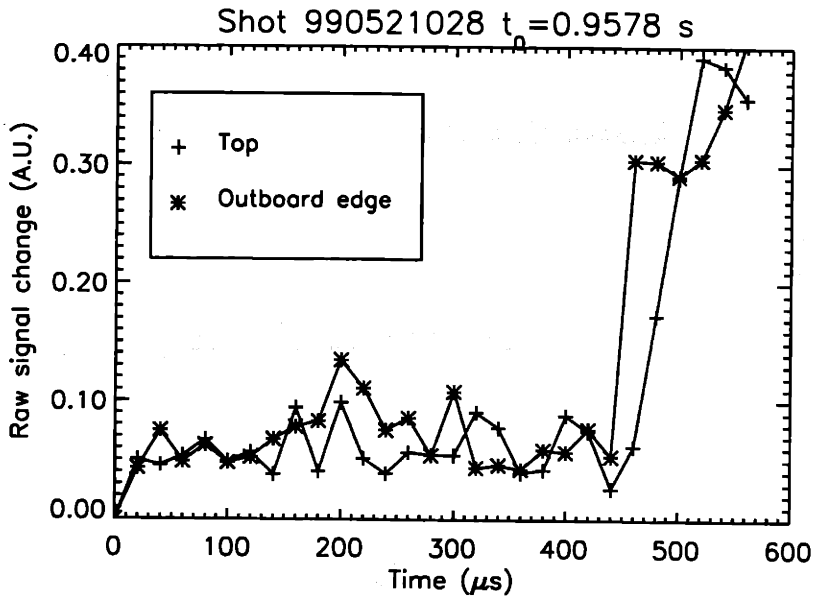

Figure 10-21: Another example of the x-ray pedestal collapse starting at the outboard edge before it starts at the top of the plasma. The sampling time is 20 μs.

emissivity profile starts changing at the outboard edge. It is seen that the onset of the pedestal collapse is delayed by at least one, and possibly two time samples at the top of the plasma compared to the outboard edge.

10.5.3 Implications of the timing difference at the H-L transition

Although the timing difference observed between the outboard edge and the top of the plasma is only on the order of one or two time samples, it is still significant. It implies that whatever destroys the H-mode transport barrier is a mode which occurs at the outboard edge before it occurs at the top of the machine. The most likely explanation is that the mode is of a ballooning-like character, ie. it is localized to the outboard midplane, where the curvature is unfavorable. Such a mode could cause large transport near the outboard midplane of the plasma edge without significantly perturbing the transport away from the outboard edge, causing a collapse of the pedestals at the midplane. Once the collapse starts occurring at the midplane, the poloidal asymmetry thus created (in the bulk plasma density and temperature as well as in the impurity density) will drive rapid parallel transport. Thus, one should

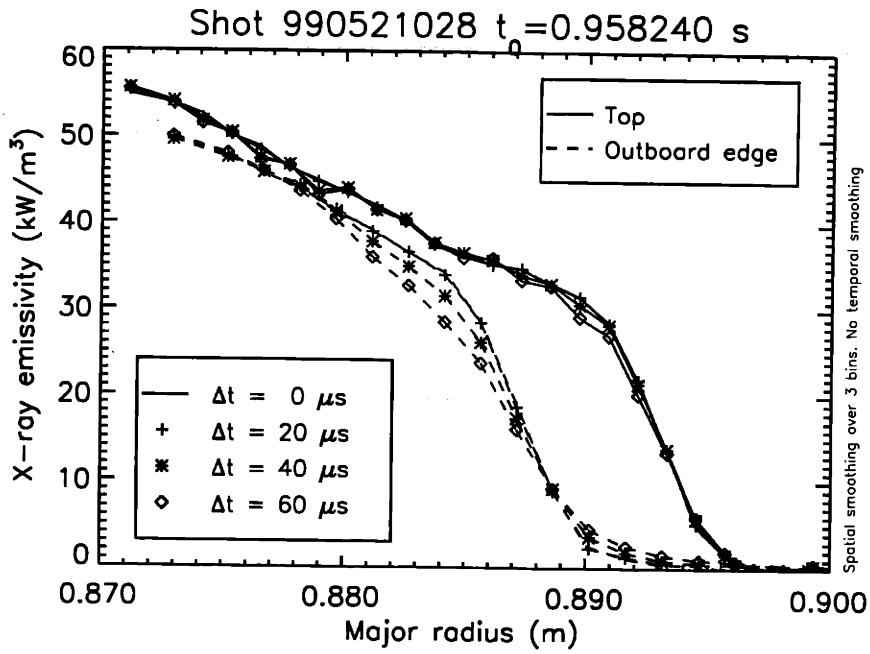

Figure 10-22: Four consecutive time samples, each separated by 20 μs, show the emissivity profile at the outboard edge visibly flattened at $\Delta t = 40\,\mu$s while the emissivity profile at the top of the plasma is practically unchanged. At $\Delta t = 60\,\mu$s, the emissivity profile is already rather flat at the outboard edge but the emissivity profile is barely perturbed at the top of the plasma.

expect to see an effect on the whole flux surface shortly after the onset of the mode at the outboard midplane. Therefore, we must compare the observed timing delay of 10-20 μs with parallel transport times for impurities and bulk plasma. The parallel impurity transport is complex, as the steady state asymmetries described in this thesis clearly demonstrate, but we can still investigate the time scale over which a significant perturbation from the steady state conditions can propagate from the outboard edge to the top of the plasma. We assume that such a perturbation will propagate along a field line at the impurity sound speed, or the thermal speed of the impurity. These are roughly equal when $T_e \approx T_I$. As a characteristic velocity of propagation along the field lines we take the parallel velocity of a thermal fluorine ion at 100 eV temperature, which is approximately 23 km/s. The parallel distance between the poloidal region of the plasma viewed at the upper outboard edge with array 4 to the top of the plasma, viewed by array 2, can be found by tracing a field line from the center view of array 4 to the top of the plasma. We have done this for the EFIT equilibrium near the H-L transition for shot 990521028, and find that the parallel connection length

between the two poloidal regions is about 1.5 m. This number depends on exactly which parts of the top view that we require to be reached by the field line. Assuming that impurity perturbations travel at approximately 23 km/s along a field line, we find that the time it takes for the impurity perturbation to travel between the two views is around 65 μs. This means that on time scales of 20 μs or less, there is no direct communication between the impurities at the outboard edge and the top of the plasma. The time delay of 20 μs of the x-ray emissivity at the top of the plasma therefore appears to be too small to be caused directly by parallel impurity transport. However, the bulk plasma can respond much quicker along a field line. Clearly the bulk plasma is heavily affected by the H-L transition, so if this transition occurs at the outboard midplane first, the change in bulk plasma density will propagate along the field lines. We assume that this change will propagate at the ion acoustic velocity, since the electrons will have to drag the bulk (deuterium) ions with them in order to maintain quasi-neutrality. Again, we assume electron and ion temperatures of 100 eV, and estimate the ion acoustic velocity to be $v_{ia} = \sqrt{T_e + 3T_i/m_D} \approx 140$ km/s [3]. At this velocity, the propagation time is 11 μs, which is close to the timing difference which we observe. If we assume instead a temperature of 200 eV, which is also a typical temperature in the pedestal region of an ohmic H-mode, we arrive at timing differences which are a $\sqrt{2}$ lower, ie. 46 μs for the direct impurity response delay, and 7 μs for the direct bulk plasma response. It follows that the flattening of the soft x-ray profile at the top of the plasma due to parallel transport driven by the flattening of the impurity density pedestal at the midplane could potentially be causing this timing delay, although the timing delay observed is somewhat smaller than these time scales. It is also possible that it is due to either the mode propagating from the midplane to the top, or due to the parallel transport of the bulk plasma. One should recall that our one-dimensional transport analysis showed that the impurities are confined in H-mode (at least at the midplane) by a strong inward pinch driven by the bulk plasma density gradient. It makes sense therefore that the impurity density pedestal starts flattening as soon as the bulk density pedestal starts flattening, and this will happen on time scales faster than those of parallel impurity transport. Of

course there is also the possibility that part of the decrease in x-ray emissivity is due to the direct decrease of electron density, since the x-ray emissivity is proportional to the electron density. At present, there are no electron density diagnostics which have millimeter spatial resolution and microsecond time resolution simultaneously, as the soft x-ray arrays do. Therefore we cannot distinguish between effects of n_e and effects of n_I for the H-L transition. In addition, impurities may be dragged along with the bulk plasma perturbation, since the ion-impurity friction is very large (mean free path on the order of 5 cm, and $\tau_{Ii} \approx 2\,\mu$s, as discussed in Section 6.1.2). This would lead to an impurity perturbation which propagates at or near the the velocity of the bulk ion perturbation. Since the x-ray emissivity is not very sensitive to changes in T_e, the parallel electron transport of heat (which can be very rapid) is not expected to have an effect on the soft x-ray emissivity.

10.6 Comparison between ohmic and RF heated H-modes

ICRF[2] heating is the largest source of plasma heating available on Alcator C-Mod. In the 1997-1998 run campaign 3.5 MW of RF heating was available with high reliability. In the 1999 run campaign transient RF heating of up to 5 MW was achieved, and in the future these levels and higher will be reached with higher reliability. The RF antennas have to couple this power at the edge plasma to the "fast-waves" and in the standard heating scenario on Alcator C-Mod, the fast magnetosonic waves travel to the center where they are absorbed at the cyclotron resonance of the hydrogen minority species, typically in a deuterium plasma. In the early days of RF heating (on other machines), significant edge perturbations were induced by the RF antennas, due to the formation of rectification sheaths. Such effects are now suppressed by the use of Faraday shields and by avoiding monopole antenna phasing. However, it is still an open question if the RF wave or antenna sheath changes the character of the

[2]ICRF stands for Ion Cyclotron Range of Frequencies.

H-mode transport barrier. If so, one might expect the soft x-ray pedestal to show differences between ohmic H-modes and RF-heated H-modes. With the soft x-ray diagnostics, it is possible to detect differences of 1-2 mm in pedestal width, or about 2-3 mm in pedestal position (with respect to the separatrix). Therefore, we are able to determine if there are any significant effects of the RF heating on the impurity transport. Ohmic H-modes usually can only be achieved at low q_{95}. This is because the only heating source is the ohmic heating, so one has to have a rather large plasma current. At the same time, empirical observations show that the H-mode power threshold increases roughly linearly with the toroidal magnetic field strength. Thus, in order to exceed the H-mode power threshold without auxiliary heating, one must run at low q_{95}, since q_{95} is proportional to B_t/I_p. This means that the comparisons to RF heated H-modes are restricted to comparisons at low q_{95}.

10.6.1 Results

During the 1999 run campaign, many good quality, reproducible ohmic H-mode discharges were produced, which made it possible to conclude rigorously that we find no systematic or significant differences in the pedestal width and height, between ohmic H-modes and similar RF heated H-modes. Therefore, it appears that the RF heating does not perturb the H-mode transport barrier. An example illustrating this point is shown in Figures 10-23 and 10-24. In order to make a direct comparison, the ohmic discharge was chosen to have a toroidal magnetic field at 5.4 T, the plasma current (which was ramping down at the time) was 1.21 MA. Almost identical conditions (B_t = 5.2 T, I_p = 1.18 MA) were used in the other discharge in the figures, but this one had 2 MW of RF heating. No significant difference is observed between the pedestals. There are many plasma discharges where the RF heating is terminated, but the plasma remains in H-mode for some time after the RF turns off. In these cases there is no change in the pedestal character at the time when the RF turns off. In addition, there are a few examples where there is a transition into an ohmic H-mode, and the RF switches on during the H-mode. We see no change in the pedestal character in these cases either. Both of these observations also support our conclusion

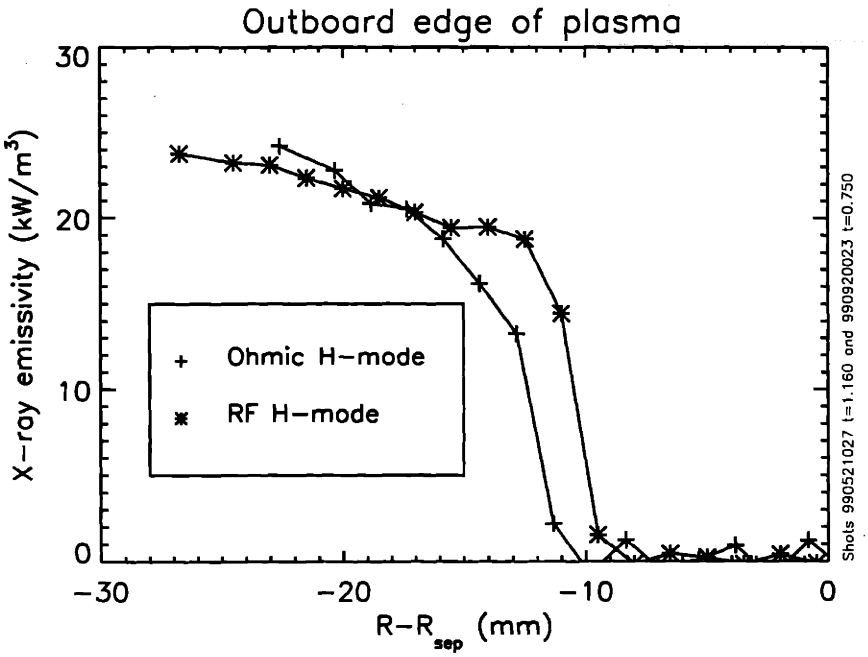

Figure 10-23: A comparison between soft x-ray pedestals at the outboard edge for an ohmic H-mode and an RF heated H-mode. The difference in position with respect to the EFIT separatrix is about 2 mm, which is less than the uncertainty in the EFIT separatrix position, so it is probably not significant. The widths are approximately the same for the two discharges, which had similar currents and toroidal magnetic fields. The RF heated H-mode had 2 MW of RF heating.

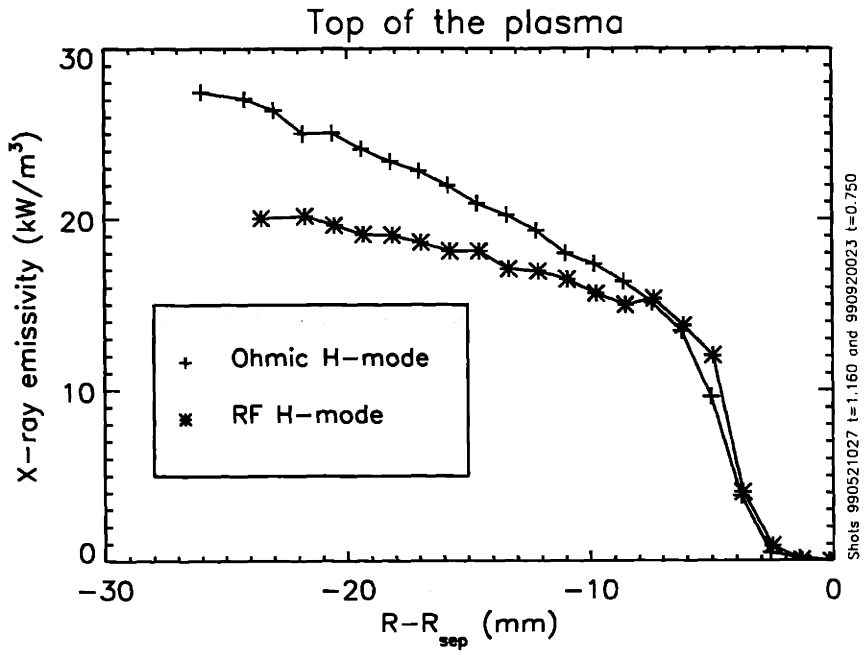

Figure 10-24: The RF heated H-mode soft x-ray emissivity pedestal is virtually identical to the ohmic H-mode pedestal at the top of the plasma. The specific time slice for the RF heated discharge was chosen in order to make the heights of the two pedestals the same.

that the RF heating does not perturb the impurity transport barrier. The transport barrier is affected by the extra heating, which generally results in higher pedestal temperatures, and usually the soft x-ray emissivity pedestal is higher also. However, it does not seem to have any other effect. These findings do not rule out that the RF wave may have an effect on the scrape-off layer, since the soft x-ray measurements only provide information about the edge plasma inside the last closed flux surface, while the antennas are typically 1-2 cm outside the separatrix.

10.7 Measurements of impurity injections

Injections of CaF_2 should increase the signal levels on both arrays, since we know from modelling that the fluorine radiates soft x-rays efficiently at the edge, and in fact the largest contributor to the signals is from fluorine in most H-mode discharges. We do in fact see clear increases in the soft x-ray emissivity. The injections are small enough that they do not affect the background plasma, so the increases in soft x-ray emissivity are due to the increased fluorine density, rather than changes in electron density or temperature. Modelling of the calcium line radiation and recombination radiation suggests that the rise in calcium density does not contribute significantly to the rise in soft x-ray emissivity. The inferred increases in fluorine density are in good agreement with inferred increases in the core density of calcium from x-ray spectroscopy [43].

10.7.1 Transient asymmetries

In addition to the clear asymmetries seen in the steady-state x-ray emissivity pedestals, large transient asymmetries are also seen during injections of CaF_2 in H-mode discharges. In Figure 10-25 we show the time evolution of the two profiles around the time of a CaF_2 injection. The laser pulse which ablates the CaF_2 occurs nominally[3] at t=0.900 s. Shortly after the injection, a distinct "bump" appears on the emissivity

[3]There is some uncertainty in the exact injection time.

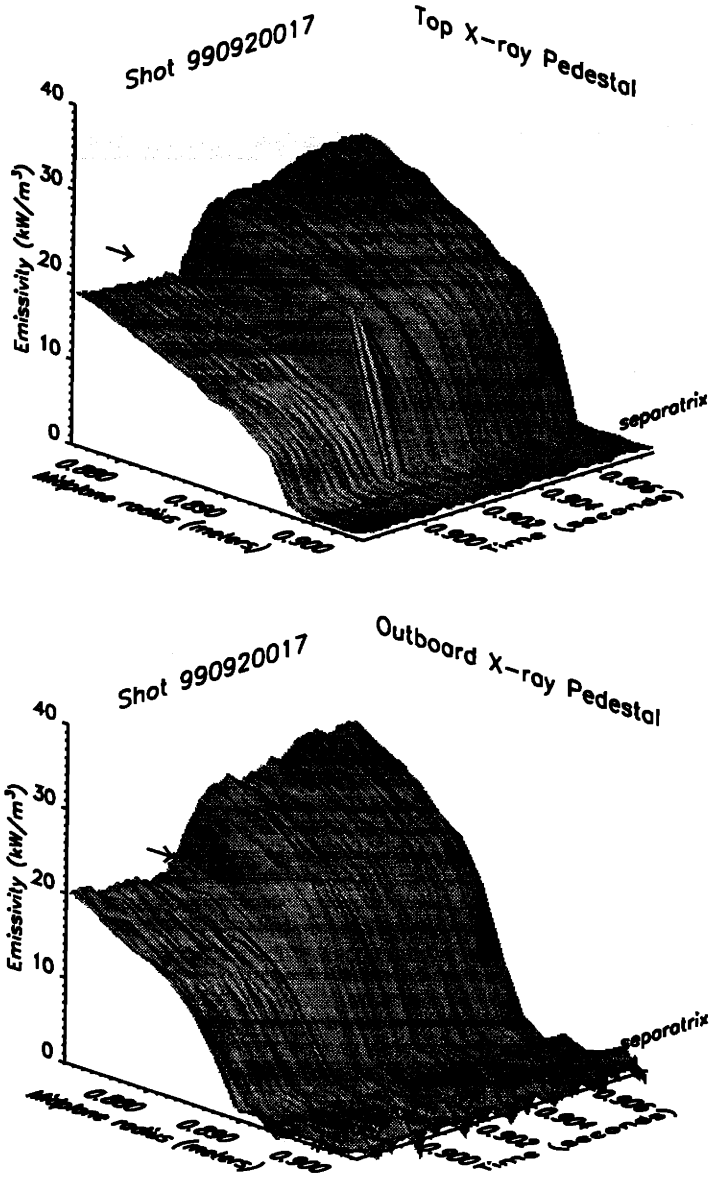

Figure 10-25: The time evolution of the soft x-ray emissivity at the top and outboard edge of the plasma. At the top, a transient bump appears following the injection of CaF_2. In black, we outline a timeslice where the bump is very clear at the top of the plasma, but there is no effect at the outboard edge yet. A gradual rise in overall emissivity is seen following the injection.

profile at the top of the plasma. At the same point in time, there is no effect on the emissivity profile at the outboard edge. The emission "bump", or radiation shell, rises to a peak in about 200-300 μs, and is followed by a gradual rise in emissivity across the whole pedestal. This gradual rise is seen simultaneously at the top and the outboard edge. The transient bump is likely due to the incoming fluorine. Modelling of the charge states of fluorine suggests that the bump could be caused by radiation from a line originating from inner-shell excitation of lithium-like fluorine (F^{+6}). The spatial localization and the characteristic rise and fall times on the order of 200 μs are consistent with those of the density of F^{+6} calculated by the MIST code, simulating the time evolution of an injection of atomic fluorine at the edge of an H-mode plasma. However, the MIST code assumes poloidal symmetry, so it cannot explain why the transient bump is seen only at the top of the plasma. We will discuss possible explanations of this asymmetry in Section 10.7.2. The injected fluorine is transported to the core plasma, and then diffuses out to the edge region, resulting in the gradual rise of x-ray emissivity seen on both arrays just after the bump disappears. Details of the whole process can be seen in Figure 10-26.

10.7.2 Explanations for the transient bump

The CaF_2 is injected over a rather large poloidal and toroidal part of the outboard plasma edge near K-port, whereas the soft x-ray measurements are done between C and D port. A large fraction of the field lines connecting the region of injection near K-port to the region of x-ray measurement end up in the field of view of the top array for a large range of q_{95} values. A simple estimate of the field line rotation based on q_{95} would indicate that at high q_{95}, a large fraction of the field lines where the injection occurs would be in the view of the outboard edge array. However, mapping of the actual field lines shows that the field lines do rotate out of the view of the outboard edge array going from K-port to C or D port. This is because the poloidal field is much stronger (by at least a factor of two) at the outboard edge than at the top or the bottom of a flux surface just inside the separatrix. This means that if one follows a field line, it takes relatively short time to move from the outboard edge to the top

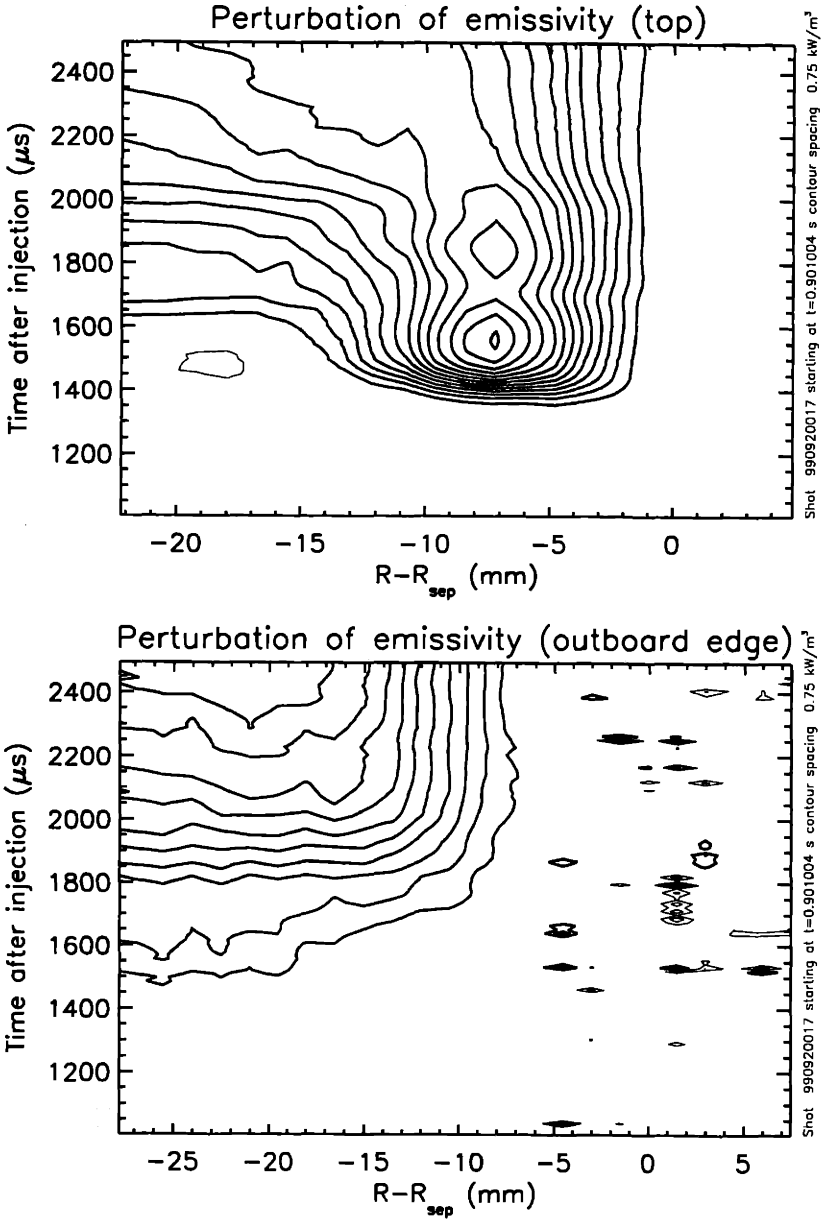

Figure 10-26: Above, we plot the changes in the emissivity profiles compared to the profiles before the CaF_2 injection. The emissivity bump appears on the top array well before any effect is seen at the outboard edge. This is followed by a gradual increase in x-ray emissivity across the profile in both locations. At the outboard midplane, it can be seen that the gradual increase in emissivity comes from the core of the plasma and diffuses to the edge. The contour spacing is 0.75 kW/m^3 on both plots. Thin lines indicate negative contours.

of the plasma, but relatively long time to rotate over the top and to the inboard edge. Therefore, it turns out that even for a large range of q_{95} values, a large fraction of the field lines of the injection will be in the view of the top array, but none of them will be in the view of the outboard edge array. Although the size of the bump varies from injection to injection, the bump always appears just inside the x-ray pedestal for all values of q_{95}, and shows no tendency to move inward at the very lowest q_{95} values. We illustrate this point in Figure 10-27, where we compare the "bump" following an injection into a rather low edge q (I_p=1.35 MA, q_{95}=2.78) discharge, with an injection on a large q_{95} discharge (I_p=0.79 MA, q_{95}=4.74). The two bumps appear to be rather similar, despite the large difference in q_{95}. Because of the field line geometry, this could be consistent with a simple parallel propagation of the injected impurities. It is also consistent with a situation where the injected fluorine gets swept to the top of the plasma, and then stays, rather than following the field lines it was injected on. This would be expected from the physical picture explaining an up-down impurity asymmetry, as discussed in Section 11.3.2.

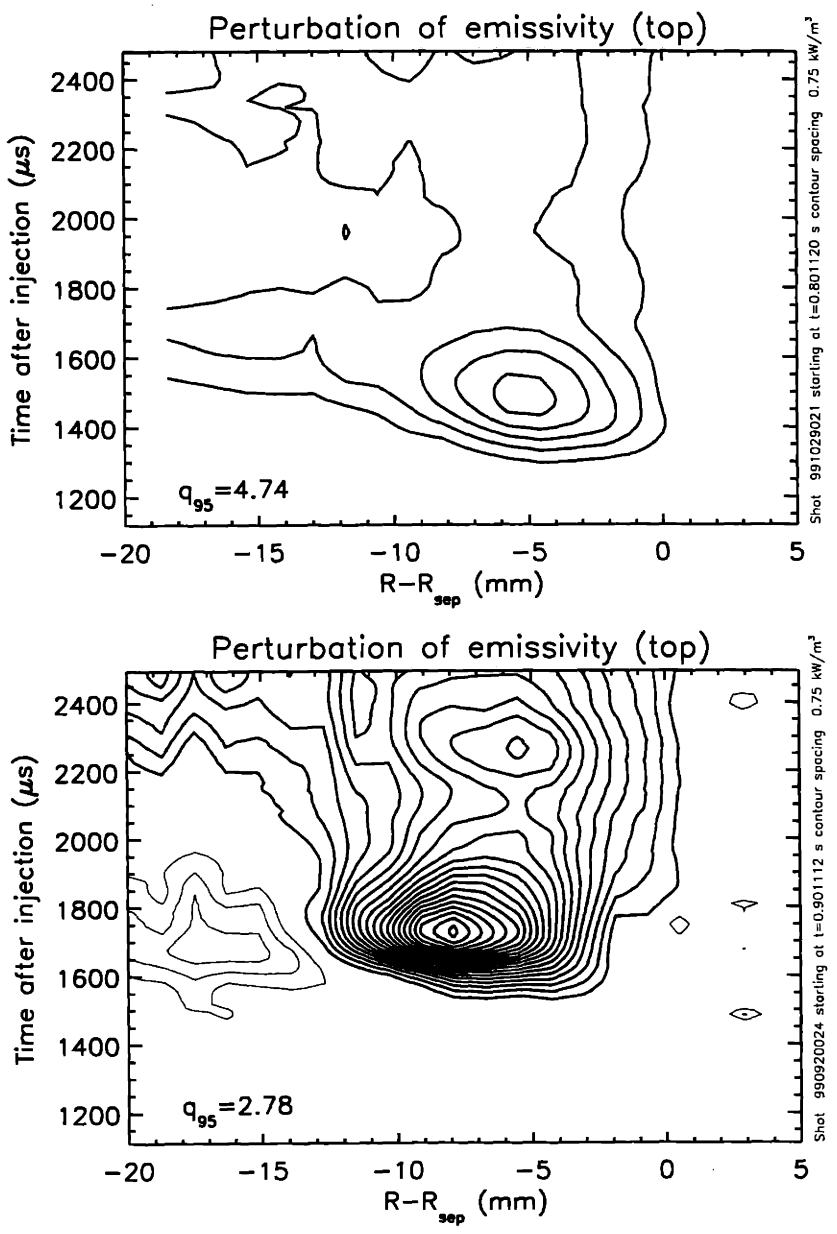

Figure 10-27: A comparison between the bumps following injections into two plasmas with very different values of q_{95}. The top contour plot shows the emissivity change after an injection in a q_{95}=4.74, I_p = 0.79 MA H-mode. The bottom contour plot shows the emissivity change after an injection into a q_{95}=2.78, I_p=1.35 MA H-mode. Both discharges had 2 MW of RF heating. Positive contours are thick, negative contours are thin. The contour spacing is 0.75 kW/m^3 in both figures.

Chapter 11

Discussion of the poloidal asymmetries

One of the most important findings of this thesis are the considerable asymmetries in the soft x-ray pedestal position and width between the outboard edge and the top of the plasma. Although it was well-known that there were moderate asymmetries in the soft x-ray emissivity [16], the asymmetries seen here are very large - easily a factor of 30 on the flux surfaces which are inside the pedestal at the top of the plasma and outside the pedestal at the outboard edge. Such large asymmetries clearly require an explanation. In this Chapter we will discuss several different possible explanations for the asymmetries we have seen, and discuss ways to find out which explanation is correct.

11.1 EFIT mapping and diagnostic position errors

11.1.1 Diagnostic position errors

Since the most prominent asymmetry between the soft x-ray pedestals at the outboard midplane and the top of the plasma is the difference in the pedestal location, it is only natural to suspect that perhaps the spatial location of the soft x-ray arrays is not accurately known. However, the spatial calibration of these arrays was done very

carefully and with 1 mm accuracy, so this cannot explain the differences in location of the pedestals of 5-15 mm which we observe. The location of the outboard edge array was measured in two different ways, which agreed within 1 mm. Other edge diagnostics have had considerable uncertainties in their positions but recent accurate calibrations have been made to the level of 2-3 mm for both the visible continuum diagnostic and the edge Thomson scattering diagnostic.

11.1.2 EFIT mapping errors

We rely on the EFIT flux surface reconstructions, not only for the inversion of raw data to emissivity profiles but also to map the measurements from real space to the plasma midplane, so we can compare the x-ray emissivity on the same flux surface. Thus, if the EFIT flux surfaces are significantly different from the real flux surfaces, we will see an apparent asymmetry on the EFIT flux surfaces even if the x-ray emissivity is constant on the real flux surfaces. Indeed there does seem to be an EFIT mapping problem, since probes at different poloidal locations see the steep rise in electron density on flux surfaces which are about 5 mm apart at the plasma midplane. It is usually believed that there can be no significant pressure gradient along a field line, so one can try to line up the pressure profiles measured at different poloidal locations to estimate what the mapping error is. For a long time it seemed that there were large discrepancies between the electron density pedestal location measured at the top of the plasma by the edge Thomson scattering system, and the electron density pedestal measured at the midplane by the visible continuum diagnostic, on the order of 10 mm. However, recent highly accurate calibrations of the absolute positions of these diagnostics have reduced the discrepancies to a few mm. The spatial locations of the reciprocating probes are calibrated to a few mm accuracy, and they still indicate that there is about 5 mm mapping error between the upper midplane and the divertor region. If there is a 5 mm mapping error between the top and the outboard edge, then this does reduce the actual x-ray emissivity pedestal asymmetry somewhat, but at high q_{95} we measure an average difference in pedestal location of more than 11 mm, so even with a mapping error of 5 mm, there is still a real asymmetry of at about 6

mm. In addition, the large asymmetries seen in the soft x-ray pedestal width at high q_{95}, which are more than a factor of 2, cannot be explained by an EFIT mapping error. If the width difference observed were due to a flux surface mapping error, it would imply that the flux expansion from the outboard midplane to the top of the plasma should be very close to 1 rather than at least a factor of two, which the EFIT equilibrium indicates. So if there is no real asymmetry in width, high q_{95} EDA H-mode plasmas have no flux expansion from the outboard edge to the top. This could perhaps be the case in a circular cross section tokamak plasma, but in the elongated plasmas in Alcator C-Mod this is impossible. In addition, any error in flux expansion implies an error of equal size in the poloidal magnetic field derived by EFIT. So if the flux expansion calculated by EFIT is off by a factor of 2, then the poloidal magnetic field is also off by a factor of 2. This seems highly unlikely. So although there are mapping errors, they can only explain part of the asymmetry. It must be concluded that there are real, and very large, asymmetries in the soft x-ray emissivity between the outboard edge and the top of the plasma, in the H-mode transport barrier region.

11.2 Bulk plasma asymmetries versus impurity density asymmetries

Since there are real poloidal asymmetries in the soft x-ray emissivity, there must be poloidal asymmetries in either impurity density, electron density, or electron temperature. Since electron thermal transport is very rapid along field lines, it seems unlikely that there can be large asymmetries along the field lines in electron temperature. Also, any significant gradients in plasma pressure along field lines would lead to large and rapid flows along the field lines until the pressure gradients disappear. If one therefore assumes that electron pressure has to be almost constant on a field line as well, then it follows that even the electron density must be rougly constant on a field line. However, near the separatrix, the parallel connection length becomes very large. In particular, at the x-point, the parallel connection length is

infinite. Therefore, there may be some poloidal asymmetry in the electron and ion density or temperature near the separatrix, in particular near the x-point. Recent two-dimensional simulations of a diverted tokamak plasma show that there can be asymmetries of about a factor of 2 in ion density and temperature on flux surfaces very close to the separatrix[1], between the x-point region and the outer midplane [40], [41], [42]. However, we see asymmetries in the soft x-ray emissivity in H-mode of a factor of 30-100, so there must be much larger asymmetries in the impurity density than in the bulk plasma parameters. In fact, as we shall discuss in the following, there are both theories and previous experiments which support that there can be large poloidal asymmetries in the impurity density of medium and high Z impurities.

11.3 Up-down impurity density asymmetry

There are several arguments supporting the notion that the impurity density asymmetry we have measured is an up-down asymmetry, in the sense that impurities tend to accumulate at the top of a particular flux surface, and tend to be depleted at the bottom of the flux surface. An up-down asymmetry would explain the pedestal asymmetries we observe. In the region from a few mm inside the separatrix to about 10 mm inside the separatrix, we infer a very high impurity density from the soft x-ray emissivity at the top of the plasma, but the impurity density is very low on the same flux surface at the outboard edge, so on these flux surfaces, there is definitely a top-outboard impurity density asymmetry, as one would expect if there is a strong top-bottom asymmetry.

11.3.1 Previous experimental measurements of an up-down asymmetry

Perhaps the strongest piece of evidence supporting that we are observing an up-down asymmetry is that such an asymmetry has been clearly demonstrated in Alcator C-

[1]Between the 99% and 100% flux surface

Mod L-mode discharges for the density of hydrogenlike argon (Ar^{+17})[44]. Just as observed in the soft x-ray measurements, the largest asymmetry occurred very close to the plasma edge, where asymmetries as large as a factor of 10 (defined as the ratio of the argon density at the top to that at the bottom on the same flux surface) were observed. The asymmetry changed sign (the argon ions collected at the bottom) when the magnetic field was reversed. This is a very important observation.

11.3.2 A neoclassical theory predicting an up-down asymmetry

A neoclassical theory has been proposed [45], which explains how up-down asymmetries in impurity density can be driven by neoclassical flows of the bulk ions. The basic physical principle is related to the effects of the ∇B drift. In the standard magnetic field configuration in Alcator C-Mod, the ∇B drift for ions is downward, and upward for electrons. On flux surfaces near the plasma edge, where there is a large density gradient, this drift leads to a depletion of ions at the top of the flux surface, and an accumulation of ions at the bottom of the same flux surface. Mathematically, this follows from the continuity equation, which is (ignoring parallel transport for now):

$$\frac{\partial n_i}{\partial t} = -\nabla \cdot (n_i \mathbf{v}_{\nabla B}) = -\nabla n_i \cdot \mathbf{v}_{\nabla B} \tag{11.1}$$

This term is negative at the top, where the density gradient and the ∇B drift are in the same direction, near zero at the midplane, where they are approximately perpendicular, and is positive at the bottom of the flux surface, where the density gradient and the ∇B drift are in opposite directions. The impurities are also ∇B drifting down, but their ∇B drift velocity is $1/Z$ smaller, so for the sake of simplicity, we assume that it is a small effect for the high charge states of fluorine and neon. Now this buildup cannot occur to any large degree since the field lines connect the bottom and the top of the plasma; the ions start flowing along the field lines from the bottom to the top of the plasma. This is known as the Pfirsch-Schlüter return flow [28], citePfirsch. In this way, a dynamic steady state is achieved for the ion flow. A schematic

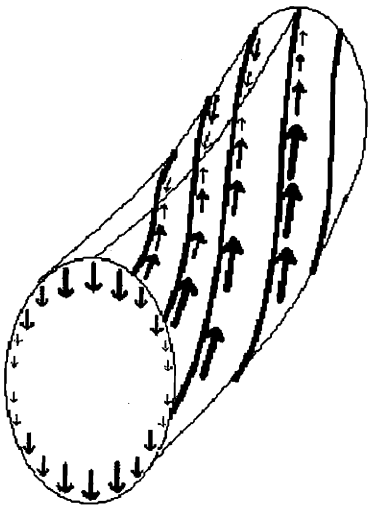

Figure 11-1: This figure illustrates the ion flow in the edge region in a situation where the ion ∇B drift is down.

of this situation is shown in Figure 11-1. The impurities are swept with this parallel return flow of the ions, because the impurity ion-background ion collision frequency $\nu Ii \approx 2\,\mu$s, is on the order of 40 times larger than the transit time (see Section 6.1.2). The ion flow returning at the top of the plasma just balances the loss due to the ∇B drift, but the impurities have a much lower ∇B drift, so they will tend to accumulate at the top. This is shown schematically in Figure 11-2. If one reverses the magnetic field, then the ion ∇B drift direction is up, and the whole picture reverses, so that impurities accumulate at the bottom of a flux surface. This was indeed observed in the L-mode experiments described in Section 11.3.1. However this theory only predicts moderate (less than a factor of two) asymmetries of the impurity density on a flux surface, so it does not agree qualitatively with our observations, which show a very strong asymmetry. The theory is valid when

$$\delta = \rho_{\theta i}/L_\perp \ll 1 \tag{11.2}$$

and

$$\Delta = \nu_i^* Z_I^2 \delta \ll 1 \tag{11.3}$$

where $L_\perp$ is the smallest characteristic radial scale length in the edge (typically, the density gradient scale length), $\rho_{\theta i}$ is the ion poloidal gyroradius, ν_i^* is the ion

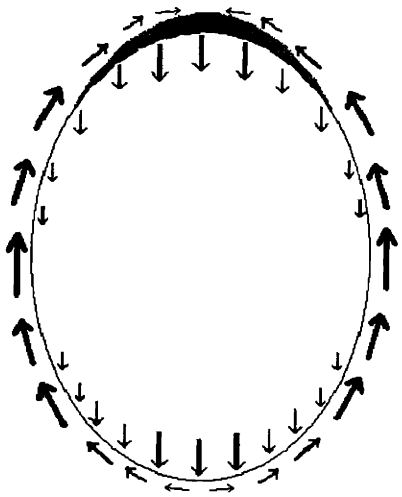

Figure 11-2: This figure shows a poloidal projection of the flows for the impurities. Although the impurities are also ∇B drifting downward, they do so at a rate which is 1/Z smaller than that of the ions. They are being carried along the field lines from the bottom to the top of the plasma with the ion return flow, which converges on the top, causing the impurities to accumulate on the top.

collisionality, and Z_I is the impurity charge. In the Alcator C-Mod H-mode edge, $\delta \approx 1$ and $\Delta \gg 1$, so the theory is not applicable. However, it does seem to capture the essential physics. It correctly predicts the change of sign of the up-down asymmetry which was observed in the hydrogen-like argon density, and it is consistent with the observations of CaF_2 injections. According to this physical picture, impurities injected at the outboard edge will be swept to the top and then start diffusing radially inward. The distinct bump seen only on the top array is completely consistent with the physical picture. In addition, this theory predicts that the asymmetry should grow with q^2. As shown in Section 10.3 the differences in x-ray pedestal location and width increase systematically with q_{95}, although the increase appears to be approximately linear rather than quadratic. Intuitively, one can understand the q^2 dependence in the following way. If the edge gradients remain the same, then the parallel ion return flow velocity must increase with q_{95} to compensate for the longer parallel path length from the bottom to the top of the plasma. The theory finds the steady state distribution of impurities by equating the parallel impurity pressure gradient force with the force on

the impurity fluid due to friction with the parallel bulk ion return flow. So this increase in return flow velocity should yield a stronger asymmetry, since one can sustain a stronger parallel impurity pressure gradient, linearly increasing with the parallel path length from the bottom to the top, πqR. At the same time, any fixed impurity parallel pressure gradient will manifest itself as a stronger poloidal impurity gradient because the parallel path length for a given poloidal excursion increases linearly with q. Combining these two effects, we find that the poloidal asymmetry should increase with q^2. The fact that we observe a scaling with q_{95} therefore supports that we have found the essential physics. The scaling we observe appears to be approximately linear with q_{95}, rather than with q_{95}^2. One may speculate that this could be because the bulk ion density gradient is inversely proportional to q_{95}. Recent results from the visible continuum diagnostic indicate that the electron density gradient does decrease with q_{95}, at least in EDA H-modes. It is well established that the particle confinement improves with higher plasma current (lower q_{95}, if B_t is kept fixed), so this would be consistent with other independent observations.

11.4 Inboard-outboard impurity density asymmetry

Another possible explanation for the observed asymmetry between the x-ray emissivity pedestal at the outboard edge and the top of the plasma is that there is a large inboard-outboard asymmetry. This would be consistent with the steady state differences observed. It would not, however, explain the injection results per se, since one would expect the injection to accumulate at the inboard side of the flux surfaces, away from the view of either soft x-ray array. However, it needs to be considered seriously because a new non-linear neoclassical theory, which incorporates the effects of the Pfirsch-Schlüter return flow, predicts that the strongest asymmetry should be an inboard-outboard asymmetry, with a significant, but weaker up-down asymmetry as well [47]. This theory is valid in the regime where $\Delta \gg 1$, which is the relevant case

for the H-mode edge in Alcator C-Mod. It still requires $\delta \ll 1$ which is usually not satisfied. When the theory is applied to a real Alcator C-Mod equilibrium, it predicts an inboard-outboard asymmetry of about 4, and an up-down asymmetry of roughly 2 [48]. This is not in agreement with our measurements. We measure an asymmetry of about a factor of 50 in H-mode. In addition, the theory does not reproduce the argon L-mode results reported by Rice et al., which showed a factor of 10 up-down asymmetry under some conditions. The theory predicts that the up-down asymmetry should change sign if the B-field is reversed, and that the inboard-outboard asymmetry should not change sign. The theory also predicts that the asymmetry should generally increase with q_{95}, although there is some nonlinear saturation mechanism, in particular for the up-down asymmetry.

11.5 Experiments at reversed magnetic field

The theoretical explanations for the impurity density asymmetry presented in this chapter predict that an up-down impurity density asymmetry should change sign if the magnetic field is reversed, but that an inboard-outboard asymmetry should not be affected by a reversed magnetic field. These predictions can be tested by reversing the magnetic field. This is not a trivial task, it requires several days of reconfiguration of the magnet power supplies, and expert physics operation of the tokamak. One week of reversed field operation was scheduled and completed in the 1999 run campaign, with one run day devoted to finding out if the impurity asymmetry would change character at reversed magnetic field. The experiment called for lower x-point H-modes at a range of plasma currents at a fixed reversed field, to investigate if the asymmetry would change character, and to establish its scaling with q_{95} at reversed magnetic field. It is a well known (but not well understood) fact that the H-mode power threshold is at least twice as high when the ion ∇B drift is away from the x-point as when it is towards the x-point. Therefore, very high RF heating power is required in order to get lower x-point H-modes at reversed field. Unfortunately, only one RF transmitter was available during the reversed field run week, limiting

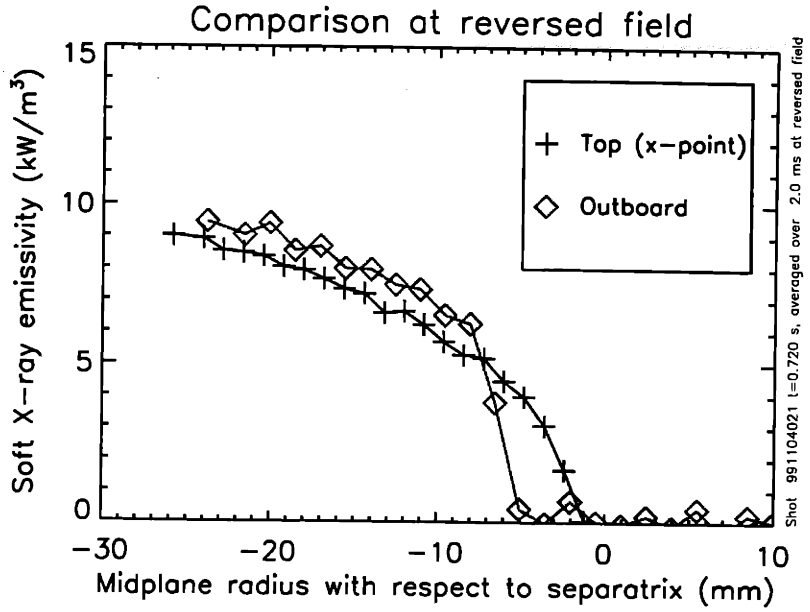

Figure 11-3: This figure shows the x-ray emissivity profiles at the top (x-point region) and the outboard edge for a reversed field, upper x-point H-mode. The profile at the outboard edge shows a distinct pedestal, similar to the pedestal seen at normal field, although it is located closer to the EFIT separatrix than at normal field. The x-ray emissivity profile at the top extends almost all the way to the separatrix (the x-point) but shows no distinct pedestal, rather the profile steepens gradually as one gets closer to the x-point.

the RF heating power to about 1.5 MW. It was not possible to produce lower x-point H-modes. However, it was possible to produce upper x-point H-modes. The up-down asymmetry in impurity density is not expected to be particularly sensitive to where the x-point is, so it was hoped that a clear signature of asymmetry reversal would be seen on these H-modes. However, this was not the case. In Figure 11-3 we show the x-ray emissivity profiles for one of the upper x-point H-modes that were achieved. The x-ray emissivity profiles at reversed field, upper x-point, are not too dissimilar from the lower x-point, normal field profiles, with the notable exception that there appears to be no clear pedestal at the top (x-point region). There is always a clear pedestal at the top in H-mode in the normal field, lower x-point H-modes we have studied so far. The pedestal at the outboard midplane is very distinct and clear, and it is located somewhat inside the separatrix, although perhaps not as far as we see in normal field operation. The soft x-ray emissivity at the top of the plasma extends almost all the way to the x-point, similar to what has been observed for normal field,

lower x-point H-modes. So, the soft x-ray emissivity pedestal position asymmetry does not seem to have changed sign in the reversed field plasma, but the absence of a distinct pedestal suggests that the physics in the x-point region is quite different from the physics in the rest of the edge plasma. It is a well-established fact that the neutral density in the x-point region is at least an order of magnitude higher than in the edge region away from the x-point, and this can lead to enhanced radiation from x-ray lines populated by a charge-exchange process with the neutrals. This effect has been measured for x-ray line photon energies around 4 keV [49], which would penetrate the beryllium filters with close to 100 % transmission, and would lead to an enhanced x-ray radiation near the x-point. This x-ray emission would be unrelated to the fluorine density profile. Therefore, we hesitate to draw any conclusions about the impurity (fluorine) density in the x-point region from these experiments. It is necessary to produce lower x-point, reversed field H-modes to get an unambiguous measurement of the impurity density profile at the top of the plasma at reversed field. This should be possible in the future, as the RF heating capability contines to be expanded and improved. These experiments should be run at high q_{95} to maximize the asymmetry.

11.6 Summary

The poloidal asymmetries observed between the soft x-ray emissivity profile at the outboard edge and the top of the plasma can only be partly explained by uncertainties in the EFIT equilibrium. At low values of q_{95} the asymmetries might be explained by such a field line mapping error, but at high values of q_{95} there are asymmetries in both pedestal location and width which are too large to be explained by EFIT mapping errors. This means that there are strong asymmetries in the soft x-ray emissivity in the region just inside the separatrix, which in turn implies that the impurity density shows a strong poloidal variation. Such strong poloidal impurity density asymmetries have previously been measured for argon on Alcator C-Mod. The asymmetry measured for argon was an up-down asymmetry, and reversed sign

when the magnetic field was reversed, which changed the ∇B direction of the ions from down to up. Neoclassical theories show some qualitative agreement with our observations, but only predict rather moderate asymmetries, at most a factor of four difference in impurity density on a field line. Depending on the theory, the dominant asymmetry predicted is either inboard-outboard, or up-down. The physical effect driving the poloidal asymmetry of impurity density is that there are strong bulk ion flows in the edge plasma, which drag impurities along field lines and can sustain parallel gradients in the impurity pressure by friction. The mechanism responsible for the up-down impurity density asymmetry is believed to be the Pfirsch-Schlüter return flow of the ∇B drifting ions. Thus, reversing the magnetic field should change the sign of the up-down asymmetry. Lower x-point H-mode discharges were attempted at reversed field, but were unsuccessful. Upper x-point H-modes were obtained at reversed field, and these show no pedestal at the top of the plasma but do show x-ray emission extending almost to the x-point, in apparent disagreement with the predictions of the theory for an up-down asymmetry. However, there is some concern that other radiation processes involving neutral atoms could lead to significant soft x-ray emission peaking near the x-point, where the neutral density is at least an order of magnitude larger than away from the x-point. This might explain that the x-ray emission extended to near the separatrix, and the observed lack of a sharp pedestal. Such x-ray emission would be essentially unrelated to the density of highly charged fluorine. Therefore, no strong conclusion can be based on the upper x-point experiment. Lower x-point, reversed field H-mode discharges must be produced to make a firm conclusion. Such discharges should preferably be run at high q_{95}, since the asymmetry is stronger. This will require very high RF heating power, which could be obtained in the near future.

Chapter 12

Conclusions and future work

12.1 Conclusions

Two generations of soft x-ray diagnostics with 1.5 mm radial resolution and 12 μs temporal resolution have been successfully designed, installed, and operated for the Alcator C-Mod run campaigns in 1997-1999. These diagnostics work reliably and have very good signal/noise ratios in H-mode, allowing detailed studies of the pedestal region. In H-mode, we observe a distinct and narrow pedestal, on the order of 1.5-6 mm, in the soft x-ray emissivity. Emissivity values at the top of the pedestal are a factor of 10-100 larger than in the same location in L-mode, where there is no sharp pedestal.

12.1.1 Radial impurity transport

A detailed analysis of the radiation processes responsible for the soft x-ray radiation has led to the conclusion that it is dominated by emission from fully ionized and hydrogen-like fluorine, except when large amounts of neon are present. In this case line emission from hydrogen-like neon dominates the soft x-ray emission at the plasma edge. When we combine the results from modelling of the radiative processes with highly resolved measurements of the electron density and temperature profiles near the plasma edge, we can extract absolutely calibrated density profiles of the fluorine

from the soft x-ray measurements. Typically, fluorine densities in H-mode are on the order of 0.1% of the electron density. These measurements show that the fluorine pedestal is shifted radially inward of the pedestals in electron density and temperature, near the top of the H-mode pedestal in the electron density. This inward shift is due to a strong inward convection of impurities. A strong inward convection localized near the H-mode edge has previously been observed in impurity injection experiments in a number of tokamaks around the world, including Alcator C-Mod. The highly resolved radial profiles of fluorine density near the plasma edge, which we derive from the soft x-ray emissivity profiles, allow us to measure the location of the inward pinch region with millimeter accuracy. It is found that the inward pinch region is located where the electron density gradient is strong, ie. in the electron density pedestal region. This is in agreement with one-dimensional neoclassical theory, which predicts a strong inward impurity pinch where there is a large plasma density gradient. Indeed, our measurements agree very well with simulations of the impurity transport if one assumes a neoclassical convection profile in combination with an empirical, anomalous diffusion coefficient. We also find that the width of the fluorine density pedestal, and therefore the width of the x-ray emissivity pedestal, increases with the diffusion coefficient D in the edge region of the plasma. Experimentally, we observe that the soft x-ray emissivity pedestal width is larger in the EDA H-mode than in ELMfree H-mode, which implies that the edge diffusion coefficient is larger in EDA H-mode, by as much as a factor of 10 in some cases, consistent with independent observations that EDA H-modes have much lower impurity confinement times than ELMfree H-modes. Other diagnostics have shown that the EDA H-mode is associated with coherent electron density fluctuations. Our measurements show that these fluctuations increase the outward diffusive transport of impurities in the edge plasma. We also observe that the x-ray pedestal width in EDA H-mode is a strongly decreasing function of plasma current, implying that the impurity diffusion coefficient decreases strongly with increasing plasma current. This suggests that the fluctuations in EDA are stronger at low current, consistent with the finding that the EDA H-mode is most easily achieved at moderate or high values of q_{95}. We also deduce that the edge diffu-

sion of impurities in EDA increases with increasing triangularity, and that it is larger when the current is ramping up than when the current is ramping down. We therefore predict that the impurity confinement time in EDA should be an increasing function of plasma current, decreasing function of triangularity, and that the impurity confinement time should be larger in EDA H-mode discharges where the current is ramping down than in discharges where the current is ramping up. These predictions can be tested independently by a series of dedicated impurity injection experiments. Thus, the soft x-ray edge diagnostics have provided new, highly resolved measurements of the radial transport of medium-Z impurities in the H-mode edge region. In particular, we have found scalings of the edge diffusivity with several plasma parameters in EDA H-mode, increasing our knowledge of the EDA H-mode and the instability which drives its enhanced transport of impurities.

12.1.2 Poloidal impurity transport and transient phenomena

The two-array diagnostic provides simultaneous measurements of the soft x-ray emissivity at the plasma edge, one at the outboard edge and the other at the top of the plasma. The diagnostic allows us to compare the soft x-ray emissivity on a millimeter radial scale and on a 12 μs time scale in two poloidally separate parts of the edge plasma. We find that in H-mode a soft x-ray emissivity pedestal exists both at the top and at the outboard edge, but the two pedestals differ with respect to location, width, and height. These differences become systematically larger at higher edge q_{95}. At low q_{95}, the differences are usually small, but at high q_{95}, the pedestal position is typically on a flux surface 11 mm further inside the plasma at the outboard edge than at the top of the plasma, and, in high q_{95} EDA H-modes, the width is typically a factor of 2 larger at the outboard edge than at the top. The height of the pedestal at the outboard edge is typically than at the top, so that the two profiles more or less overlap in the region inside the outboard edge pedestal. These differences imply that there are strong poloidal asymmetries in the impurity density in the transport barrier region, and thus, large parallel gradients in the impurity density exist. These parallel gradients are most likely driven by friction between the impurities and strongly flow-

ing background ions. This friction force can be large because the ion-impurity collision frequency is very large in the high density, moderate temperature edge region. If the ion flow is primarily due to the Pfirsch-Schlüter ion return flow, one should expect accumulation of impurities at the top of the plasma when the ion ∇B direction is down, as is usually the case in Alcator C-Mod. This is consistent with the asymmetry we observe. If one reverses the magnetic field direction, the ∇B drift changes sign, and the impurities would be expected to accumulate at the bottom of a flux surface instead. Experiments to produce H-modes at reversed field and upper x-point did not demonstrate this effect, but are hard to interpret because the top of the plasma is also the x-point region where the neutral density is very high. There is no sharp pedestal in the soft x-ray emissivity near the x-point in this situation. In order to resolve this issue, lower x-point reversed field H-modes at high q_{95} are needed. There are neoclassical theories which predict asymmetries in the distribution of impurities along field lines in the edge region, but none are applicable in the Alcator C-Mod H-mode edge. These theories show some qualitative agreement with our measurements, but there is no quantitative agreement. Our measurements imply that the impurity density can vary by factors of 10-30 on a field line, whereas the theories find at most factors of 4-5. Our measurements clearly show that the transport of impurities in the H-mode transport barrier region is at least two-dimensional, involving both the poloidal and radial transport, and that there is a need for more sophisticated theoretical work in order to accurately model the transport of impurities in the H-mode pedestal region. It is perhaps somewhat of a coincidence that the one-dimensional modelling of the radial transport using a neoclassical inward convection yields such good agreement with our experimental results at the outboard edge, since a one-dimensional model is not sufficient in the edge region of the plasma. We have also measured transitions from H-mode to L-mode where there is a timing difference between the transition at the outboard edge and that at the top of the plasma. The transition occurs first at the outboard edge, and then, with a delay of 10-20 μs, it is seen at the top of the plasma. This suggests that the instability which causes the transition is ballooning-like, that is, it is localized near the outboard edge.

12.2 Future work

The strong poloidal asymmetries in the impurity density measured by the soft x-ray arrays indicate that there are strong flows in the edge plasma, and that the transport of impurities is highly two-dimensional. In order to increase our understanding of these processes, a significant amount of both experimental and theoretical work needs to be done. On the experimental side, it is important to achieve H-modes at high q_{95} with reversed field and lower x-point, in order to unambiguously establish if the asymmetry changes sign when the ∇B direction changes sign. It would also be desirable to add a soft x-ray diagnostic on the inboard side, since there are some theoretical indications that there should be an inboard-outboard asymmetry in the impurity density. On the theoretical side, the theory by Fülöp and Helander [47], although probably the most sophisticated and accurate theory on this topic, is not valid in the Alcator C-Mod plasma edge in H-mode, because it assumes that the ion poloidal gyroradius is much smaller than the gradient scale lengths, which is not true in the C-Mod edge. It is very difficult to do analytic theory when the ion gyroradius is on the order of, or exceeds the gradient scale lengths. It may be necessary to resort to two-dimensional simulations of the impurity transport in order to address this issue more accurately. In addition, there is another, more subtle, assumption, which is not fulfilled. It is assumed in the theory that the parallel transport time scales are much smaller than the radial transport time scale, so one can solve for the parallel distribution of impurities without considering the radial transport. However, with a 2 mm radial scale length and a radial inward pinch velocity of 100 m/s, the time scale for radial transport can be as low as 20 μs. An impurity particle with a parallel (near-thermal) velocity of 20 km/s can travel 40 cm along a field line in that time, a very short distance compared to the parallel connection length, which, near the plasma edge, is tens of meters. It therefore appears that it is necessary to solve the radial and poloidal transport equations simultaneously, maintaining the assumption that there is toroidal symmetry. This would probably require a two-dimensional computer model of the impurity transport, similar to the one-dimensional MIST code, but with

information about the poloidal flows of the background ions built into the model. One approach would be to use the output of some of the existing two-dimensional bulk plasma simulation codes which have been developed recently [40], [41], [42], or detailed experimental measurements of the ion flows in the edge region, if these are available. It would be highly desirable to measure directly the ion flows in the edge region of the plasma with high radial resolution and some poloidal resolution, since poloidal and radial variations are expected to be significant, if these flows are the cause of the large asymmetries that we observe. The observations of timing differences between the H-L transition at the outboard edge and the top of the plasma should be examined further, with a faster response time of the electronics, and perhaps higher sampling frequencies. If the timing delay is due to parallel propagation of the plasma perturbation along field lines from the outboard edge to the top of the plasma, then the delay should be larger at higher q_{95}, and it should be larger when the x-point is at the top rather than at the bottom of the plasma. These predictions can and should be tested experimentally.

Appendix A

Noise reduction techniques

Most of the noise on the raw signals of edge x-ray diodes is random noise which can be reduced by time-averaging the data, thus lowering the temporal resolution. Systematic noise is also found in the data, and this is sometimes a problem. This Appendix describes the efforts to identify the sources of the systematic noise, and the efforts to eliminate such noise from the measured signals. The systematic noise sources were the same for both arrays 2 and 4, and we observed no change in the noise character for array 2 between the 1997-1998 run campaign and the 1999 run campaign.

A.0.1 Circuit board voltage pickup noise

When looking at data with rather low signal levels, such as L-mode data or very weak H-mode data, the random noise is often a significant fraction of the measured signal, and thus, the data is smoothed by averaging over several time samples. This means that the temporal resolution is degraded, but this is acceptable if the phenomenon studied does not vary rapidly in time. When studying raw signals of L-mode data with signal amplitudes around 10-50 nW (H-mode amplitudes are typically 500-1000 nW), a systematic source of noise was discovered, since it does not disappear when averaged over many time samples (10-100 ms). An example of data averaged over 200 ms during a period where there was no plasma in the view of the edge x-ray array

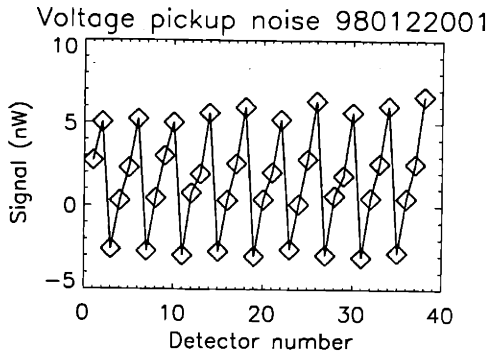

Figure A-1: Voltage pickup noise in the absence of plasma, showing the cyclic behavior. Data averaged over 200 ms.

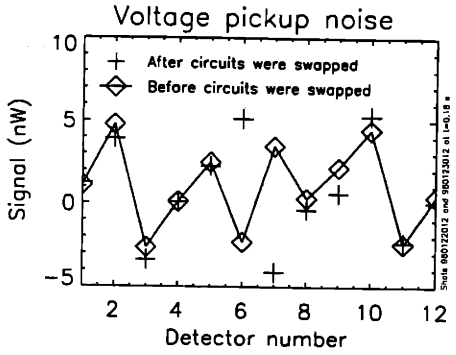

Figure A-2: Pickup noise on channels 1-12 before and after the inputs and outputs to the circuit boards were switched for detectors 6 and 7. It is seen that the pickup noise on detectors 6 and 7 has been swapped as well.

is shown in Figure A-1. The cyclic nature of the noise as a function of the detector number indicates clearly that this is no plasma phenomenon. The amplitude is so low that the random noise completely dominates unless one averages over many time samples.

Identification

The noise signal has been identified as voltage pickup in the circuit boards, which are located below the Alcator C-Mod tokamak. This has been confirmed by switching cables around for detectors 6 and 7, such that the signals from detector 6 went through the circuit previously used by detector 7, and vice versa, but everything else remained the same, eg. the digitizer used for detector 7 was the same before and after the switch. After the switch was made, the noise levels on detector 6 and 7 were swapped, as seen on Figure A-2. Thus, it was established that the noise originates in the circuit boards.

The magnitude of this circuit board pickup noise correlates with the voltage on the EF4 magnet, and also seems to depend on the voltage on the OH1 coil (closely related to the plasma loop voltage), although it was not possible to find a simple linear relationship between the magnitude of the pickup noise and various magnet voltages.

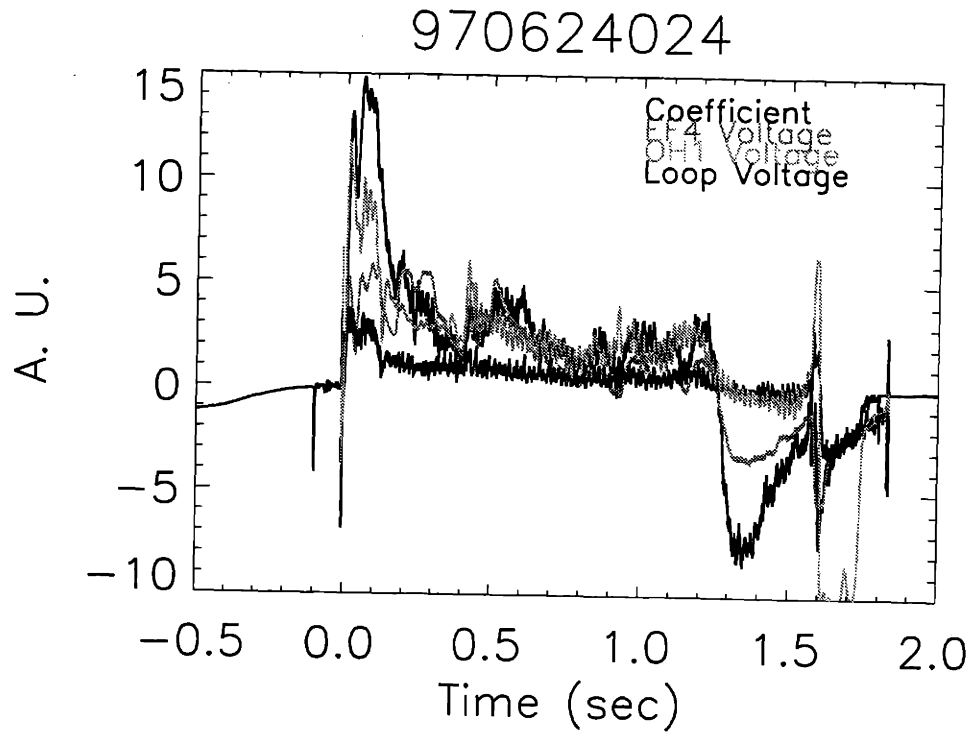

Figure A-3: Time traces of the pickup noise amplitude coefficient, the OH1 and EF4 coil voltages and the loop voltage (arbitrary units)

An example of the noise amplitude (as calculated in Section A.0.1), and various voltages is shown in Figure A-3. This indicates that the electric circuits in the circuit boards link flux from EF4 and possibly other magnets, so that voltages are induced in the circuit boards when coil fluxes change. Luckily, the main flux changes occur at the very beginning of the shot, and at the termination of the shot, so the pickup noise is usually low when there is significant plasma signal. The difficulty in finding a simple linear relationship between the coil voltages and the pickup noise amplitude can be explained by noting that flux changes in the coils induce eddy currents in the stainless steel cylinder surrounding the coils, thus making the coupling between the circuit board and the coil magnetic fluxes time dependent.

Removal

A method for determining the amplitude of the pickup noise, and then removing it from the signals, has been developed. Software has been written to do this automatically. The procedure is outlined in the following. The raw signal profile at a given instant in time can be thought of as a vector in a 38-dimensional space, one dimension for each detector signal. It was confirmed for a number of shots that the pickup noise always showed the same cyclic pattern, so the noise vector in the 38-dimensional space always points in the same direction. Thus, one can define a unit vector in that direction, $\mathbf{n}_{38}$, and the component of any signal vector in the direction of the noise vector can be calculated by a simple projection formula, and can then be subtracted from the signals. This method, although it works reasonably well, is somewhat flawed. The problem is, that a given measured signal, $\mathbf{s}_t$, consists of a noise component. $\mathbf{s}_n$, parallel to the noise unit vector, plus a plasma signal component, $\mathbf{s}_p$, which in general also has a finite component in the direction of the unit noise vector. Mathematically,

$$\mathbf{s}_t = \mathbf{s}_p + \mathbf{s}_n \tag{A.1}$$

and generally

$$\mathbf{s}_p \cdot \mathbf{n}_{38} \neq 0 \tag{A.2}$$

Thus, if one simply subtracts the projection of the total signal vector onto the unit noise vector direction, one will remove more (or less) than just the noise component $\mathbf{s}_n$ itself. In order to minimize this error, a slightly more sophisticated technique was used. The outermost channels (1-12)[1] usually only have rather low signal levels, and never see the steep gradient region indicative of the H-mode transport barrier. They are affected by the pickup noise to the same extent that all other channels are (see Figure A-1), and therefore the signals on these channels are well suited for determination of the pickup noise amplitude (ie. the magnitude of the pickup noise component of the signal). So it is beneficial to estimate the noise amplitdue from

[1]For the new apertures, channels 27-38 were the outermost channels. The noise reduction technique for the old array, described in this section, was successfully used for the new designs by using detectors 27-38 instead of 1-12 to estimate the noise level.

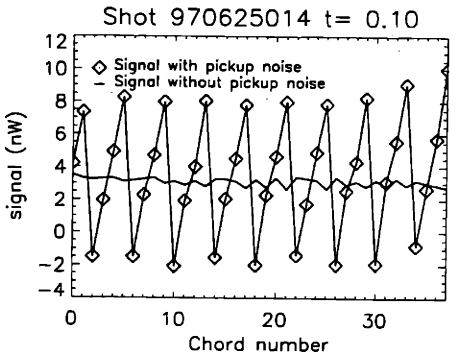

Figure A-4: Demonstration of voltage pickup removal on signal in the absence of plasma

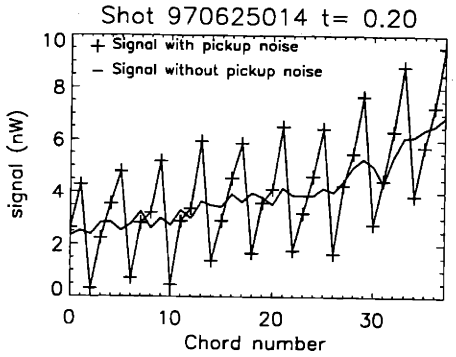

Figure A-5: Voltage pickup removal on signal from very tenuous plasma

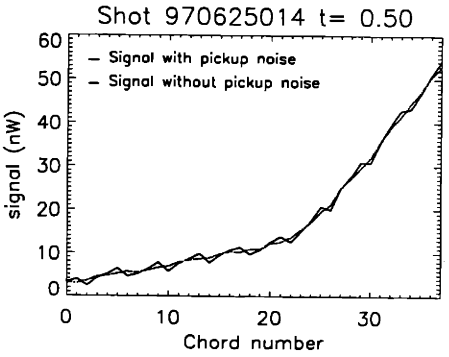

Figure A-6: Example of voltage pickup removal on signal for L-mode plasma

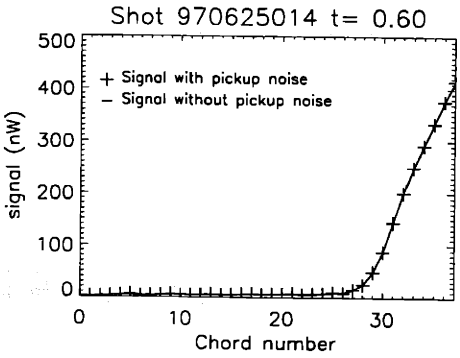

Figure A-7: Voltage pickup removal on signal from H-mode plasma. Note that due to the large signal, the voltage pickup no longer affects the signal.

detectors 1-12 only. In addition, it is generally true that the (small) plasma signal on channels 1-12 only rises slowly, and approximately linearly, since these channels usually only view open field lines. By making sure that the 12-dimensional unit noise vector $\mathbf{n}_{12}$ is orthogonal to a linearly increasing signal (which requires slight alterations of the noise vector), one can minimize the component of $\mathbf{n}_{12}$ onto the plasma signal, ie. one can minimize the aforementioned error. Thus, the coefficient $c = \mathbf{n}_{12} \cdot \mathbf{s}_t(1:12)$ is used when subtracting $\mathbf{n}_{38}$ (suitably normalized) from $\mathbf{s}_t$. Examples of the method employed for various signal levels are shown in Figures A-4 to A-7. The examples show that the method works quite well, so that the plasma signal can be extracted,

even in the cases where the pickup noise dominates the signal. In the case of good H-mode data, the signals are so strong that the pickup noise does not affect the data at all, and consequently, it makes no difference if it is removed or not.

Effects on emissivity profiles

The voltage pickup noise is a serious problem for inverted data, since it introduces an error between adjacent detectors. It has been shown by Ramsey and Diesso [19] that a detector-to-detector error results in relative errors in the deduced emissivities whose magnitudes are 3-4 times the relative detector signals themselves. This can be understood intuitively, since, in a simplified picture, the emissivity on a given flux surface is deduced by looking at the difference of adjacent chord integrated raw signals. For the edge x-ray inversion, the emissivity profiles are much more strongly affected than the raw signals themselves. As an example of this, one can compare the profile of raw data in Figure A-6 with the surface plot of emissivity for the same shot, around the same time, shown in Figure A-8. In this example the noise reduction algorithm is necessary to see the real data at all. In Figure A-9 the same data is shown, with the noise reduction algorithm applied. The noise reduction algorithm works very well, although there is still some residual noise present. This noise can be further reduced by degrading the radial resolution from 1.7 mm to 2.5 mm, as is shown in Figure A-10. The resulting emissivity profiles show a pedestal-like shape, the steep gradient region being near the separatrix. It is impossible to see such details in the noisy emissivity profile in Figure A-8. In Figures A-11 to A-12 another example of inverted L-mode data is shown. In this case, neon was injected into the plasma, so the emissivity was quite high. Therefore the pickup noise did not affect the data as much as the example shown in Figures A-8 to A-10. However, the noise reduction is still necessary, and does improve the data significantly. A steep region near the separatrix is also visible in this case, although it is less evident.

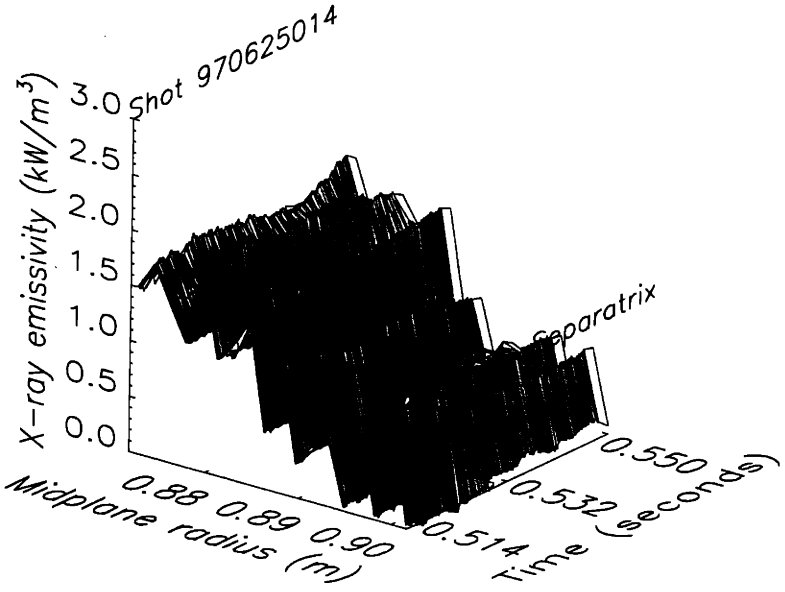

Figure A-8: A surface plot of the radial emissivity profile during an L-mode shows the pickup noise very clearly. The real plasma signal is difficult to make out, even though the data has been smoothed over 13.6 ms.

A.0.2 EFC noise removal

Identification

When the pedestal fitting routine was automated, it was found that the pedestal parameters would oscillate with what appeared to be a fixed frequency, when the data was sampled at 83.3 kHz (12 μs sampling time). A Fourier analysis of the raw data showed a rather strong peak around 3240 Hz and another one at twice that frequency. An example of a Fourier spectrum is shown in Figure A-14. The oscillation is visible in the raw data, with an amplitude which in the worst cases observed is about 30 nW peak to peak, or about 2-3 times the random noise. It is as large even on the detectors which are far in the scrape-off layer. The x-ray emissivity signal is very low on these channels, so this convinced us that the oscillations are not due to real oscillations in the soft x-ray emissivity, but must be some kind of noise. This frequency is very similar to the frequency of the fast power supply to the EFC magnet, responsible for the feedback stabilization of the vertical position of the

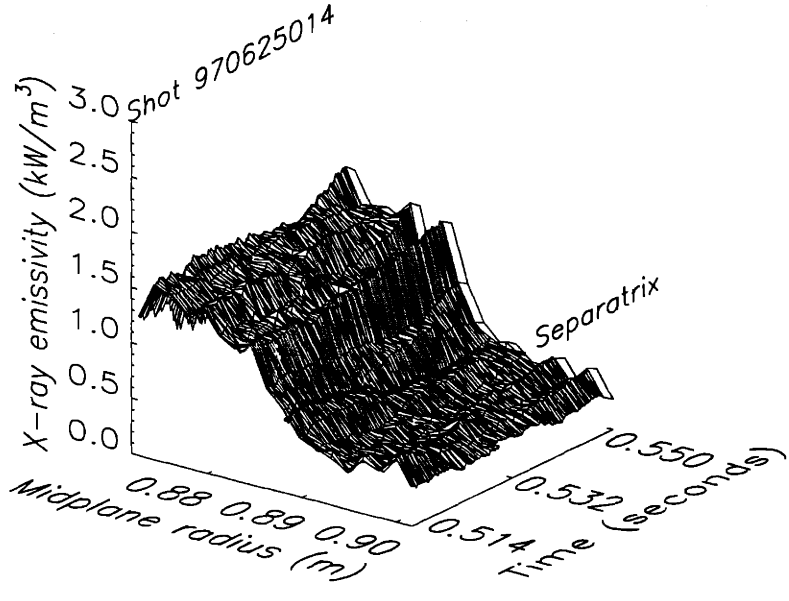

Figure A-9: A surface plot of the radial emissivity profile for the same data as in Figure A-8, but with the pickup noise removal algorithm applied to the raw data. Now the plasma signal is clearly seen, although some residual noise still appears. The data has also been averaged over 13.6 ms to reduce the random fluctuations.

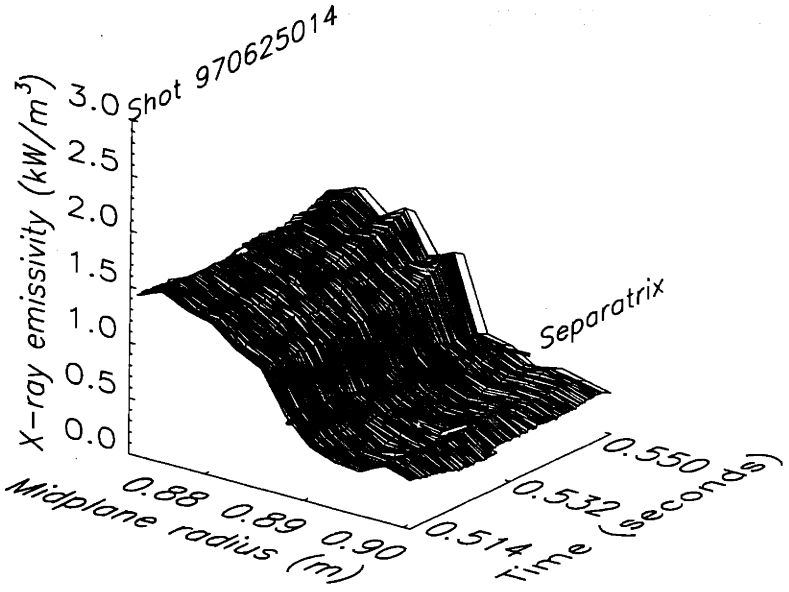

Figure A-10: A surface plot of the radial emissivity profile with the pickup noise removed and the radial resolution degraded from 1.7 mm to 2.5 mm. Now the pickup noise is virtually absent. Signals have been smoothed in time over 13.6 ms.

plasma. It was confirmed that the frequency of the fast power supply is indeed the same as the frequency of the oscillation in the raw data, within the error bars, which are small. In Figure A-15 we show a time trace of raw data together with the EFC bus voltage, where the correlation is visible.

Removal

In Figure A-15 we also show a time trace of the same raw data after the EFC noise has been filtered away. The filtering routine is rather straightforward, since the spectral signature of the noise is so distinct. The peaks at 3240 and 6480 Hz are simply suppressed by reducing the Fourier components of the two peaks to amplitudes similar to those found for frequencies close to the peaks. The fast sampled data are divided up into windows of approximately 2.4 ms, and the noise reduction is done by performing a forward discrete Fourier transform, removing the peaks, and performing the inverse discrete Fourier transform afterwards. It was found that if one used a

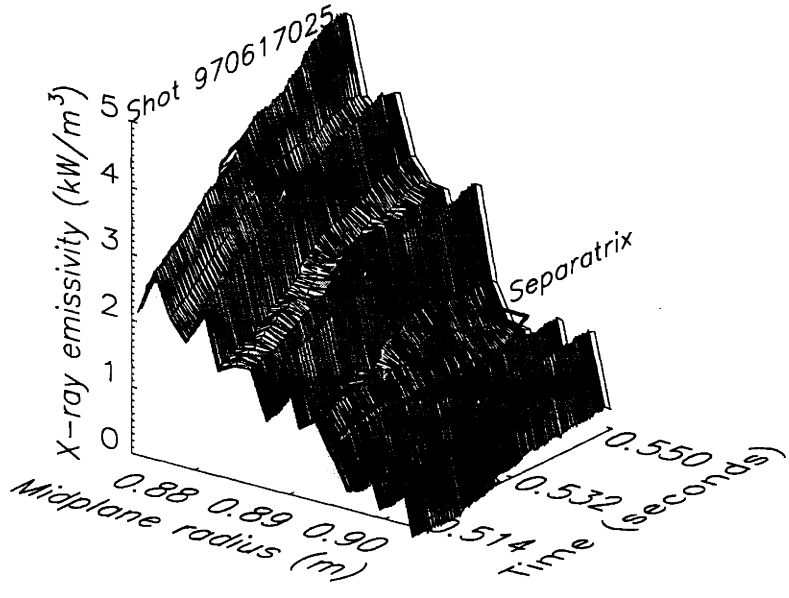

Figure A-11: A surface plot of the radial emissivity profile during another L-mode, after a neon injection. Because the neon injection enhances the x-ray emissivity, the pickup noise does not completely dominate the signal, as it does in Figure A-8. However, it makes it hard to see any details in the profile. Data has been smoothed over 13.6 ms.

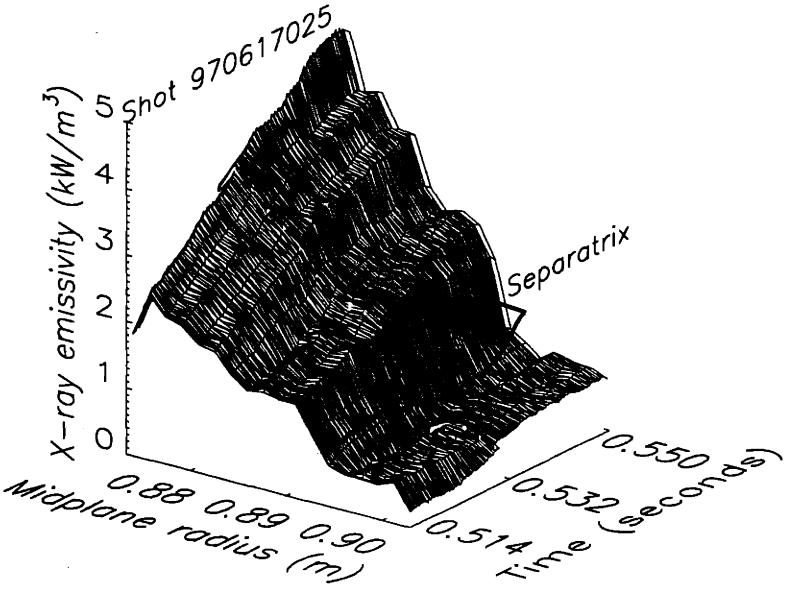

Figure A-12: A surface plot of the radial emissivity profile for the same data as in Figure A-11, but with the pickup noise removal algorithm applied to the raw data, showing a marked improvement. Data has been averaged over 13.6 ms.

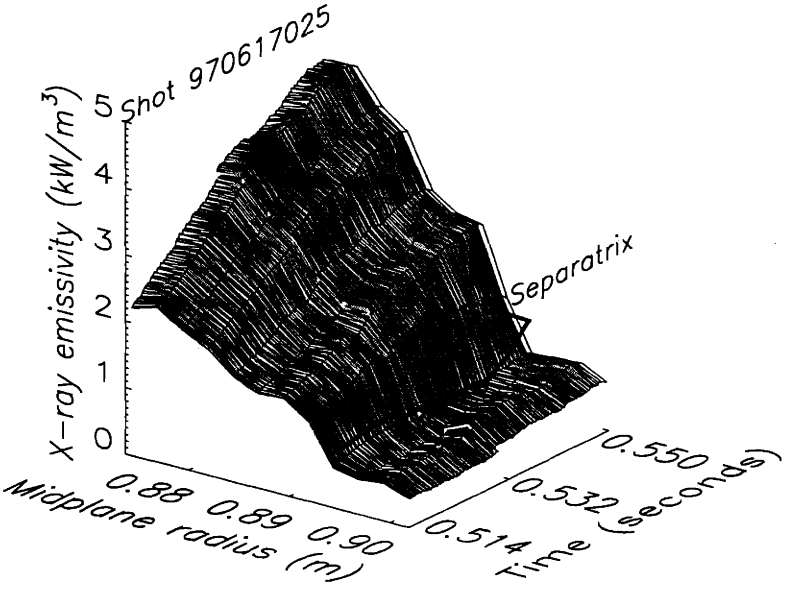

Figure A-13: A surface plot of the radial emissivity profile with the pickup noise removed and the radial resolution degraded from 1.7 mm to 2.5 mm. A rather smooth profile appears.

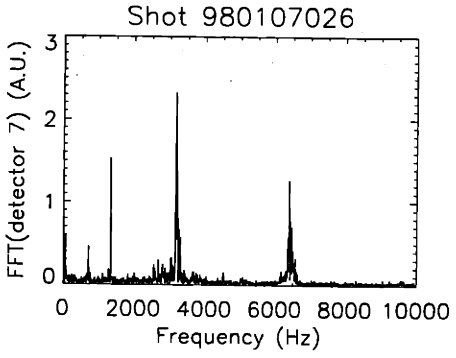

Figure A-14: Fourier spectrum of raw signal. The two peaks at around 3240 Hz and 6480 Hz are clearly visible, as are two other peaks. These other peaks are not always present in the data but are also believed to be unrelated to the plasma x-ray radiation.

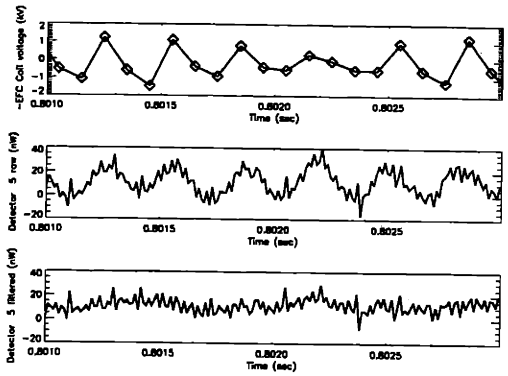

Figure A-15: Time traces of the EFC Bus voltage, the raw signal from one of the edge x-ray detectors, and the same signal, filtered to eliminate the EFC-correlated noise.

significantly longer time window, the noise would only be reduced in part of the signal but actually worsened at other times of the shot. The window had to be kept longer than a few wavelengths of the noise signal in order to ensure that it could be identified unambiguously compared to the rest of the signal. Results for two of the pedestal parameters are shown in Figures A-16 and A-17. It is clear from the data that the noise influences the pedestal data rather heavily, and that the noise reduction algorithm reduces the fluctuation amplitude by more than a factor of two. Since the frequencies filtered away are so distinct, the data still contains information about fast fluctuations, such as Edge Localized Modes (ELMs). These fluctuations are not affected by the filtering. However, the filtering appears to be less efficient when the plasma is in ELMy H-mode. Because of the broadband character of the frequency spectrum when ELMs are present, the amplitudes of Fourier modes with frequencies close to the noise frequency are elevated, and thus less signal is subtracted.

It was decided not to attempt filtering away the noise from the slow sampled data (5 kHz or 0.2 ms), even though it is present, aliased to 5000-3240=1760 Hz. Simply averaging over 5 samples also gets rid of the noise. The corresponding degradation from 0.2 ms to 1 ms temporal resolution is usually not important. For the fast sampled data, this approach would have led to a degradation of the spatial resolution from 12

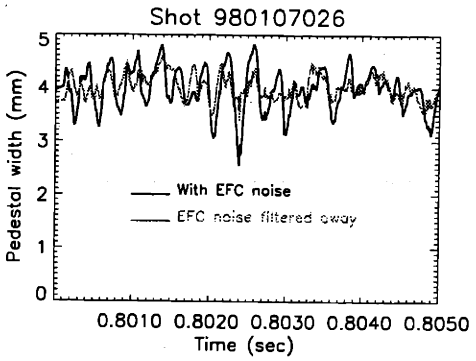

Figure A-16: Demonstration of noise removal from the fitted pedestal widths in H-mode plasmas. It is seen that the oscillations induced are rather large, with peak-to-peak amplitudes on the order of 1 mm. The noise level on the fitted pedestal width after filtering is much smaller, by more than a factor of two.

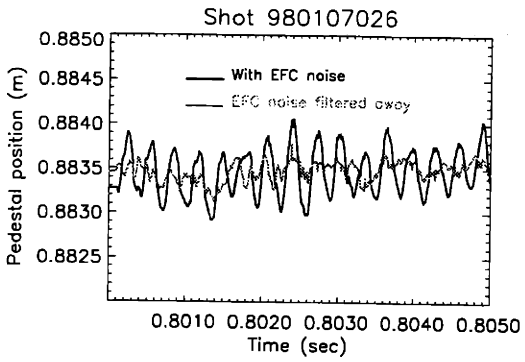

Figure A-17: Effects of the EFC noise on the fitted pedestal position in H-mode. In this case a 1 mm oscillation is visible before filtering. Filtering reduces the noise amplitude by more than a factor of two.

μs to 1 ms, and thus important information about eg. ELMs would have been lost.

Appendix B

Optimization procedure for new apertures

The new edge x-ray apertures were designed to give optimal performance in terms of having the best edge coverage, resolution, and signal/noise ratio achievable. The optimization process was done by modelling the performance on a computer in the following way:

- A particular design is chosen, ie. the position, orientation and width of the aperture are specified.
- The geometry matrix for this design is calculated, ie. the region in the view of the detectors is broken into many small volumes (voxels) and for each of these volumes, its contribution to the signal on each detector is calculated.
- In order to model a typical H-mode plasma, a pedestal-like emissivity profile $\mathbf{e}_{\text{assumed}}$, consistent with profiles measured with the previous x-ray diagnostic, is assumed.
- The emissivity is assumed constant on a flux surface, as given by a typical EFIT H-mode plasma equilibrium.
- The chord integrated emissivities (brightnesses, or incident photon power) for each detector in the array are calculated using the matrix inversion program.

The matrix inversion program calculates the emissivity given a certain EFIT equilibrium and the chord integrated emissivities s_i by calculating the matrix $\mathbf{C}$ linking the emissivity profile $\mathbf{e}$ to the chord integrals (raw signals) $\mathbf{s}$ by the equation $\mathbf{C}\times\mathbf{e}=\mathbf{s}$. It then inverts the relationship so that $\mathbf{e}$ can be calculated given $\mathbf{s}$ (see Section 3.1 for more details). In this case, we use the matrix $\mathbf{C}$ directly to calculate the expected raw signals, given the particular geometry and the assumed emissivity profile $\mathbf{s}_{\text{simulated}} = \mathbf{C}\times\mathbf{e}_{\text{assumed}}$.

- Random noise is added to the calculated raw signals to simulate the real noise levels on the detectors. The random noise is at a constant level, independent of the signal level. This is consistent with what has been observed on the first edge x-ray diagnostic. Therefore, a higher signal level automatically yields a higher signal/noise ratio.

- The inversion program is then used to calculate an emissivity profile $\mathbf{e}_{\text{noisy}}$from the noisy raw signals.

- The assumed emissivity profile $\mathbf{e}_{\text{assumed}}$ is compared to $\mathbf{e}_{\text{noisy}}$.

- This procedure is repeated with smaller and smaller flux shell thicknesses, until the inversion becomes unreliable due to noise sensitivity. This way, the best possible spatial resolution is established for a particular design.

- As a byproduct of these calculations, the coverage is established, ie. which region of the plasma is viewed. Since the number of detectors is fixed at 38, increased coverage means decreased spatial resolution and vice versa.

Solving iteratively, we found the optimum design which gives adequate coverage of the edge region at high spatial resolution and high signal/noise ratio. This optimization process led to a design for the top array which had roughly 3 times better signal/noise ratio, and a 30% better spatial resolution. This design does not cover much of the scrape-off layer, in fact it may not cover the separatrix for some plasma equilibria, but since the x-ray pedestal at the outboard edge was located some 10 mm inside

the separatrix, this was thought to be acceptable. This assumption turned out to be wrong, as discussed in Chapter 10

References

[1] J. Wesson, "Tokamaks", Oxford Science Publications, 2nd edition (1997)

[2] L.A. Artsimovich, G.A. Bobrovsky, E.P. Gorbunov, D.P. Ivanov, V.D. Kirillov, E.I. Kuznetsov, S.V. Mirnov, M.P. Petrov, K.A. Razumova, V.S Strelkov, Nucl. Fusion, Special suppl. (1969), p. 17

[3] F.F. Chen, "Introduction to plasma physics", Plenum Press, New York, 2nd edition, (1984).

[4] W.M. Stacey, "Fusion Plasma Analysis", John Wiley and Sons, New York (1981)

[5] J.P. Freidberg, "Magnetohydrodynamics", Plenum Press (1987)

[6] K.H. Burrell, Phys. Plasmas **4** (1997), p. 1499

[7] I.H. Hutchinson et al., Phys. Plasmas **1** (1994), p. 1511

[8] F. Wagner, G. Becker, K. Behringer, D. Campbell, A. Eberhagen, W. Engelhardt, G. Fussmann, O. Gehre, J. von Gernhardt, G. Gierke, G. Haas, M. Huang, F. Karger, M. Keilhacker, O. Klüber, M. Kornherr, K. Lackner, G. Lisitano, G.G. Lister, H.M. Mayer, D. Meisel, E.R. Müller, H. Murmann, H. Niedermeyer, W. Poschenrieder, H. Rapp, H. Röhr, F. Schneider, G. Siller, E. Speth, A. Stäbler, K.H. Steuer, G. Venus, O. Vollmer, Z. Yu, Phys. Rev. Letters **49**, p. 1408 (1982)

[9] M. Greenwald, R.L. Boivin, F. Bombarda, et al, Nucl. Fusion **37**, p. 793 (1997)

[10] W. Suttrop et al, Plasma Phys. Contr. Fusion **39**, p. 2051 (1997)

[11] M. Kotschenreuter, W. Dorland, et al, Fusion Energy 1996 (Proc. 16th IAEA Conference, Montreal), p. 371 (1996)

[12] H. Zohm, Plasma Phys. Contr. Fusion **38** 1996, p. 1213

[13] M. Greenwald, R. Boivin, P. Bonoli, R. Budny, C. Fiore, J. Goetz, R. Granetz, A. Hubbard, I. Hutchinson, J. Irby, B. LaBombard, Y. Lin, B. Lipschultz, E. Marmar, A. Mazurenko, D. Mossessian, T. Sunn Pedersen, C.S. Pitcher, M. Porkolab, J. Rice, W. Rowan, J. Snipes, G. Schilling, Y. Takase, J. Terry, S. Wolfe, J. Weaver, B. Welch, S. Wukitch, Phys. Plasmas, **6**, p. 1943, (1999)

[14] M. Bures, D.J. Campbell, N.A.C. Gottardi, J.J. Jacquinot, M. Mattioli, P.D. Morgan, D. Pasini, D.F.H. Start, Nucl. Fusion **32** (1992), p. 539

[15] K. Burrell reported on a confinement mode rather similar to the EDA H-mode in an oral contribution at the 41st APS DPP Meeting in Seattle, WA, Nov. 1999

[16] M.C. Borrás and R.S. Granetz, Plasma Phys. Controlled Fusion, **38** (1996), p. 289

[17] L.L. Lao, H. St. John, R.D. Stambaugh, A.G. Kellman, and W. Pfeiffer, Nucl. Fusion **25** (1985) p. 1611

[18] R.J. Groebner and T.N. Carlstrom, Plasma Phys. Controlled Fusion **40** (1998) p. 673

[19] A.T. Ramsey and M.Diesso, Rev. Sci. Instruments **95** (1999) p. 380

[20] A.E. Hubbard, R.L. Boivin, R.S. Granetz, M. Greenwald, I.H. Hutchinson, J.H. Irby, Y. In, J. Kesner, B. LaBombard, Y. Lin, J.E. Rice, T. Sunn Pedersen, J.A. Snipes, P.C. Stek, Y. Takase, S.M. Wolfe, S. Wukitch, Phys. Plasmas **5** (1998), p. 1744

[21] T. Sunn Pedersen and R.S. Granetz, Rev. Sci. Instrum. **70** (1999), p. 588

[22] A.E. Hubbard, "Physics and Scaling of the H-mode Pedestal", submitted to Plasma Phys. Contr. Fusion in October 1999

[23] M.A. Graf, J.E. Rice, J.L. Terry, E.S. Marmar, J.A. Goetz, G.M. McCracken, Rev. Sci. Instruments, **66**, p. 636 (1998)

[24] A.W. Leonard, A. Hermann, K. Itami, J. Lingertat, A. Loarte, T.H. Osborne, W. Suttrop, the ITER Divertor Modelling and Database Expert Group, the ITER Divertor Physics Expert Group, J. Nucl. Materials, **266-269** (1999), p. 109

[25] J.A. Snipes, R.S. Granetz, M. Greenwald, A.E. Hubbard, I.H. Hutchinson, J. Irby, J. Kesner, S. Migliuolo, T. Sunn Pedersen, J. Ramos, J. Rice, P.C. Stek, Y. Takase, S.M. Wolfe, Plasma Phys. Contr. Fusion **40** (1998), p. 765

[26] J. Terry, private communication

[27] R.C. Isler, Nucl. Fusion **24** (1984), p. 1599

[28] F.L. Hinton and R.D. Hazeltine, Reviews of Modern Physics, **48** (1976), p. 239

[29] C.T. Hsu and D.J. Sigmar, Plasma Phy. Contr. Fusion **32** (1990), p. 499

[30] P.H. Rutherford, Phys. Fluids **17** (1974), p. 1782

[31] R.H. Huddlestone and S.L. Leonard (eds.), "Plasma diagnostic techniques", p. 388, Academic Press (1965)

[32] R.A. Hulse, Nuclear Technology/Fusion **3** (1983) p. 259

[33] The NRL Plasma Formulary, revised edition (1998), p. 28

[34] The NRL Plasma Formulary, revised edition (1998) p. 32. The $\nu_{\|}$ formulas were used ("fast" for ν_{iI}, and "slow" for ν_{Ii}).

[35] J.E. Rice, J.L. Terry, J.A. Goetz, Y. Wang, E.S. Marmar, M. Greenwald, I. Hutchinson, Y. Takase, S. Wolfe, H. Ohkawa, and A. Hubbard, Phys. Plasmas **4** (1997), p. 1605

[36] J.E. Rice, private communication

[37] D. Pasini, R. Giannella, L. Lauro Taroni, M. Mattioli, B. Denne-Hinnov, N. Hawkes, G. Magyar and H. Weisen, Plasma Phys. Contr. Fusion **34** (1992), p. 677

[38] M.E. Perry, N.H. Brooks, D.A. Content, R.A. Hulse, M. Ali Mahdavi, H.W. Moos, Nucl. Fusion **31** (1991), p. 1859

[39] ASDEX Team, Nucl. Fusion **29** (1989), p. 1959

[40] T.D. Rognlien, D.D. Ryutov, N. Mattor, Czechoslovak Journal of Physics, **48**, p. 201 (1998)

[41] T.D. Rognlien, D.D. Ryutov, N. Mattor, G.D. Porter, Phys. Plasmas **6**, p. 1851 (1999)

[42] X. Xu, Invited talk at the APS DPP Meeting in Seattle, WA, (1999). Submitted to Phys. Plasmas

[43] J.E. Rice, private communication

[44] J.E. Rice *et al.*, Nucl. Fusion **37**, p. 241 (1997)

[45] K. Burrell, S.K. Wong, Nucl. Fusion **19**, p. 1571 (1979)

[46] D. Pfirsch and A. Schlüter, Max Planck Institut Report MPI/PA/7/62 (unpublished) (1962)

[47] T. Fülöp and P. Helander, Phys. Plasmas **6**, p. 3066 (1999)

[48] P. Helander, private communication

[49] J.E. Rice, F. Bombarda, M.A. Graf, E.S. Marmar, J.L. Terry, Y. Wang, Fusion Eng. and Design, **34-35**, p. 159 (1997)